Experimental and Finite Element Investigation of Springback of Aerospace/Automotive Sheet Metal Products

by

Ihab Ragai, M.Sc., P.Eng.

A thesis submitted to McGill University in partial fulfillment of the requirements of the degree of Doctor of Philosophy

Department of Mechanical Engineering

McGill University

Montreal, Quebec, Canada

August 2006

Your file Votre référence
ISBN: 978-0-494-32232-1
Our file Notre référence
ISBN: 978-0-494-32232-1

"If we knew what it was we were doing,
it would not be called research, would it?"
– Albert Einstein

ABSTRACT

Springback is a phenomenon that occurs when nonhomogeneous elastic and plastic deformation occurs throughout a component during forming processes. Since the elastic deformation is recovered when the forming load is removed, geometrical changes occur. Springback is particularly important in sheet forming; therefore, in order to provide formed parts of close tolerances it is essential to first have a good understanding of the factors which affect springback and to be able to determine the extent those factors have. It is also important to be able to predict springback under different conditions so that it can either be minimized or properly accounted for in the process design. This research presents work done thus far on understanding and predicting springback in sheet metal forming of stainless steel 410 and inconel 718, which have a wide range of usage in the aerospace industry as well as dual-phase steels 600/300 and 600/400 which are used in the automotive sector.

The role that the anisotropy plays in the springback is assessed in this work. The effect of normal anisotropy on springback for the aerospace materials is considered while the automotive materials were considered perfectly isotropic and only the effect of forming conditions was studied. In order to characterize the materials and their anisotropic behaviour, a series of mechanical tests is conducted. These tests include standard uniaxial tension and uniaxial tension-compression tests. Moreover, a series of simple multiple-bending experiments were conducted on the aerospace materials (steel and Ni based alloys) to examine the effect of specimen orientation on the springback in simple bending.

Furthermore, since process conditions have an obvious effect on springback and one of the most important of these is the blank holding force, 2D draw bending experiments are conducted with varying blank holding force to assess its role in springback of the formed part. The combined effect of anisotropy and blank holding force was also studied for the aerospace materials.

Finite element simulations that include only either classical isotropic hardening or kinematic hardening did not show close agreement with the experimental findings especially for springback prediction. Therefore, to properly simulate springback a material model that combines both hardening effects, along with the material anisotropy, has been developed in this work. The developed finite element model implements isotropic hardening as well as kinematic hardening based on the Mróz multiple-yield surface formulation. Hill's 1948 yield function with normal anisotropy is considered. The developed material model has been tested by simulating the tension-compression experiments and a good agreement was reached.

Furthermore, to demonstrate the model capability, bending experiments were simulated. Springback angles predicted by the model reflected those obtained experimentally for the simple multiple-bending experiments. Moreover, draw-bending experiments were simulated with the developed material model, which showed good agreement with the experiments.

Finally, the capability of the model can be readily extended to cover real forming operations, which will reduce cost and enhance the quality of the formed parts.

RÉSUMÉ

Le retour élastique est un phénomène qui se produit quand une déformation élastique et plastique non homogène se produit dans un composant pendant sa mise en forme. Puisque la déformation élastique est récupérée quand la charge de mise en forme est enlevée, des changements géométriques se produisent en conséquence. Le retour élastique est particulièrement important dans le processus d'emboutissage des tôles minces; donc, afin de précisément coter les pièces embouties et de leur assigner des tolérances précises il est essentiel tout d'abord de bien comprendre les facteurs qui influencent ce phénomène et ensuite de cerner la sensibilité à chacun de ces facteurs. Il est également important de pouvoir prévoir le retour élastique dans différentes conditions de sorte qu'il puisse être réduit au minimum ou correctement expliqué dans la conception de processus. Cette étude présente le travail effectué jusqu'à présent sur la compréhension et la prédétermination du retour élastique de l'emboutissage des tôles minces en acier inoxydable 410 et en inconel 718, qui ont un large éventail d'utilisation dans l'industrie aérospatiale aussi bien que les aciers biphasiques 600/300 et 600/400 qui sont employés dans le secteur automobile.

Le rôle que joue l'anisotropie dans le retour élastique est évalué dans ce travail. L'effet de l'anisotropie sur le retour élastique est considéré pour les matériaux aérospatiaux tandis qu'il est négligé pour les matériaux des véhicules automobiles qui sont considérés parfaitement isotropes et seule l'effet des conditions d'emboutissage est étudié. Afin de caractériser les matériaux et leur comportement anisotrope, une série d'essais mécaniques est effectuée. Ces essais incluent des tests de tension uniaxiale standard ainsi que des tests de tension-compression unixiale. De plus, une série de flexions simples et multiples a été entreprise sur les matériaux aérospatiaux pour examiner l'effet de l'orientation du spécimen sur le retour élastique en flexion pure.

En outre, puisque les conditions d'emboutissage ont un effet évident sur le retour élastique et un des plus importante de ces derniers est la force du serre-flan, des essais d'emboutissage sont entrepris en variant la force du serre-flan pour évaluer son rôle dans le retour élastique de la pièce emboutie. L'effet combiné de l'anisotropie et de la force du serre-flan a également été étudié pour les matériaux aérospatiaux.

Les simulations par la méthode des éléments finies, qui n'incluent que l'écrouissage isotrope classique ou l'écrouissage cinématique n'ont pas induits une corrélation précise avec les résultats expérimentaux particulièrement pour ce qui a trait avec la prédiction du retour élastique. Par conséquent, pour simuler correctement le retour élastique, un modèle matériau qui combine les deux effets d'écrouissage ajouté à l'anisotropie matérielle, a été développé dans ce travail. Le modèle d'éléments fini développé inclus les deux types d'écrouissage isotrope et cinématique basée sur la formulation de limite élastique multi surfacique de Mróz. La formulation d'anisotropie de Hill de 1948 est utilisée. Le modèle de matériau développé a été validé en simulant avec bonne corrélation les essais expérimentaux de tension-compression.

En outre, pour démontrer le comportement du modèle, des essais de flexion ont été simulés. Les angles de retour élastique prédits par le modèle corrèlent bien avec ceux obtenus expérimentalement par des essais de flexions simples ou multiples. De plus, des essais d'emboutissage ont été simulées avec le modèle de matériau en question, et ont montré également une bonne corrélation avec les résultats expérimentaux.

En conclusion, les capacités du modèle peuvent être aisément élargie pour couvrir de vraies opérations d'emboutissage, qui réduiront le coût et augmenteront la qualité des pièces embouties.

ACKNOWLEDGMENTS

First and foremost, I would like to express my sincerest gratitude to my mother for her continuous love, care, encouragement, and moral and spiritual support throughout the years of this work.

My sincerest gratitude is extended to my supervisor, Prof. James A. Nemes, for his expert guidance and professional support. I am grateful for the tremendous amount of knowledge he conveyed to me, careful and insightful supervision, and his friendly and supportive leadership throughout my years at McGill.

Grateful acknowledgement is made to Professors L. Lessard and P. Hubert for their professional support and valuable discussions in the area of solid mechanics. I extend my gratitude to my former colleague D. Lazim for his inspiring collaboration in the early stages of this research. I would also like to thank my colleague and friend W. Dabboussi for his moral support during the hard times of this project. Special thanks to my friend Dr. F. Ben Yahia for his continuous moral and technical support during various stages of this work.

Appreciation is extended to the staff members of the Machine Tool Lab and the Measurements Lab, Prof. R. Sumner, Mr. D. Chellan, Mr. A. Micozzi, Mr. N. De Palma, Mr. G. Tewfik, and Mr. M. Iacobaccio, for their technical help and valuable support.

I would also like to acknowledge the support of Pratt and Whitney Canada and Auto21 – Canada Network of Centres of Excellence for their partial funding of this project.

Finally, I would like to dedicate this thesis to the memory of my father. Without the discipline, dedication, and professionalism he taught me in my early years, I would have never achieved a part of what I have accomplished so far.

TABLE OF CONTENTS

LIST OF FIGURES

LIST OF TABLES

NOMENCLATURE

Roman Letters

A_i	Instantaneous gage cross-sectional area
A_o	Gage initial cross-sectional area
B	A parameter for quantitative measurement of Bauschinger effect in Eq. (2.2)
BHF	Blank holding force
$\mathbb{C}_1$, $\mathbb{C}_2$	Defined as functions of the stress increments, $d\sigma_{11}, d\sigma_{22}$, and $d\sigma_{12}$
$C_{\Re}$	Material parameter characterizing the isotropic hardening in Sinou and Macquaire (2003)
E	Young's modulus
E'	Generalized elastic modulus
F_b	Tensile force in Wang *et al.* (2004a) and Wang *et al.* (2005)
F_i	Instantaneous tensile load measured by the load cell during testing,
G	Shear modulus
H	Plastic modulus of the monotonic loading curve
H_{eff}	Effective plastic modulus in Appiah and Jain (2004)
H_f	Plastic modulus for the forward loading at the moment of stress reversal in Geng and Wagoner (2002)
H_i	Plastic moduli corresponding to yield surface translation in Appiah and Jain (2004) , $i = T, S, D$
H_r	Plastic modulus for the reverse loading at the moment of stress reversal in Geng and Wagoner (2002)
J_i	First invariants of the stress tensor, i = 1, 2, 3
J_i'	Deviatoric stress invariants, i = 1, 2, 3
K	Parameter indicating the work-hardening-ability of the material
K_1, K_2	Stress components in Barlat-Lian 1989 yield criterion

K^p	Work-hardening modulus for kinematic hardening
$\bar{K}$	Work-hardening variable depends on material properties
L_i	Instantaneous gage length
L_o	Initial gage length
M	A parameter characterizing the yield surface's shape in Suh *et al.* (1996)
Q	Hardening parameters in the isotropic hardening model
R_φ	Plastic strain ratio or R-value with respect to angle φ to the rolling direction
R_1, R_2	Strain ratios measured in 1 and 2 directions
$\bar{R}$	Normal anisotropy parameter
ΔR	Planar anisotropy parameter
R_{aj}	Distorted sample coordinate vector in Żmudzki *et al.* (2004)
R_c	Radius of curvature
R_f	Radius of curvature of the sheet after springback
R_d	Die radius
R_o	Radius of curvature of the sheet before springback
R_p	Punch radius
$\Re$	Isotropic hardening variable in Sinou and Macquaire (2003)
$\Re_{sat}$	Material parameter characterizing the isotropic hardening in Sinou and Macquaire (2003
U_c	Complementary strain energy
W	Specimen's width
W^p	Total plastic work
X	A weighting factor between 0 and 1
e_{ij}	Deviatoric components of the elastic strain tensor
e_o	Material constant, $e_o = \frac{\gamma_o}{\sqrt{2}}$
$f^{(l)}$	Activated yield surface, l = 1, 2...10
Δh	Depth of the anticlastic profile

k	Bauschinger effect constant in Eq. (2.1)
k_τ	Material constant depends on the yield condition and other material parameters in Mattiasson and Sigvant (2004)
m	Bauschinger effect exponent in Eq. (2.1)
n	Parameter indicating the work-hardening-ability of the material
n_r	Tensile load ratio in El-Domiaty *et al.* (1996)
n_{ij}	The outward unit normal to the yield surface
r	Radius of curvature of the neutral layer before springback
r'	Radius of curvature of the neutral layer after springback
s_{ij}	Stress parameter including back stress, $s_{ij} = \left(\sigma_{ij} - \alpha_{ij}\right)$
t	Sheet thickness

Greek Letters

Γ, Ψ	Quantity related to the non-zero components of the stress tensor in Banabic *et al.* (2003) and Banabic *et al.* (2004)
α_{ij}	Components of the back stress tensor, $i, j = 1, 2, 3$
$d\alpha_{ij}$	Components of back stress increment
β	Unit tensor
β	A parameter for quantitative measurement of Bauschinger effect
δ_{ij}	Kronecker delta, $\delta_{ij} \equiv \begin{cases} 0 & \text{for } i \neq j \\ 1 & \text{for } i = j \end{cases}$
ε_T	True tangential strain in bending
ε_{eng}	Engineering strain
ε_l	Length strain
ε_t	Thickness strain
ε_w	Width strain

ε^p	Plastic prestrain
$d\bar{\varepsilon}^p$	Equivalent plastic strain
ε_{ij}^{el}	Elastic strain components
ε_{ij}^{pl}	Plastic strain components
$d\varepsilon_{ij}^{total}$	Total strain increment components, $d\varepsilon_{ij}^{total} = d\varepsilon_{ij}^{el} + d\varepsilon_{ij}^{pl}$
$d\varepsilon_{ij}^{total,combined}$	Total strain increment components for the combined hardening model $d\varepsilon_{ij}^{total,combined} = Xd\varepsilon_{ij}^{total,iso} + (1-X)d\varepsilon_{ij}^{pl,kin}$
$d\varepsilon_{ij}^{el}$	Elastic strain increments
$d\varepsilon_{ij}^{pl}$	Plastic strain increments
$d\varepsilon_{ij}^{pl,iso}$	Plastic strain increments contribution due to the isotropic hardening
$d\varepsilon_{ij}^{pl,kin}$	Plastic strain increments contribution due to the kinematic hardening
$d\varepsilon_{ij}^{total,iso}$	Total strain increments due to isotropic hardening
$d\varepsilon_{ij}^{total,kin}$	Total strain increments due to kinematic hardening
φ	Angle to the rolling direction
γ	Material parameter related to hardening
γ_{ij}	Hardening parameter in Wang and Barkey (1999), $\gamma_{ij} = \frac{\alpha_{ij}}{2G}$
γ_o	Initial yield strain in shear, $\gamma_o = \frac{\tau_o}{G}$
γ_{12}^{pl}	Plastic shear deformation
γ_F	Forward prestrain
$d\lambda$	Proportional positive scalar factor
$d\mu$	Material parameter in Mróz model determined
μ	Coefficient of friction
ν	Poisson's ratio
θ	Springback angle
ρ	Curvature

ρ_e	Curvature at the initiation of the elastic–plastic bending
σ_B	Bauschinger parameter defined as the stress offset between the forward and reverse deformations
$\sigma_B^{(t)}$	Bauschinger parameter defined as the transient softening
$\sigma_B^{(p)}$	Bauschinger parameter defined as the permanent softening
σ_T	True tangential stress in bending
σ_Y	Yield stress
σ_{Y_1} , σ_{Y_2}	Yield strengths in the 1- and 2-direction tension tests
σ_{Y_c}	Yield stress in compression
σ_{Y_t}	Yield stress in tension
σ_b	Biaxial tensile stress
σ_{eng}	Engineering stress
σ_f	Forward flow stresses
σ_i	Components of the principal stress, i = 1, 2, 3
σ_{ij}	Components of the stress tensor, i, j = 1, 2, 3
σ_{ij}^{end}	Stress in an element at the end of the loading process
$\sigma_{ij}^{reverse}$	Stress in an element at the end of the elastic reverse loading process
σ_i'	Principal components of the deviatoric stress, i = 1, 2, 3
σ_{ij}'	Components of the deviatoric, or reduced, stress tensor, i, j = 1, 2, 3
σ_m	The mean or hydrostatic component of the stress
σ_o	The size of the yield surface at zero plastic strain
σ_r	Reverse flow stresses
σ_u	Uniaxial tensile stress
$\sigma_{\beta o}$	Size of the bounding surface in Geng and Wagoner (2002) model
$\sigma_{\beta_{ij}}$	A stress point on the bounding surface in Geng and Wagoner (2002) model

$\bar{\sigma}$	Equivalent stress
τ	Shear stress
τ'	Yield stress in shear at 45° to the orthotropic axes in Hill's 1990 yield criterion
τ_B	Bauschinger stress in $\tau_B = k\gamma_F^m$
τ_Y	Yield stress in shear
ω	Material constant
ψ_i	Coefficients represents the relative contribution of the plastic moduli in Appiah and Jain (2004), $i = T, S, D$
ζ	Planar plastic anisotropy ratio, $\zeta = \frac{R_{90}}{R_0}$

CHAPTER 1

Introduction

1.1. Overview

In sheet metal forming operations, geometrical inaccuracy due to springback is a reason for considerable efforts in the development of tools and forming processes. Its occurrence is in every stage of the production process, not only in the deep drawing operation but also in each subsequent operation such as trimming, flanging, and hemming. In general, springback compensation is done in the preceding causing forming operation, with the exception of the trimming operation, where the springback compensation has to be done in the previous forming operation (Weiher *et al.*, 2004). Figure (1.1) shows a 2D draw-bending part that was made in a draw die; it is clear that the angles of the hat-shape deviate from the required 90°, and the cause is attributed to springback.

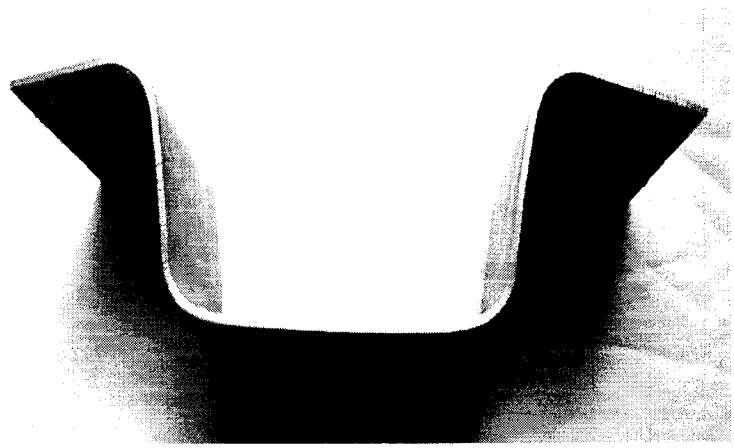

Fig. (1.1) Springback of a 2D draw-bending part

Springback is a phenomenon that occurs when nonhomogeneous elastic and plastic deformation occurs throughout a component during forming processes. When a blank is loaded, during the forming operation, and then fully unloaded, by removing it from the die, the internal stresses redistribute in the part and elastic recovery occurs; which causes springback. This elastic recovery can be simply explained on the stress–strain curve shown in Fig. (1.2). Loading the part to the plastic deformation, point A, and unloading it from that zone, the unloading path would follow line AB to point B. The permanent plastic deformation in this case would be OB and BC would be the elastic recovered deformation. Although this elastic recovery at a given location is very small, it can cause significant shape change in other locations when bending deformations are involved. This affects the assembly of parts and the proper functioning of the product. In general, it is extremely difficult to eliminate springback; however, what is done in the industry is trying to find methods to compensate for it. Traditional methods for springback compensation have been based on on-shop-floor trial and error and prior personnel experience (Kulkarni, 2004).

Therefore, in order to provide formed parts of close tolerances it is essential to first have a good understanding of the factors which affect springback and to be able to determine the extent those factors have. Secondly it is important to be able to predict springback

under different conditions so that it can either be minimized or properly accounted for in the process design.

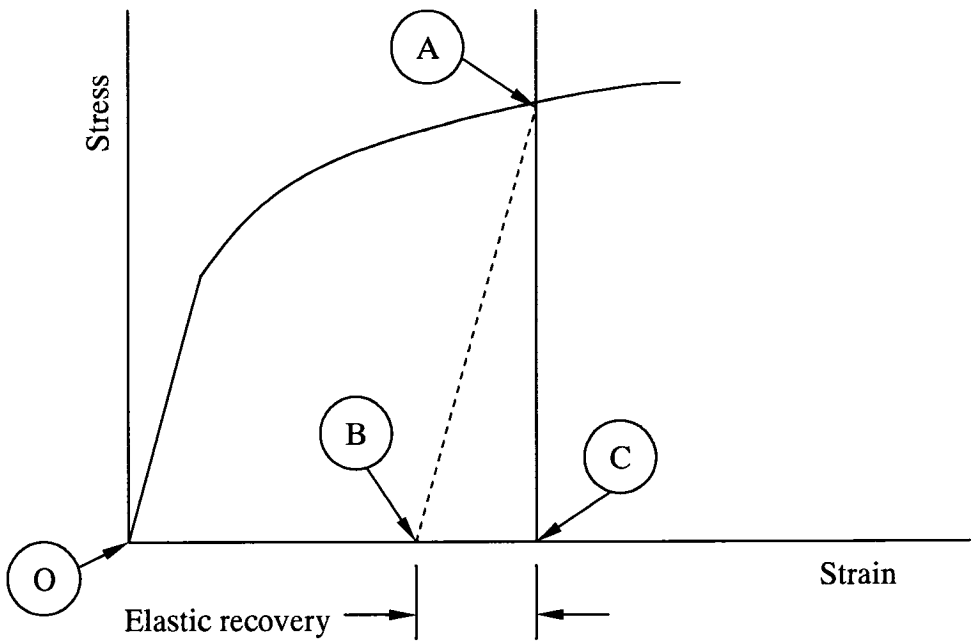

Fig. (1.2) Elastic recovery of an element in the sheet metal

An important factor to be addressed is the initial anisotropy of the sheet. Since sheets are produced by rolling, grains are aligned along preferred directions which results in anisotropy of the mechanical behaviour. In addition to variability that comes from sheet orientation, there is the natural variability that comes from the material itself. Since material may be procured from different suppliers there is some variation in the mechanical behaviour, even if the material is supplied to the same specification.

Process conditions have an obvious effect on springback and one of the most important of these is the clamping or blank holding force. By clamping the specimen between two plates it is possible to control how the material is drawn into the die. Using a small

clamping force lets the specimen be drawn easily into the die, producing a state of almost pure bending, which results in a large amount of springback. Increasing the clamping force restricts the specimen, which then has to be drawn as well as bent. This condition of draw-bending produces a more uniform distribution of plastic strain through the specimen thickness, with a reduction in springback. However, increasing the clamping force has limitations, as excessive drawing will result in tearing of the specimen.

The industrial use of trial and error approaches have been reduced with advances in computer capabilities, which have resulted in a reduction of the sheet metal forming process cost. Currently, it is feasible to simulate a complete forming process with the appropriate conditions optimized before the actual industrial process is carried out. However, caution has to be taken when introducing a variety of physically motivated simplifications into the simulations. Among these simplifications is to neglect the time dependency of the material, use a dimensionally reduced model, or assume a simplified constitutive law (Muthler *et al.*, 2004). In sheet metal forming simulations, researchers have found that in addition to the factors stated previously that affect springback; the constitutive description of the deformation behaviour of the material is of great significance (Appiah and Jain, 2004).

In many forming operations, the material undergoes a cycle of loading, unloading, and reverse loading. A typical stress–strain behaviour of an element in a formed part is shown in Fig. (1.3). It is shown that the direction of loading has been reversed, which raises the importance of describing the so called Bauschinger effect in the material description used in finite element modeling. The Bauschinger effect can be described as the observation of a reduction in the yield stress when the direction of loading is reversed from the original loading direction; as shown in Fig. (1.4), if the specimen is loaded into the plastic region and the load is removed and reloaded in the reverse direction until yield, the yield stress obtained in the reverse direction $\left(\sigma_{Y_2}\right)$ is significantly less than the yield stress $\left(\sigma_{Y_1}\right)$ obtained in the original loading direction (Khan and Huang, 1995). This phenomenon has been observed in single crystals and polycrystalline metals. The reason for this

phenomenon can be attributed to the anisotropy of the dislocation fields caused by the original loading (Khan and Huang, 1995).

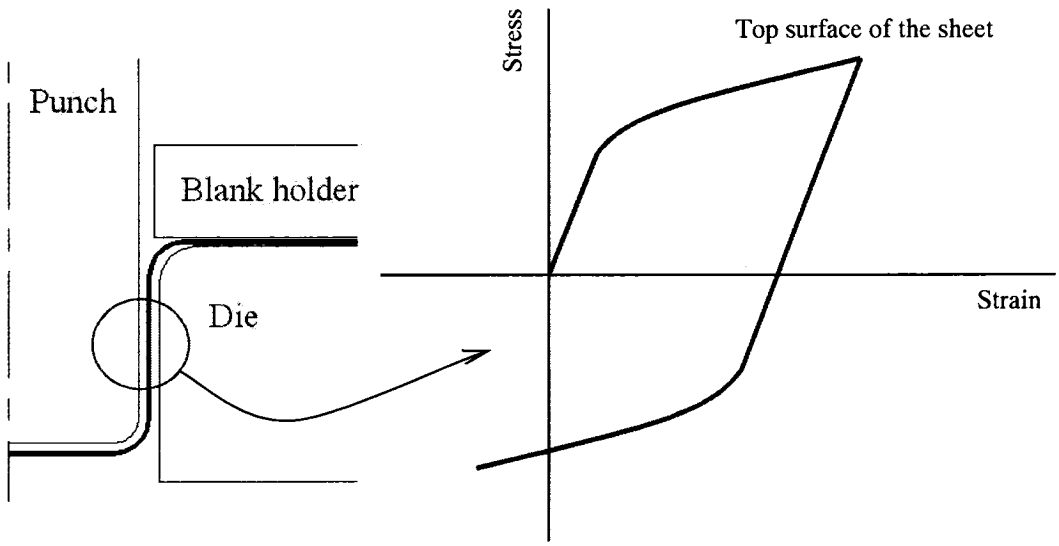

Fig. (1.3) A typical history of an element in a bending/unbending process

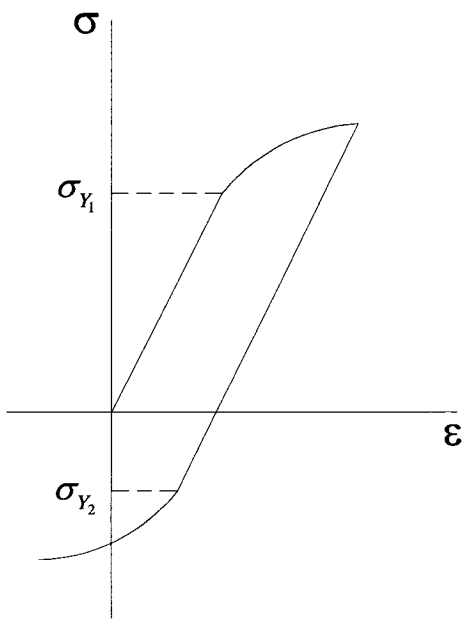

Fig. (1.4) Experimental observation of the Bauschinger effect
(adapted from Khan and Huang, 1995)

The presence of the Bauschinger effect affects the material hardening description and accordingly affects the accurate prediction of the behaviour of the material. Previously, the evidence of the anisotropic hardening due to the presence of the Bauschinger effect in relation to deformation analysis was neglected. The justification for this was based on the grounds that the effect is rather small and essentially transient in the soft ductile alloys commonly used in industrial cold-forming processes (Hill, 1950). However, the validity of this assumption is limited increasingly by the growth in applications of dispersion hardened alloys and dual-phase steels, in cold forming process (Bate and Wilson, 1986).

1.2. Materials

Nowadays, material developments are the key to aerospace and automotive advances. The material selection criterion in the aerospace and automotive industries requires that the material should be stronger, stiffer, more resistant to heat, lighter, and, of course, more affordable. Stronger and stiffer characteristics are to serve the design purposes. More resistant to heat materials means that these materials maintain their mechanical properties at elevated temperatures. Lighter materials are required to save weight for fuel consumption. Finally, these materials should be cost effective in terms of producibility, durability, maintainability and manufacturability.

In the automotive industry, current vehicles have experienced a major reduction in weight. This reduction in weight has been achieved by the development of better steels. The term "light metal" is not very accurate in the case of steel since it has a density of 7500 to 8000 kg/m^3; however, some grades are called so due to their good mechanical properties and, consequently, the dimensions can often been reduced drastically such that the components have thin walls and become lighter in weight. Also, steels have a unique combination of low cost and versatility; moreover, corrosion is no longer an issue; for example, many auto makers offer a life-time guarantee on certain parts. Among the types of steels that are being used extensively in the automotive industry are stainless steel and dual-phase steels.

Furthermore, the increased performance demanded in the aerospace industry requires an improvement in the materials of construction. For example, the operation range of fighter aircrafts has increased drastically with supersonic persistence at great turn rates. A major part of this advancement is given to the improved materials and the role they play in reducing the structural weight. Therefore, the unique mechanical properties of stainless steel and nickel alloys, possessing superior corrosion resistance and high temperature operation ranges, made these materials of great importance for the aerospace industry. Some of their applications include, but are not limited to, jet engine components, rocket motors, and missile components.

In this research, four types of aerospace and automotive materials are investigated. For the automotive materials, two grades of dual-phase steels were included in this research, namely DP600/300 and 600/400. As for the aerospace materials, stainless steel 410 and inconel 718 were also studied. The following sections give a brief introduction about each of the materials and their application in the corresponding industry.

1.2.1. Stainless Steel Type 410 (SS410)

As shown in Fig. (1.5) stainless steel Type 410 is a basic martensitic grade. By adding alloying elements to that grade, it is possible to produce other grades with different properties. For example, the corrosion resistance can be increased by adding phosphorous and sulfur, which results in obtaining the stainless steel 416 grade. The SS410 contains the lowest alloying elements among the three basic stainless steel grades (304, 430, and 410). The chemical composition is listed in Table (1.1). The martensitic grades are chromium steels that are corrosion resistant and hardenable by heat treatments and mainly used where hardness, strength, and wear resistance are required (Stainless Plate Products, 2005). The SS410 is a low cost alloy that is used widely where moderate corrosion resistance and high mechanical properties are required. Typical applications for

this alloy include steam and gas turbine blades, automotive exhausts, manifolds and high temperature engine components.

Table (1.1) Chemical composition of stainless steel 410 alloy, wt%

C	Mn	P	S	Si	Cr	Fe
0.15 max	1 max	0.04 max	0.03 max	1 max	11.5 – 13.50	Bal.

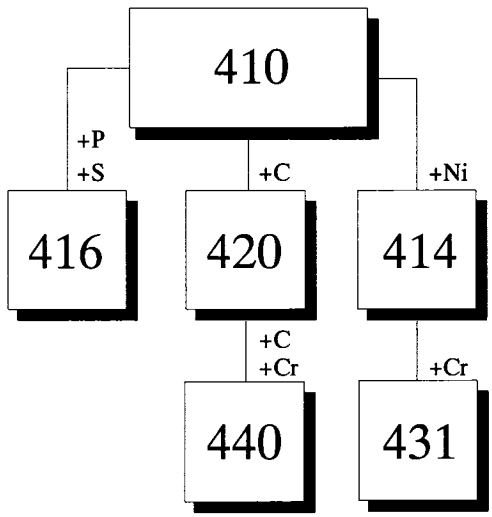

Fig. (1.5) Stainless steel martensitic grades (adapted from Stainless Plate Products, 2005)

1.2.2. Inconel 718 (IN718)

This alloy was first developed by International Nickel "INCO" at its research laboratories and plant in Suffern, New York and Huntington, West Virginia, in 1959. It is high strength, high temperature resistant, and corrosion resistant. Moreover, it has good ductility and may be readily formed by all conventional methods; however, it requires more powerful equipment to accomplish forming (INCO, 1985). Because of its superior properties, inconel 718 became one of the most important superalloys used in the aerospace industry for components in the hot section of the gas turbine engines (Sharman, *et al.*, 2001). The chemical composition of the alloy is shown in Table (1.2).

Table (1.2) Chemical composition of inconel 718 alloy, wt%

Al	B	C	Cr	Co	Cu	Mn	Mo
0.2 – 0.8	0.006 max	0.08 max	17 – 21	1 max	0.3 max	0.35 max	2.8 – 3.3
Ni	Nb	P	Si	S	Ti	Fe	
50 – 55	4.75 – 5.5	0.015 max	0.35 max	0.015 max	0.65 – 1.15	Bal.	

1.2.3. Dual–Phase Steels (DP Steels)

There is a trend in the automotive industry for increased use of DP steels since they improve fuel economy by weight reduction. DP steels offer an exceptional combination of high tensile strength and excellent formability and also exhibit a higher initial work hardening rate and higher uniform and total elongation compared to conventional high strength steels. In a recent study, it was proposed that up to 74% of auto body parts can be manufactured from DP steels (World Auto Steel, 2005).

DP steels are characterized by a matrix of fine ferrite that contains small particles of martensite. The good formability is obtained from the ductile ferrite while the martensite particles provide substantial strengthening to the material (Kot and Morris, 1979).

Currently, DP steels are commonly used in automotive structural applications where they have replaced more conventional steels. Their applications include front and rear rails, crush cans, rocker reinforcements, cowl inner/outer, body panels, cross members, bumpers, and door intrusion beams (Yan *et al.*, 2000).

The DP steels used throughout this work, DP600/300 and DP600/400, were received as cold rolled sheets. The chemical composition is listed in Table (1.3). As can be seen, the chemical composition is the same for the two grades; however, the main difference between the two grades is that the DP600/400 has a higher yield strength that was

attained by stretching or tension leveling in the longitudinal direction after the coil was produced, resulting in the increased yield.

Table (1.3) Chemical composition of DP 600/300 and 600/400, wt%

C	Mn	Si	Cu	Ni	Cr	Mo	Ti	Al	Fe
0.07	1.84	0.09	0.011	0.011	0.032	0.15	0.011	0.037	Bal.

1.3. Objectives and Scope of Work

The general objective of this research is to improve the manufacturing capability and dimensional control of sheet metal forming. The optimal goal is to develop a finite element model that can be used for a robust and optimum sheet forming process along with experimental work and simulations.

Specifically, this research focuses on the characterization and numerical modeling of the material behaviour of stainless steel 410 (SS410), inconel 718 (IN718), and dual-phase steels 600/300 and 600/400 (DP600/300 and DP600/400) and the effect of their mechanical properties on springback of sheet products made of these materials.

The strategy to meet the objectives includes:

a) Properly characterize the materials by a series of experimental procedures
b) Properly simulate the mechanical behaviour of the materials, using an appropriate constitutive model
c) Identify the parameters affecting springback prediction
d) Properly simulate the forming conditions and the consequent springback after forming

1.4. The Structure of this thesis

A general introduction discussing the springback phenomena in sheet metal forming and some of its causes, as well as the materials under study has been presented in this chapter, Chapter 1. An extensive literature review is presented in Chapter 2. In Chapter 3, a detailed description of the experimental procedure is explained. A discussion about material characterization and bending experiments takes place in that chapter. The experimental results are presented and discussed in Chapter 4. Modeling techniques and the development of the finite element model are presented in Chapter 5. In Chapter 6, simulation procedures and numerical implementation are discussed along with the simulation results and findings. Finally, Chapter 7 includes the final conclusions, comments, and recommendations for future work.

CHAPTER 2

Literature Review

2.1. Bauschinger Effect in Metals

Johann Bauschinger (1834-1893) was the first to report, in 1886, the steel behaviour when the direction of loading is reversed. He conducted tension-compression experiments on several steel bars, of 46.00 mm diameter and 60.00 mm gage length, and was able to record the accompanying plastic deformation listed in a series of tables. Bauschinger was able to detect two extreme values for the yield point; the higher value was observed when the bar was unloaded and reloaded in the same original direction and the lower value was observed when the bar was unloaded and reloaded in the reverse direction (Skelton *et al.*, 1997). It was found that the more the bar was deformed in compression, for example, the higher the reduction in the subsequent tensile yield stress. Figure (2.1) shows a plot of the data taken from one of the original tables; it clearly shows the depression in the yield stress in tension after the initial loading of the bar in compression.

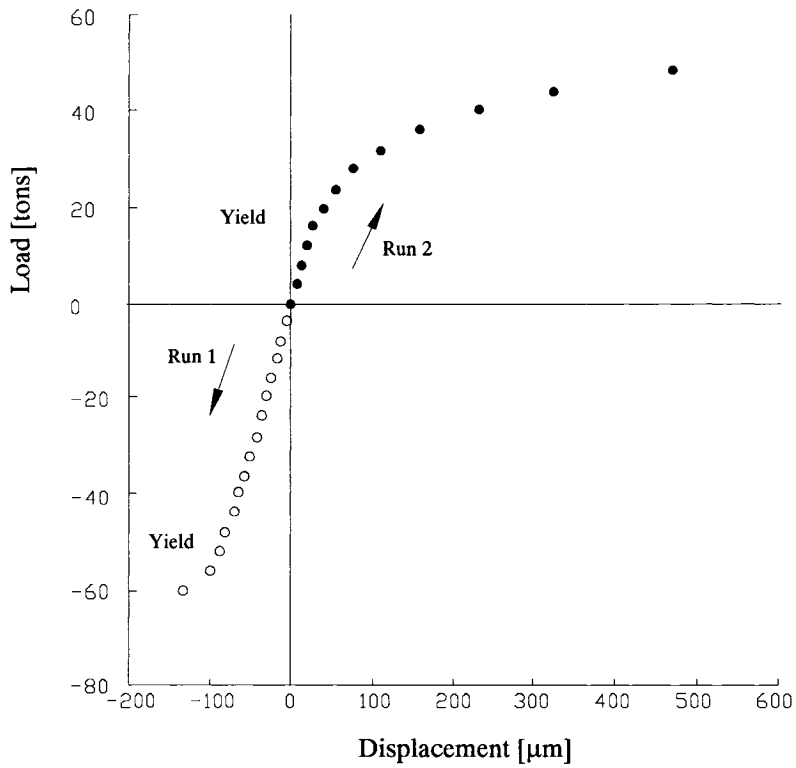

Fig. (2.1) Data plotted from Bauschinger's original report. Note the reduced yield stress in tension after the initial loading in compression (adapted from Skelton *et al.*, 1997)

As reported by Dillamore *et al.* (1971), the presence of the Bauschinger effect demonstrates different distribution of stresses. Also, Dingli *et al.* (2000) reported that the presence of the Bauschinger effect in cyclic loading applications is generally observed due to the presence of microscopic internal stresses. It was also reported that it comes from kinematic hardening. The Bauschinger effect is of engineering interest, generally in industrial processes where materials undergo forward and reverse loading; specifically, in sheet metal forming, where sheets experience successive bending and straitening or unbending (Lorentzen *et al.*, 2002).

Kishi and Tanabe (1973) measured the change in the strength due to the presence of the Bauschinger effect by the use of reversible torsion equipment. The shear stress-shear strain curves were obtained from the torque-angle curves, assuming a uniform stress distribution over the tube specimen's cross section. The decreased yield stress, as shown

in Fig. (2.2), due to the Bauschinger effect was called "the Bauschinger stress (τ_B),", and was calculated as

$$\tau_B = k\gamma_F^m \tag{2.1}$$

where γ_F is the forward prestrain, k was called the Bauschinger effect constant, and m was called the Bauschinger effect exponent. k and m are constants determined from the grain size and metallurgical structure of the material. For carbon steel, it was reported that with the increase of the carbon content in the steel, the value of m decreased and the value of k increased.

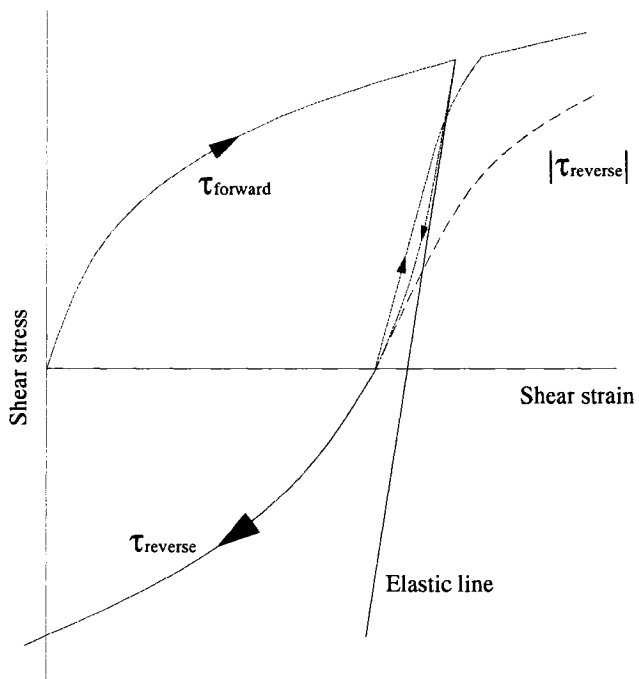

Fig. (2.2) Schematic shear stress-shear strain curve showing the Bauschinger effect (adapted from Kishi and Tanabe, 1973)

Sowerby *et al.* (1979) reviewed some aspects affecting the Bauschinger effect in metals. Also, a number of microscopic and macroscopic models to reproduce the forward and reverse flow behaviour of the materials were discussed. It was reported that one of the most common tests to reveal the Bauschinger effect is the unidirectional loading, where a

specimen is prestrained in tension followed by reverse straining in compression, or vice versa. A typical shape of stress-strain for reverse loading is shown in Fig. (2.3); where the reverse loading curve was shown in the tensile domain.

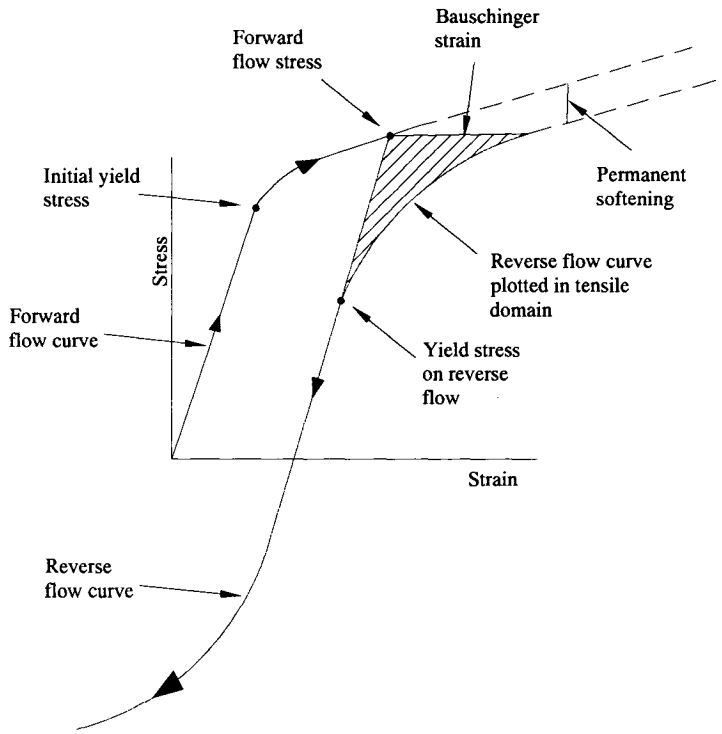

Fig. (2.3) Schematic diagram of the uniaxial stress-strain behaviour for many real metals during forward and reverse loading tests (adapted from Sowerby *et al.*, 1979)

The reduction in the flow stresses, forward and reverse flow stresses, and the well-rounded nature of the initial plastic portion of the reverse curve was reported to be a typical behaviour of some real metals (Sowerby *et al.*, 1979). Similarly, Bate and Wilson (1986) reported that the amount of permanent softening in metals can be determined from the Bauschinger tests, where the forward and reverse stress-strain curves are plotted in terms of absolute stress and absolute total strain measured at the reverse strain. The amount of permanent softening is also shown in Fig. (2.3).

Tan *et al.* (1994) carried out experiments on stainless steel, aluminum, and dual-phase steels to define quantitatively the parameters defining the Bauschinger effect. In their study, a parameter for quantitative measurement of Bauschinger effect was suggested as

$$B = \frac{|\sigma_f| - |\sigma_r|}{|\sigma_f|} \tag{2.2}$$

where σ_f and σ_r are the forward and reverse flow stresses, respectively. In the absence of Bauschinger effect, the parameter $B = 0$.

Since B does not explicitly incorporate the hardening ability of a material, another parameter, β, was suggested by the authors, and is calculated as

$$\beta = \frac{|\sigma_f| - |\sigma_r|}{|\sigma_f| - |\sigma_Y|} = B(\varepsilon^p)\left(\frac{|\sigma_Y|}{K|\varepsilon^p|^n} + 1\right) \tag{2.3}$$

where σ_Y is the yield stress, ε^p is the plastic prestrain, and K and n are parameters indicating the work-hardening-ability of the material.

In case of isotropic hardening, i.e. no Bauschinger effect, $|\sigma_f| = |\sigma_r|$, and accordingly $B = \beta = 0$. In the kinematic hardening model, it was assumed that $|\sigma_f| + |\sigma_r| = 2|\sigma_Y|$. Substituting this assumption into Eq. (2.3), $\beta = 2$. If σ_r is considered to be equal in magnitude as the original yield stress; i.e., $|\sigma_r| = |\sigma_Y|$; hence, $\beta = 1$.

Generally, it was suggested that β must be determined experimentally to evaluate the work hardening and softening effect with respect to the Bauschinger effect of a material (Tan *et al.*, 1994).

As reported by Chun *et al.* (2002a), permanent softening is due to the unsaturated reverse loading curve to the monotonic loading curve, in addition to the reduction in the subsequent yield stress, the Bauschinger effect. It was reported that three basic requirements are needed to properly account for the Bauschinger effect in modeling of cases where cyclic loading takes place:

i- non-linearity correction of stress-strain loop,

ii- elastic limit reduction at reverse loading, and

iii- permanent offset for some materials.

Yoshida *et al.* (2002) reported that the Bauschinger effect is characterized by two distinct phenomena, one is called "transient Bauschinger" which is the smooth transient softening at the early stage of stress reversal, and the other is the permanent softening that appears after the transient period, both stages are shown in Fig. (2.4). As a measure of the Bauschinger effect, the author suggested the form

$$\sigma_B = \sigma_B^{(t)} + \sigma_B^{(p)} \tag{2.4}$$

where σ_B is the stress offset between the forward and reverse deformations and $\sigma_B^{(t)}$ is the transient softening, which is defined as the difference between the reverse stress–strain curve (region c–d in Fig. 2.4) and the extrapolated curve of the region of permanent softening, $\sigma_B^{(p)}$, (region d–g in Fig.2.4).

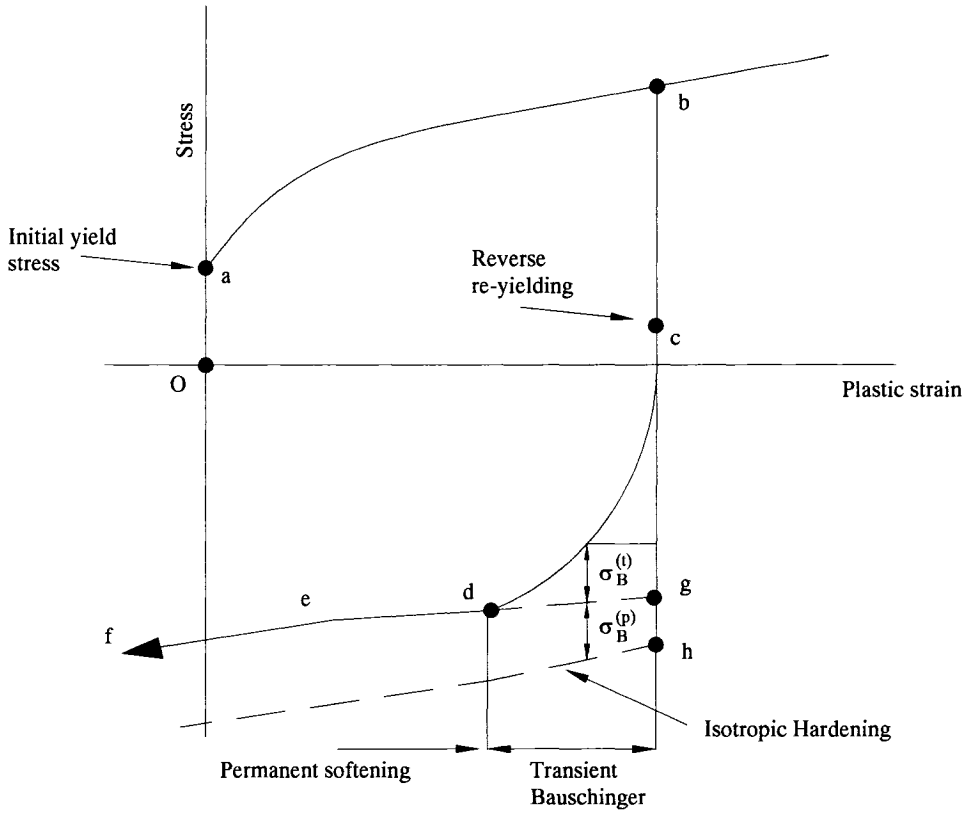

Fig. (2.4) Stress-strain curve showing the transient and permanent softening (adapted from Yoshida *et al.*, 2002)

The American Iron and Steel Institute (2003) published a report on New Generation Steels where they explained a method of determining the so-called Bauschinger effect factor (BEF). That factor was taken to be the ratio of the reverse yield strength to the forward flow stress determined at four prestrains. The experiments were conducted on dog-bone shaped specimens, of 7.62 mm gage-length, loaded in tension to the specified strains, unloaded, and then reloaded in compression until buckling was detected. The main finding was that the increase in the magnitude of the tensile prestrain would result in an increase in the Bauschinger effect. Also, steels with higher strength exhibited higher Bauschinger effect.

Lee *et al.* (2005b) evaluated the amount of Bauschinger effect for three materials used in the automotive industry, namely AA6111-T4 and AA5754-O aluminum alloy sheets and dual-phase high strength steel sheets. A Bauschinger ratio was defined as

$$B.R. = \frac{\sigma_f - \sigma_r}{2\sigma_f} \quad (\leq 1.0) \tag{2.5}$$

where σ_f was defined as the yield stress at the start of unloading and σ_r was defined to be the initial yield stress in the reverse loading. It was observed that the smaller the *B.R.* the larger the Bauschinger effect. For pure isotropic hardening, $\sigma_f = -\sigma_r$, the *B.R.* becomes unity. For the three materials tested, it was found that, during the early straining, the *B.R.* quickly saturates and the ultimate values for *B.R.* is 0.66 for DP-steel and 0.8 – 0.9 for the aluminum sheets, as shown in Fig. (2.5).

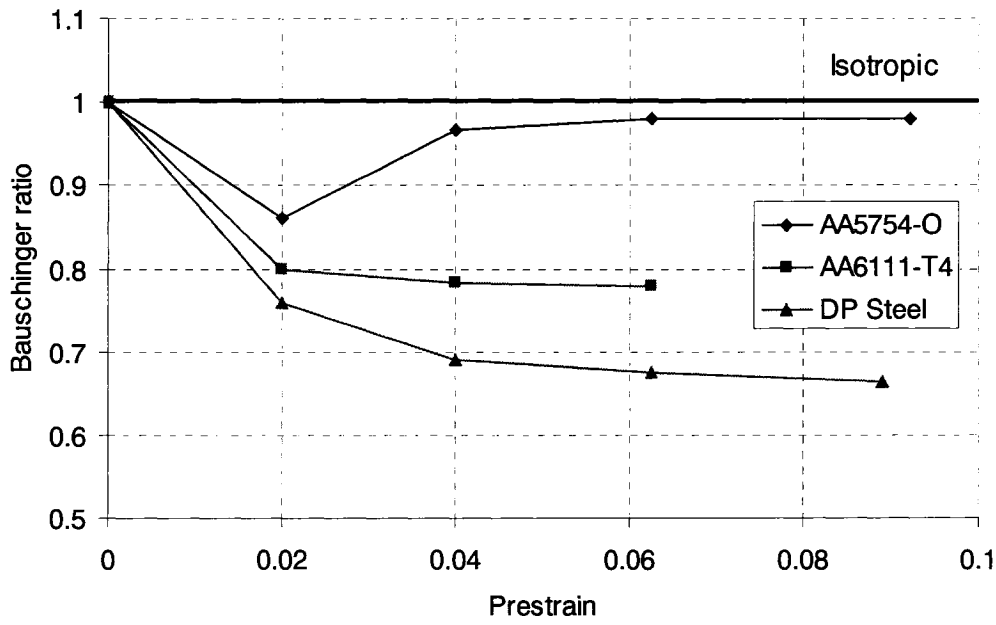

Fig. (2.5)Bauschinger ratio as a function of prestrain (adapted from Lee *et al.*, 2005b)

2.2. Plastic Anisotropy in Sheet Metal

Assuming that, for sheet forming simulations, every material element remains isotropic during deformation is a poor approximation. Material grains elongate in the direction of the greater tensile strain during rolling. Furthermore, grains tend to rotate towards some limiting orientation parallel to the direction of the applied load. Accordingly, a material with initially randomly oriented grains, and hence considered isotropic, is turned anisotropic when plastic deformation takes place.

If the reference axes, in a rolled sheet, are chosen so that *1* is the rolling direction, *2* the transverse direction in the sheet plane, and *3* the through-thickness direction, as shown in Fig. (2.6), then for a tensile specimen cut at an angle φ to the rolling direction, the stress components will be

$$\sigma_{11} = \sigma \cos^2 \varphi,\ \sigma_{22} = \sigma \sin^2 \varphi,\ \text{and}\ \sigma_{12} = \sigma \sin \varphi \cos \varphi \tag{2.6}$$

where σ is the stress in the loading direction. From Hill's yield function for anisotropic materials in the plane stress condition ($\sigma_{33} = \sigma_{23} = \sigma_{13} = 0$),

$$(g+h)\sigma_{11}^2 - 2h\sigma_{11}\sigma_{22} + (f+h)\sigma_{22}^2 + 2n\sigma_{12}^2 - 1 = 0 \tag{2.7}$$

and substituting Eq. (2.6) back into Eq. (2.7) gives

$$\sigma = \left[f \sin^2 \varphi + g \cos^2 \varphi + h - (f+g+4h-2n) \sin^2 \varphi \cos^2 \varphi \right]^{-1/2} \tag{2.8}$$

where values of *f*, *g*, *h* and *n* can be deduced from the observed dependence of the yield stress on the orientation (Hill, 1950).

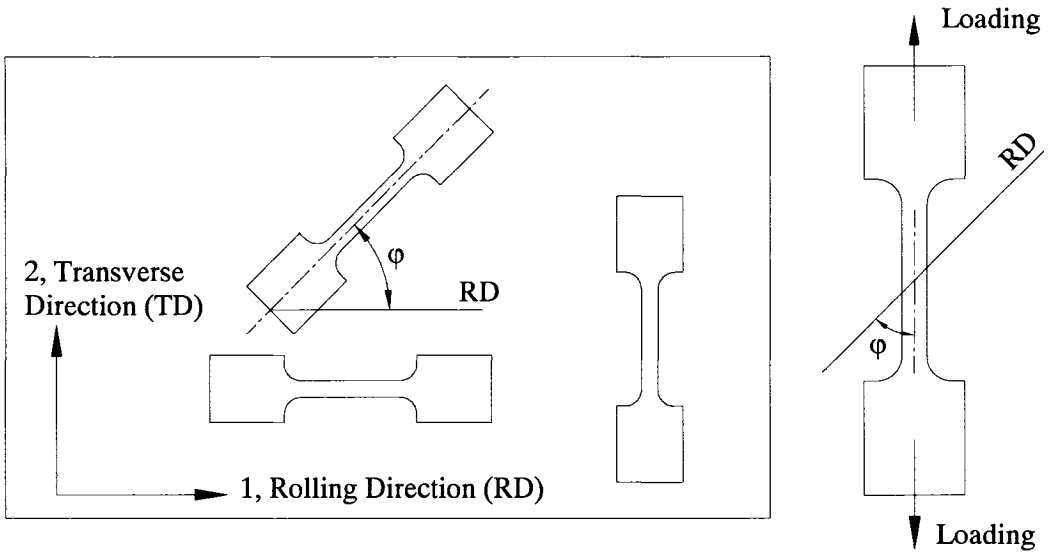

Fig. (2.6) Rolled sheet reference axes and the definition of angle φ to the rolling direction

The plastic properties of rolled sheets differ from the through-thickness direction, which is called normal anisotropy, and vary with orientation in the plane of the sheet, which is called planar anisotropy (Lee and To, 1995). At a given angle (φ) to the rolling direction, the anisotropy of the sheet is characterized by the plastic strain ratio or the *R*-value (ASTM, 1998, Carleer *et al.*, 1996 and Danckert and Nielsen, 1998), which is equal to

$$R_{\varphi} = \frac{\varepsilon_w}{\varepsilon_t} \tag{2.9}$$

where ε_w and ε_t are the width and thickness true strains, respectively, of a uniaxial tension specimen cut at an angle φ to the rolling direction.

For perfectly isotropic materials this *R*-value is equal to 1. For thin sheets, which are considered here, it is very difficult to measure the thickness strain. Therefore, it is usually deduced from the constancy of volume, which will be discussed in Section 4.1, that

$$\varepsilon_l + \varepsilon_t + \varepsilon_w = 0 \tag{2.10}$$

which yields,

$$R_{\varphi} = \frac{-\varepsilon_w}{\varepsilon_l + \varepsilon_w} \tag{2.11}$$

where ε_l is the length strain. Since the R-value often depends on the specimen's orientation angle, it is common to describe an average R-value, $\overline{R}$, (Hertzberg, 1995) obtained from three directions: 0° (parallel), 45° (diagonal) and 90° (transverse) to the rolling direction. This $\overline{R}$, normal anisotropy, is equal to

$$\overline{R} = \frac{R_0 + 2R_{45} + R_{90}}{4} \tag{2.12}$$

Another parameter, ΔR, can describe the degree of anisotropy in the plane of the sheet, planar anisotropy (Han, 1992). This parameter is a measure of the tendency of sheet to draw in nonuniformly and to form ears in the flange of deep-drawn cylindrical parts in the direction of the higher R-value (ASTM, 1998). It is calculated by

$$\Delta R = \frac{R_0 + R_{90} - 2R_{45}}{2} \tag{2.13}$$

Lee and To (1995) studied the effect of rolling schedule on the plastic anisotropy of aluminum sheets. The average plastic strain ratio, $\overline{R}$, was taken to be

$$\overline{R} = \frac{1}{36}\left[R_0 + 2R_5 + 2R_{10} + ...2R_{80} + 2R_{85} + R_{90}\right] \tag{2.14}$$

Sheets were rolled 2 to 20 rolling passes to reach a thickness reduction from 40% to 80%. It was found that combining a higher overall reduction with a lower number of rolling passes results in a higher $\overline{R}$-value. Figure (2.7) shows the effect of overall reduction and number of rolling passes on the $\overline{R}$-value.

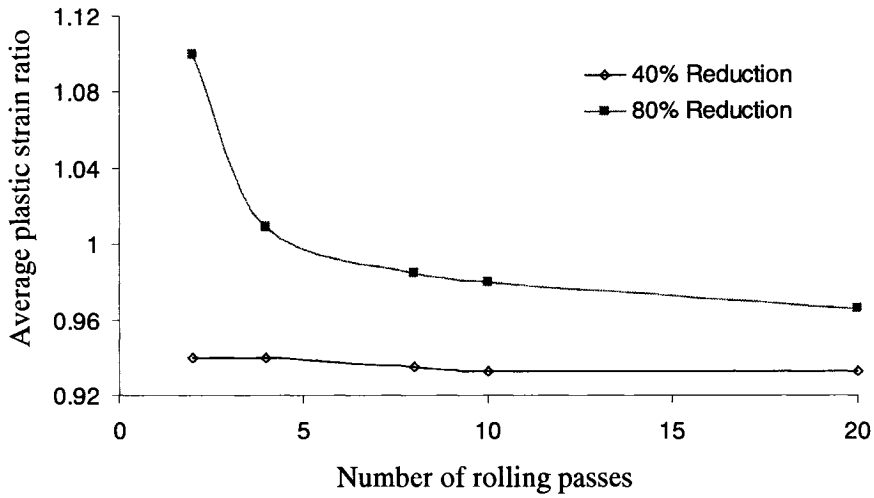

Fig. (2.7) The effect of overall reduction and number of rolling passes on the $\overline{R}$-value (adapted from Lee and To, 1995)

Takahashi *et al.* (1996) investigated experimentally and theoretically the plastic anisotropy of the 1050 aluminum rolled sheets. The sheets were additionally rolled with 50% and 75% reduction in three directions RD = 0°, 45°, and 90° measured from the initial rolling direction. Tensile specimens were cut off in every 15° direction and the flow stress σ_Y and the R-values were measured. Figure (2.8) shows the variation of σ_Y and R-value with respect to the specimen's angle for the 50% reduction tests.

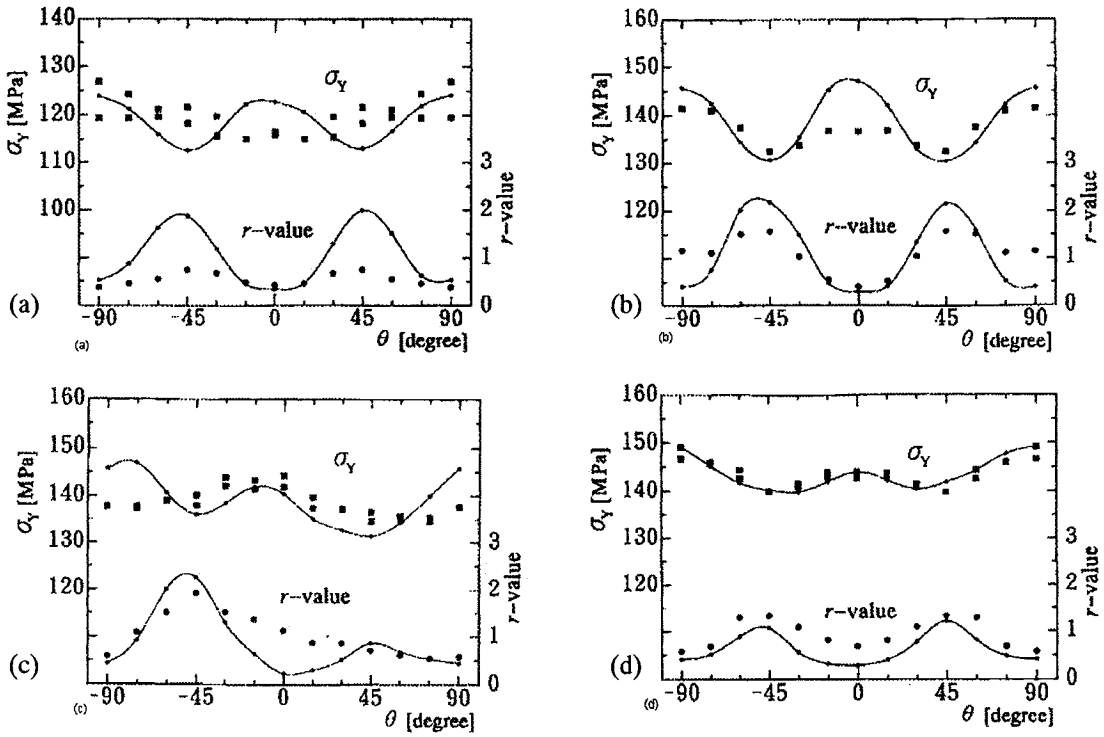

Fig. (2.8) Anisotropy in Al-1050 sheets, as received and additionally rolled to 50% reduction, (a) as received, (b) RD = 0°, (c) RD = 45°, and (d) RD = 90° (— Calculation, and ■ ● Experiments) (Reprinted from Takahashi *et al.* (1996) with permission from Elsevier)

It was reported by Rauch (1998) that plastic anisotropy of sheet metals can be determined by simple shear tests. To do that, a device was designed to impose a parallel displacement of two lateral grips. The required deformation of a rectangular specimen is shown in Fig. (2.9a). The device was used to determine the shear strain-shear stress, Fig. (2.9b), for Fe-2.9% Si single-crystal sheared in different orientations. It is shown that the change in orientation clearly affects the yield stress of the tested specimens.

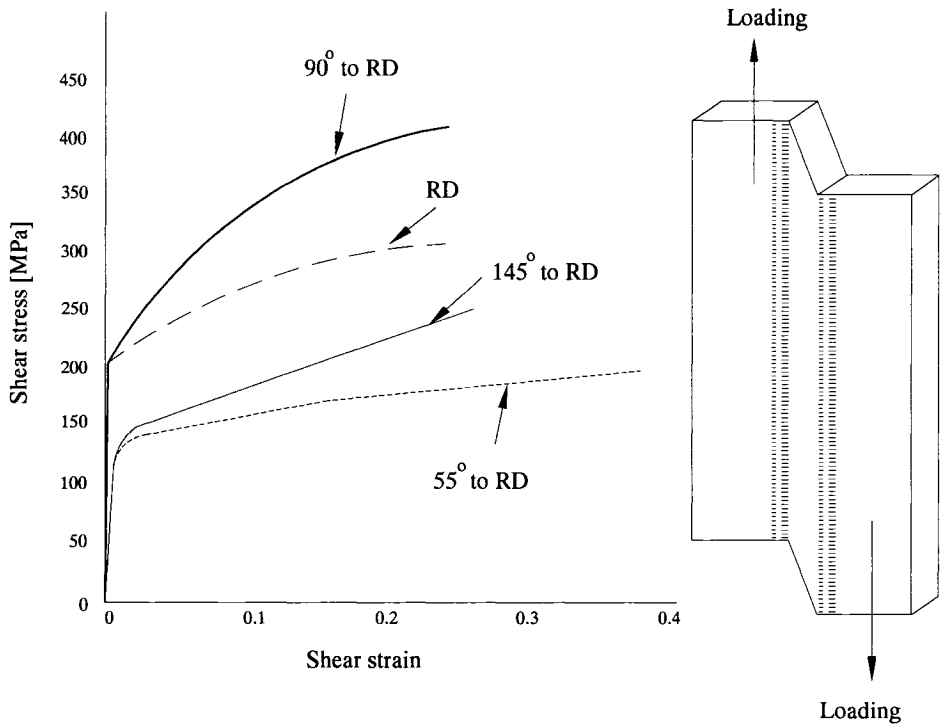

Fig. (2.9) Experimental shear stress-shear strain curves for different specimen's orientation of a shear sample. The indentation in the geometry is a result from lateral grips clamping (adapted from Rauch, 1998)

Hu *et al.* (1998) studied the influence of the shear strain rate, $\dot{\varepsilon}_{12}$, component on the in-plane plastic anisotropy for annealed aluminum sheets. It is worth mentioning that the annealing process took place after a 90% thickness reduction in cold rolling. The yield loci were plotted in strain rate space and it was found that the loci exhibited significant change in shape with the increase in the shear strain rate. The change was in the form of size reduction rather than rotation. Thus, it was concluded that the increase in the shear strain rate would result in a reduction in the in-plane anisotropy of the sheet.

The effect of anisotropy on the earing in cup drawing was investigated by Zaky *et al.* (1998). It was reported that the anisotropy does not only depend on the range of orientation but also depends on the microstructure of the material. Moreover, the more the anisotropy, referred to by the directional anisotropy (R_φ), the more the radial strains are obtained during deep drawing; which assists the material to draw in the same

direction. Hence, it was observed that all the ears were formed in the direction where R_φ was a maximum. Based on this observation, modifying the blank shape, rather than fully circular, was investigated. It was reported that using the modified blanks after calculating an optimum shape, taking into account the sheet anisotropy, resulted in a significant reduction in the creation of ears in the drawn cups.

The effect of plastic anisotropy on compressive instability in sheet metal forming was studied by Kim *et al.* (2000). Hill's yield criterion was used within the work. The effect of the normal anisotropic coefficient R-value ($R = R_0 = R_{90}$) and the planar plastic anisotropy ratio $\zeta = \frac{R_{90}}{R_0}$ on the yield locus was studied. To study the plastic anisotropy effect on compressive instability, a square sheet (10.0×10.0 mm) was subjected to compression in the rolling direction and tension in the transverse direction, as shown in Fig. (2.10).

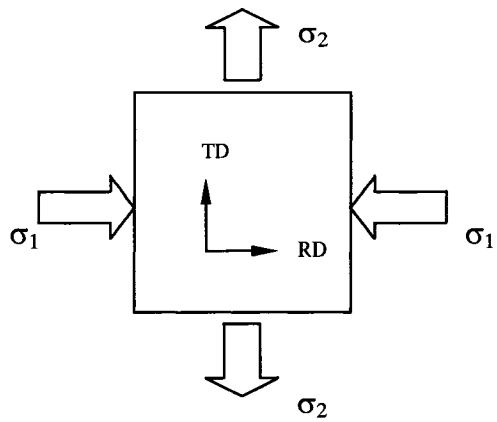

Fig. (2.10) Schematic diagram of the buckling test of a square plate
(adapted from Kim *et al.*, 2000)

The effect of R-value and ζ on the yield locus is shown in Fig. (2.11). For the second quarter section of the yield locus, one edge in tension and the other in compression, it is shown that as R and ζ increase the yield stress decreases.

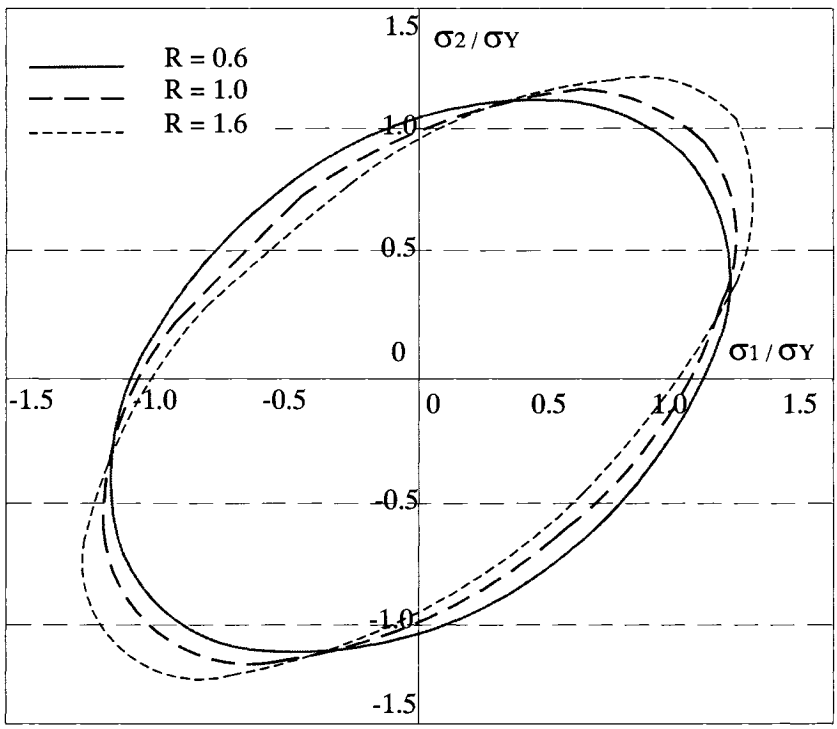

(a)

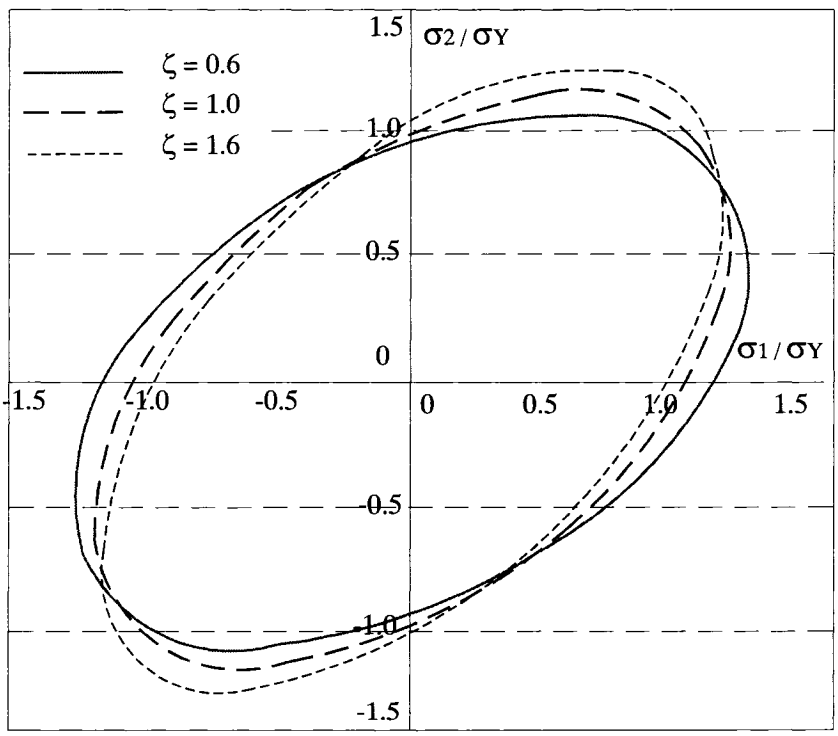

(b)

Fig. (2.11) Yield locus for Hill's yield criterion; (a) for various values of normal anisotropic coefficient R, and (b) for various value of planar anisotropy ratio ζ (adapted from Kim *et al.*, 2000)

Kim *et al.* (2000) also modeled the spherical cup deep drawing process with different *R*-values to validate the results. It was reported that the plastically deforming region increases with the increase in the *R*-value as a result of decreasing the yield stress.

Li *et al.* (2003) pointed out that experimental studies showed that interrupted metal forming operations, i.e. multi-stage forming, are also a source of plastic anisotropy of the parts. This takes place at the transition, between stages, due to the interruption in the flow stresses and the work hardening rate.

2.3. Yield Criteria

The yield criterion is an assumption about a material that assists in determining the beginning of plastic deformation. It is a mathematical expression that is satisfied at the initiation of the plastic flow due to the combination of the stress components. Assuming that the material is homogeneous, the yield function can be mathematically represented as

$$F(\sigma_{ij}) = 0 \tag{2.15}$$

If the stress state at a point satisfies the previous equation, then this point deforms plastically; if not, it is still in the elastic region (Khan and Huang, 1995). In other words

$$\begin{aligned} F(\sigma_{ij}) &< 0 \quad \text{elastic deformation region} \\ F(\sigma_{ij}) &= 0 \quad \text{plastic deformation region} \end{aligned} \tag{2.16}$$

For isotropic materials, the plastic yielding depends only on the magnitude, not the direction, of the principal applied stress (Hill, 1950). For such materials, the yield criterion is given by

$$F(\sigma_1,\sigma_2,\sigma_3)=0, \text{ or}$$
$$F(J_1,J_2,J_3)=0 \tag{2.17}$$

where σ_1, σ_2, and σ_3 are the principal components of stress and J_1, J_2, and J_3 are the first three invariants of the stress tensor σ_{ij}. The stress tensor's components can be represented by

$$[\sigma_{ij}]=\begin{bmatrix}\sigma_{11} & \sigma_{12} & \sigma_{13}\\ \sigma_{21} & \sigma_{22} & \sigma_{23}\\ \sigma_{31} & \sigma_{32} & \sigma_{33}\end{bmatrix} \tag{2.18}$$

The principal stresses can be calculated from (Boresi *et al.*, 1993)

$$\left|\sigma_{ij}-\sigma\delta_{ij}\right|=0 \tag{2.19}$$

i.e. they are the roots of the cubic equation

$$\sigma^3-J_1\sigma^2+J_2\sigma-J_3=0 \tag{2.20}$$

where

$$\begin{aligned}J_1&=\sigma_{ii}=\sigma_{11}+\sigma_{22}+\sigma_{33}\\ J_2&=\frac{1}{2}\left(\sigma_{ii}\sigma_{kk}-\sigma_{ij}\sigma_{ij}\right)=\sigma_{11}\sigma_{22}+\sigma_{22}\sigma_{33}+\sigma_{11}\sigma_{33}-\sigma_{12}^2+\sigma_{13}^2+\sigma_{23}^2\\ J_3&=\det\left[\sigma_{ij}\right]\end{aligned} \tag{2.21}$$

It has been shown experimentally that a moderate hydrostatic pressure has no effect on the yield (Hill, 1948 and Khan and Huang, 1995). Hence, the yield criterion can be

written in terms of the principal components $(\sigma_1', \sigma_2', \sigma_3')$ of the deviatoric, or reduced, stress tensor

$$\sigma_{ij}' = \sigma_{ij} - \sigma_m \delta_{ij} \tag{2.22}$$

where $\sigma_m = \frac{1}{3}\sigma_{ii} = \frac{1}{3}J_1$ is the hydrostatic component of the stress. Therefore, the yield criterion reduces to the form

$$F(J_2', J_3') = 0 \tag{2.23}$$

where J_2' and J_3' are the deviatoric stress invariants and

$$\begin{aligned} J_1' &= \sigma_{ii}' = \sigma_1' + \sigma_2' + \sigma_3' = 0 \\ J_2' &= \frac{1}{2}\sigma_{ij}'\sigma_{ij}' = \frac{1}{2}\left(\sigma_1'^2 + \sigma_2'^2 + \sigma_3'^2\right) \\ &= \frac{1}{6}\left[(\sigma_{11} - \sigma_{22})^2 + (\sigma_{22} - \sigma_{33})^2 + (\sigma_{33} - \sigma_{11})^2\right] + \sigma_{12}^2 + \sigma_{23}^2 + \sigma_{13}^2 \\ J_3' &= \det\left[\sigma_{ij}'\right] = \sigma_1'\sigma_2'\sigma_3' \end{aligned} \tag{2.24}$$

2.3.1. Tresca Yield Criterion (1864)

This criterion assumes that yielding of an isotropic material will take place when the maximum shear stress reaches a critical value, τ_Y. In uniaxial tension, the yield begins when $\sigma_1 = \sigma_Y, \sigma_2 = \sigma_3 = 0$ and hence, the yielding critical value is

$$\tau_Y = \frac{\sigma_Y}{2} \tag{2.25}$$

Accordingly, the maximum shear stress yield criterion, in terms of principal stresses, can take the form

$$F = Max\left[\frac{1}{2}|\sigma_1 - \sigma_2|, \frac{1}{2}|\sigma_2 - \sigma_3|, \frac{1}{2}|\sigma_1 - \sigma_3|\right] = \frac{\sigma_Y}{2} \tag{2.26}$$

2.3.2. Von Mises Yield Criterion (1913)

This criterion assumes that yielding will take place when the second deviatoric stress invariant J_2' reaches a critical value k^2 (Khan and Huang, 1995), which is a material property and is given by

$$\begin{aligned} J_2' < k^2 \quad & \text{elastic deformation region} \\ J_2' - k^2 = 0 \quad & \text{yielding or plastic deformation region} \end{aligned} \tag{2.27}$$

The von Mises criterion can be written in terms of stress components in the form

$$\frac{1}{6}\left[(\sigma_{11} - \sigma_{22})^2 + (\sigma_{22} - \sigma_{33})^2 + (\sigma_{33} - \sigma_{11})^2\right] + \sigma_{12}^2 + \sigma_{23}^2 + \sigma_{13}^2 = k^2 \tag{2.28}$$

or in terms of principal stresses as

$$\frac{1}{6}\left[(\sigma_1 - \sigma_2)^2 + (\sigma_2 - \sigma_3)^2 + (\sigma_3 - \sigma_1)^2\right] = k^2 \tag{2.29}$$

In case of plane-stress conditions ($\sigma_3 = 0$) and from a simple tension test, $\sigma_1 = \sigma_Y$ and $\sigma_2 = \sigma_3 = 0$, $k = \frac{\sigma_Y}{\sqrt{3}}$, where σ_Y is the yield stress in simple tension.

2.3.3. Hill Yield Criterion (1948)

Hill (1948) started the search for yield criterion for anisotropic materials by trying to modify the von Mises criterion for isotropic materials to describe the yielding of anisotropic materials using additional material constants.

Hill's yield criterion was assumed to be in the form

$$\begin{aligned} 2F(\sigma_{ij}) \equiv f(\sigma_{22}-\sigma_{33})^2 + g(\sigma_{33}-\sigma_{11})^2 + h(\sigma_{11}-\sigma_{22})^2 \\ + 2l\sigma_{23}^2 + 2m\sigma_{31}^2 + 2n\sigma_{12}^2 - 1 = 0 \end{aligned} \tag{2.30}$$

where *f, g, h, l, m,* and *n* are material constants characterizing the current state of anisotropic yield behaviour (Hill, 1948).

When $l=m=n=3f=3g=3h$, the yield function will be reduced to the form

$$\frac{1}{6}\left[(\sigma_{11}-\sigma_{22})^2 + (\sigma_{22}-\sigma_{33})^2 + (\sigma_{33}-\sigma_{11})^2\right] + \sigma_{12}^2 + \sigma_{23}^2 + \sigma_{13}^2 = \text{constant} \tag{2.31}$$

which is the von Mises criterion for isotropic materials, Eq. (2.28).

To determine these six material constants, it is necessary to measure three normal and three pure shear stresses in the principal directions and orthogonal planes of anisotropy, respectively (Khan and Huang, 1995). In case of plane-stress ($\sigma_{33}=\sigma_{23}=\sigma_{13}=0$), the yield function, Eq. (2.30), is reduced to the form

$$(g+h)\sigma_{11}^2 - 2h\sigma_{11}\sigma_{22} + (f+h)\sigma_{22}^2 + 2n\sigma_{12}^2 - 1 = 0 \tag{2.32}$$

Another form of Hill's yield function, in terms of the uniaxial tensile yield stress, σ_Y, in the 1-direction and plane stress condition takes the form (Hill, 1948)

$$\left[(g+h)\,\sigma_{11}^2 \;-\; 2h\,\sigma_{11}\,\sigma_{22} \;+\; (f+h)\,\sigma_{22}^2 \;+\; 2\,n\,\sigma_{12}^2\right]^{1/2} = \sigma_Y \tag{2.33}$$

In this case, Eq. (2.33), values of f, g, h, and n can be determined from the R-values measured at 0°, 45°, and 90° to the rolling direction. Generally, for a specimen cut at an angle φ to the rolling direction, the R-value can be determined as a function of the plastic strains (Hill, 1950). The ratio of the transverse to the through-thickness strain is

$$\begin{aligned} R_\varphi &= \frac{d\varepsilon_{11}\sin^2\varphi + d\varepsilon_{22}\cos^2\varphi - 2d\varepsilon_{12}\sin\varphi\cos\varphi}{d\varepsilon_{33}} \\ &= \frac{h+(2n-f-g-4h)\sin^2\varphi\cos^2\varphi}{f\sin^2\varphi + g\cos^2\varphi} \end{aligned} \tag{2.34}$$

Hence, the parameters in Hill's yield function, Eq. (2.33), are determined to be (Geng and Wagoner, 2002)

$$\begin{aligned} f &= \frac{R_0}{R_{90}(1+R_0)}, \quad g = \frac{1}{1+R_0} \\ h &= \frac{R_0}{1+R_0}, \qquad n = \frac{(R_0+R_{90})(1+2R_{45})}{2R_{90}(1+R_0)} \end{aligned} \tag{2.35}$$

When applying Hill's yield function to planar isotropic material and plane-stress conditions it takes the form (Huétink *et al.*, 1995)

$$(\bar{R}+1)(\sigma_{11}+\sigma_{22})^2 - 2(2\bar{R}+1)(\sigma_{11}\sigma_{22}-\sigma_{12}^2) - (\bar{R}+1)\sigma_Y^2 = 0 \tag{2.36}$$

where $\bar{R}$ is the average R-value. Hill's criterion is most widely known in its simplified form

$$(\sigma_1+\sigma_2)^2 + (1+2\bar{R})(\sigma_1-\sigma_2)^2 = 2(1+\bar{R})\sigma_Y^2 \tag{2.37}$$

where σ_1 and σ_2 are the principal stresses in the sheet plane and σ_Y is the yield stress in the uniaxial tension (Mellor, 1982). When $\bar{R}$ = 1, Eq. (2.37) reduces to von Mises criterion for isotropic criterion, Eq. (2.29) with $\sigma_3 = 0$. A plot comparing both yield criteria, von Mises and Hill's, is presented in Fig. (5.3).

2.3.4. Hosford Yield Criterion (1972)

A generalized extension of the von Mises criterion was presented by Hosford (1972). His isotropic yield function facilitated the representation of yield surfaces that lie between von Misses and Tresca. The equivalent stress, in terms of principal stresses, was defined as

$$\left[\frac{1}{2}\left(|\sigma_1-\sigma_2|^m+|\sigma_2-\sigma_3|^m+|\sigma_1-\sigma_3|^m\right)\right]^{\frac{1}{m}}=\bar{\sigma} \tag{2.38}$$

where $\sigma_1 \geq \sigma_2 \geq \sigma_3$ and $\infty \geq m \geq 1$. The von Mises yield function is retrieved when m = 2 or 4 and the Tresca yield function is obtained with m = 1 or ∞ (Hosford, 1972).

2.3.5. Hill Yield Criterion (1979)

Hill (1979) proposed a further generalization to his criterion. The proposed modification to the criterion is based on the assumption that the yield surface can be described mathematically as

$$\phi\left(\sigma_{ij}\right)=\left(\beta_{ijkl}\sigma_{ij}\sigma_{kl}\right)^{\frac{1}{2}}=c \tag{2.39}$$

and for a merely convex surface, it requires

$$\beta_{iikl} = 0 = \beta_{klii} \tag{2.40}$$

For a symmetric orthotropic material texture, the proposed quadratic yield function takes the form

$$\left[\begin{array}{c} f(\sigma_{22}-\sigma_{33})^2 + g(\sigma_{33}-\sigma_{11})^2 + h(\sigma_{11}-\sigma_{22})^2 \\ +2l\sigma_{23}^2 + 2m\sigma_{31}^2 + 2n\sigma_{12}^2 \end{array} \right]^{\frac{1}{2}} = \sigma_Y \tag{2.41}$$

where the coefficients *f*, *g*, *h*, *l*, *m*, and *n* are pure numbers and the original (1948) yield function can be recovered by identifying *f*, *g*, ... with $\frac{f}{\sigma_Y}, \frac{g}{\sigma_Y}, \ldots$.

For an in–plane isotropic material, $f = g$ and $\sigma_{33} = 0$. Equation (2.41) in principal components is reduced to

$$\left[f(\sigma_1^2 - \sigma_2^2) + h(\sigma_1 - \sigma_2)^2 \right]^{\frac{1}{2}} = \sigma_Y \tag{2.42}$$

Accordingly, under uniaxial tension, σ_u, i.e. $(\sigma_1, \sigma_2) = (\sigma_u, 0)$, Eq. (2.42) gives

$$(f+h)\sigma_u^2 = \sigma_Y^2 \tag{2.43}$$

and under biaxial tension, σ_b, i.e. $(\sigma_1, \sigma_2) = (\sigma_b, \sigma_b)$, Eq. (2.42) gives

$$2f\sigma_b^2 = \sigma_Y^2 \tag{2.44}$$

Another non-quadratic yield function was discussed in the same work of Hill (1979), which, in principal components, takes the form

$$f|\sigma_2-\sigma_3|^m+g|\sigma_3-\sigma_1|^m+h|\sigma_1-\sigma_2|^m=\sigma_Y^m \tag{2.45}$$

where the loading is coaxial with the orthotropy and $m > 1$.

2.3.6. Logan – Hosford Yield Criterion (1980)

Logan and Hosford (1980) proposed a yield criterion for textured BCC metals with rotational symmetry. The yield loci were calculated taking into consideration the crystallographic texture and the crystallographic nature of slip. The proposed yield function in terms of principal stresses, for plane stress loading, takes the form

$$|\sigma_1|^m+|\sigma_2|^m+R|\sigma_1-\sigma_2|^m=(R+1)\sigma_Y^m \tag{2.46}$$

where R is the strain ratio. For BCC materials, $m = 6$, and for FCC materials, $8 \leq m \leq 10$. It was also reported that as m increases from 2 to 6, the yield loci approach the Tresca criterion.

2.3.7. Barlat – Lian Yield Criterion (1989)

This yield criterion is limited to plane stress conditions. It involves an additional parameter to Hill's (1948) criterion, namely the stress exponent m. The yield condition takes the mathematical form

$$F=\left[\frac{1}{2}\left(a|K_1+K_2|^m+a|K_1-K_2|^m+c|2K_2|^m\right)\right]^{\frac{1}{m}}-\bar{\sigma}=0 \tag{2.47}$$

where $\bar{\sigma}$ is the effective stress, and the components K_1 and K_2 respectively take the forms

$$K_1 = \frac{1}{2}(\sigma_{11} + h\sigma_{22})$$
$$K_2 = \left[\left(\frac{\sigma_{11} - h\sigma_{22}}{2}\right)^2 + p\sigma_{12}\right]^{\frac{1}{2}} \tag{2.48}$$

The constants a, c, and h can be expressed in terms of the anisotropy parameters as

$$a = 2 - 2\left[\frac{R_0 R_{90}}{(1+R_0)(1+R_{90})}\right]^{\frac{1}{2}}$$
$$c = 2 - a \tag{2.49}$$
$$h = \left[\frac{R_0(1+R_{90})}{R_{90}(1+R_0)}\right]^{\frac{1}{2}}$$

and the parameter p can be solved for implicitly from the form

$$R_{45} = \frac{-1}{2}\left[1 - \frac{\dfrac{\partial F}{\partial \sigma_{12}}}{\left(\dfrac{\partial F}{\partial \sigma_{11}} + \dfrac{\partial F}{\partial \sigma_{22}}\right)}\right] \tag{2.50}$$

When the stress exponent m = 2 and the parameter p is determined according to the previous relation, the Barlat – Lian criterion becomes identical to Hill's 1948 criterion.

2.3.8. Hill's Improved Yield Criterion (1990)

Based on the previously established 1948 yield criterion, Hill (1990) proposed an improved yield function for plane stress that takes the form

$$\frac{1}{4}(f+g)(\sigma_{11}+\sigma_{22})^2+\frac{1}{4}(f+g+4h)(\sigma_{11}-\sigma_{22})^2 - \frac{1}{2}(f-g)\left(\sigma_{11}^2+\sigma_{22}^2\right)^2+2n\sigma_{12}^2=1 \tag{2.51}$$

substituting

$$\begin{aligned}&(\sigma_{11}+\sigma_{22})=(\sigma_1+\sigma_2),\\ &(\sigma_{11}-\sigma_{22})=(\sigma_1-\sigma_2)\cos 2\varphi, \text{ and}\\ &2\sigma_{12}=(\sigma_1-\sigma_2)\sin 2\varphi\end{aligned} \tag{2.52}$$

where σ_1 and σ_2 are the principal components of stress and are typically directed at an anticlockwise angle φ to the sheet coordinates. The yield function is expressed as

$$(\sigma_1+\sigma_2)^2+\left(\frac{\sigma}{\tau}\right)^2(\sigma_1-\sigma_2)^2-2a\left(\sigma_1^2+\sigma_2^2\right)\cos 2\varphi + b(\sigma_1-\sigma_2)^2\cos^2 2\varphi=(2\sigma)^2 \tag{2.53}$$

where $\sigma=(f+h)^{\frac{-1}{2}}$ for yielding under equi-biaxial tension, and $\tau=(2n)^{\frac{-1}{2}}$ for yielding under pure shear, $a=\dfrac{(f-g)}{(f+g)}>1$, and $b=\dfrac{(f+g+4h-2n)}{(f+g)}$.

Parameters *a* and *b* are dimensionless parameters that characterize the state of anisotropy of the material. By measuring four yield stresses, normal and shear, the anisotropic parameters, *a* and *b*, can be determined from

$$a=\left(\frac{\sigma}{\sigma_{90}}\right)^2-\left(\frac{\sigma}{\sigma_0}\right)^2$$
$$b=\frac{1}{2}\left[\left(\frac{2\sigma}{\sigma_0}\right)^2+\left(\frac{2\sigma}{\sigma_{90}}\right)^2\right]-\left(\frac{2\sigma}{\sigma_{45}}\right)^2=\left(\frac{\sigma}{\tau'}\right)^2-\left(\frac{\sigma}{\tau}\right)^2 \tag{2.54}$$

where τ' is the yield stress in shear at 45° to the orthotropic axes. Accordingly, the improved yield criterion takes the form

$$\begin{aligned}&|\sigma_1+\sigma_2|^m+\left(\frac{\sigma}{\tau}\right)^m|\sigma_1-\sigma_2|^m\\&+\left|\sigma_1^2+\sigma_2^2\right|^{\left(\frac{m}{2}-1\right)}\left[-2a\left(\sigma_1^2-\sigma_2^2\right)+b\left(\sigma_1-\sigma_2\right)^2\cos 2\varphi\right]\cos 2\varphi=(2\sigma)^m\end{aligned} \tag{2.55}$$

where $m > 1$.

In this case, the state of the material is characterized by five parameters: the yield stress in biaxial tension, σ, the yield stress in pure shear, τ, and the dimensionless parameters a, b, and m. This criterion given by Eq. (2.55) is reduced to Eq. (2.53) when $m = 2$.

2.3.9. Hosford Yield Criteria (1996)

Considering the crystallographic texture of the material, Hosford (1996) proposed a yield function that takes the form

$$R|\sigma_2-\sigma_3|^m+P|\sigma_3-\sigma_1|^m+RP|\sigma_1-\sigma_2|^m=P(R+1)\sigma_{Y_1}^m=R(P+1)\sigma_{Y_2}^m \tag{2.56}$$

where R and P are the ratios of lateral contraction strains in tension tests along the longitudinal and transverse directions, respectively, and σ_{Y_1} and σ_{Y_2} are the yield

strengths in the 1- and 2-direction tension tests. The exponent m is equal to 6 for BCC metals and 8 for FCC metals.

This criterion is a generalization of the Hill's (1948) anisotropic yield criterion Eq. (2.36) and Hosford's (1972) yield criterion, Eq. (2.38). It was reported that the shortcoming of this criterion is that it can only be used when the principal stress axes and the principal symmetry axes coincide, i.e. no presence of shear stresses.

2.3.10. Cazacu – Barlat Criterion (2004)

Cazacu and Barlat (2004) and Cazacu *et al.* (2004) presented a yield criterion for anisotropic material of the form

$$F = \left[\frac{1}{6}(a_1+a_3)\sigma_{11}^2 - \frac{a_1}{3}\sigma_{11}\sigma_{22} + \frac{1}{6}(a_1+a_2)\sigma_{22}^2 + a_4\sigma_{12}^2\right]^{\frac{3}{2}} - c\left[\begin{array}{l}\frac{1}{27}(b_1+b_2)\sigma_{11}^3 + \frac{1}{27}(b_3+b_4)\sigma_{22}^3 - \frac{1}{9}(b_1\sigma_{11}+b_4\sigma_{22})\sigma_{11}\sigma_{22} \\ -\frac{1}{3}\sigma_{12}^2\left[(b_5-2b_{10})\sigma_{11} - b_5\sigma_{22}\right]\end{array}\right] = \tau_Y^3 \tag{2.57}$$

a_k (k = 1, ... 4), b_k (k = 1, ... 5) and b_{10} are anisotropy coefficients, c is a material constant, and τ_Y is the yield stress in pure shear. The material constants are determined from a series of particular tests, namely uniaxial tension and compression tests, performed at rolling and transverse directions, and biaxial tension and compression tests. For equal yield stresses in tension and compression, or c = 0, the criterion reduces to the von Mises criterion.

The proposed criterion was applied to a textured Mg-Li alloy. The shapes of the yield loci for different strain ranges are shown in Fig. (2.12).

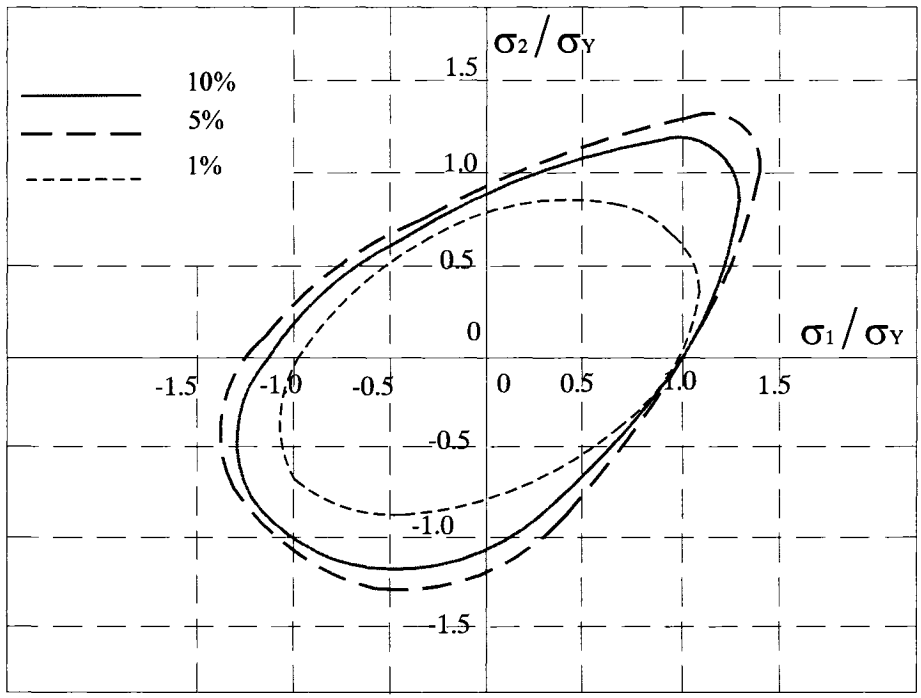

Fig. (2.12) Yield loci for Mg-4%Li alloy at different strain levels
(adapted from Cazacu *et al.*, 2004)

2.3.11. Other Yield Criteria

Hosford (1985) suggested an anisotropic criterion that abandons the convention of expressing the stress components along the principal axes of anisotropy. He assumed that the principal stress and principal strain axes coincide, whether or not they are parallel to the principal axes. It was noted that this assumption may introduce errors; however, it was reported that these errors are much less than the errors that arise from the planar isotropy assumption. A yield function, for in-plane loading, may take the form

$$R_2\sigma_1^m + R_1\sigma_2^m + R_1R_2\left(\sigma_1 - \sigma_2\right)^m = R_2\left(R_1 + 1\right)\sigma_{Y_1}^m \tag{2.58}$$

where R_1 and R_2 are the strain ratios measured in the 1 and 2 directions, respectively, and σ_{Y_1} is the yield stress in the 1-direction. It was reported that the exponent m = 6 or 8 may give a better approximation for anisotropic metals.

Tan *et al.* (1994) proposed a yield criterion that includes the Bauschinger effect factor, B given in Eq. (2.2). In the case of biaxial stresses, the yield criterion, for plane stress conditions, can be written as

$$\sigma_1^2+\sigma_2^2-\sigma_1\sigma_2-\sigma_t B(\sigma_1+\sigma_2)=(1-B)\sigma_f^2 \tag{2.59}$$

where σ_f is the forward yield stress in tension. In the absence of the Bauschinger effect in the material, B = 0, the model reduces to the von Mises criterion. A comparison of the yield locus of SS1147, given by this criterion, with other classical assumptions is shown in Fig. (2.13).

Suh *et al.* (1996) reviewed many anisotropic yield functions by different authors and reported that the effective stress, $\bar{\sigma}$, can be expressed in terms of principal stresses in a plane-stress case as

$$|\sigma_1+\sigma_2|^M+(1+2R)|\sigma_1-\sigma_2|^M=2(1+R)\bar{\sigma}^M \tag{2.60}$$

where M is a parameter that characterizing the yield surface's shape and R is the normal anisotropy parameter. The exponent M = 2 with R=1 reduces the criterion to the von Mises yield function. The M value was evaluated, for 2004-T4 aluminum alloy and 70/30 brass, as a function of strain using the curves for the stress-strain curves obtained from uniaxial tension and the effective stress-effective strain obtained from plane-strain.

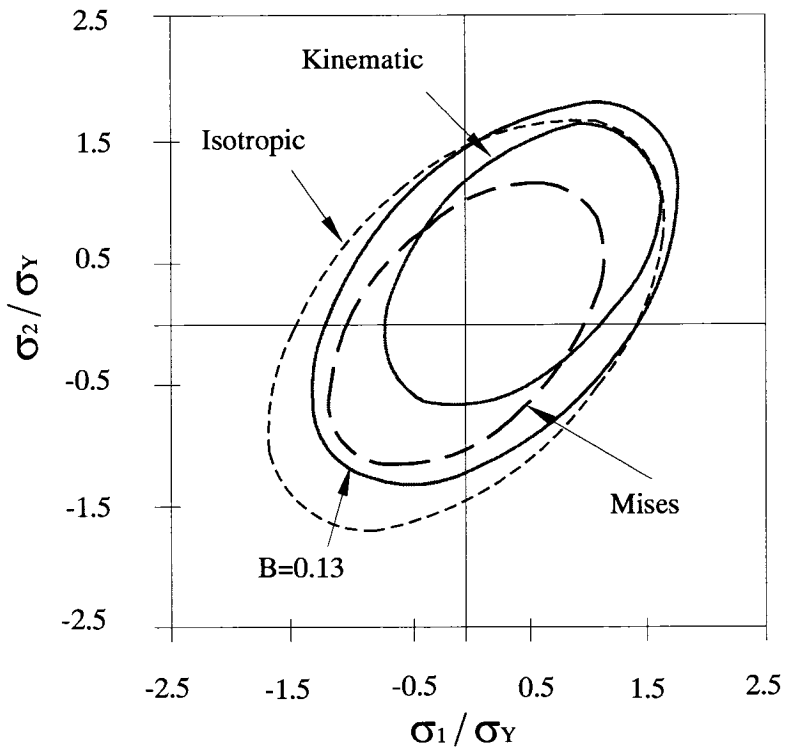

Fig. (2.13) Comparison of yield loci given by various hardening models for sheet SS1147. The Bauschinger stress factor B is measured at σ_f = 220 MPa and prestrain = 0.034 (adapted from Tan *et al.*, 1994)

Banabic *et al.* (2003) and Banabic *et al.* (2004) proposed non-quadratic yield criteria for orthotropic materials under plane stress conditions. Their yield criteria were derived from Barlat and Lian (1989). The equivalent stress was defined as

$$\bar{\sigma} = \left[a\left(b\Gamma + c\Psi\right)^{2k} + a\left(b\Gamma - c\Psi\right)^{2k} + \left(1-a\right)\left(2c\Psi\right)^{2k} \right]^{\frac{1}{2k}} \tag{2.61}$$

where a, b, c and k are material parameters. The value of k strictly depends on the crystallographic structure of the material: k = 3 and 4 for BCC and FCC alloys, respectively. Moreover, Γ and Ψ are quantities related to the non-zero components of the

stress tensor and can be expressed as explicit dependencies of the actual stress components as

$$\Gamma = (d+e)\sigma_{11} + (e+f)\sigma_{22}$$
$$\Psi = \left[\left(\frac{d+e}{2}\sigma_{11} - \frac{e-f}{2}\sigma_{22}\right)^2 + g^2\sigma_{12}\sigma_{21}\right]^{\frac{1}{2}} \tag{2.62}$$

The parameters *a*, *b*, *c*, *d*, *e*, *f* and *g* are parameters that define the shape of the yield surface; a strategy for defining these parameters was established to minimize the error function

$$F(a,b,c,d,e,f,g) = \left(\frac{\sigma_0}{\sigma_0^{exp}} - 1\right)^2 + \left(\frac{\sigma_{90}}{\sigma_{90}^{exp}} - 1\right)^2 + \left(\frac{\sigma_{45}}{\sigma_{45}^{exp}} - 1\right)^2 + \left(\frac{\sigma_b}{\sigma_b^{exp}} - 1\right)^2 + \left(\frac{R_0}{R_0^{exp}} - 1\right)^2 + \left(\frac{R_{90}}{R_{90}^{exp}} - 1\right)^2 + \left(\frac{R_{45}}{R_{45}^{exp}} - 1\right)^2 \tag{2.63}$$

where $\sigma_0, \sigma_{45}, \sigma_{90}$ are the uniaxial yield stresses, σ_b is the equi-biaxial yield stress, and R_0, R_{45}, R_{90} are the coefficients of plastic anisotropy predicted by the model. The superscript, exp, denotes the experimental values.

Two materials were tested and compared with the theoretical findings, namely 6000 series aluminum alloy sheet and Al-killed cold-rolled steel sheet. For the equi-biaxial tension test, the same configuration described in Kuwabara *et al.* (2004) was used. The shape of the yield surface and the experimental data, for the 6000 series aluminum alloy, are shown in Fig. (2.14).

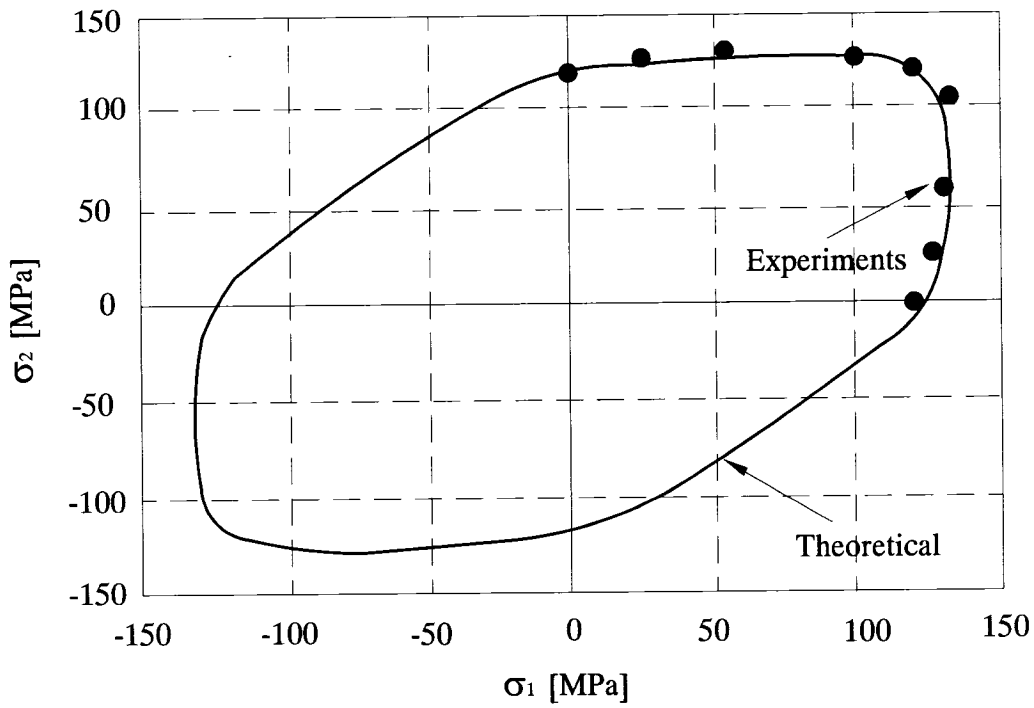

Fig. (2.14) Yield surface for A6XXX-T4 (adapted from Banabic *et al.*, 2004)

2.4. Hardening Models

The theory of plasticity is based on three basic relations, namely the yield surface or yield criterion, the flow rule, and the hardening model or hardening rule. The classical theory of plasticity uses a single yield surface to define the elastic and plastic behaviour. As discussed in the previous section, the yield surface divides the stress space into two regions: the inside region where only reversible or elastic strain occurs, and outside region where stresses exceed those corresponding to the state of yielding. Prager and Providence (1956) and Drucker and Palgen (1981) are famous examples of a single yield surface criterion. Further approaches lead to multiple– and two – surface plasticity theories; Mróz (1967) is one of the famous examples of this theory.

The second concept in plastic behaviour is the flow rule, by which the direction of the plastic strain or flow of plastic deformation is defined at any stage of the loading process.

The direction of the plastic strain increment, $d\varepsilon_{ij}^{pl}$, is defined by the so-called plastic potential function. This plastic potential function can take the form of the yield function and, in this case, the flow rule is called the associative flow rule (Khan and Huang, 1995).

Finally, the third concept is the hardening rule or the model by which the stress or strength of the material increases with the increase in the plastic strain. If there is no hardening, the material behaviour is considered elastic-perfectly plastic. In other words, the strength of the material remains constant after the stress condition reaches the yield surface. In this case, the yield surface is fixed in the stress space and no hardening rule is defined.

2.4.1. Isotropic Hardening Model

Isotropic hardening assumes that the material is isotropic at the annealed state and the Bauschinger effect and the anisotropy developed due to deformation may be neglected (Khan and Huang, 1995). It also assumes that the subsequent yield surface is a uniform expansion of the initial yield surface, Fig. (2.15), and hence the isotropic response of the material to yielding does not change during plastic deformation (Chakrabarty, 1987).

The isotropic hardening behaviour is described mathematically as

$$f\left(J_2', J_3'\right) - k = 0 \tag{2.64}$$

where k is a material constant characterizing the isotropic hardening effect and is the only parameter dependent on plastic deformation (Khan and Huang, 1995). However, according to von Mises's criterion, only the second deviatoric stress invariant J_2' is taken into account, then the isotropic hardening behaviour can take the form

$$f\left(J_2'\right) - k\left(\xi\right) = 0 \tag{2.65}$$

where ξ represents either the total equivalent plastic strain $\left(\bar{\varepsilon}^{p}\right)$ or the total plastic work $\left(W^{p}\right)$:

$$\begin{aligned} \xi &= \bar{\varepsilon}^{p} = \int d\bar{\varepsilon}^{p}, \text{ or} \\ \xi &= W^{p} = \int \sigma_{ij} d\varepsilon_{ij}^{pl} \end{aligned} \tag{2.66}$$

Accurate material cyclic behaviour cannot always be predicted by an isotropic hardening model; therefore, more effort was focused on establishing models that can properly account for complex loading of the material (Chu, 1987).

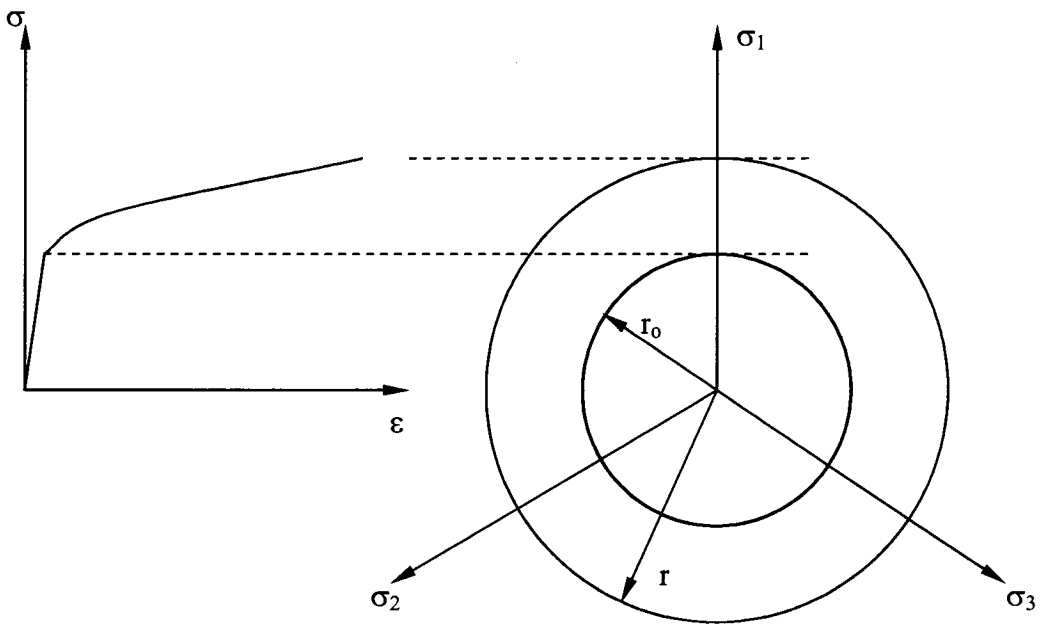

Fig. (2.15) Isotropic hardening yield surfaces

2.4.2. Kinematic Hardening Model

This model is also known as Prager's model. It assumes that the yield surface translates as a rigid body in the stress space during the plastic deformation (Jiang, 1994). Therefore, the shape of the subsequent yield surface does not change during plastic deformation, Fig. (2.16). The basic concept of kinematic hardening is that when the yield surface translates in stress space, the straining in one direction will result in a reduction in the yield stress in the opposite direction (Brunet *et al.*, 2001).

Since the initial yield surface can be described by

$$f\left(\sigma_{ij}\right)-k=0 \tag{2.67}$$

where k is a constant, the resultant displacement of the subsequent yield surface can be denoted by a symmetric tensor α, usually called the back stress, and the yield surface at any stage can take the form (Chakrabarty, 1987, and Khan and Huang, 1995)

$$f\left(\sigma_{ij}-\alpha_{ij}\right)-k=0 \tag{2.68}$$

The incremental translation of the yield surface is assumed to be in the direction of the plastic strain increment $d\varepsilon_{ij}^{pl}$ (Chakrabarty, 1987). Thus, the back stress increment (Prager and Providence, 1956) is defined as

$$d\alpha_{ij}=cd\varepsilon_{ij}^{pl} \tag{2.69}$$

where c is a material constant.

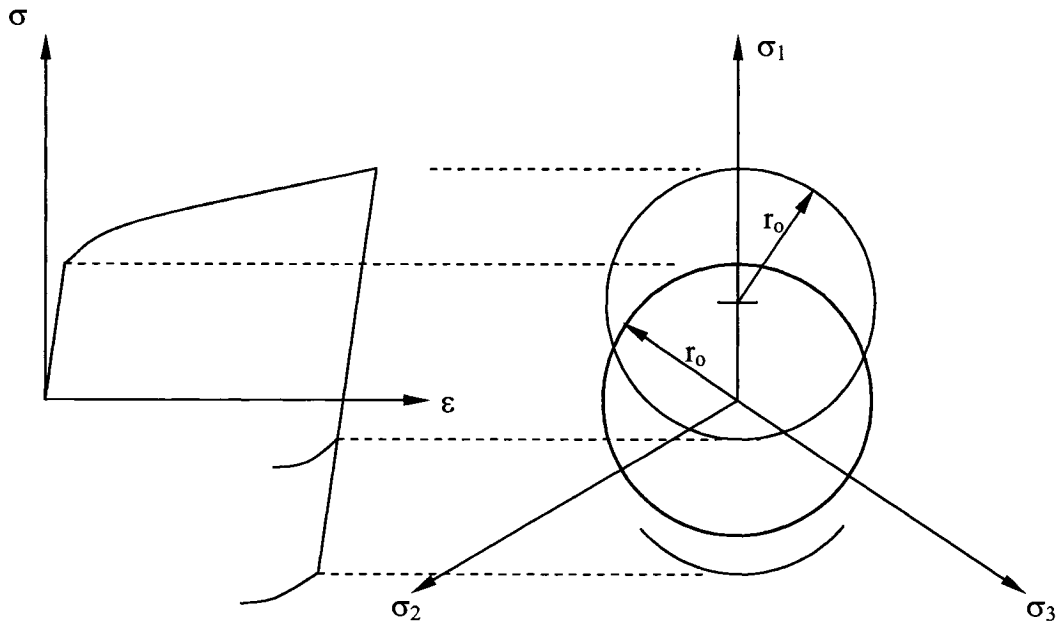

Fig. (2.16) Kinematic hardening yield surfaces

If a tension specimen is loaded in the 1-direction causing plastic flow for an isotropic material

$$\begin{aligned} d\varepsilon_{11}^{pl} &= d\varepsilon^{pl} \\ d\varepsilon_{22}^{pl} &= d\varepsilon_{33}^{pl} = -\frac{1}{2} d\varepsilon^{pl} \end{aligned} \tag{2.70}$$

and hence,

$$\begin{aligned} d\alpha_{11} &= c d\varepsilon^{pl} \\ d\alpha_{22} &= d\alpha_{33} = -\frac{1}{2} d\alpha_{11} = -\frac{1}{2} c d\varepsilon^{pl} \end{aligned} \tag{2.71}$$

If c is a constant, it is called the linear hardening rule. On the other hand, c can be defined as a function of the deformation history, therefore, representing a nonlinear hardening rule (Khan and Huang, 1995).

Ziegler (1959) defined the back stress increment as

$$d\alpha_{ij} = \frac{C}{\sigma_Y}\left(\sigma_{ij} - \alpha_{ij}\right) d\bar{\varepsilon}^p \tag{2.72}$$

where σ_Y, $d\bar{\varepsilon}^p$, and C are the yield stress, effective plastic strain increment, and a material constant, respectively. His model predicts a linear relationship between stress and strain and provides a constant hardening modulus, which was reported to be inadequate in representing the real material behaviour in experiments.

It was reported that the Prager and Providence (1956) and Ziegler (1959) models have the disadvantage of including some degrees of arbitrariness in their formulations, specifically in the way of defining the flow stress. The arbitrariness comes from the dependence of the yield surface, which is assumed constant, on the definition of the flow stress (Chu, 1987).

In a review of the Armstrong-Frederick (1966) kinematic hardening model, Jiang and Kurath (1996) reported that the A-F model is an improvement over Ziegler's model by specifying the direction and the magnitude of the yield surface translation. The model is a nonlinear model which gives a better description of the Bauschinger effect compared to the linear models proposed by Prager and Providence (1956) and Ziegler (1959). Appiah and Jain (2004) described the increment of back stress in the A-F model as

$$d\alpha_{ij} = \frac{2}{3} c d\varepsilon_{ij}^{pl} - \gamma \alpha_{ij} d\bar{\varepsilon}^p \tag{2.73}$$

where c and γ are material parameters.

Later, Chaboche (1986) modified the A-F model by decomposing the total back stress into a number of additive parts so that

$$\alpha_{ij} = \sum_{k=1}^{m} \alpha_{ij}^{(k)} \tag{2.74}$$

and each part of the back stress follows the A-F format. Accordingly, the back stress increment in Eq. (2.73) will take the form

$$d\alpha_{ij}^{(k)} = \frac{2}{3} c^{(k)} d\varepsilon_{ij}^{pl} - \gamma^{(k)} \alpha_{ij}^{(k)} d\bar{\varepsilon}^{p} \tag{2.75}$$

Chaboche (1986) suggested that k can take the values of 1, 2, and 3; representing three kinematic variables, which is sufficient to cover strain ranges from 0.01% to 4%.

Wang and Barkey (1999) proposed a nonlinear kinematic hardening rule based on the strain space rather than the stress space as most of the hardening rules. The yield function in terms of strain takes the form

$$\phi = \left(e_{ij} - \gamma_{ij}\right)\left(e_{ij} - \gamma_{ij}\right) - e_o^2 = 0 \tag{2.76}$$

where e_{ij} is the deviatoric components of the elastic strain tensor, γ_{ij} is a hardening parameter which equals $\frac{\alpha_{ij}}{2G}$, and $e_o = \frac{\gamma_o}{\sqrt{2}}$, where $\gamma_o = \frac{\tau_o}{G}$ is the initial yield strain in shear and G is the shear modulus. It was reported that the model is equivalent to the A-F kinematic hardening model for work-hardening materials; however, further elaboration was needed to account for the work-softening material behaviour.

2.4.3. Combined Isotropic and Kinematic Hardening Model

The general case, matching observations on common metals, includes a mixture of both effects, that is isotropic hardening or softening (Bauschinger effect) and nonlinear kinematic hardening.

The yield criterion can be described mathematically as a function of the work hardening and Prager's kinematic hardening model; that is

$$f\left(\sigma_{ij}-\alpha_{ij}\right)-k\left(W^{p}\right)=0 \tag{2.77}$$

where W^P is the total plastic work (Khan and Huang, 1995).

Hodge (1957) proposed a combined hardening model, which assumes that the plastic strain increment can be linearly composed into two parts, one caused by kinematic hardening and the other by isotropic hardening so that

$$d\varepsilon_{ij}^{pl}=d\varepsilon_{ij}^{iso}+\varepsilon_{ij}^{kin} \tag{2.78}$$

The drawback of this model is that the nonlinear elastic-plastic transition cannot be reproduced upon load reversal.

A generalization of the linear kinematic hardening rule, which led to multi-surface models, was introduced by Mróz (1967). He introduced the concept of a "field of workhardening moduli" instead of a single modulus c given in Eq. (2.69). In Mróz's model, a number of nested yield surfaces exist and a plastic modulus is associated with each yield surface. Mróz (1967) assumed that the centers of the yield surfaces are initially concentric at the origin of the stress space, as shown in Fig. (2.17a). After plastic deformation takes place, these yield surfaces become eccentric, as shown in Fig. (2.17b). Each surface can be described by

$$f^{(l)}=\phi\left(\sigma_{ij}-\alpha_{ij}^{(l)}\right)-\left(\sigma_{o}^{(l)}\right)^{n}=0 \tag{2.79}$$

where ϕ is a homogeneous function of order n of its arguments, $\alpha_{ij}^{(l)}$ and $\sigma_{o}^{(l)}$ correspond to the surface's center and size, respectively (Chaboche, 1986). It was assumed that each

surface, at a specific plastic deformation, is actuated and experiences translation in the stress space until it tangentially contacts the next yield surface and then both surfaces translate simultaneously towards the next surface, and so on, as shown in Fig. (2.17b).

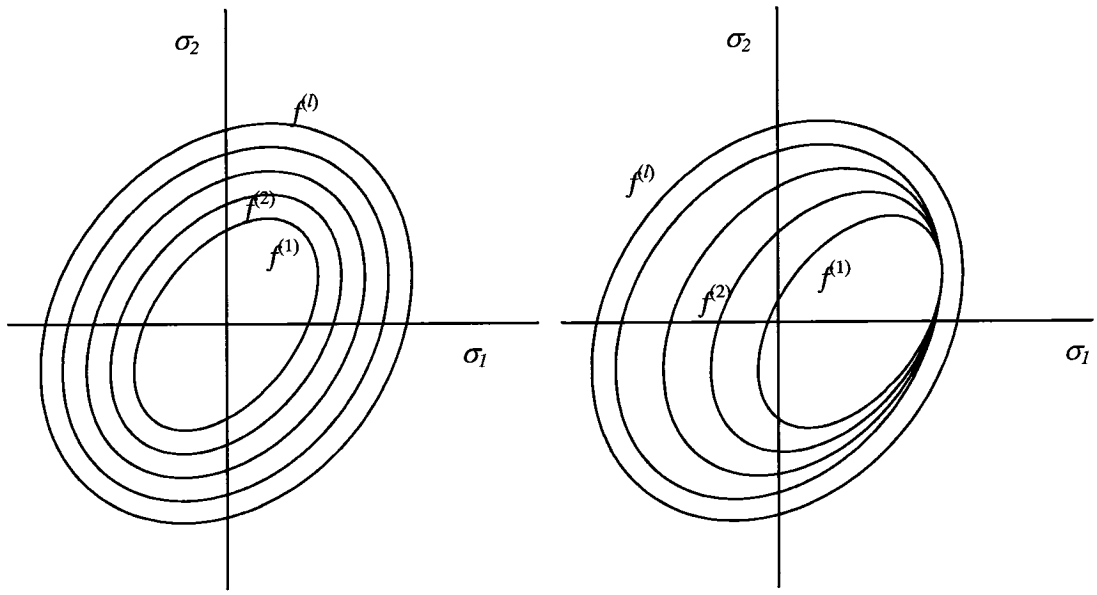

Fig. (2.17) Representation of the stress space for Mróz yield surfaces (a) before plastic deformation, and (b) after plastic deformation takes place

The translation of the active yield surface, $f^{(l)}$, is given by

$$d\alpha_{ij}^{(l)} = \frac{d\mu}{\sigma_o^{(l)}}\left[\left(\sigma_o^{(l+1)} - \sigma_o^{(l)}\right)\sigma_{ij}^{(l)} - \left(\alpha_{ij}^{(l)}\sigma_o^{(l+1)} - \alpha_{ij}^{(l+1)}\sigma_o^{(l)}\right)\right] \tag{2.80}$$

where the parameter $d\mu$ is determined, assuming that the stress point remains on the yield surface, from

$$d\mu = \frac{\frac{\partial f}{\partial \sigma_{ij}} d\sigma_{ij}}{\frac{\partial f}{\partial \sigma_{kl}} \left(\sigma_{kl}^{(l+1)} - \sigma_{kl}^{(l)}\right)} \tag{2.81}$$

Describing actual material behaviour using the Mróz model requires a large number of yield surfaces, each surface requires the storage of a tensor variable, usually six components, and a scalar quantity. This is considered one of the main difficulties with that model. Several attempts were done to develop models that use only two surfaces, a yield surface and a bounding surface, in order to achieve the same specific properties (Chaboche, 1986).

Based on the Mróz model, Chu (1984) developed an incremental three-dimensional constitutive relationship to study the influence of complicated loading histories on material behaviour. In his work, Chu (1984) assumed a material with a von Mises yield function that was expressed as

$$F = \left(\frac{3}{2}\right)\left(\sigma'_{ij} - \alpha_{ij}\right)\left(\sigma'_{ij} - \alpha_{ij}\right) - k^2 = 0 \tag{2.82}$$

where σ'_{ij} are the deviatoric components of the stress tensor, α_{ij} are the back stress or the components of the position tensor of the center of the active yield surface, and k is the equivalent flow stress. From Mróz's assumption that the stress point remains on the yield surface, the differential form of the yield function is

$$\left(\frac{3}{2}\right)\left(\sigma'_{ij} - \alpha_{ij}\right)\left(d\sigma'_{ij} - d\alpha_{ij}\right) - kdk = 0 \tag{2.83}$$

It was suggested that the increment of the back stress $d\alpha_{ij}$ must be determined first before dk. Assuming that the yield surface moves along a unit tensor β, the magnitude of $d\alpha_{ij}$ is then can be determined as

$$d\alpha_{ij} = \left(\sqrt{\frac{2}{3}}\right) dk\beta_{ij} \tag{2.84}$$

and hence, *dk* can be determined from

$$dk = \left(\frac{3}{2}\right)\frac{\left(\sigma'_{ij} - \alpha_{ij}\right)d\sigma'_{ij}}{\bar{k}} \tag{2.85}$$

where $\bar{k}$ is determined from

$$\bar{k} = k + \left(\sqrt{\frac{3}{2}}\right)\left(\sigma'_{ij} - \alpha_{ij}\right)\beta_{ij} \tag{2.86}$$

The Chu (1984) constitutive law was employed in the analysis of sheet metal problems and it was reported that it provided more accurate prediction in material response subject to complicated loading histories.

Brunet *et al.* (2001) used the inverse approach to identify the constitutive parameters in a combined hardening model. The isotropic hardening portion was defined by the size of the elastic range, $\bar{\sigma}$, as a function of the equivalent plastic strain $\bar{\varepsilon}^p$ as

$$\bar{\sigma} = \sigma_o + Q\left(1 - e^{-b\bar{\varepsilon}^p}\right) \tag{2.87}$$

where σ_o is the size of the yield surface at zero plastic strain, and Q and b are hardening parameters. The evolution of the kinematic hardening components is defined by

$$d\alpha_{ij} = C\frac{d\bar{\varepsilon}^p}{\bar{\sigma}}\left(\sigma_{ij} - \alpha_{ij}\right) - \gamma\alpha_{ij}d\bar{\varepsilon}^p \tag{2.88}$$

where C and γ are additional material parameters.

The four constitutive parameters, Q, b, C and γ, were identified inversely by means of bending tests and tensile tests. It was reported that the model has some limitations and uncertainties due to measurement errors and by the fact that the strain state in the sample is not exactly a pure strain state of bending. However, for the sheet metal forming simulations, it is sufficient to identify the parameters based on the first moment-curvature cycle and the monotonic tensile curve.

A so-called "anisotropic" hardening model that combines isotropic and nonlinear kinematic hardening was formulated by Geng and Wagoner (2002). Their model can be considered as a two-surface hardening model with the exception that the bounding surface is allowed to act in a combined hardening manner, i.e. expands and translates in the stress space. The hardening rule is expressed in a similar way to the A-F model with an additional term to allow for expansion and translation of the bounding surface. It can be expressed as

$$d\alpha_{ij} = \frac{C}{\sigma_o}\left(\sigma_{ij} - \alpha_{ij}\right)d\bar{\varepsilon}^p - \gamma\left(\alpha_{ij} - \beta_{ij}\right)d\bar{\varepsilon}^p \tag{2.89}$$

where the model parameters are as defined before and the additional term β_{ij} represents the center of the bounding surface. The translation and expansion of the bounding surface is given by

$$d\beta_{ij} = \frac{mH}{\sigma_{\beta o}}\left(\sigma_{\beta_{ij}} - \beta_{ij}\right)d\bar{\varepsilon}^p \tag{2.90}$$

where $m \leq 1$ is the ratio of the kinematic response to the isotropic response, i.e. translation to expansion, of the bounding surface, H is the plastic modulus of the monotonic loading curve, $\sigma_{\beta o}$ is the size of the bounding surface and $\sigma_{\beta_{ij}}$ represents a stress point on the bounding surface.

Moreover, Geng *et al.* (2002) used a simple bend/unbend test to investigate the cyclic loading of 6022-T4 aluminum alloy, high-strength low-alloy (HSLA) steel, and drawing-quality silicon-killed (DQSK) steel. A three-point bending device was used and specimens of 25.40 mm width were tested.

Also, the bend/unbend test was simulated using the von Mises yield function. Shell, solid, plane strain, and plane stress elements were used in their simulations. It was found that the shell element and the 3D solid element models accurately reproduced the experimental results while the plane-strain simulations over-estimated the load and the plane-stress simulation under-predicted it. The simulation results for the aluminum sheet are shown in Fig. (2.18).

In their study, the material model used followed the A-F, Chaboche and Ziegler hardening models, so that the increment of the back stress was given by

$$d\alpha_{ij} = \frac{C}{\sigma_o}\left(\sigma_{ij} - \alpha_{ij}\right)d\bar{\varepsilon}^p - \gamma\alpha_{ij}d\bar{\varepsilon}^p \tag{2.91}$$

They reported that the parameters obtained, C and γ, from their bend/unbend test to reflect the hardening behaviour of the material are only accurate within a limited range of strain, typically less than 0.02. Accordingly, the material parameters were adjusted by trial and error to obtain best-fit values to the experiments.

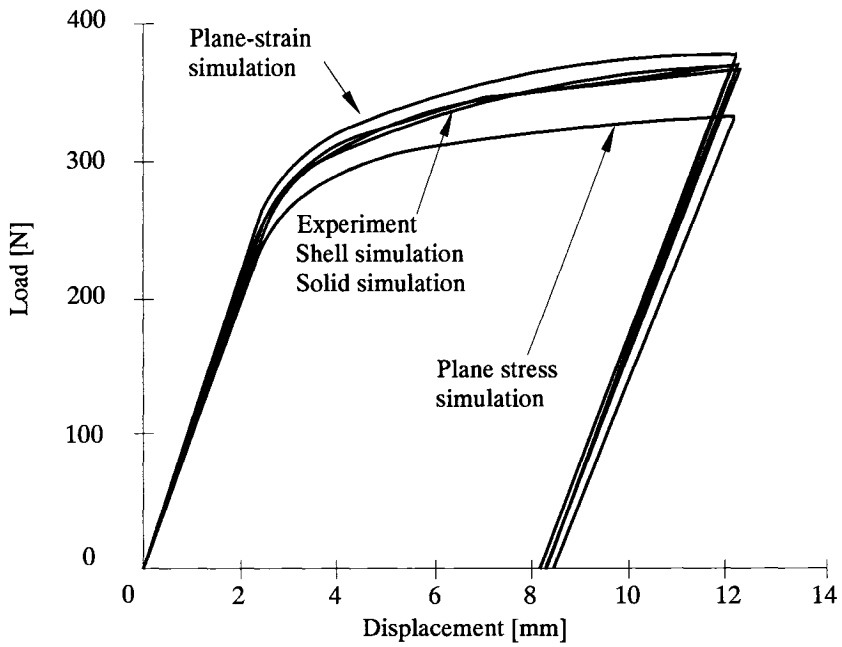

Fig. (2.18) Differences among 2-D and 3-D simulations of the bend/unbend tests (adapted from Geng *et al.*, 2002)

Brunhs *et al.* (2003) suggested a combined hardening model that depends on the Tresca criterion. An extension of the Tresca yield function, that includes the back stress, takes the form

$$F = \frac{(\sigma_1 - \sigma_2) - (\alpha_1 - \alpha_2)}{2} - \bar{k}\left(W^p\right) \tag{2.92}$$

where σ_1 and σ_2 are the largest and smallest principal stresses, α_1 and α_2 are the normal components of the back stress, and $\bar{k}\left(W^p\right)$ is the current yield shear stress depending on the plastic work, which characterizes the isotropic hardening component.

Sinou and Macquaire (2003) defined a combined hardening model based on Hill's yield criterion so that

$$F(\sigma,\alpha)=\left[\frac{1}{2}\begin{pmatrix} h(\sigma_{11}-\alpha_{11}-\sigma_{22}+\alpha_{22})^2 \\ +f(\sigma_{22}-\alpha_{22}-\sigma_{33}+\alpha_{33})^2 \\ +g(\sigma_{33}-\alpha_{33}-\sigma_{11}+\alpha_{11})^2 \\ +2l(\sigma_{23}-\alpha_{23})^2 \\ +2m(\sigma_{31}-\alpha_{31})^2 \\ +2n(\sigma_{12}-\alpha_{12})^2 \end{pmatrix}\right]^{\frac{1}{2}} - \Re = 0 \qquad (2.93)$$

where $\Re$ is an isotropic hardening variable, f, g, h, l, m, and n are Hill's anisotropic parameters. The kinematic and isotropic hardening laws were defined, respectively, as

$$\begin{aligned} d\alpha_{ij} &= C_o d\varepsilon_{ij}^{pl} - \gamma\alpha_{ij} d\lambda, \text{ and} \\ d\Re &= C_{\Re}\left(\Re_{sat} - \Re\right) d\bar{\varepsilon}^{p} \end{aligned} \qquad (2.94)$$

where C_o and γ are material parameters characterizing the kinematic hardening, $C_{\Re}$ and $\Re_{sat}$ are material parameters characterizing the isotropic hardening, $d\varepsilon_{ij}^{pl}$ defines the incremental plastic strains, $d\lambda$ is a constant, and $d\bar{\varepsilon}^{p}$ is the equivalent plastic strain, which can be determined as

$$d\bar{\varepsilon}^{p} = \left[2\left(\begin{matrix} \dfrac{f\left(hd\varepsilon_{33}^{pl} - gd\varepsilon_{22}^{pl}\right)^2 + g\left(fd\varepsilon_{11}^{pl} - hd\varepsilon_{33}^{pl}\right)^2 + h\left(gd\varepsilon_{22}^{pl} - fd\varepsilon_{11}^{pl}\right)^2}{\left(gh+fg+hf\right)^2} \\ +2\dfrac{\left(d\varepsilon_{12}^{pl}\right)^2}{n} + 2\dfrac{\left(d\varepsilon_{23}^{pl}\right)^2}{l} + 2\dfrac{\left(d\varepsilon_{31}^{pl}\right)^2}{m} \end{matrix}\right)\right]^{\frac{1}{2}} \qquad (2.95)$$

The parameters C_o, γ, $C_{\Re}$, and $\Re_{sat}$ were determined analytically from the evolution of the yield locus and the isotropic hardening parameter $\Re$ during a complex loading path.

Appiah and Jain (2004) proposed a combined hardening model that accounts not only for translation and change in size of the yield surface but also for the distortion or shape change. The change of the center of the yield surface is given by

$$d\alpha_{ij} = H_{eff} d\bar{\varepsilon}^{p} n_{ij} \tag{2.96}$$

where $d\bar{\varepsilon}^{p}$ is the effective plastic strain, n_{ij} is the direction of the plastic flow, and H_{eff} is the effective plastic modulus and is given by

$$H_{eff} = \psi_T H_T + \psi_S H_S + \psi_D H_D \tag{2.97}$$

where H_T, H_S, and H_D are the plastic moduli corresponding to translation, size change and shape distortion, respectively. The coefficients ψ_i [i = T, S, D] are the relative contributions of each corresponding plastic modulus. Using the A-F kinematic hardening model, the translation modulus, H_T, was obtained as

$$H_T = C - \frac{3}{2}\gamma\alpha_{ij} n_{ij} \tag{2.98}$$

where C and γ are parameters to be determined. The plastic modulus corresponding to the change of the yield surface size, H_S, was obtained as

$$H_S = \pm\eta_1 S_o e^{-\eta_1 \bar{\varepsilon}^{p}} \tag{2.99}$$

where S_o and η_1 are the initial size of the yield surface and its evolution rate, respectively. The ± sign corresponds to expansion and contraction of the yield surface, the positive sign must be used for expansion and the negative sign is for contraction.

The plastic modulus, H_D, accounts for distortion or shape change of the yield surface was calculated as

$$H_D = \omega\sqrt{n_{jk}n_{jk}} \tag{2.100}$$

where ω is a material constant and n_{ij} are the plastic flow direction components.

2.5. Material Characterization

In sheet metal forming simulations, the accuracy of the model highly depends on accurate characterization of the material properties. Many researchers have worked on methods of determining the appropriate material parameters to reflect the actual behaviour of the material. Some of the efforts in the area of material characterization are presented in this section.

To obtain the material properties for steel sheets under compression, Schedin and Melander (1987) performed compression tests on cubic specimens made by gluing together approximately eight sheets which were then machined to the required specimen's dimensions. The effective stress and strain components were, respectively, evaluated in terms of the true stress and strain in the direction normal to the sheet as

$$\begin{aligned} \bar{\sigma} &= -\left(2\left(1-\frac{1}{b}\right)\right)^{\frac{1}{2}}\sigma_{33}, \\ \bar{\varepsilon} &= -\left(\frac{b\left(b+2\rho+b\rho^2\right)}{b^2-1}\right)^{\frac{1}{2}}\left(\frac{1}{1+\rho}\right)\varepsilon_{33} \end{aligned} \tag{2.101}$$

where

$$\rho = \frac{\varepsilon_{11}}{\varepsilon_{22}}, \qquad b = \frac{1+\bar{R}}{\bar{R}} \tag{2.102}$$

Furthermore, the flow curves, for the materials included in their study, were obtained using Hollomon's model with double work-hardening exponents n_1 and n_2 as

$$\begin{aligned} &\bar{\sigma} = K\bar{\varepsilon}^{n_1}, \text{ for } \bar{\varepsilon} \le 0.21, \\ &\bar{\sigma} = K'\bar{\varepsilon}^{n_2}, \text{ for } \bar{\varepsilon} > 0.21, \\ &K' = K\bar{\varepsilon}^{*(n_1-n_2)} \end{aligned} \tag{2.103}$$

For most of the materials tested, only one n-value was sufficient to characterize the flow curves; except the deep drawing quality steel was represented by the two n-values n_1 and n_2.

Jain (1990) conducted uniaxial cyclic tests on cylindrical specimens made of commercially pure (99.99%) polycrystalline copper to determine the size of the yield surface, σ_{iso}, for isotropic hardening and the back stress, α, for the kinematic hardening. The experimental procedures involved measuring the dynamic yield stress in tension, σ_{Y_t} and the dynamic yield stress in compression, σ_{Y_c}, at several predetermined strain levels within the cycle. It is worth mentioning that applying the compressive loading had to stop immediately after yielding in order to use the specimen for subsequent measurements. The size of the yield surface and the back stress, at a specific strain level, were respectively defined to be

$$\sigma_{iso} = \frac{\sigma_{Y_t} - \sigma_{Y_c}}{2}, \qquad \alpha = \frac{\sigma_{Y_t} + \sigma_{Y_c}}{2} \tag{2.104}$$

Similarly, Khan and Jackson (1999) determined the hardening parameters for oxygen-free-high-conductivity copper cylinders. The specimens were tested for strains up to 50% in both tensile and compressive directions with a strain rate of 10^{-4} per second. The calculation for the isotropic and kinematic hardening parameters was done the same way presented in Eq. (2.104) with σ_A and σ_B replacing σ_{Y_t} and σ_{Y_c}, respectively. A schematic diagram showing σ_A and σ_B along with the von Mises yield surface is shown in Fig. (2.19).

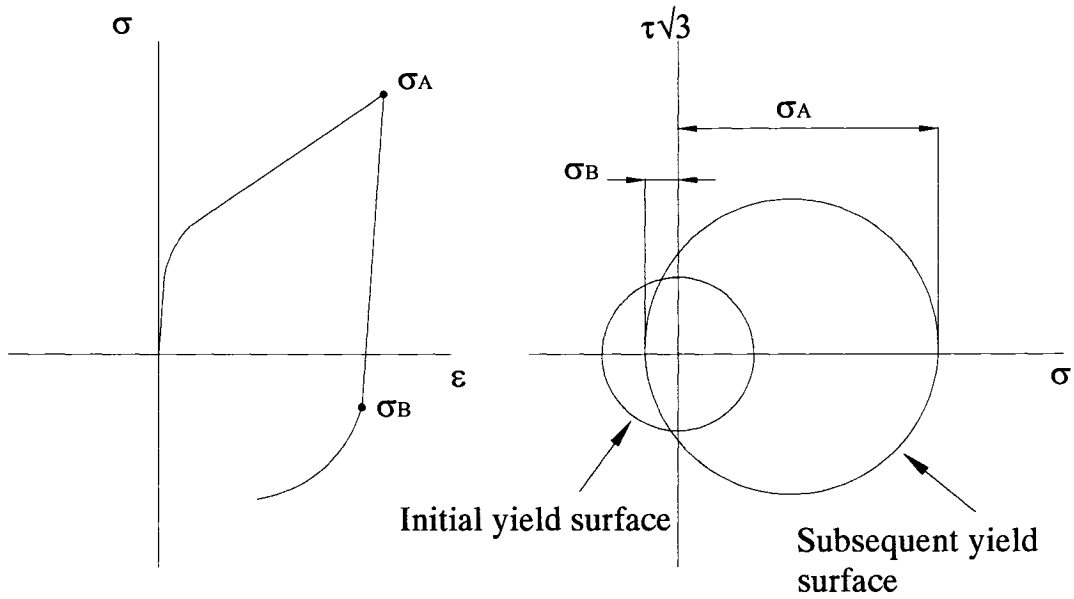

Fig. (2.19) Method of determining σ_A and σ_B, and their representation on yield surfaces (adapted from Khan and Jackson, 1999)

Krieg and Brown (1996) developed an anisotropic viscoplastic model that includes various effects, including anisotropic elasticity, anisotropic plasticity, kinematic hardening, scalar hardening, and rate dependence. This model has been implemented in the MSC/Dytran code. According to this model, the number of constants required to fully describe an anisotropic material is 106.

Aerens (1997) reported a method to obtain the material parameters from bending tests. This method basically depends on measuring the bending moment and the bending strains. The moment was referred to as the *unit moment* and was calculated as

$$\sigma^* = \frac{\left(\frac{2}{\sqrt{3}}\right)^{n+1} C}{2(n+2)} \varepsilon_b^n \tag{2.105}$$

which is basically an equation of stress, where C and n are material parameters determined from the best fit of the power law $\sigma = C\varepsilon^n$, where ε is the true strain and ε_b is the bending strain measured and calculated by means of a CCD camera and an image processing system. This model was reported to be valid for the range of $\varepsilon_b > 0.03$. Also, it was reported that the unit moments measured were systematically lower than the computed ones from the tensile tests.

Yoshida *et al.* (1998) developed a method for identifying the hardening parameters for sheet metals subject to cyclic bending from moment-curvature curves. The same technique was also suggested in Yoshida and Uemori (2002). The constitutive equation governing both isotropic and nonlinear kinematic hardening, respectively, took the forms

$$\begin{aligned} d\Re &= b(Q - \Re)d\bar{\varepsilon}^p \\ d\alpha_{ij} &= C\left(\frac{2}{3} a d\varepsilon_{ij}^{pl} - \alpha_{ij} d\bar{\varepsilon}^p\right) \end{aligned} \tag{2.106}$$

where b and Q are isotropic hardening parameters and C and a are nonlinear kinematic hardening parameters. Identifying the parameters was based on iterative approximation technique that involves a minimization of an objective function that includes these parameters among four others. The target of the optimization was to find the vector $\boldsymbol{x}$ that minimizes the objective function

$$F(\boldsymbol{x}) = \sum_{k=1}^{L} w_k F_k(\boldsymbol{x}) \tag{2.107}$$

where w is a coefficient that determines the relative contribution of the experimental data, L is the total number of the individual responses (k) which can be measured experimentally, and $F(\boldsymbol{x})$ is a dimensionless function that measures the deviation between the computed individual responses and the measured ones.

Zhao and Lee (2001a and 2001b) used three-point cyclic bending tests, along with an optimization technique to determine the hardening parameters. The objective function in the optimization problem was defined as the normalized error of bending moments

$$\Phi(\boldsymbol{x}) = \frac{\sum_{k=1}^{L} \left(\tilde{M}_k(\boldsymbol{x}) - \hat{M}_k \right)^2}{\sum_{l=1}^{L} \left(\hat{M}_l \right)^2} \tag{2.108}$$

where L is the total number of measurements, vector $\boldsymbol{x}$ consists of seven material parameters (Q, b, C, and γ plus three other parameters, namely E, $\bar{R}$, and σ_o), and $\tilde{M}_k$ and $\hat{M}_k$ represent the calculated and measured bending moments, respectively.

The measured bending moment is computed as

$$\hat{M}_k = \frac{P_k}{2} \left[L + |y_k| \frac{|\tan\theta_k| \pm \mu}{1 \pm \mu |\tan\theta_k|} \right] \tag{2.109}$$

where P is the punch load, L is the distance between the punch head and the bearing center, y is the punch displacement, θ is the rotation angle in bending, and μ is the coefficient of friction, which was taken to be 0.05. The alternating sign in the above equation is for bending and reverse bending, respectively. Through a sensitivity analysis, it was observed that the objective function is most sensitive to the size of the yield

surface, σ_o, followed by the elastic modulus, E, then the kinematic hardening parameters C and γ, the anisotropy coefficient $\overline{R}$, and finally the isotropic hardening parameters Q and b.

Geng and Wagoner (2002) and Geng *et al.* (2002) suggested that the material parameters C and γ, at the time of load reversal, can be determined from the uniaxial loading-reverse-loading curves as

$$C = \frac{H_f\left(\varepsilon^{pl}\right) - H_r\left(\varepsilon^{pl}\right)}{2} - \frac{d\sigma_o}{d\varepsilon^{pl}}, \qquad \gamma = \frac{H_r\left(\varepsilon^{pl}\right) - H_f\left(\varepsilon^{pl}\right)}{2\alpha} \tag{2.110}$$

where H_f and H_r are plastic moduli for the forward and reverse loading at the moment of stress reversal, respectively, and both are functions of the plastic strain. The size of the yield surface, σ_o, and the back stress, α, can be found from the measured forward and reverse loading curves. It was reported that the hardening parameters were adjusted depending on the curve fitting results between measured and calculated values, which is facilitated quantitatively because larger γ, with fixed C, will result in an increase in the reverse yield stress and larger C, with fixed γ, will result in a decrease in the reverse yield stress.

To study the behaviour of materials in unloading and reverse yielding, Cleveland and Ghosh (2002) conducted compression tests on stacked-sheet specimens. The tensile specimens were tested to 6% tensile strain, then the uniform part of the sample was cut and glued together. The compressive loads were applied to the cut samples and the reverse plastic yielding was captured. The stress-strain curve of Al 6022-T4 was obtained following this technique and is shown in Fig. (2.20), by which many material parameters can be obtained.

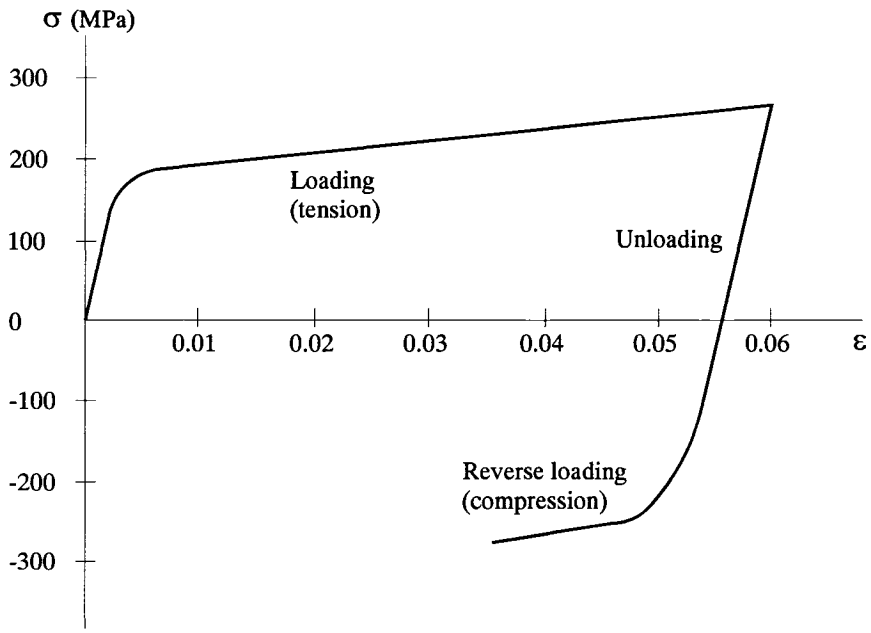

Fig. (2.20) Stress–strain curve for uniaxial tensile loading and unloading, followed by compression for Al 6022-T4 alloy (adapted from Cleveland and Ghosh, 2002)

In a similar manner, Yoshida *et al.* (2002) conducted uniaxial tension-compression experiments on specimens that were stacked, glued together and machined to the required dimensions. Before stacking the specimens to perform the cyclic loading, they were individually pre-strained to specific tensile strains before the localized necking would appear. Stacked specimens were then tested in uniaxial tension-compression cycles to determine the hardening parameters.

Lindkvist and Lindbäck (2004) used the inverse method to obtain the material parameters for SSAB Domex 650 MCD steel sheets. The aim of their research was to find the material parameters that minimize the difference between the experimental results and the results obtained from the finite element simulations. The unconstrained subspace-searching simplex method was used. The three-point bending experimental setup was used and the comparison data were in the form of punch force, $(PF)^{exp}$ and punch displacement, $(PD)^{exp}$.

The MSC MARC finite element code was used and the blank was modeled by shell elements. Output data from the simulation were in the form of punch force and punch displacement, $(PF)^{fem}$ and $(PD)^{fem}$, respectively.

The minimization objective function took the form

$$f(x_k)=\sum_{i=1}^{100}\left[(PF)_i^{\exp}-(PF)_i^{fem}(x_k)\right]^2,\ k=1,...,N \tag{2.111}$$

where x_k are material parameters in the material constitutive equation and $2 \leq N \leq 6$, depending on the model. The resulting parameters are then considered to be optimum when a global minimum is found. Four von Mises elastic-plastic material constitutive models with isotropic hardening were used. The models took the forms

$$\text{Linear Model: } \sigma=\sigma_{Y_o}+H'\bar{\varepsilon}^p \tag{2.112}$$

$$\text{Piecewise Linear Model: } \begin{aligned}\sigma=\sigma_{Y_o}&+H_1'\left(\bar{\varepsilon}^p=0.0\right)+H_2'\left(\bar{\varepsilon}^p=0.075\right)\\&+H_3'\left(\bar{\varepsilon}^p=0.15\right)+H_4'\left(\bar{\varepsilon}^p=0.30\right)\\&+H_5'\left(\bar{\varepsilon}^p=0.45\right)\end{aligned} \tag{2.113}$$

$$\text{Power Law Model: } \sigma=\sigma_{Y_o}+C\left(\bar{\varepsilon}^p\right)^n \tag{2.114}$$

$$\text{Combined Model: } \sigma=\sigma_{Y_o}+Q_1\bar{\varepsilon}^p+Q_2\left(1-e^{-b\bar{\varepsilon}^p}\right) \tag{2.115}$$

where H_k' are the hardening moduli, σ_{Y_o} is the initial yield stress, $\bar{\varepsilon}^p$ is the equivalent plastic strain, C, Q_1 and Q_2 are strength hardening coefficients, and n and b are hardening exponents.

It was reported that there was a difference of at most 6% of the optimized initial yield stress, σ_{Y_o}, due to the model used. The difference was considered acceptable based on the observation that it is common in experiments to have about 10% variation in the yield limit for sheets tested from the same batch (Lindkvist and Lindbäck, 2004). Moreover, it was concluded that material properties derived from the standard uniaxial test to fit a linear hardening model ($\sigma = H\varepsilon$) do not show good agreement with the results.

Harth *et al.* (2004) studied the influence of scattering test data on material parameters identification. They considered eleven kinds of experiments to determine the material parameters, among these experiments were the tension-compression tests. There was no indication about the specimen's geometry; however, the tests were performed at constant strain rates of 10^{-3}, 10^{-4}, and 10^{-5} per second and the maximum strain reached was 0.5%. It was reported that a deviation of the measured results can exceed 10%, for specimens taken from the same lot, due to measurement errors. It was also observed that identification of material parameters might lead to different results for the same material due to the scatter of the material data taken from different lots.

Mattiasson and Sigvant (2004) studied the identification of a material law, for zinc-coated high-strength steel, that can provide improvement in the forming simulation using a shear test, Fig. (2.21).

The effective stress and effective plastic strain were identified, respectively, as

$$\begin{aligned} \bar{\sigma} &= k_\tau \left|\tau_{12}\right| \\ \bar{\varepsilon}^p &= \frac{1}{k_\tau}\left|\gamma_{12}^{pl}\right| \end{aligned} \tag{2.116}$$

where τ_{12} is the shear stress, γ_{12}^{pl} is the plastic shear deformation, and k_τ is a constant that depends on the yield condition and other material parameters. Figure (2.22) shows the fitting of the shear stress curve with the uniaxial stress for an optimal value of k_τ from the previous equation.

The discrepancy between the two curves, uniaxial and shear, at the beginning was contributed to the change in the shape of the yield surface during loading up to about 10% effective plastic strain.

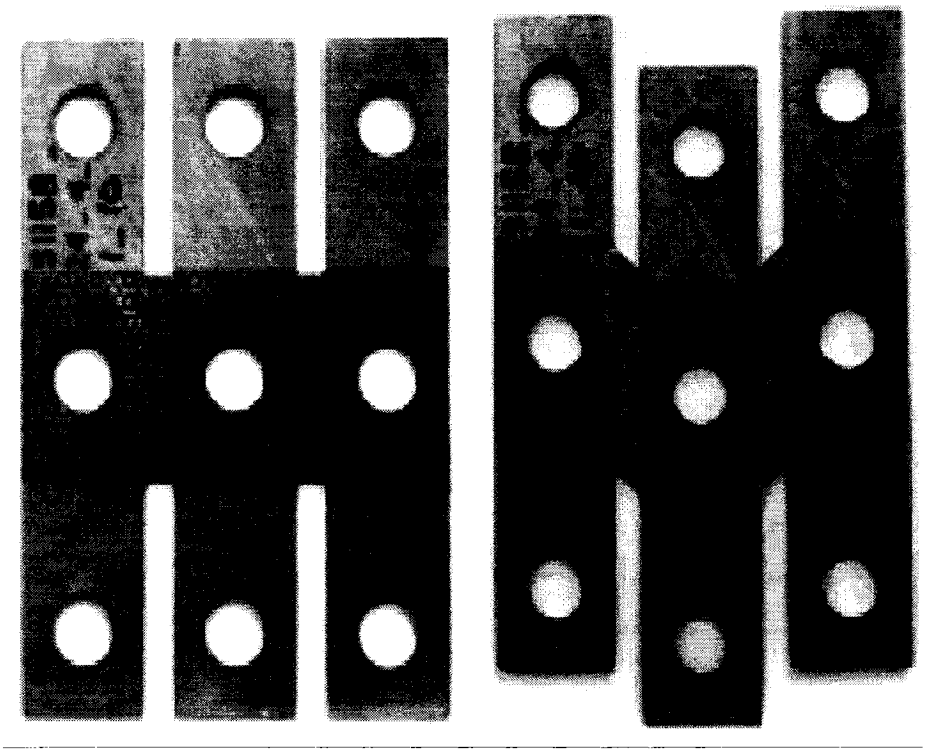

Fig. (2.21) Shear test specimen before and after deformation

[Reused with permission from Kjell Mattiasson and Mats Sigvant, in Material Characterization and Modeling for Industrial Sheet Forming Simulations, S. Ghosh (ed), Conference Proceeding 712, 875 (2004). Copyright 2004, American Institute of Physics.]

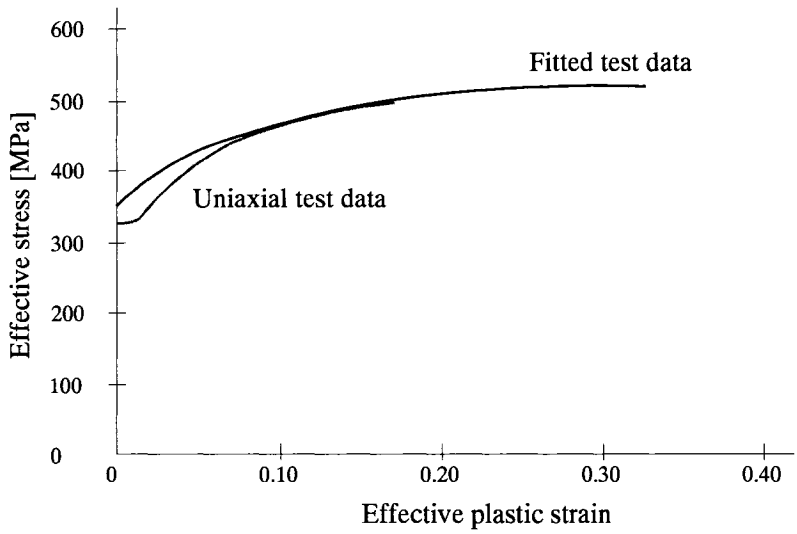

Fig. (2.22) Shear results fitted to the uniaxial stress-strain curve
(adapted from Mattiasson and Sigvant, 2004)

Kuwabara *et al.* (2004) conducted experiments on JSC340P, a high-strength steel with yield strength of 340 MPa, and compared the experimental material behaviour curves to those obtained by theoretical models. The tests conducted include biaxial tension and plane-strain tension tests. A schematic drawing of the test specimens is shown in Fig. (2.23).

The measured stress values from the biaxial test, for particular values of plastic strain, ε^{pl}, were normalized by the uniaxial true stress in the rolling direction, σ_0, and plotted in the stress space along with the yield loci calculated from the theoretical models, Fig. (2.24a). It was found that Hosford's yield function is in closer agreement than von Mises' or Hill's functions with the experimental data. On the other hand, the stress-strain curve constructed from the plane-strain tension test, Fig. (2.24b), was found to be in closer agreement with both von Mises' and Hosford's yield functions than Hill's.

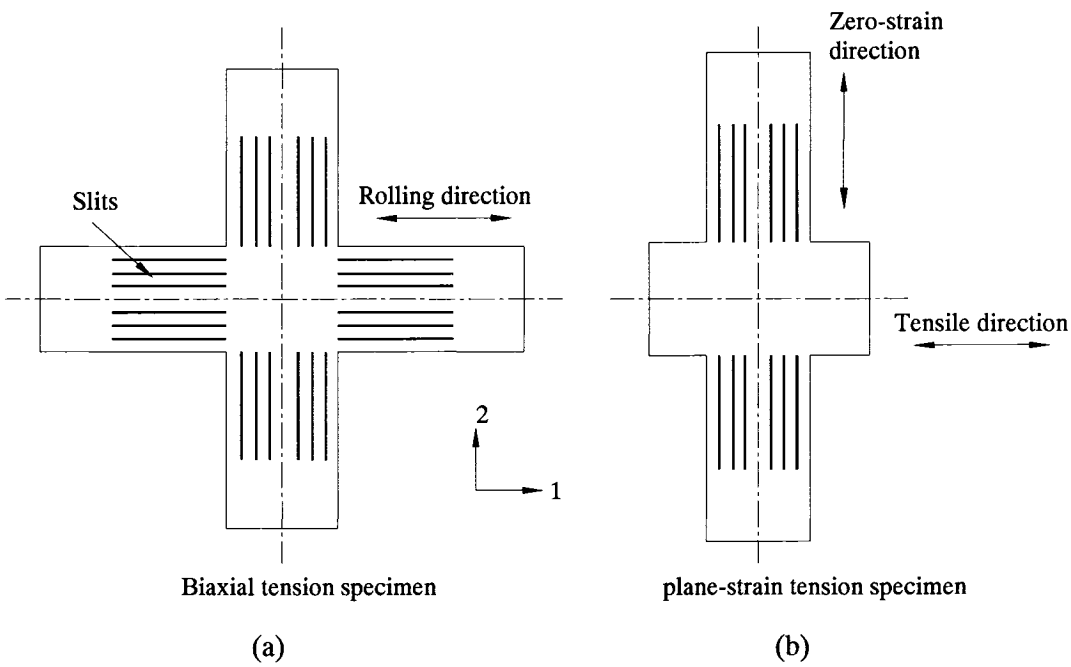

Fig. (2.23) Cruciform specimens for (a) biaxial and (b) plane-strain tension tests (adapted from Kuwabara *et al.*, 2004)

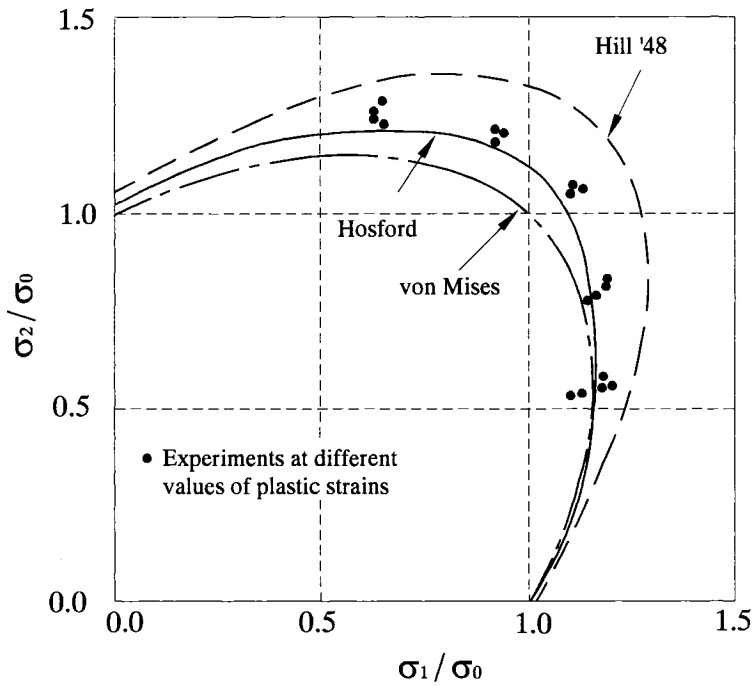

(a)

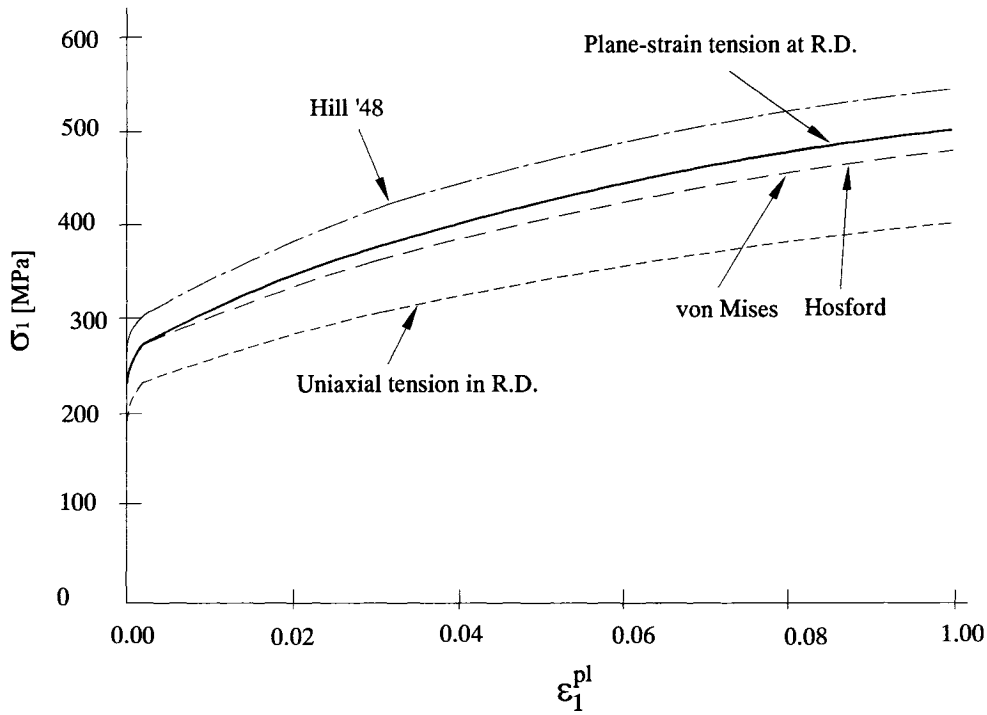

(b)

Fig. (2.24) (a) Experimental data from biaxial test compared with yield loci for different yield functions, and (b) stress-strain curve for plane-strain tension test compared with those predicted by different theoretical models (adapted from Kuwabara *et al.*, 2004)

To produce the reverse loading path that the material experiences in forming, Wang *et al.* (2004b) conducted compression-tension-unloading tests. Before applying the compressive loads, the specimens were sandwiched between two flat plates on which lateral force was applied to avoid buckling of the specimens. Teflon was used between the anti-buckling device and the surface of the specimen to reduce friction.

First, the specimens were compressed to a strain of approximately 0.045. Second, the load direction was reversed and the specimens were pulled to tensile strains of approximately 0.011, 0.04, and 0.11. The geometry of the specimen and the produced stress-strain curve is shown in Fig. (2.25).

Lee *et al.* (2005b) and Boger *et al.* (2005) used the same idea of having an anti-buckling device to support the specimens while applying the compressive loads. The anti-buckling device was operated by a hydraulic system, as shown in Fig. (2.26).

Lee *et al.* (2005b) conducted the experiments at a strain rate of 0.0005 per second and reported that good alignment of the specimen was required to prevent early buckling. To account for the clamping force during testing, a clamping force was 2.0 kN was applied and the engineering tensile flow curves were compared to those obtained without clamping. The adjustment to the compressive flow curves were made by accounting for the friction coefficient measured in tension. From the tension-compression tests the size of the yield surface and the back stress were calculated using in Eq. (2.104).

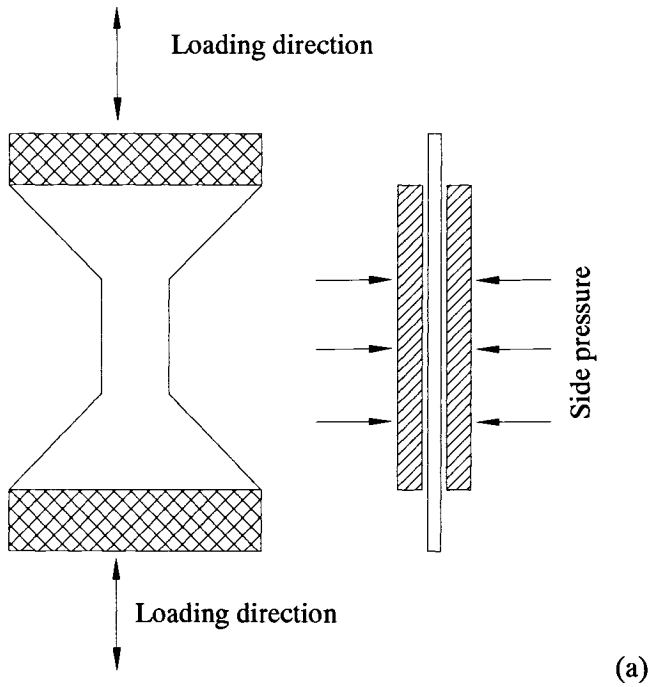

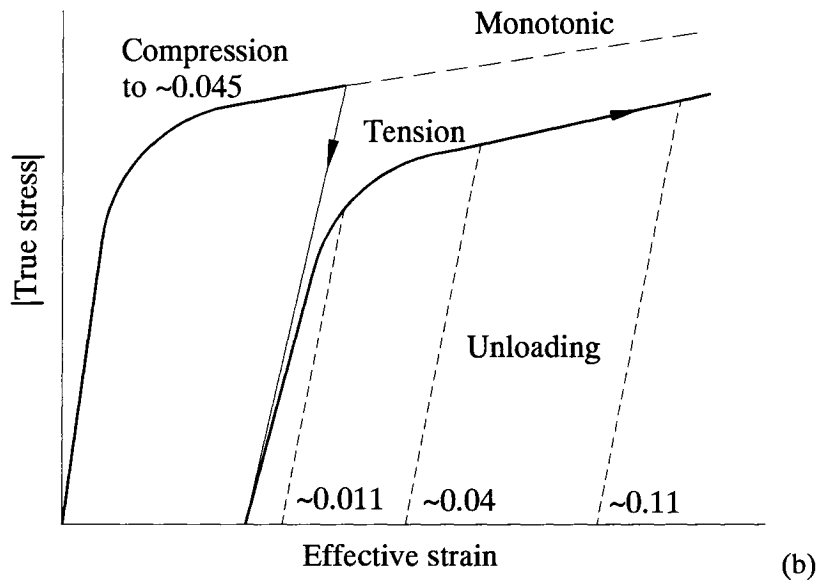

Fig. (2.25) Schematic of compression/tension/unloading test: (a) specimen geometry and the anti-buckling fixture, and (b) general load path (adapted from Wang *et al.*, 2004b)

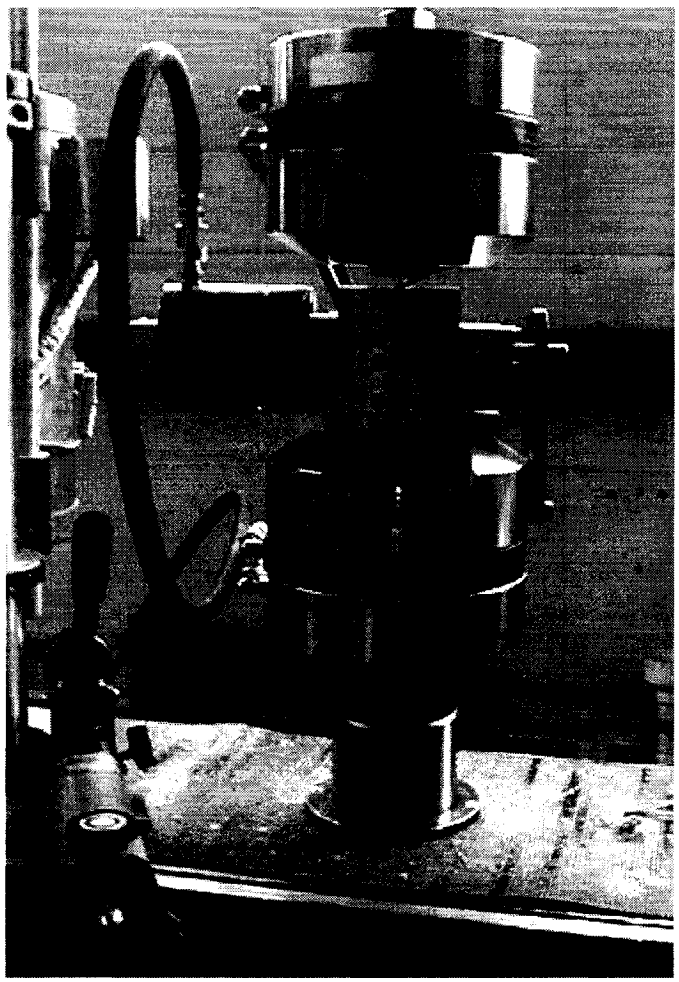

Fig. (2.26) The hydraulic anti-buckling device
(Reprinted from Boger *et al.* (2005) with permission from Elsevier)

The most extensive research done on inconel 718 in terms of yielding, inelastic response, and constitutive modeling was done by Gil *et al.* (1999a and b), Lissenden *et al.* (1999), and Iyer and Lissenden (2000).

Gil *et al.* (1999b) discussed the determination of the yield loci of inconel 718 using an axial-torsion loading technique for a range of temperatures up to approximately 650 °C. From the experiments, the so-called small offset yield locus was determined. Experiments were conducted under strain control and the target value for the maximum

strain offset was chosen to be 30 με (30 × 10^{-6} m/m). The yield loci were plotted along with the von Mises yield surface in the modified axial-shear stress plane $\left(\sigma_{11} - \sqrt{3} \cdot \sigma_{12}\right)$. Two material heat treatment states, solutioned and aged, were considered in that study.

For solutioned inconel 718 specimens, it was reported that the size of the yield loci decreased with the increase in the temperature without changing its shape. Moreover, at approximately 25 °C, the centers of the von Mises and the inconel 718 yield surfaces coincided; however, after increasing the temperature a shift in the inconel yield surface was observed. On the other hand, the yield surface of the aged inconel 718 specimens was extremely eccentric at 25 °C. The eccentricity of the yield locus was observed to be in the compression direction, as shown in Fig. (2.27). It was reported by Gil *et al.* (1999b) and Lissenden *et al.* (1999) that the eccentricity of the yield locus in the compression direction is representative of the presence of the so called "*strength differential effect,* SD," which was defined to be the increase in the yield strength in compression rather than a decrease.

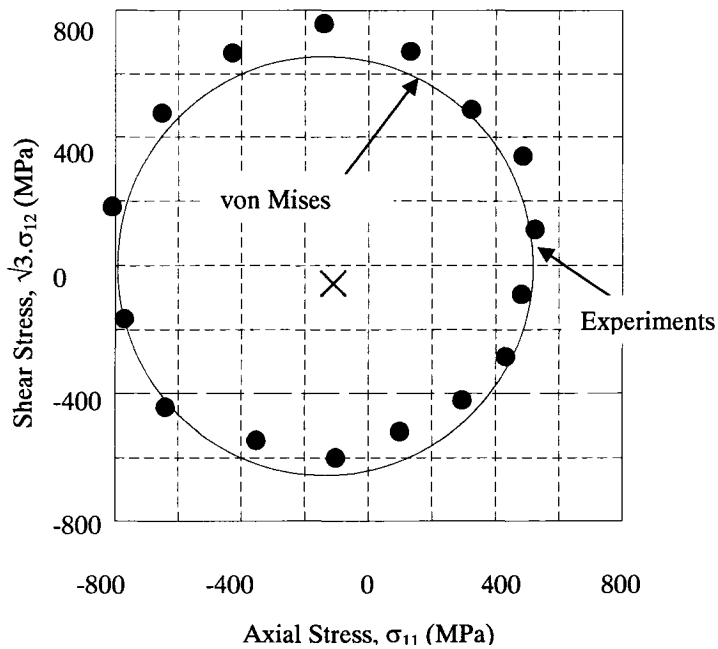

Fig. (2.27) Yield loci of aged inconel 718 at 25 °C compared to the von Mises yield surface (adapted from Gil *et al.*, 1999b)

2.6. Methods for Springback Prediction

Springback is a phenomenon that occurs in cold-working processes. If the metal is deformed into the plastic region, the total strain can be divided into two parts: an elastic part and another one that is plastic. When removing the deformation load, a stress reduction will occur and accordingly the total strain will decrease by the amount of the elastic part, which is causing the springback (DeGarmo *et al.*, 1988).

Moreover, in sheet metal forming, the blank is subjected to stretch bending when passing through the die radii, followed by a subsequent unbending after passing the die corner. After this process, unloading takes place causing the elastic springback. However, in some cases re-yielding occurs due to the Bauschinger effect (Yoshida *et al.*, 2002), as shown in Fig. (2.28).

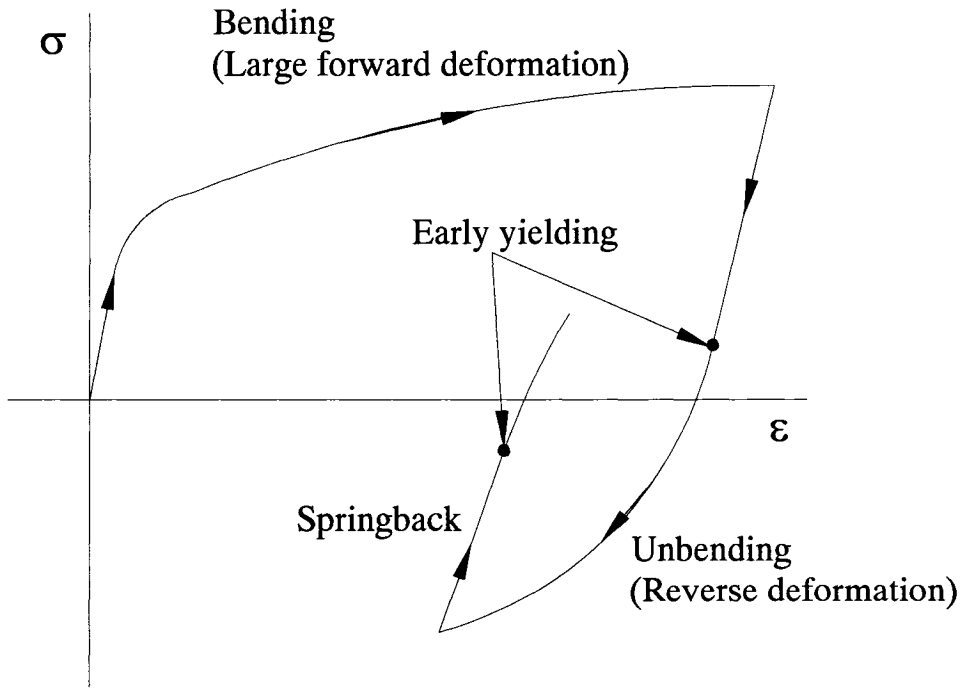

Fig. (2.28) Schematic drawing of the stress-strain path during stretch bending and the subsequent springback (adapted from Yoshida *et al.*, 2002)

From the elementary theory of bending, Gardiner and Philadelphia (1957) derived a mathematical formula for springback prediction of elastic-perfectly-plastic metals under pure bending. The derived formula takes the form

$$\frac{R_o}{R_f} = 4\left(\frac{R_o\sigma_Y}{Et}\right)^3 - 3\left(\frac{R_o\sigma_Y}{Et}\right) + 1 \tag{2.117}$$

where R_o and R_f are the radii of curvature of the sheet before and after springback, respectively, σ_Y is the yield stress and t is the sheet thickness. This formula relates the springback $\left(\frac{R_o}{R_f}\right)$ to the sheet properties $\left(\frac{\sigma_Y}{Et}\right)$, which is shown graphically in Fig. (2.29).

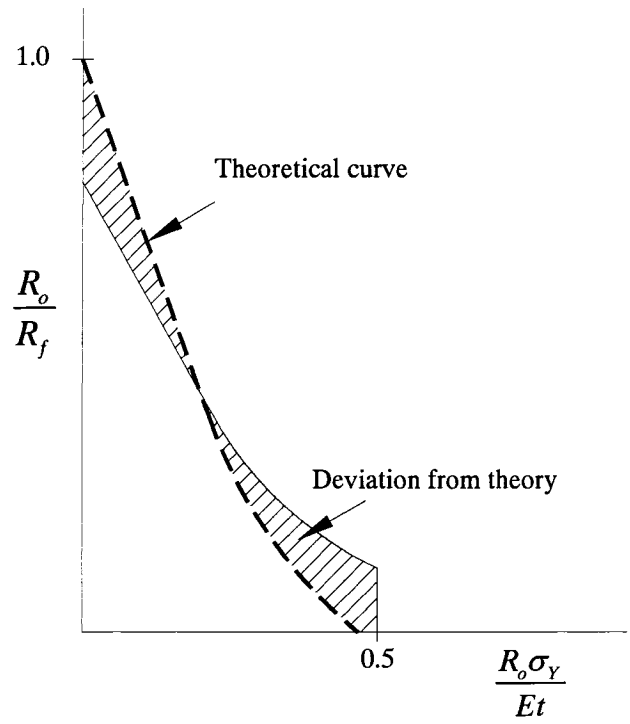

Fig. (2.29) Graphical representation of the relationship between springback and material properties (adapted from Gardiner and Philadelphia, 1957)

Queener and De Angelis (1968) derived a formula for springback after pure bending based on the following assumption: (i) material is isotropic, (ii) plane strain conditions apply and small curvature, (iii) neutral axis of the sheet always coincides with the middle surface, (iv) shear and transverse stresses and thickness change are neglected, and (v) material behaviour follows power law hardening, $\sigma = K\varepsilon^n$. The formula takes the form

$$\frac{R_o}{R_f} \approx 1 - \frac{3K\left(1-\nu^2\right)}{E\left(2+n\right)\left(\frac{3}{4}\right)^{\frac{1+n}{2}}}\left(\frac{2R_o}{t}\right)^{1-n} \tag{2.118}$$

where R_o and R_f are the radii of curvature of the sheet before and after springback, respectively, K and n are empirical material constants in the power-law, and t is the sheet thickness. The ratio $\left(\frac{R_o}{R_f}\right)$ has an upper bound of 1.0 in case of no springback and a lower bound of zero in case of fully elastic recovery.

In the case of simple bending, Fig. (2.30), Hosford and Caddell (1983) proposed that

$$\frac{1}{R_o} - \frac{1}{R_f} = \frac{3\sigma_Y}{tE}\frac{\bar{R}+1}{(2\bar{R}+1)^{1/2}} \tag{2.119}$$

where R_o is the original bend radius, R_f is the bend radius after springback, t is the sheet thickness, E is the elastic modulus, $\bar{R}$ is the anisotropy parameter, and σ_Y is the uniaxial yield stress.

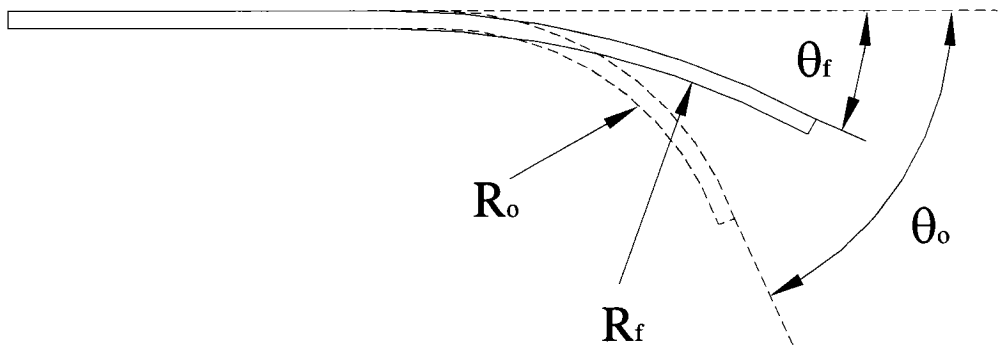

Fig. (2.30) Springback in simple bending

Pearce (1991) reported that the relationship proposed by Hosford and Caddell (1983) overestimates the magnitude of the springback in simple bending and does not help in the case of complex pressings. Moreover, it ignores the elastic core and becomes more inaccurate as the bend radius increases. Of course, other mathematical relations have been derived but they are only successful in describing the simple bending. For more complex pressings, trial and error was still the only tool.

In an early attempt to reduce or eliminate the springback in sheet metal forming operations, Karafillis and Boyce (1992) suggested that the information obtained from the finite element modeling on traction distribution during the forming process can be used in designing the die shape which yields the desired part shape. This is because the traction distribution in the fully loaded state determines the amount of the springback since it is a result of release of the traction distribution in the fully loaded part.

The effect of anisotropy on pure bending of sheet metals was studied by Tan *et al.* (1995). Two models were presented, one describing the anisotropic material without the Bauschinger effect and the other interpreting the Bauschinger effect by the kinematic hardening theory. The main finding is that the second model predicts much greater thickness reduction than the first one. It was experimentally found that sheets experience

little thinning when the axis of bending is aligned with the rolling direction of the specimen.

In regards to metal thinning during deformation, Gotoh *et al.* (1997) experimentally investigated the effect of tool geometry on sheet thinning during the stretch-bending process. Sheets of thickness 0.20 to 1.00 mm from eleven different materials were involved in the experiments. Throughout the experiments, the punch speed was kept very low to avoid inertia effects on the results, and the blank holding force was chosen to be between the allowable lowest for prevention of wrinkling and the highest value for prevention of tearing of the sheet metal.

It was reported that, for a smaller die profile radius, thinning in the wall occurs to greater extent and a deeper cup can be drawn by using a smaller die radius. Also, materials with larger n-value have more tendency to resist thinning while the R-value contributes more in thickening due to the flange shrinkage action.

Tan *et al.* (1994) reported that springback and residual stresses can be expressed as functions of the geometric parameters and the material properties of the sheet metals. The analysis presented in their work included the prediction of residual stresses resulting from the elastic springback on unloading by the constitutive equations in terms of bending curvature, thickness, and material properties.

The main assumptions made are: (i) large radius of curvature compared to thickness ($r/t \geq 25$) and, accordingly, the stresses in the thickness direction can be neglected, (ii) plane strain bending (width/thickness ≥ 10), (iii) all plane sections perpendicular to the axis of the plate remain plane and perpendicular, before and after bending, (iv) the neutral layer always coincides with the mid-layer during bending, and (v) the material follows the isotropic work hardening rule and von Mises yield criterion.

Using the above mentioned assumptions, the authors reported that the springback, in the form of bending curvature variation, can be expressed as

$$\frac{1}{r}-\frac{1}{r'}=\frac{M}{rE'h^2} \tag{2.120}$$

where r and r' are the radii of curvature of the neutral layer before and after springback, respectively. E' is the generalized elastic modulus and is given by

$$E'=\frac{E}{\left(1-\nu^2\right)} \tag{2.121}$$

M, the applied bending moment, and h^2 are given by

$$M=2Er^2\left(\frac{K}{E}\right)^{\frac{3}{1-n}}\left[\frac{\left(1-\nu^2\right)^2}{3\left(1-\nu+\nu^2\right)^{\frac{3}{2}}}-\frac{\left(\frac{2}{\sqrt{3}}\right)^{n+1}}{n+2}\left(\frac{1-\nu^2}{\sqrt{1-\nu+\nu^2}}\right)^{n+2}\right]$$
$$+\left(\frac{t}{r}\right)^n\frac{kt^2}{(n+2)\left(\sqrt{3}\right)^{n+1}},\ \text{and} \tag{2.122}$$
$$h^2=-rt+r^2\ln\frac{r+\frac{t}{2}}{r-\frac{t}{2}}$$

where E, K, and n are material parameters and t is the sheet thickness.

Pourboghrat and Chu (1995b) developed a method to predict bending, stretching, and unbending strains as well as springback for plane-strain stretch/draw operations. The constitutive law that was used to model the material behaviour takes the form

$$\sigma_T = K\left(\frac{1+\bar{R}}{\sqrt{1+2\bar{R}}}\right)^{n+1}\varepsilon_T^n$$
$$\varepsilon_T = \ln\left(\frac{t_o(R_c+z)}{R_c t}\right) \tag{2.123}$$

where σ_T and ε_T are the true tangential stress and strain, respectively, K and n are the strength coefficient and the strain hardening exponent in the Holloman power law, $\bar{R}$ is the normal anisotropy parameter, R_c is the radius of curvature, t_o and t are the original and current thickness, respectively, and z is an axis with origin at the centerline of the sheet.

El-Domiaty *et al.* (1996) studied the stretch-bendability of some aluminum and steel sheets. The term bendability was defined as the ability of a sheet to stretch/bend without failure.

It was found that the stretch-bendability of 2024 aluminum alloy and 4340 steel is the highest when compared with other aluminum alloys and other steels, respectively. It was also found that the springback after stretch-bending is highly dependent on the tensile load ratio, n_r, applied during forming, which is given by

$$n_r = \frac{\text{Axial tensile force}}{\text{Maximum elastic tensile force}} \tag{2.124}$$

For complete plastic deformation, it was recommended that the tension force should be sufficiently high but should not exceed the ultimate tensile stress. Springback is expected to be large when the deformation is elastic-plastic. A springback index (R/R_f) was used; which is the ratio between the forming die (R) and the final radii of curvature (R_f). When this index is 1.0, the final and the forming die radii are equal, i.e. no springback occurs. However, the more the index becomes smaller than 1.0 the more the springback problems become severe.

Leu (1997) formulated a mathematical model to study the effect of sheet anisotropy value, $\bar{R}$, and the strain hardening exponent, n, on the springback and minimum bending radius, bendability, in sheet metal forming. Hill's yield criterion and elementary bending theory were adopted and the strain rate and Bauschinger effect were neglected in the analysis.

It was found that: (i) bendability is improved when the $\bar{R}$-value is increased; (ii) the higher the $\bar{R}$-value the greater the springback; (iii) the lower the strain hardening exponent n the greater the springback; (iv) sheets with smaller sheet-thickness have a smaller minimum bending radius.

A semi-analytical method for springback prediction of aluminum 2008-T4 in draw-bending tests was developed by Pourboghrat *et al.* (1998). Results obtained from finite element analysis using membrane theory were analytically superposed by bending and unbending deformation increments. Hill's 1948 yield criterion was used along with isotropic and kinematic hardening laws during modeling. The main finding of this research is that it is important to include Bauschinger effect and kinematic hardening in predicting the springback.

Samuel (2000) proposed an expression for the springback ratio in the U-bending process, the expression takes the form

$$\frac{\Delta\theta}{\theta} = K\left(\frac{1+\bar{R}}{\sqrt{1+2\bar{R}}}\right)^{1+n}\left(\frac{3\left(1-\nu^2\right)}{2E\left(1+n\right)}\right)\left(\frac{t}{2R_o}\right)^{n-1} \tag{2.125}$$

where t is the current thickness of the strip, R_o is the radius of the centre line curvature before unloading, θ is the angle between the blank and the punch and $\Delta\theta$ is the difference in angle before and after bending, which is given by

$$\Delta\theta = R_o\left[\frac{1}{R_o} - \frac{1}{R_f}\right] \tag{2.126}$$

where R_f is the radius of the centre line curvature after unloading. It was reported that springback decreases with the decrease in the punch and die radii with the application of significantly high BHF. Also, it was noted that the stress over the punch corner is the most significant factor that affects the magnitude of springback.

Cao *et al.* (2000a) proposed a method to control springback in channel forming that is based on artificial neural network control along with a stepped blank holding force trajectory. This stepped force trajectory is a jump from a low blank holding force to a higher one at a specified percentage of the total punch displacement. The use of a neural network was to accommodate for the process parameters. The input to the system is the punch force trajectory; based on this force the neural network provided the blank holding force and the punch displacement for the next step. It was reported that values of springback angles obtained were in the range of 0.2 to 0.6 degrees.

The effect of the flange length, in straight flanging operation, on springback was studied by Song *et al.* (2001). They observed that if the flange length is larger than a specific value, denoted by the critical length, then the springback angle is insensitive to the increase in the length. However, if the flange length is smaller than the critical length, there is a rapid increase in the springback angle with the decrease in the flange length. Relating the flange length and the gap between the die and the punch to the springback angle, it was also reported that the critical flange length increases as the gap increases. It was reported later by Buranathiti and Cao (2004) that changing the die corner radius has a more significant effect on springback than changing the gap

Carden *et al.* (2002) investigated the role of tool radius, friction, and tension on springback in draw-bend experiments. The apparatus used in this study, which was also used later by Wang *et al.* (2004a), is discussed next and shown in Fig. (2.32). It was reported that friction did not have a measurable effect on springback, which contradicts

other reported experimental findings that relate springback to friction. The reason was attributed to the amount of tension in the sheet. In Carden's experiments the amount of tension was controlled which was not the case for the other reported findings. It was concluded that the role of friction depends on the modification in the sheet tension. As for the role of tension, it was observed that the increase in the tension resulted in a drastic reduction in the springback. It was found that rapid decrease of springback angle occurs when the tension reaches the tensile yield strength of the sheet. Finally, it was found that springback decreases with the decrease in the tool radii.

The effect of anticlastic curvature on springback in draw-bending tests was studied by Wang *et al.* (2004a) and Wang *et al.* (2005). The anticlastic curvature can be defined as the transverse curvature parallel to the bending axis when a moment M is applied to bend a thin sheet of uniform thickness, as shown in Fig. (2.31).

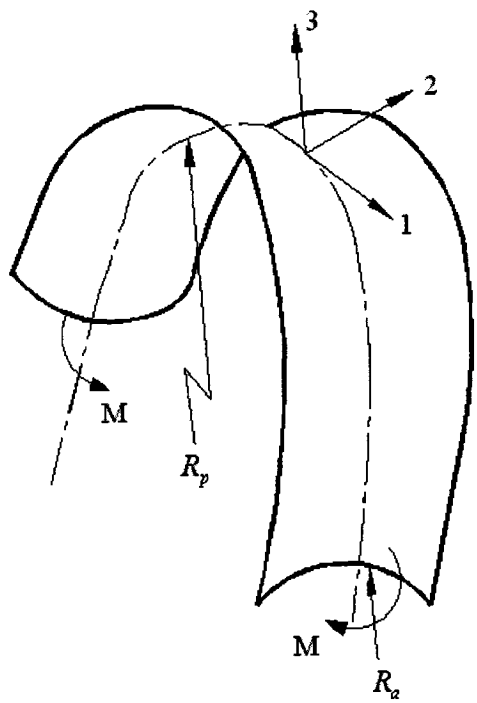

Fig. (2.31) Anticlastic surface after pure bending (adapted from Wang *et al.*, 2004a)

In their study, aluminum 6022-T4 sheets were tested using the draw-bend apparatus shown in Fig. (2.32). A tensile force, named as F_b, was expressed as a fraction of the yielding force in uniaxial tension, was applied followed by drawing over a cylindrical tool at a constant velocity. After unloading, the springback angle, $\Delta\theta$, the radii R' and r' were measured and the anticlastic curvature is calculated as

$$R_a = \frac{\Delta h}{2} + \frac{W^2}{8\Delta h} \tag{2.127}$$

where Δh is the depth of the anticlastic profile at the center of the curled region and W is the specimen's width.

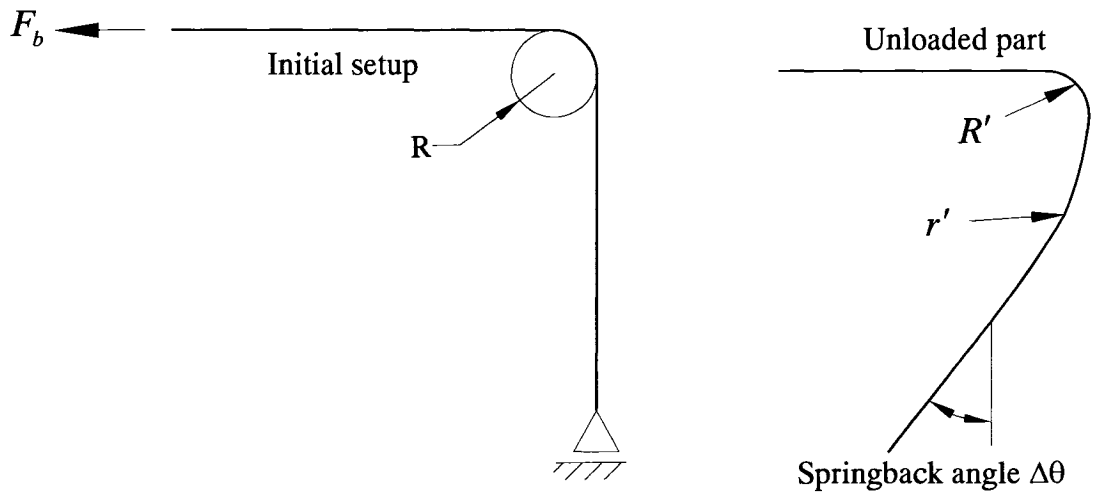

Fig. (2.32) Schematic of the draw-bend test procedure and typical geometry of an unloaded sample (adapted from Wang *et al.*, 2004a)

It was found that the springback angle, $\Delta\theta$, decreased with the increase in the initial tensile force, F_b. Also, for small F_b, the localization of the anticlastic deflection is toward the edges of the specimen. On the other hand, when F_b reaches 0.80, the cross-section

appears to be circular. It was concluded that if F_b exceeds a certain critical value, the anticlastic curvature will persist after springback. The reason for persistence of anticlastic curvature was attributed to the increase in the section moment of inertia.

The effect of blank holding force on springback for aluminum alloys was investigated by Liu *et al.* (2002). A variable blank holding force algorithm was discussed and the springback was evaluated in terms of the vertical displacement of the edge of the 2D draw bending specimens.

Similarly, Du *et al.* (2004) investigated the effect of the blank holder force on DP590 steel and ultra low carbon mild steel. Two blank holding force profiles were considered in their study, constant binder force (CBF) and variable binder force (VBF). During the forming operation, the holding force was varied and its influence on the side-wall curl of a channel with a hat-shaped cross section was observed. The die and geometry of the part are shown in Fig. (2.33).

For the springback measurements, a white-light scanner was used to scan the shape of the formed specimens and five equally-spaced parallel sections were cut from the scan clouds along the length of the channel. As shown in Fig. (2.34) for mild steel, applying the maximum holding force in the CBF resulted in a minimization of the side-wall curl; also, increasing the blank holding force in the VBF resulted in a reduction in the side-wall curl and accordingly the springback, as expected.

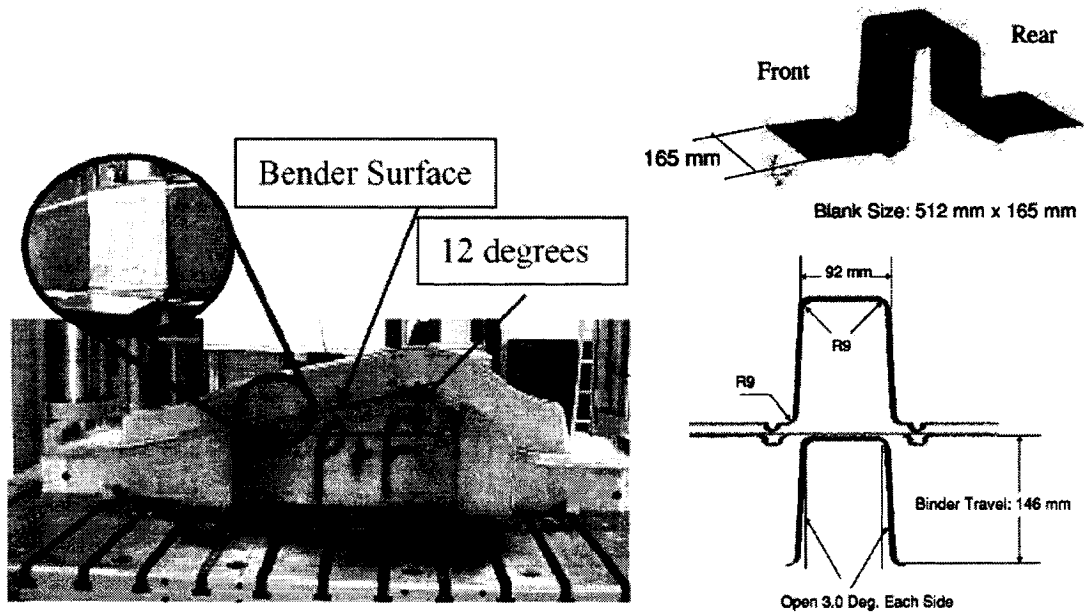

Fig. (2.33) Channel sample and die, and part geometry and setup

[Reused with permission from Changqing Du, Jin Wu, Marcio Militisky, James Principe, Mark Garnett, and Li Zhang, in Springback Control With Variable Binder Force – Experiments And FEA Simulation, S. Ghosh (ed), Conference Proceeding 712, 970 (2004). Copyright 2004, American Institute of Physics.]

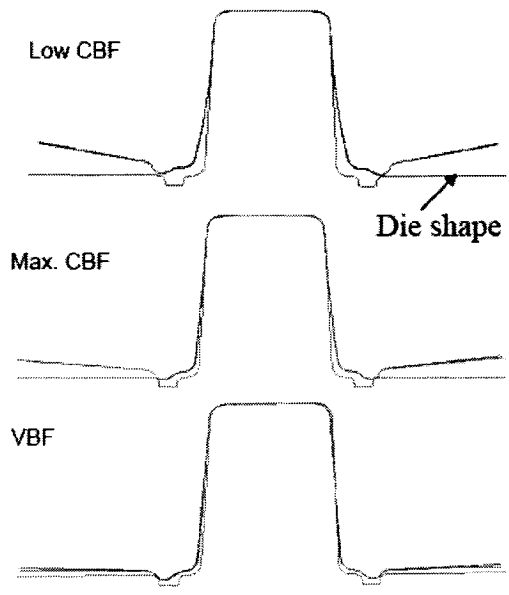

Fig. (2.34) Springback in mild steel for minimum CBF, maximum CBF, and VBF

[Reused with permission from Changqing Du, Jin Wu, Marcio Militisky, James Principe, Mark Garnett, and Li Zhang, in Springback Control With Variable Binder Force – Experiments And FEA Simulation, S. Ghosh (ed), Conference Proceeding 712, 970 (2004). Copyright 2004, American Institute of Physics.]

Du *et al.* (2004) also simulated the effect of fixed and variable binder force on side-wall curl and springback and they reported that, for mild steel, 80% of the measurement points deviated by less than 2.00 mm from the simulations. As for the DP 590, the same amount of deviation, about 2.00 mm, occurred in 50% of the measurement points.

Delannay *et el.* (2004) conducted a study for springback prediction on ZnTi sheets. The setup of the bending experiment is shown in Fig. (2.35). The samples were tested at 0^{o} and 90^{o} to the rolling direction and the springback angles were measured after different bending punch strokes.

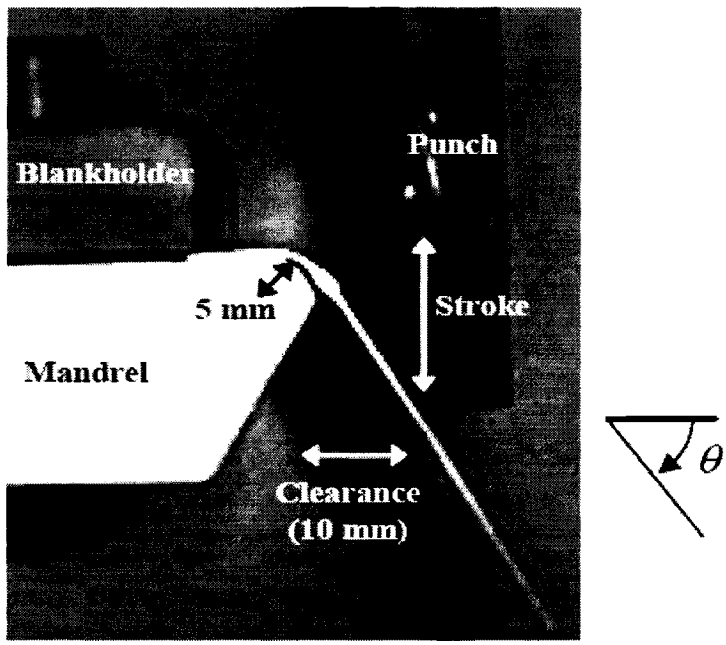

Fig. (2.35) Bending experiment setup

[Reused with permission from L. Delannay, R. E. Logé, J. W. Signorelli, and Y. Chastel, in Prediction of the planar anisotropy of springback after bending of a textured zinc sheet, S. Ghosh (ed), Conference Proceeding 712, 1058 (2004). Copyright 2004, American Institute of Physics.]

The bending angle, after a given punch displacement, was calculated as

$$\theta(l) = \int_0^l \frac{dl}{R(l)} \tag{2.128}$$

where R is the radius of curvature of the bend. Calculations were conducted for R varying from 10^6 mm down to 5.00 mm, which is the radius of the mandrel tip. The springback, $\Delta\theta$, was calculated as the difference between the angles before and after removing the punch load. Fig. (2.36) shows different profiles of the bent specimens under different punch strokes, 10.50 mm and 40.50 mm, Load (I) and Load (II), respectively.

It was reported that larger springback angles were observed in the case of specimens cut at 90^o to the rolling direction.

Naceur *et al.* (2004) studied the optimization of tool geometry in sheet metal forming in order to reduce the springback after forming. The method proposed in their work was the Response Surface Method, RSM, based on Diffuse Approximation, DA, along with the Inverse Approach, IA. A geometrical procedure that takes the history of deformation into account was presented and the pure bending theory of beams was implemented.

The objective in their optimization problem is to determine the punch radius, R_p, and the die radius, R_d, that minimize the maximum opening distance d_i, which is the distance at each node between the position at the end of the forming operation and the final opened part.

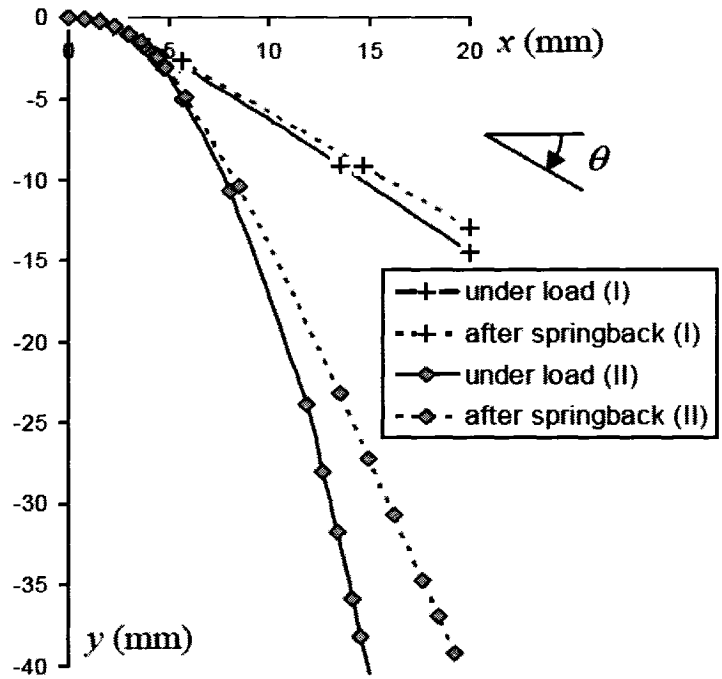

Fig. (2.36) Profile of the bent sheet after two punch strokes 10.50 mm and 40.50 mm, load I and II, respectively

[Reused with permission from L. Delannay, R. E. Logé, J. W. Signorelli, and Y. Chastel, in Prediction of the planar anisotropy of springback after bending of a textured zinc sheet, S. Ghosh (ed), Conference Proceeding 712, 1058 (2004). Copyright 2004, American Institute of Physics.]

Lee *et al.* (2005b and c) reported that springback is highly affected by the material's elastic properties, such as Young's and shear moduli. It was presented mathematically that the smaller the Young's modulus the larger the springback. After releasing the bending moment, the amount of springback in curvature for plain strain bending was given as

$$\Delta\rho = \frac{3\sigma_Y}{E't}\left(1-\frac{1}{3}\left(\frac{\rho_e}{\rho}\right)^2\right) \tag{2.129}$$

where ρ is the curvature, ρ_e is the curvature at the initiation of the elastic–plastic bending and $E' = \frac{E}{(1-\nu^2)}$.

2.7. Finite Element Modeling of Sheet Metal Forming

The finite element method has become an integral part of the computer aided engineering process. Currently, finite element programs are being used extensively in many engineering applications such as solid mechanics, manufacturing processes, fluid mechanics, aerodynamics, and many more. With the increased use of the method, the challenges in modeling are also increased due to the complex physical phenomena involved with either the material or the process itself.

In modeling of manufacturing processes, the challenges faced include complex geometries, large deformations, contact conditions, material behaviour, and many others. The accuracy of the model depends on the proper identification of the process parameters, material model, elements types, and the model simplification.

Tang (1994) used a triangular shell element model to simulate the deformation behaviour of automotive parts manufactured by sheet forming processes. The generalized Hooke's law was used to characterize the elastic behaviour of the material; while the Hill's theory with isotropic hardening rule and Prandtl-Reuss flow rule was used for the plastic behaviour. The material properties were determined from uniaxial tensile tests. A quasi-static formulation was adopted after ignoring the punch speed during the forming process. It was reported that the measured amount of draw-in was slightly smaller than the computed ones due to ignoring the ironing effect in the simulation.

Pourboghrat and Chu (1995b) verified their springback theoretical prediction by comparing the results with those obtained experimentally. Moreover, the results were also compared to a finite element model using ABAQUS. Aluminum 2008-T4 specimens

were used in the 2D draw-bending experiments. After unloading, it was observed that curls were formed on the sidewall of the parts and these curls are more pronounced for parts formed to a sharper die radius and tighter clearance.

Eight-node plane-strain elements were used in the model. Two blank-holding forces, BHF = 50 and 19.60 kN, were implemented in both theory and simulation. It was found that when a BHF = 50 kN is applied to the sheet it develops large enough tension that causes the sheet to be stretched fully plastic which eliminates sidewall curl and springback, as shown in Fig. (2.37).

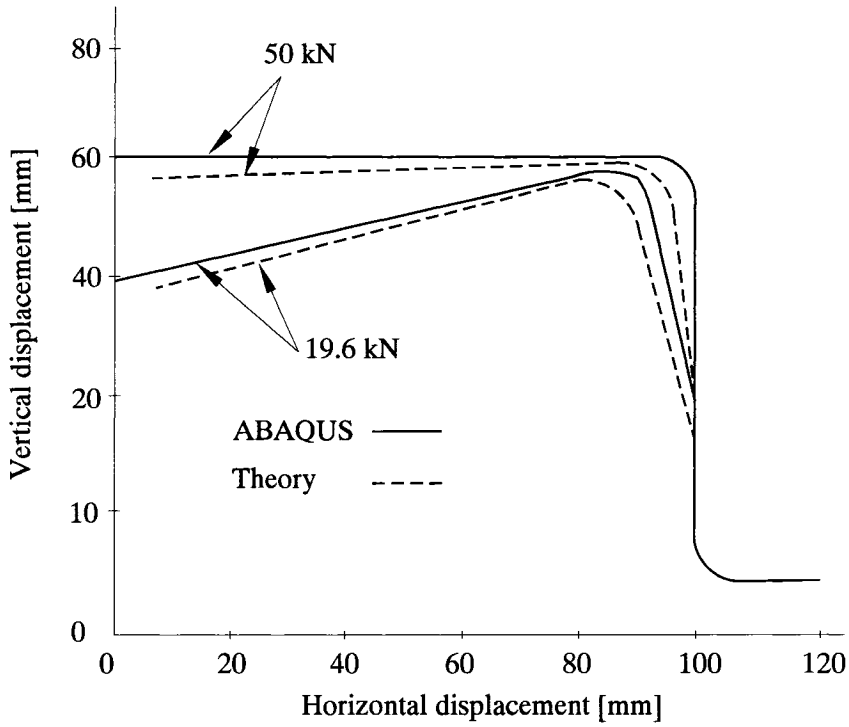

Fig. (2.37) Predicted and measured unloaded shape of the sheet
(adapted from Pourboghrat and Chu, 1995b)

The difference between both results, theory and ABAQUS, were reported to be due to: (i) the theory uses a kinematic hardening model while ABAQUS uses an isotropic hardening model; (ii) theoretically, tensions in the sheet were calculated by using uniform pressure

and blank holder geometry. In ABAQUS, tensions were calculated using the restraining forces using the specified frictional conditions under blank holder.

Lee and Yang (1998) conducted a comprehensive assessment of the numerical factors affecting the accuracy in simulating springback. The 2D-draw bending process and Taguchi method were used in the assessment scheme. Five numerical factors were considered, namely contact damping parameter, penalty parameter, blank element size, number of corner elements, and punch velocity. It was reported that the most important factors affecting the springback angles, in order of their importance, are the blank element size, number of corner elements, and contact damping parameter. Less important are the other two factors. For the side-wall curl, blank element size, number of corner elements, and punch velocity have the most significant effect. Optimal combination of the five factors was also proposed. Moreover, it was reported that the implementation of kinematic hardening model would give more realistic results.

Pourboghrat *et al.* (2000) and Yoon *et al.* (2002) developed the so-called "hybrid membrane/shell" method to model the springback in sheet metal stamping. Since the membrane solution does not capture the bending effects in metal forming; therefore, the bending effect was superposed onto the membrane calculations incrementally. Throughout the analysis, the strains and stresses during bending were calculated incrementally using the extended membrane analysis. After the end of the bending process, the final strains, stresses, and part shape were used in a shell finite element model to perform the unloading and obtaining the subsequent springback. It was reported that this hybrid method saves 50% of the computation time compared to using shell elements in the analysis for the initial loading processes.

Viswanathan *et al.* (2000) simulated the channel forming process using ABAQUS. The sheet was modeled using 2-D 8-node plane-strain elements (CPE8R). Hill's criterion and isotropic hardening law were implemented in the model. The simulation aimed to study the blank-holding force (BHF), binding force, and the forming depth on the springback angle. It was found that increasing the forming depth would result in an increase in the

springback angle. Additionally, decreasing the BHF would result in an increase in the springback angle.

A modified membrane finite element formulation was developed by Huh and Choi (2000). Their formulation incorporated the bending effect that is not included in the membrane formulation for conventional membrane elements. Also, in their study, they developed a scheme for application of the blank holding force.

The conventional method for applying the BHF is to assume a uniform traction along the edge of the flange. Their method, however, takes into account the equilibrium of the traction force according to the thickness variation during the deformation process. The modified method assumes that the equilibrium equation between the blank holder and the sheet takes the form

$$\sum_{e=1}^{N_e} \int_{\Omega^e} \sigma^{BHF}\left(t, t_c\right) d\Omega = F^{BHF} \tag{2.130}$$

where t is the thickness of the sheet and t_c is the average thickness of the sheet, as shown in Fig. (2.38).

Moreover, N_e was defined as the number of elements that have larger thickness t than t_c, and σ^{BHF} is the virtual compressive stress, which is assumed to have a relationship with the thickness strain as

$$\sigma^{\mathrm{BHF}} = ak\left(\beta\varepsilon^{BHF} + \varepsilon_o\right)^n \tag{2.131}$$

where k and n are the material constant and hardening exponent, respectively, ε_o is the pre-strain at the initial yield state, α and β are weighting factors, and ε^{BHF} is the compressive strain, which is defined as

$$\varepsilon^{BHF} = \ln\left(\frac{t}{t_c}\right) \tag{2.132}$$

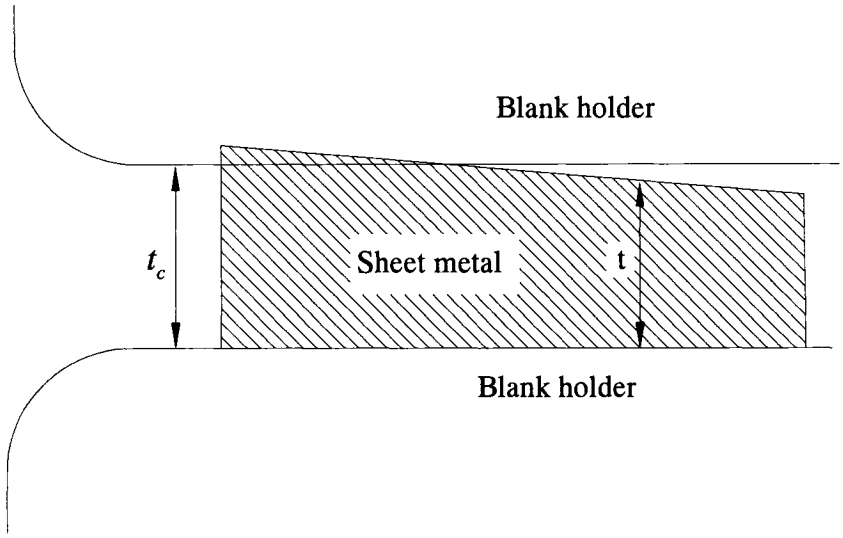

Fig. (2.38) Virtual compressed thickness in the modified scheme for the blank holding force (adapted from Huh and Choi, 2000)

The analysis was carried out for cylindrical and rectangular cup drawing. Punch load versus punch displacement for the rectangular cup drawing is shown in Fig. (2.39). It is shown that the results using the conventional membrane element do not agree well with the experiments while the proposed models do.

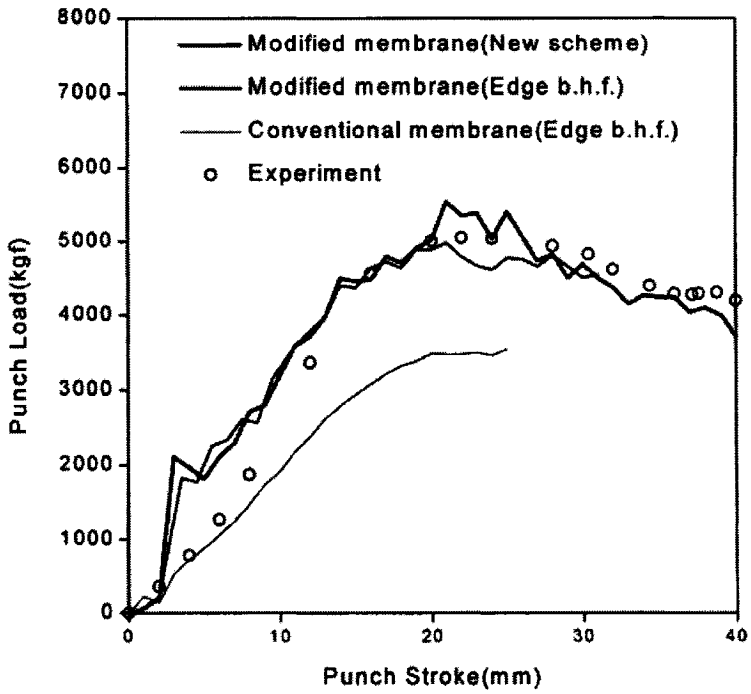

Fig. (2.39) Comparison of the punch load versus punch displacement for the rectangular cup drawing (Reprinted from Huh and Choi (2000) with permission from Elsevier)

Uemori *et al.* (2000) modeled the hat-bending and the subsequent springback using finite element analysis. Three different constitutive models were used in the analysis: isotropic hardening, kinematic hardening, and combined (isotropic plus kinematic) hardening laws. Comparison between experimental observations and numerical simulation results was performed to investigate the accuracy of predicting the springback with special reference to the choice of constitutive models. Material parameters introduced into the finite element model were determined by means of both uniaxial tension tests and cyclic loading tests.

It was found that the combined hardening model agrees fairly well with the experimental observations. On the other hand, isotropic and kinematic hardening models underestimate the springback since they do not accurately describe the Bauschinger effect.

Experiments and simulation of the flanging operation and springback were conducted by Song *et al.*(2001). Aluminum 5182-O, commonly used in industry, was used for the test and assumed to follow the power hardening law ($\sigma = K\ \varepsilon^n$). Springback angles were measured by a Coordinate Measuring Machine (CMM).

The ABAQUS finite element code was used in the simulation. Two element types were tried, 8-node plane-strain solid elements (CPE8R) and 4-node shell elements (S4R) with 6 layers and 13 integration points through the sheet thickness, respectively. Furthermore, the Bauschinger effect during modeling was considered during unloading by employing a kinematic hardening law in the analysis using the solid elements.

The main findings of this study were that the solid-element analysis had better correlation with experiments and the kinematic hardening law analysis had better results than those obtained from the isotropic hardening law analysis.

Tang *et al.* (2001) proposed a method for calculating the stress increment, from Mróz hardening rule, for a given strain increment in sheet metal forming simulations. Their method was called the "*radial return*" method. Two cases, S-Rail and a cross member in a vehicle, were modeled using the proposed method and the springback was predicted. The cases were modeled with triangular shell elements using an in-house finite element code.

The drawing depth for the S-Rail was 37.00 mm and for the cross member was 50.40 mm. The predicted shapes after springback are shown in Fig. (2.40). Fair agreement with experiments was reported to be obtained.

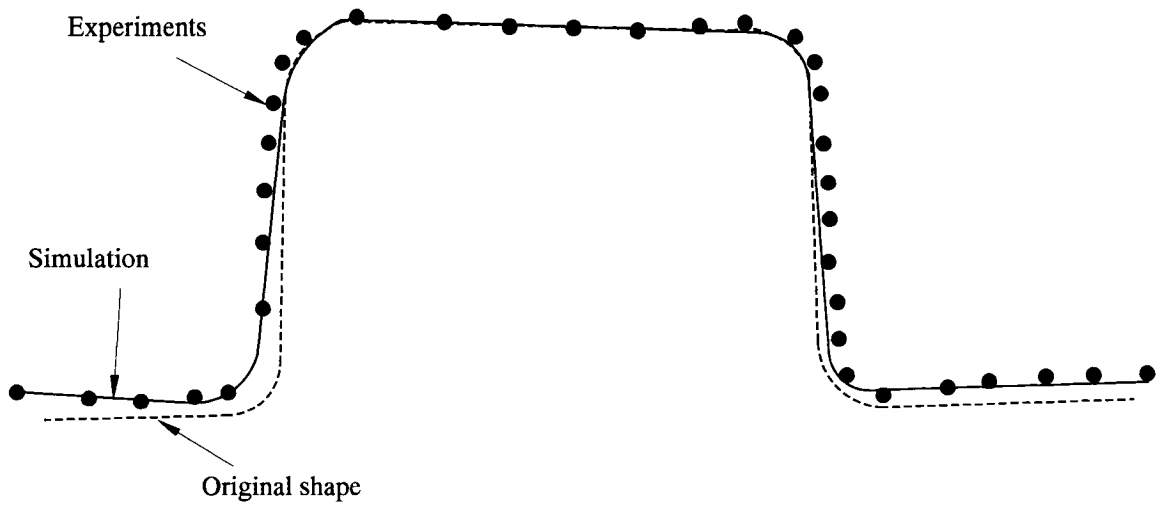

Fig. (2.40) Springback angles for the S-Rail shape (adapted from Tang *et al.*, 2001)

To control the material flow into the die cavity in sheet metal forming processes, draw-beads are often used. Material under the draw-beads passes through multiple bending and unbending processes. Huang *et al.* (2001) modeled the material behaviour under the draw-bead using different hardening models and von Mises yield criterion. It was found that using the kinematic hardening model gives smaller thickness strain prediction. Also, predicted strains using the combined hardening model fall between those predicted by each model individually, isotropic or kinematic hardening alone. Moreover, shell and solid elements were used in the model and it was reported that models using shell elements gave more accurate predictions for stresses and strains.

Li *et al.* (2002a) modeled the draw-bend operation and highlighted some of the factors that affect the accuracy of the finite element model. They recommended, as reported by other researchers in the literature, that accounting for the Bauschinger effect highly affects the model's accuracy, as its presence alters springback angles significantly. Also, it was reported that 3D shell and nonlinear solid elements are preferred in modeling springback to capture the anticlastic curvature. Moreover, for a ratio of tool radius to sheet thickness (R/t) that is greater than 5 – 6, solid elements are considered

computationally expensive; however, for R/t less than 5 – 6, nonlinear 3D solid elements are required for accurate springback predictions. Furthermore, Li *et al.* (2002b) simulated the springback in the V free-bending process. It was reported that varying the elastic modulus, E, with plastic deformation can enhance the springback prediction. Also, the material hardening model used in the simulation directly affects the accuracy of springback prediction.

Papeleux and Ponthot (2002) modeled the 2D draw-bending process with emphasis on the effect of several parameters on springback, namely BHF, friction coefficient, and constitutive model. It was reported that, in agreement with other findings reported in the literature, increasing the BHF will result in a decrease in the springback angles. For the effect of friction coefficient, it was stated that the models are highly sensitive to the change of friction coefficient. The coefficients of friction used in their simulations were 0.144, 0.129, and 0.162 for mild steel, high strength steel, and aluminum, respectively. As for the effect of the hardening model, it was reported that the springback angle around the punch tip, defined as θ_1, in Fig. (2.41), is less sensitive to kinematic hardening; however, the angle around the die radius, defined as θ_2, in Fig. (2.41), is more sensitive to the kinematic hardening definition. The reason was attributed to the fact that the region defining angle θ_1 is bent once, around the punch tip, during the process and accordingly there was no subsequent unloading. On the other hand, the region defining angle θ_2 experienced bending and unbending, around the die corner, and accordingly was affected by the presence of the Bauschinger effect in the material and the kinematic hardening formulation defining it.

Park and Oh (2004) modeled the springback of the U-bending test using a newly developed shell element. That element is a 4-node shell element with 6 degrees of freedom at each node, which gives a better description of bending than the conventional shell element used in the commercial finite element packages.

To quantitatively observe the springback, springback angles were defined as shown in Fig. (2.41). It was reported that using this element resulted in a more precise prediction of the springback angles using a lower number of elements.

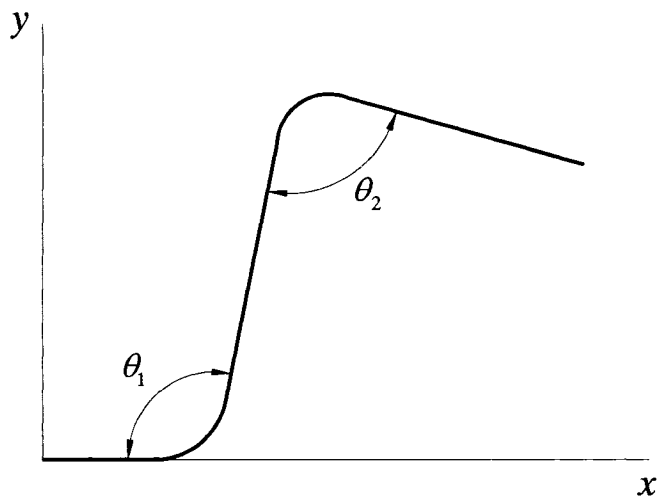

Fig. (2.41) Definition of springback angles according to Park and Oh (2004)

Takamura *et al.* (2004) considered the elastic deformation of the tools in a square cup deep drawing finite element simulation. To compare the model to a physical experiment, tests were conducted using two blank holders with different stiffnesses – a low stiffness blank holder of 3.00 mm thickness and a high stiffness blank holder of 50.00 mm thickness. In the finite element model, the lower stiffness blank holder was modeled as an elastic body with σ_Y = 155.60 MPa, E = 206 GPa and ν = 0.3, while the higher stiffness blank holder was modeled as a rigid body. Figure (2.42) shows the geometry of the tools for the experiments and the simulation and the two types of blank holders used in the study.

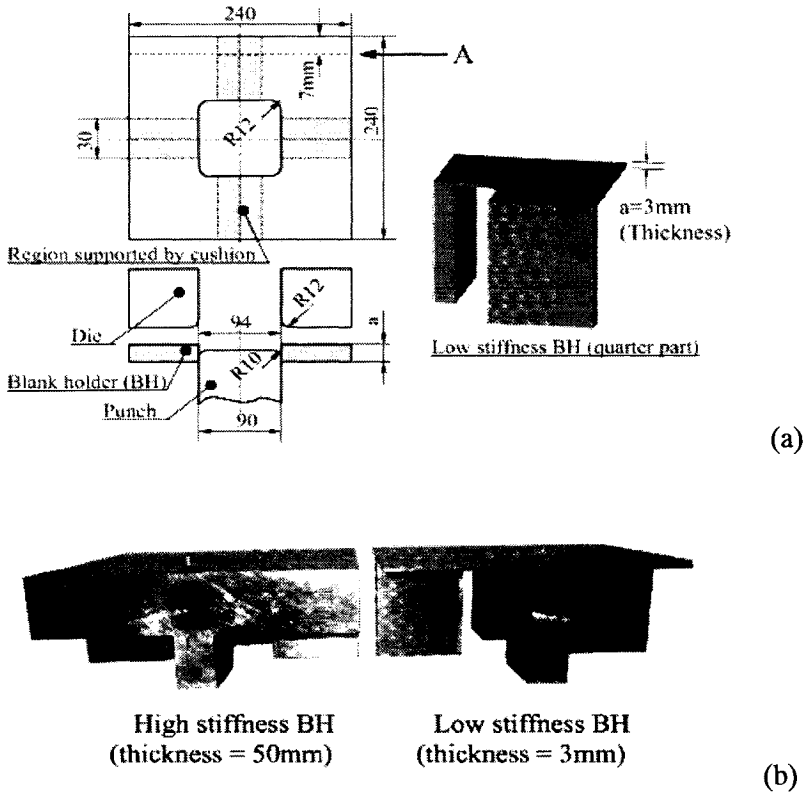

Fig. (2.42) (a) Geometry of tools, and (b) Types of blank holders

It was reported that the influence of the die stiffness on the draw-in of positions B in Fig. (2.43), mid point in the side of the pan, is only 2.20 mm less in case of using the lower stiffness die. It was also reported that the draw-in difference is not significant, 0.15 mm, at position C shown in Fig. (2.43), the flange corner. The simulations predicted almost the same difference for both positions, as shown in Fig. (2.44).

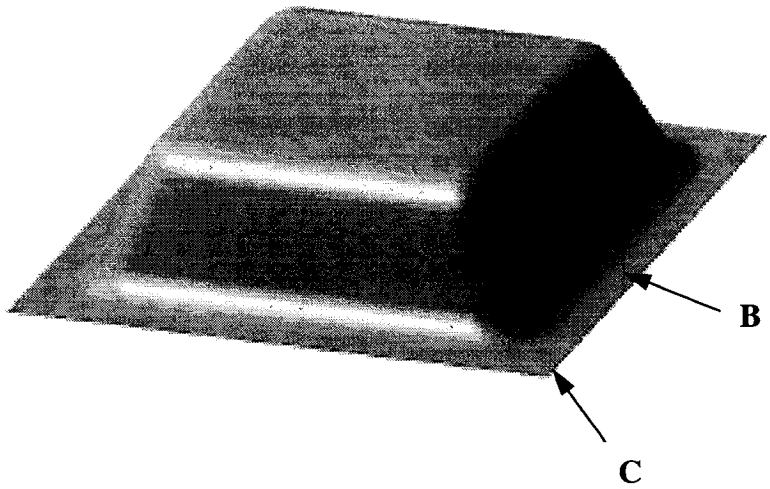

Fig. (2.43) Positions of draw-in measurements according to Takamura *et al.* (2004)

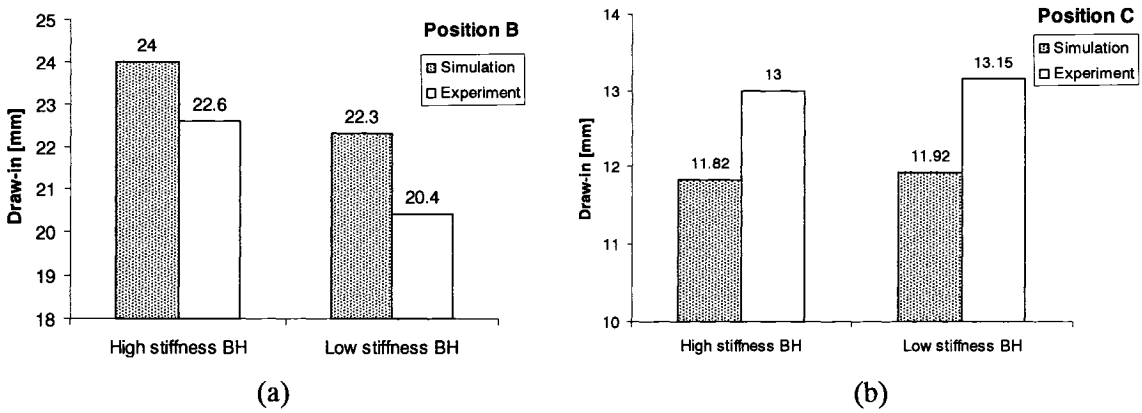

Fig. (2.44) Comparison of draw-in at (a) position B, and (b) position C
(adapted from Takamura *et al.*, 2004)

Bjørkhaug and Welo (2004) used LS-Dyna to model the springback of a rotary stretch bending operation of an aluminum AA718 profile. They used shell elements and varied the material description model. The two constitutive models that were used in their study are the isotropic von Mises and the anisotropic Barlat 96 yield criteria. The main findings

were that the models using isotropic yield criterion predicted consistent results in bending, independently of mesh refining and number of integration points. Moreover, it was found that using Barlat's criterion has a negligible effect on springback calculations; however, the prediction of cross sectional geometry was more accurate.

Vij and Date (2004) investigated the springback behaviour along the curved line of bend with varying BHF, with respect to area, through finite element simulations using PAM-STAMP 2G software. Materials modeled were standard steel (E = 210 GPa and ν = .30) and Al-Li alloy. The coefficient of friction was specified as 0.04 and an isotropic hardening model was used. Two geometric shapes were modeled, S-Rail and C-Tray.

It was found that variation of springback with respect to uniform BHF is almost the same as in the variable BHF. Also, higher BHF was reported to be ineffective in containing higher values of springback along the curved line of bend.

The effect of high strain rate material properties, number of integration points through the thickness, and the artificial high punch speed on the accuracy of springback prediction was studied statistically by Kulkarni (2004). The 2D draw-bending specimens made of stainless steel 304 were simulated using LS-Dyna finite element software. The strain rate properties were introduced as the material properties (stress-strain curve) obtained by performing the characterization at two different cross-head speeds. It was found that the model is sensitive to the strain rate properties. Moreover, the punch speed was found to be not a statistically significant factor for the range chosen in the analysis.

Żmudzki *et al.* (2004) studied the minimization of the anisotropic effect in thin products of sheet forming processes. The anisotropic effect discussed in their study refers to the inhomogenities of component's thickness and final shape caused by the process conditions and material properties. Their optimization method was based on an Artificial Neural Network optimization strategy. The objective function was based on the final shape of an unbounded bulging of a thin cup. The cup was formed using a superelastic medium and the optimization variable was the punch velocity.

The sheet was modeled using an elasto-plastic material model where Hill's yield condition was implemented as

$$\sigma_H = \left[\begin{matrix} h(\sigma_{11}-\sigma_{22})^m + f(\sigma_{22}-\sigma_{33})^m + g(\sigma_{33}-\sigma_{11})^m \\ +2l\sigma_{23}^m + 2m\sigma_{13}^m + 2n\sigma_{12}^m \end{matrix} \right]^{\frac{1}{m}} \tag{2.133}$$

where $m = 2$ and h, f, g, l, m, and n were calculated as functions of the parameters R_1 to R_6, that were determined from tension tests performed at various strain rates and temperatures, from

$$\begin{aligned} f &= \frac{1}{2}\left[-\left(\frac{1}{R_1}\right)^2 + \left(\frac{1}{R_2}\right)^2 + \left(\frac{1}{R_3}\right)^2 \right] \\ g &= \frac{1}{2}\left[+\left(\frac{1}{R_1}\right)^2 - \left(\frac{1}{R_2}\right)^2 + \left(\frac{1}{R_3}\right)^2 \right] \\ h &= \frac{1}{2}\left[+\left(\frac{1}{R_1}\right)^2 + \left(\frac{1}{R_2}\right)^2 - \left(\frac{1}{R_3}\right)^2 \right] \\ l &= \frac{3}{2}R_6, \quad m = \frac{3}{2}R_5, \quad n = \frac{3}{2}R_4 \end{aligned} \tag{2.134}$$

The optimization problem was defined as a function of the ideal roundness of the cup. The objective function for optimization was defined in terms of coordinates as

$$\Phi = \frac{1}{n}\sqrt{\sum_{j=1}^{n}\left(\frac{R_{aj}(x_j, y_j) - R_i}{R_{aj}(x_j, y_j)}\right)^2} \tag{2.135}$$

where R_{aj} is the distorted sample coordinate vector and R_i is the perfect round shape radius, as shown in Fig. (2.45).

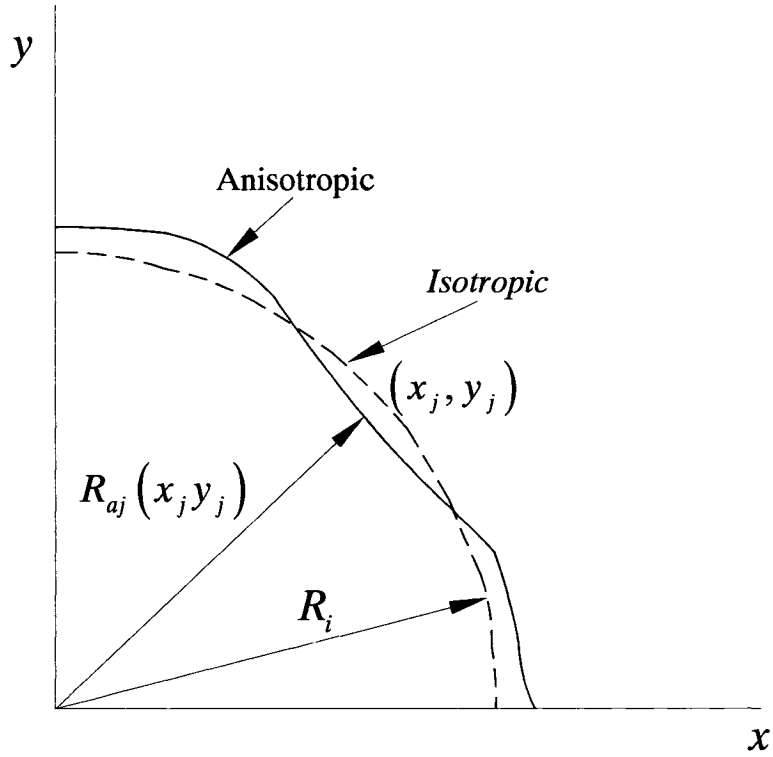

Fig. (2.45) Schematic cross section of bulged sample, here in this figure anisotropic and isotropic refer to the shape not to the material (adapted from Żmudzki *et al.*, 2004)

It was found that the higher values for the objective function were obtained with the decrease of the punch velocity. The optimum punch velocity was found to be 0.74 mm/s. It was also reported that there is a strong shape anisotropy effect at slower punch velocities; however, more homogenous thickness distribution was obtained.

Lee *et al.* (2005a) modeled the unconstrained cylindrical bending benchmark problem of NUMISHEET 2002. There is no blank holder for this process so that the bending effect dominates. In the model, shell elements were used with 9 integration points through the thickness of the shell. The coefficient of friction between the tools and the sheet was chosen to be 0.10. It was reported that the springback angle was overestimated for all the models; however, the difference was in the range of the experimental errors. It was

concluded that the springback is proportional to the ratio of the yield stress with respect to the modulus of elasticity and the sheet thickness.

As an extension to their simulations, Lee *et al.* (2005a) also simulated the 2D draw-bending test using 300 shell elements and 9 through-thickness integration points. Also, 0.1 was used as the friction coefficient between the tools and the sheet. They reported that primary tests showed 10 m/s can be considered an optimum punch speed for the simulation. Isotropic, kinematic, and combined hardening models were used in the simulations. It was observed that the value of springback angles slightly changed with respect to the hardening model. However, as a general observation, kinematic hardening models underestimated the predicted springback. Combined hardening models well predicted the side-wall curl and the springback angle. Also, the analysis showed that the larger BHF suppresses the springback, most significantly for the sidewall curl.

2.8. Summary and Research Approach

This chapter discussed a number of topics that are directly linked to the scope of work conducted in this research. This section provides a summary of work done thus far by other researchers and its applicability to better achieve the goals and scope of work presented in Section 1.3.

As presented in Section 2.1, it is clear that Bauschinger effect plays an important role when describing the material behaviour when cycling loading takes place, in the deformation history of a part. Since the problem addressed in this work takes into account bending, unbending, and reverse bending processes, a model that includes the Bauschinger effect should be adapted in the material model description.

As will be explained in Chapter 3, all the materials included herein were received as sheets. Because these sheets were produced by rolling, initial anisotropy existed in the materials. The equations presented in Section 2.2, describing both types of material

anisotropy, namely normal and planar anisotropy. The material anisotropy parameters for the tested sheets (R-values) will be determined experimentally, and the normal anisotropy parameter, in particular, will be used in the material description in the finite element modeling, presented in Chapter 5.

Several yield criteria were presented in Section 2.3. Some of these criteria; for example, Tresca, von Mises and Hosford (1972), do not include the material anisotropy and are limited to isotropic materials. Moreover, some other criteria that include anisotropy in their definition are not applicable in general cases. An example of this limitation is found in Hosford (1996), where it can only be applied when shear stresses are not present.

Therefore, a yield criterion that includes the material anisotropy in its formulation, in addition to the reasonable experimental work needed to determine its parameters, needs to be considered in this work. Researchers, such as Barlat and Lian, (1989) and Cazacu and Barlat, (2003), reported that Hill's 1948 yield criterion is suitable for metals with a normal anisotropic value, $\bar{R}$, greater than one, especially steels. Also, Bron and Besson (2004) reported that the Hill's 1948 criterion can easily be implemented in the simulations of sheet metal forming processes. Furthermore, researchers, such as Leu (1997), Pourboghrat *et al.* (1998), and Sinou and Macquaire (2003), adopted the criterion in their analytical and numerical models and reported to provide reasonably accurate results. Accordingly, Hill's 1948 criterion, for planar isotropic materials, is then used in Chapter 5, where the material model is described.

Two classical hardening models, namely isotropic and kinematic hardening, were discussed in Section 2.4. It was mentioned that using only the isotropic hardening model does not account for the Bauschinger effect. Also, using only the kinematic hardening model does not lead to an accurate prediction of the material behaviour. Therefore, to match the observations of common metals, a combined hardening model is required.

Several combined hardening models were discussed in Section 2.4, among which was the Brunet *et al.* model (2001). This model has limitations due to the uncertainties in the

measurement method to obtain the model parameters. Moreover, Geng *et al.* (2002) developed a combined hardening model; however, it was reported that using the model parameters reflects the material behaviour only up to a strain of 2 per cent. Also, these parameters have to be adjusted by trial and error to reflect as accurately as possible the experimental tests.

Most of the references reviewed; for example, Chu (1984), Chaboche (1986), and Gau and Kinzel (2001), indicated that for better material behaviour prediction, multiple-yield-surface models can be used. However, due to the complexity of such models, they are not widely implemented. One of the well established multiple-surface models is the Mróz (1967) model, which was also discussed in detail in Section 2.4. The model leads to a better material behaviour prediction than single-surface and two-surface models; however, due to the complexity of the model and the fact that it requires expensive computational resources, it has not been widely implemented, especially in the finite element analysis. With the current advance in computers, in terms of capacity and speed, the concern about computational resources are minimized. Therefore, in this work, a combined hardening model that is based on Mróz (1967) formulation is considered. This model will be implemented in the material model developed herein as will be discussed in detail in Chapters 5.

In order to obtain the material properties that will be used in the finite element analysis, presented in Chapters 5 and 6, several material characterization techniques were reviewed and presented in Section 2.5. To characterize the materials, some standard techniques, such as standard tensile testing, will be implemented, as will be discussed Chapter 3.

Furthermore, tension-compression testing requires specialized techniques since sheets tend to buckle in compression. The experiment techniques of Jain (1990) and Khan and Jackson (1999) cannot be implemented since they used cylindrical specimens, not sheets. Moreover, Aerens (1997), Yoshida *et al.* (1998), Zhao and Lee (2001a and 2001b), Yoshida and Uemori (2002), obtained the material behaviour of sheets in compression indirectly from bending-reverse bending tests; which includes a number of assumptions

in obtaining the compressive behavior and a number of calibration techniques. The Schedin and Melander (1987), Yoshida *et al.* (2002), as well as Cleveland and Ghosh (2002) experiments required a large number of specimens, approximately eight specimens per test, as well as machining and preparation stages that might affect the accuracy of the data. Moreover, Mattiasson and Sigvant (2004) used shear tests in order to indirectly obtain the uniaxial cyclic behaviour of the sheets.

Therefore, a test that can directly produce the material curves in tension-compression is required. Accordingly, as will be discussed in Chapter 3, an anti-buckling device was designed and used for that purpose. A similar approach was adopted by other researchers such as Wang *et al.* (2004b), Lee *et al.* (2005b) and Boger *et al.* (2005).

Methods for springback prediction were discussed in Section 2.6. Some of these methods were based on the assumption that the material is elastic-perfectly-plastic as in Gardiner and Philadelphia (1957), or the assumption of isotropic material and plane strain conditions as in Queener and De Angelis (1968). The formulations for these methods, as well as Hosford and Caddell (1983), were derived for simple bending, which means these methods cannot be implemented for prediction of springback in complex bending of intricate geometries.

The effect of process parameters was studied by a number of researchers, such as Karafillis and Boyce (1992), Tan *et al.* (1994), El-Domiaty *et al.* (1996) Gotoh *et al.* (1997), and Samuel (2000). They indicated the importance of the bending radius, sheet thickness, and the blank holding force on the springback angle. It was found that the increase in the bending radius, the decrease in the sheet thickness, or the decrease in the blank holding force will result in an increase in the springback angle. Moreover, the effect of material parameters, such as anisotropy and the strain hardening exponent, as well as the hardening assumption, on the predicted springback angles was studied by Tan *et al.* (1995), Leu (1997), Pourboghrat *et al.* (1998), Delannay *et el.* (2004), and others. A general conclusion from the researchers' findings is that the increase in sheet anisotropy or the decrease in the strain hardening exponent will result in an increase in the

springback. As for the effect of hardening models on springback, the researchers drew the attention to the importance of including the Bauschinger effect and the kinematic hardening when describing the material, in order to better predict the springback. Furthermore, researchers such as Gau and Kinzel (2001) and Geng and Wagoner (2002) emphasized the importance of including a combined hardening model in the material description to better reflect the material behaviour and accordingly the springback prediction. Therefore, a combined hardening model is implemented in this work, as will be presented in Chapter 5.

Finite element modeling is being extensively used in sheet forming processes for its cost effectiveness compared to experimental trial and errors. The quality of the model depends on many parameters such as accurate material description, the selection of element type, and the proper description of the forming process. In Section 2.7, several papers about finite element modeling of metal forming processes were reviewed. The outcome of this review is that, according to many researchers; for example, Tang (1994), Huang *et al.* (2001), Park and Oh (2004), and others, shell elements have been widely implemented in the sheet forming simulations, particularly when modeling springback is considered. Moreover, modeling 2D draw-bending was carried out by Pourboghrat and Chu (1995b), Lee and Yang (1998), Papeleux and Ponthot (2002), Kulkarni (2004), and Lee *et al.* (2005a). Accordingly, the concept of 2D draw-bending was considered in this work for both experiments, as will be discussed in Section 3.4, and in the simulations, as will be discussed in Section 6.3.2, to examine the model capability in prediction of the springback angles when using different forming conditions.

In conclusion, in order to achieve the objectives given in Section 1.3 a material model that accounts for Bauschinger effect, material anisotropy, and combined hardening is needed to better capture the material behaviour in sheet forming and to accurately predict the subsequent springback. The developed material model is described in detail in Chapter 5. The developed model was used to simulate both simple bending and 2D draw-bending processes, as will be discussed in Chapter 6. Finally, the model results were validated by comparing them to the experimental results presented in Chapter 4.

CHAPTER 3

Experimental Setup

3.1. Introduction

As discussed in Section 2.2, material properties of rolled sheets vary with respect to the orientation to the rolling direction, which is called planar anisotropy, and through thickness direction, which is the normal anisotropy. Therefore, tests need to be conducted at different directions to the rolling to properly characterize the material.

This chapter discuses the experimental procedures and the tests used to determine the mechanical properties of the materials included in this study. As mentioned in Section 1.2, the materials included in this research are set into two categories, aerospace materials, which include SS410 and IN718 sheets. The other category is for automotive materials, which includes DP600/300 and DP600/400.

All materials included in this research were received in sheet form; Table (3.1) shows the thickness of the sheets for these materials. Therefore, to characterize the mechanical properties and the anisotropy parameters, specimens were cut from these sheets at different angles to the rolling direction, as shown in Fig. (3.1), and sets of uniaxial tension and uniaxial tension-compression tests were conducted. Also, specimens from the same sheets were prepared and tested in simple bending and 2D draw bending experiments, as will be discussed in this chapter.

Table (3.1) List of sheets tested from different materials

Application	Material	Thickness, mm
Aerospace	SS410 (Thick)	1.575
	SS410 (Thin)	0.686 – 0.787
Automotive	DP 600/300 (Thick)	1.741
	DP 600/300 (Thin)	1.045
Automotive	DP 600/400	1.700
Aerospace	IN718	0.635 – 0.661

Simple bending experiments were performed to examine the effect of anisotropy with respect to the specimen orientation, on springback angles. Rectangular specimens were cut from the sheets, also at different angles to the rolling direction, and simple bending tests were performed. Figure (3.1) shows the schemes followed in cutting tension, tension-compression, and bending specimens from the original sheets.

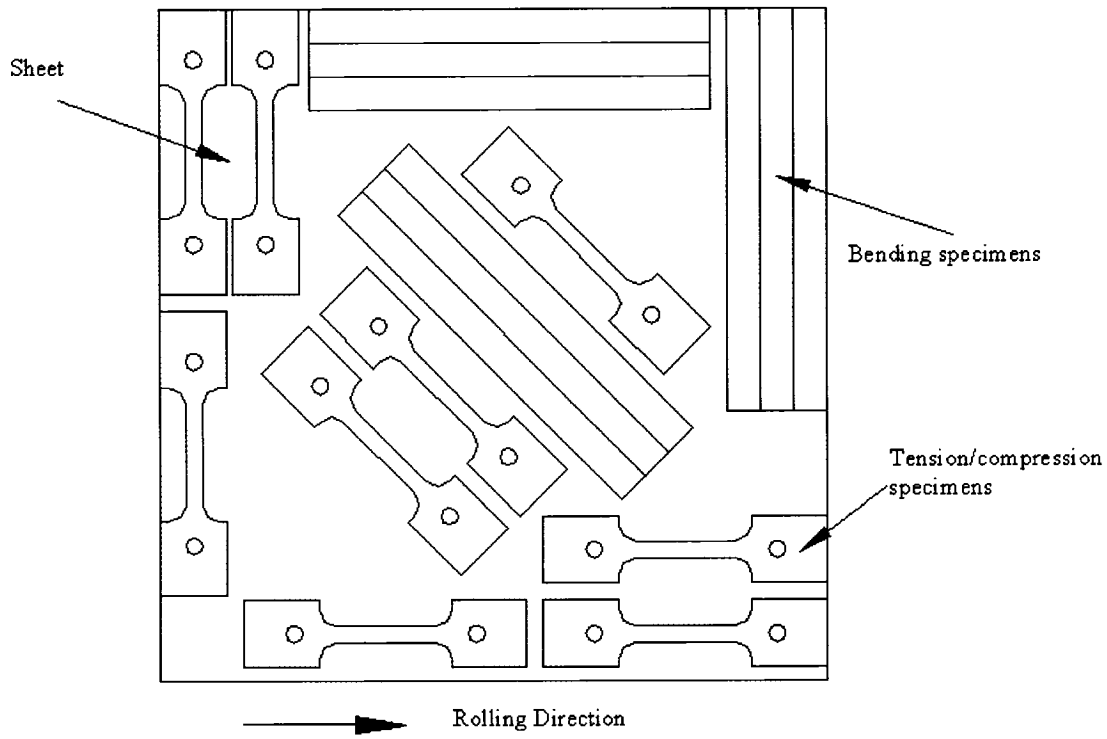

Fig. (3.1) Schematic drawing showing the specimen orientations on the sheet

Finally, to include the combined effect of anisotropy and forming conditions, 2D draw bending experiments were performed on rectangular specimens that were cut, also at different directions to the rolling, and the final springback angles were measured. In addition, experiments to study the effect of varying forming conditions, such as blank holding force, on the springback angles of the specimens were also conducted.

3.2. Uniaxial Tension Tests

To characterize the material properties and its anisotropy, specimens were cut from the sheets in different orientations to the rolling direction, namely 0°, 45°, and 90°. The geometry of the tensile specimen (ASTM, 1999) is shown in Fig. (3.2). The tests were conducted to determine the stress-strain curves as well as its anisotropy parameters, R_φ with respect to the rolling direction, and accordingly, the materials' $\overline{R}$ and ΔR values.

The procedure used to calculate and measure the material parameters is described in detail in Chapter 4.

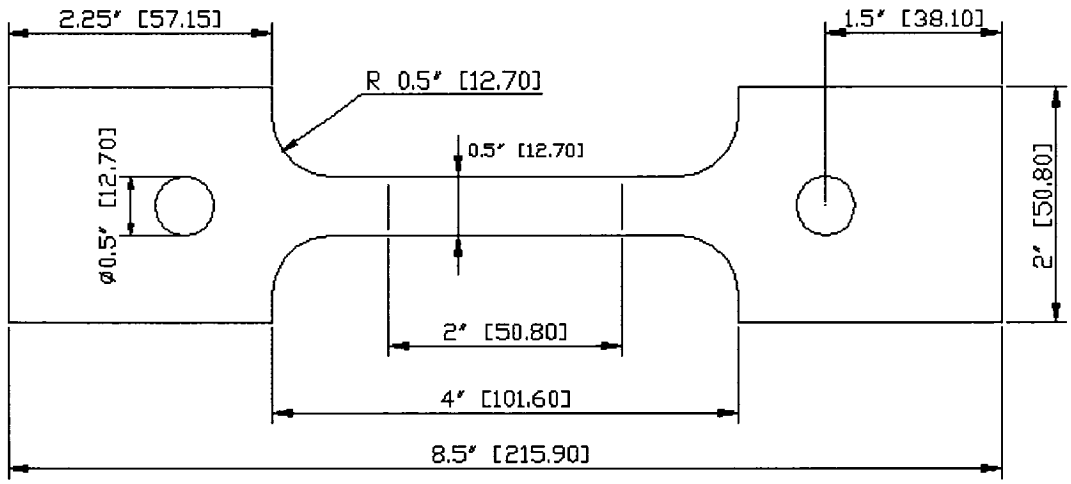

Fig. (3.2) Tensile specimen's geometry, inch [mm]

To perform the tests, an MTS hydraulic test machine, with a load cell capacity of 250 kN and an MTS 458.20 microconsole controller, was used for both tensile and bending tests. The simple bending and draw-bending experiments are discussed in the next sections. The tensile test preparation and test procedures are discussed here.

The initial dimensions of the cross-section, at the reduced section of the specimen, are measured to determine the reference cross-sectional area, A_o. Gage marks are drawn with ink to assist determining the gage length at which the anisotropic parameters are calculated.

The MTS machine is set up such that the force and the strain transducers are manually adjusted to a reading of zero at the beginning of the testing. Afterwards, the specimens are mounted by means of pins, which connect the specimen to the fixture. These pins transmit the force from the test machine to the specimens being tested. To ensure that the rate of displacement of the cross-head does not affect the results, a small rate was chosen

so that the tests are performed in quasi-static conditions. The cross-head was adjusted to move with a constant crosshead velocity resulting in a nominal strain rate of approximately 2×10^{-3} per second, which eliminates the factors of dynamic effects and rate dependency so that the quasi-static tension conditions are maintained.

The strain is measured during the tests by means of a 25.40 mm – gage extensometer (1.00 in.), which is connected to the controller as well as the gage-section of the specimen. Figure (3.3) shows a specimen mounted on the MTS machine with the extensometer installed. The recorded output signals during the test are the cross-head displacement, the load-cell measured force, and the engineering strain recorded by the extensometer.

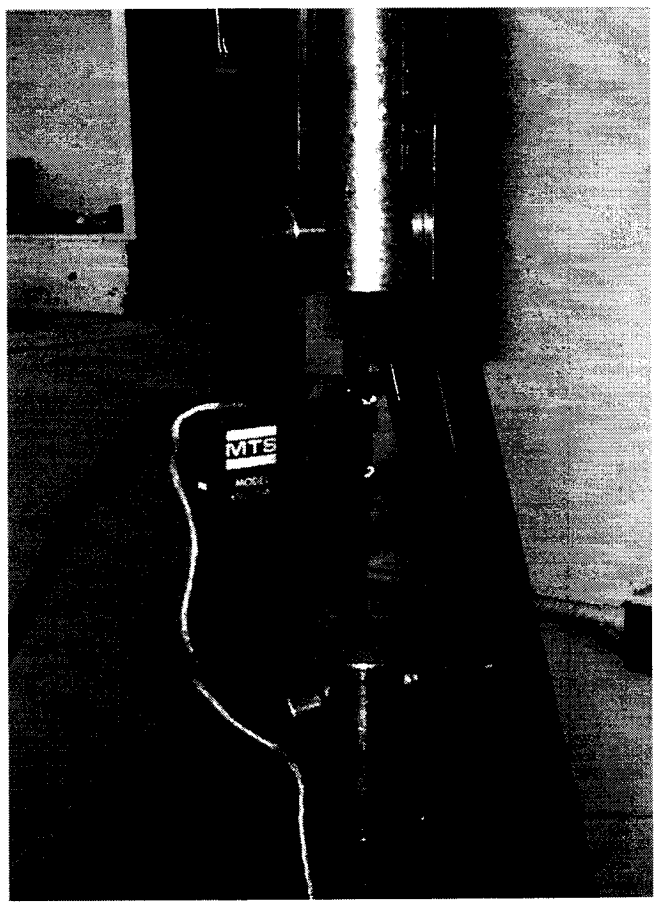

Fig. (3.3) Tensile specimen's installation on the MTS machine

3.3. Uniaxial Tension-Compression Tests

During many forming operations, materials undergo loading, unloading and reverse loading conditions; therefore, material parameters in compression need to be obtained. As discussed in Section 2.5, several researchers used different designs to study the material behaviour in compression. In this study, a specially designed anti-buckling device was designed and fabricated to perform that task, which is to test specimens, having the same geometry as for the tensile tests, under compressive loads.

As shown in Figures (3.4) to (3.6), the anti-buckling device consists of three main parts. Two of the parts are to support the wide clamping-area. These parts were machined to a surface roughness of Ra 125 μ" to increase the contact friction between the wide part of the specimen and the anti-buckling device. Such a design would serve the main function of these parts which is to reduce the bearing stresses induced by the pin on the specimen during loading and reverse loading. Moreover, four holes were drilled in both the specimen and the device; these holes were used for the alignment of the specimen and the device by using four pins.

The third part is to support the gage-section area and to avoid buckling. This part was grooved to minimize the contact area between the anti-buckling device and the gage section. Also, the friction was minimized by using layers of Teflon and a commercial lubricant.

After installing the device, the dimensions of the specimen with the anti-buckling device installed are identical to those of the tension specimen without the device. The specimen is then prestrained in tension up to approximately 2.5% which results in a gap between the wide part of the anti-buckling device and the gage support. The objective is to close that gap by applying a compressive force while avoiding buckling, which is the main function of the gage-section support.

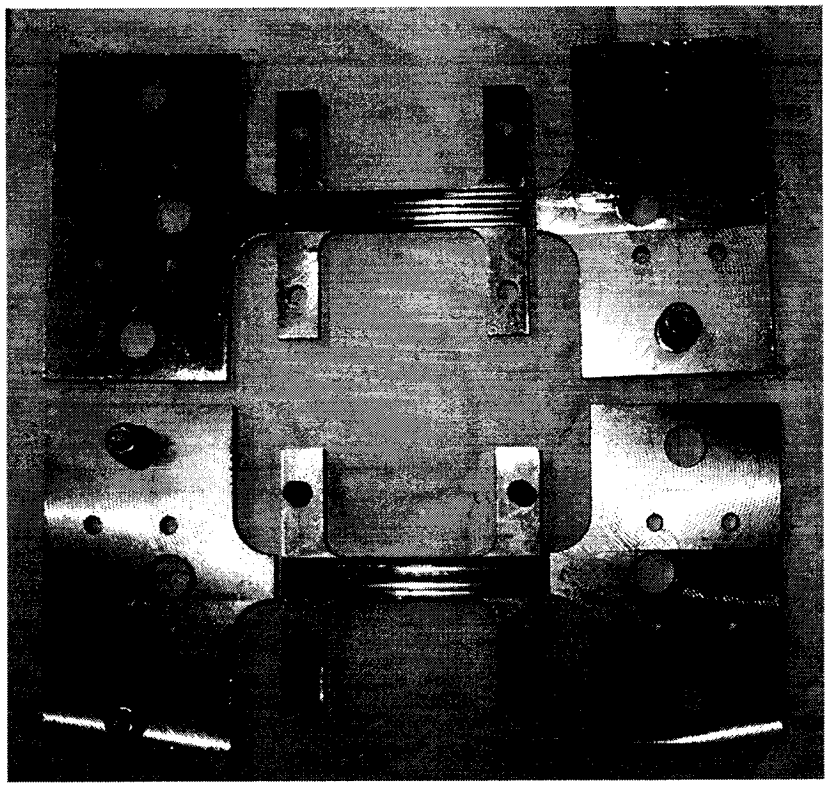

(a)

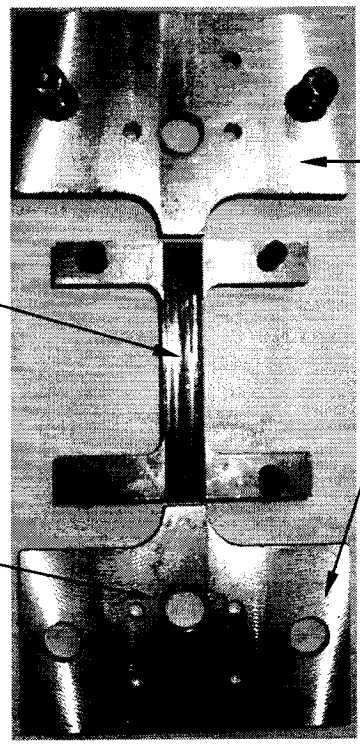

(b)

Fig. (3.4) (a) Parts of the anti-bucking device, (b) detailed description

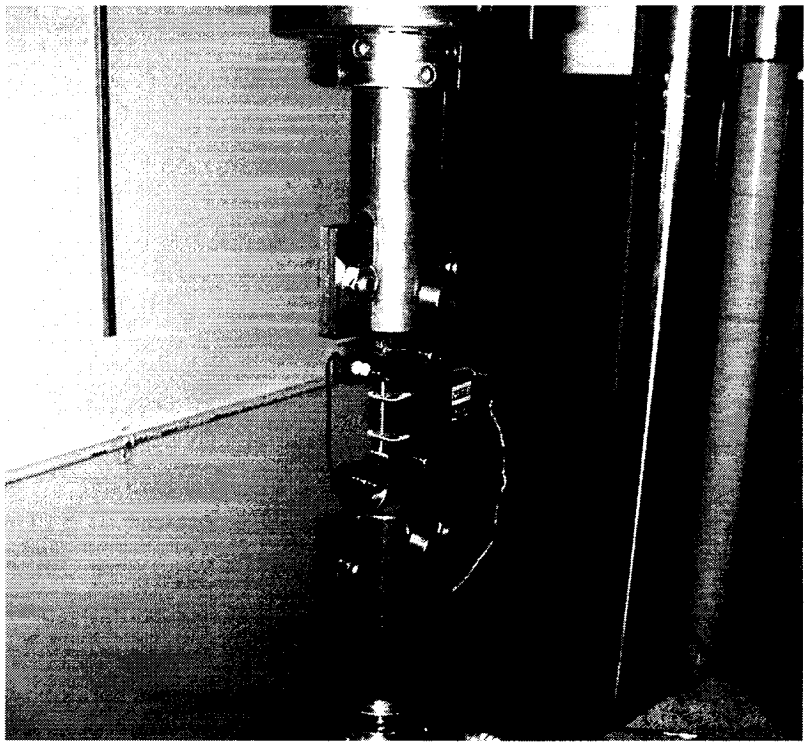

Fig. (3.5) Installation of the anti-bucking device

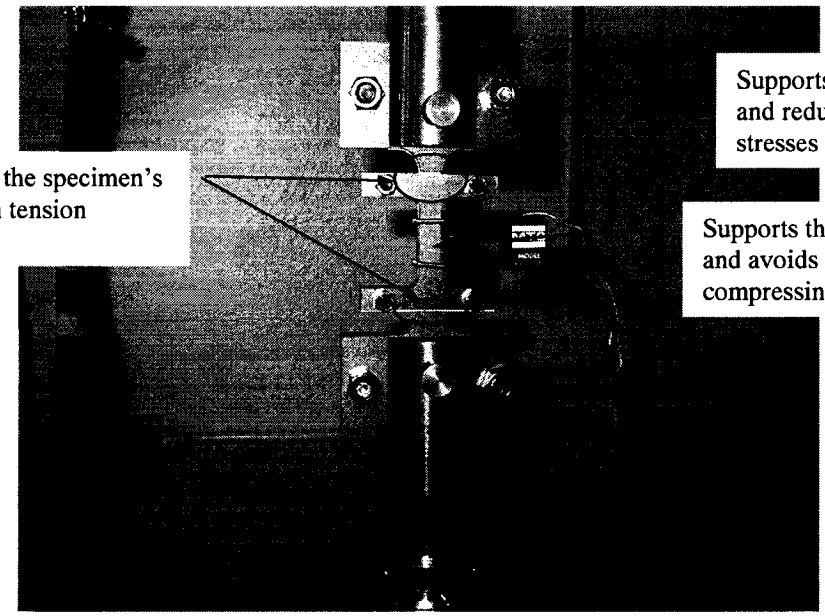

Fig. (3.6) The anti-buckling device with the functions of its parts

3.4. Bending Experiments

In sheet metal forming processes, material often experiences cycles of loading stages, i.e. bending-unbending at the die entrance radii and reverse bending-unbending at the punch shoulder. In such a case, the presence of the Bauschinger effect appears to be more important when metals undergo cycles of bending-reverse bending loading (Chun *et al.*, 2002a).

To study the influence of anisotropy and the forming conditions, two types of bending experiments are discussed in this section, namely the simple bending and the 2D draw bending experiments. Both types of experiments were performed using a specially designed and manufactured apparatus. The same apparatus was used for both types of experiments; however, the geometry of the punch insert and the holder used in each type of bending experiment depends on the type of the bending process performed, as discussed below.

3.4.1. 2D-Draw-Bending Experiments

In order to perform the 2D draw-bending experiments, some limitations concerning the available MTS testing machine had to be considered. Since the hydraulic test machine that is used for the experiments is a single action press with a capacity of 250 kN, a special fixture was required that would allow for separate actions, namely a blank holding stage and a bend forming stage.

Furthermore, the small working space inside the press made the earlier design of Swift (1948) and Carden *et al.* (2002) unusable. Therefore, an alternate design based on the work of Bayraktar and Altintas (1996) was used. Uemori *et al.* (2000) used a similar design with slight differences in the dimensions and the materials of the die and the specimens.

3.4.1.1. Fixture Description

Figure (3.7) shows a schematic for the bending apparatus. The device consists of five main parts, namely the base plate, the die, the blank holder, the punch, and the upper plate. The die and the base plate are fixed to the hydraulic ram after alignment with the punch, which is attached to the load cell.

The upper plate is separated from the blank holder by means of four springs that are mounted on four pins installed at the corners of the apparatus. The four springs are then used to introduce the required blank holding force.

The blank holder, mounted on four smaller springs, can move in the vertical direction through the alignment with the four pins attached to the base plate. The lower four springs assure that the blank holder is kept at a small distance from the die, so that the specimens can be inserted easily.

The upper plate, blank holder, and base plate are made of low-carbon steel M36 and the die is made of D2 tool steel. Furthermore, to increase the surface hardness of the tools in contact with the bending specimens, the blank holder was heat-treated by nitrite to increase its surface hardness to 32 HRC and the die was hardened to 55 HRC.

For the other parts of the apparatus, namely the steel pins and the bronze shoulder bushings, standard parts were used. The pins are attached to the base plate by press fitting, as well as the bushings and the upper plate. The complete draw-bending apparatus, installed within the MTS hydraulic test machine, is shown in Fig. (3.8). Also a detailed description of the die is shown in Fig. (3.9).

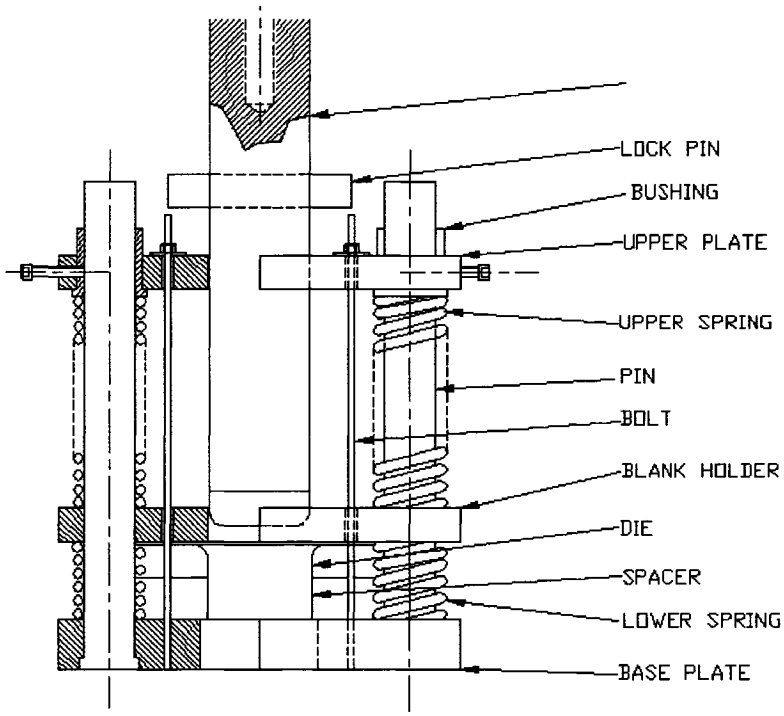

Fig. (3.7) Schematic illustration of the draw-bending fixture

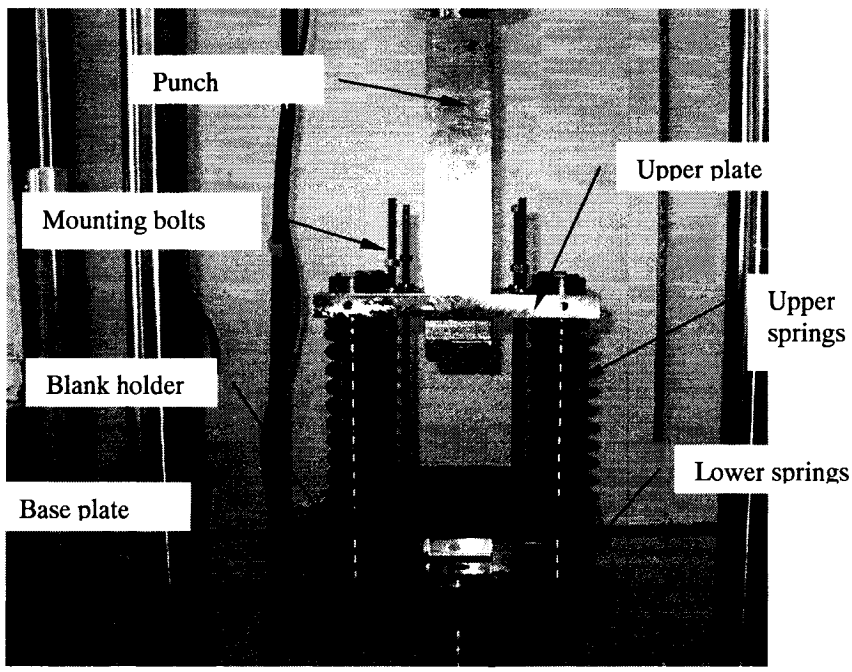

Fig. (3.8) Draw-bending experimental setup

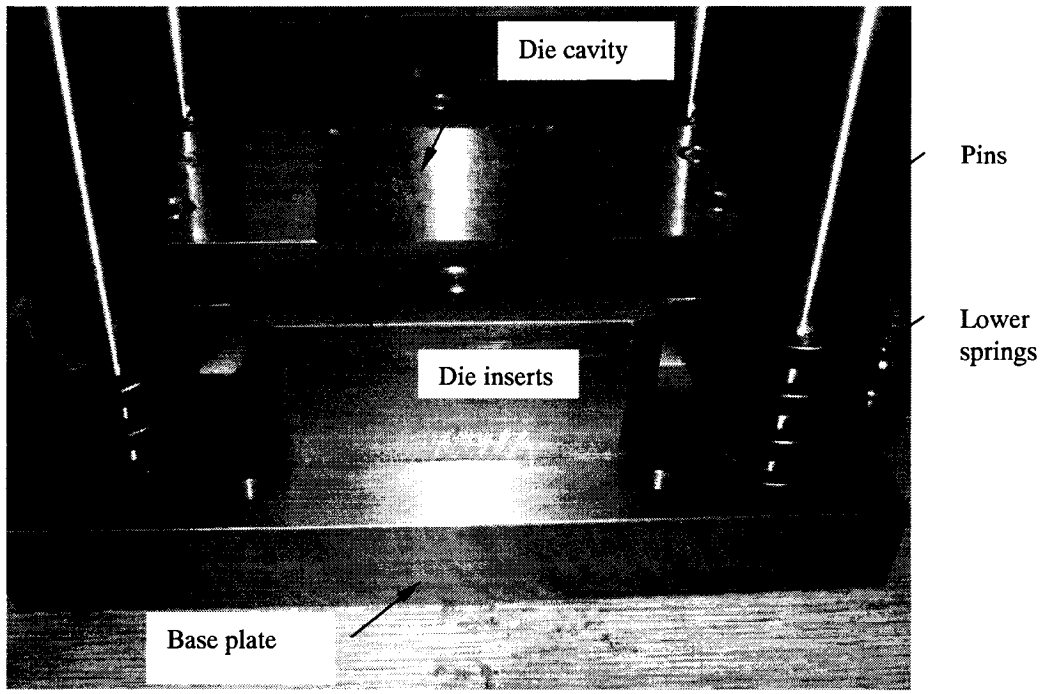

Fig. (3.9) The upper surface of the forming die

3.4.1.2. Fixture Mechanism

To produce the blank holding force using the fixture, the specimen is held between the die and the blank holder. The force required for this action is transmitted from the upper plate through the springs to the blank holder by plugging the lock pin in the punch, which causes the blank holding plate to move downward towards the upper surface of the die, where the specimen is placed, Fig. (3.9). This action will be resisted by the lower springs, which have a limited travel before contact of the platen onto the specimen. The amount of the blank holding pressure needed to overcome this resistance is subtracted from the reading of the load cell force to give the actual amount of the blank holding force acting on the specimen.

Continuing to press the upper platen will increase the blank holding force on the specimen until the desired force is reached. After that, the blank holding plate is held by tightening the four mounting bolts attached to the base plate and the upper plate to keep

the upper springs compressed, which maintains the blank holding force at the desired amount.

Afterward, the punch is moved upward leaving the three plates tightened together. Then, the lock pin is removed from the punch, so the punch is ready to be moved downward to perform the forming action, which is the draw-bending stage.

3.4.1.3. Experimental Setup

Test specimens were cut to the required size of 25.40 mm (1.00 in.) by 228.60 mm (9.00 in.) and carefully placed on the die. After inserting the specimen, the upper plate is pressed against the blank holder by means of the springs, while monitoring the force. Once the required blank holding force is reached, the upper plate is restrained by the four bolts to maintain the holding force as close to the specified value as possible.

The experiments were performed by moving the cross head at the speed of 0.0833 mm/sec to maintain the quasi-static conditions. The punch was moved down until its stroke reached 40 mm. Afterwards, the punch was moved up and the blank holding force was released. An illustration of the specimen after testing is shown in Fig. (3.10). Various blank holding forces, as will be described in the next chapter, were considered in the test scheme. Moreover, to examine the effect of anisotropy on springback, blanks with different orientation to the rolling direction were tested. Experiments were repeated for the minimum and the maximum blank holding force and the results are discussed in Chapter 4.

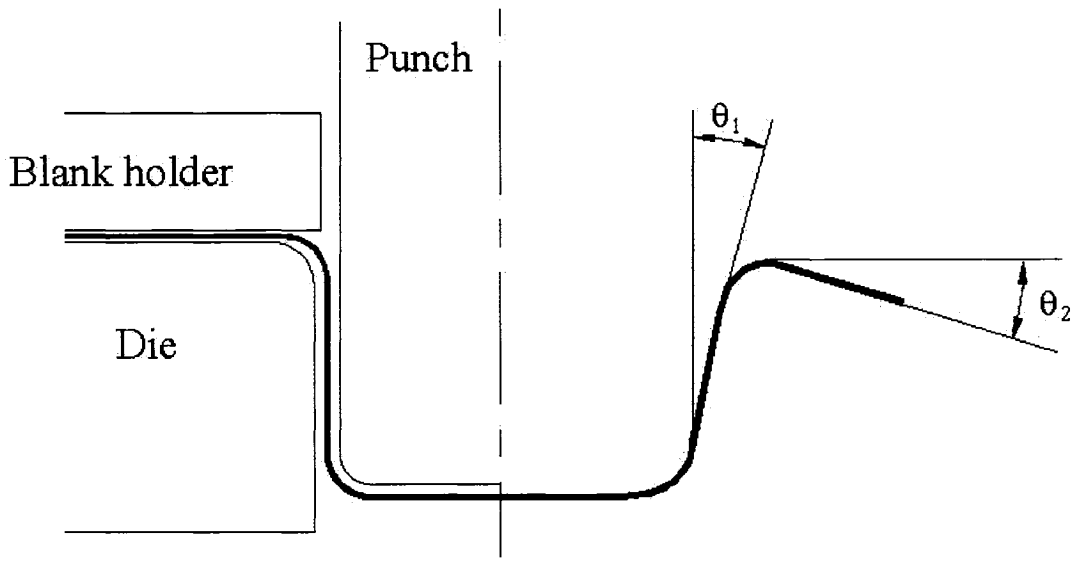

Fig. (3.10) Illustration of the draw-bending process and the springback angles after draw-bending.

3.4.1.4. Measurement Procedures

To measure the springback angles, meshed sheets with divisions of 10.00 mm by 10.00 mm in both directions were used to trace the specimens after the testing, as shown in Fig. (3.11). The angles were measured by means of a protractor with an accuracy of 5 minutes ($\approx 0.08^{o}$). Attention was paid to ensure the symmetry of angles on both sides of the specimen. The notation used to describe each springback angle is also shown in Fig. (3.11). Also, a point in the free portion between the punch and die radii was chosen, as accurately as possible, to be at the middle of this portion of the sample to measure the thickness of the tested specimens. The thickness was measured by means of a vernier caliper with an accuracy of 0.05 mm.

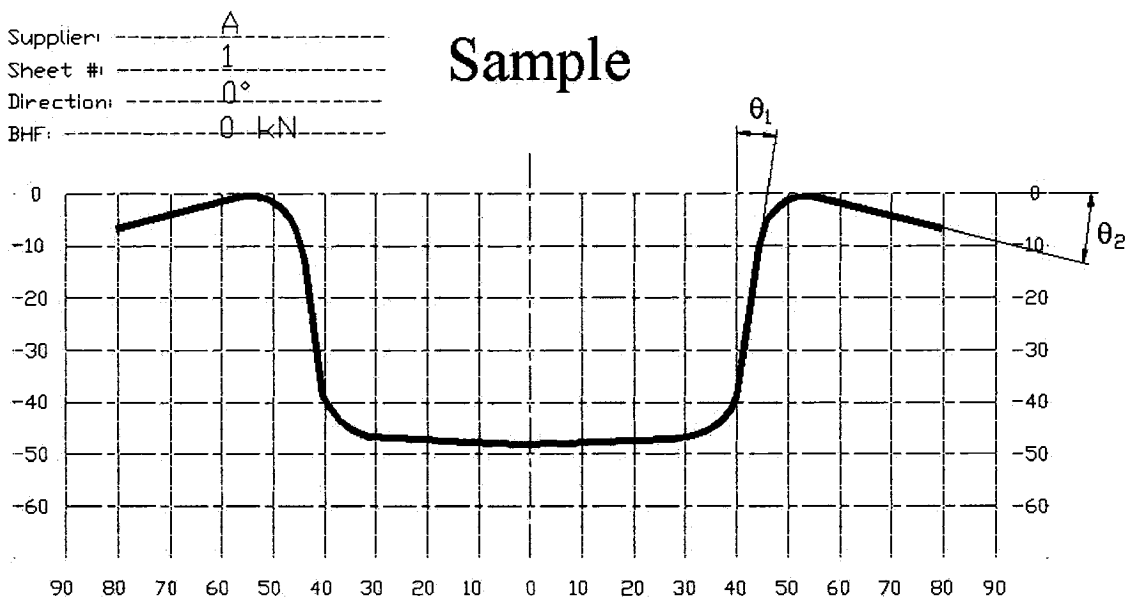

Fig. (3.11) Schematic illustration of the way used to measure the specimens' springback angles

3.4.2. Simple Bending Tests

To conduct the simple bending experiments, the fixture used for draw-bending was modified by changing the punch insert and the blank holder. An illustration of the simple bending process is shown in Fig. (3.12). Simple bending experiments were performed only for SS410 (thin), DP 600/300 (thin), and IN718 specimens since the springback angles would be more pronounced for these thinner sheets.

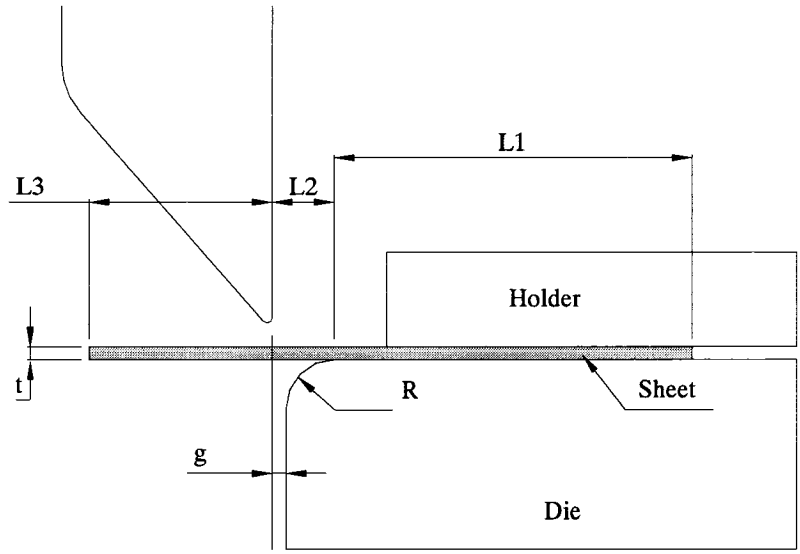

Fig. (3.12) Simple bending process, dimensions in mm

For the simple bending experiments, specimens of 127.00 mm (5.00 in.) by 25.40 mm (1.00 in.) were used. After the specimens were cut to the desired dimensions, the thickness was measured at five different locations along the length of the strip and the average thickness was used in the subsequent analysis. The effect of anisotropy was investigated by testing specimens cut at different angles to the rolling direction.

Because of the presence of the gap, g, between the punch and the die, the bending angle, θ_i, is less than 90°. An analytical formula, given in Eq. (3.1), based on the geometry of the sheet after bending, is solved iteratively to calculate the springback angle. The derivation of Eq. (3.1) is presented in Appendix (A).

$$L_2\left(1-\cos\theta_i\right)-L_3\cos\theta_i+\left(R+\frac{t}{2}\right)\theta_i\cos\theta_i-R\sin\theta_i-t\sin\theta_i=0 \qquad (3.1)$$

The springback angle, θ, is obtained from

$$\theta=\theta_i-\theta_f \qquad (3.2)$$

where θ_f is the final angle after springback.

Four different multiple bending stages took place in the experiments:

1- pure bending (B);
2- the bent specimens, (B) specimens, were flipped and bent in reverse (BR);
3- the BR specimens were bent one more time in the original direction (BRB);
4- finally the BRB specimens were bent in the reverse direction one more time (BRBR).

Figures (3.13) and (3.14) show the sequence on (B) and (BR) operations. Each set of experiments was repeated three times, not only to check the repeatability of the results but also to examine the deviation in the measurements with respect to the specimen's direction to the rolling direction. The angular measurements were performed using a protractor with an accuracy of 5 minutes (0.08^o).

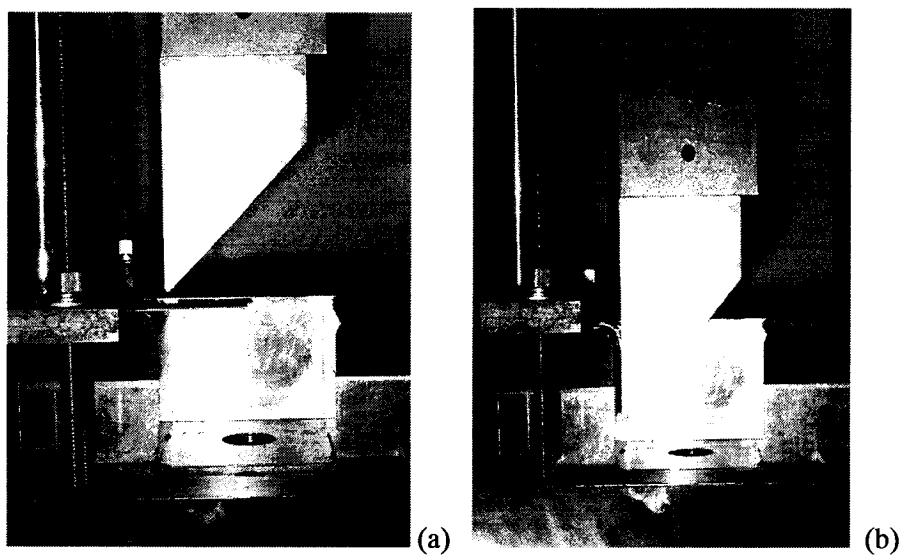

Fig. (3.13) Simple bending experiments, (a) Before bending, and (b) Bending (B),

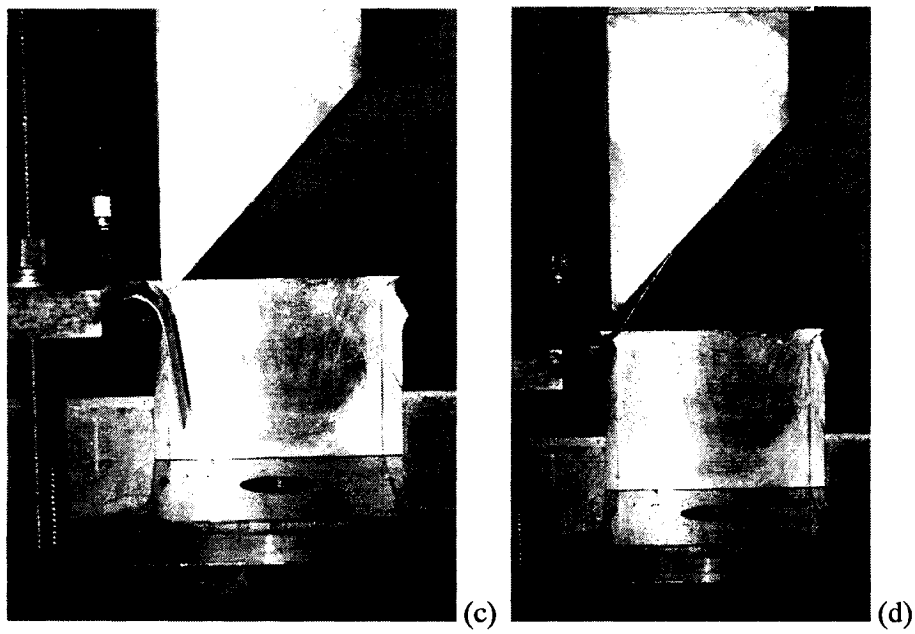

Fig. (3.14) Simple bending experiments, (a) Springback for B, and (b) Reverse bending (BR)

3.5. Experiments Summary

In this chapter, several types of experiments were discussed. Uniaxial tensile tests were conducted in order to obtain the stress-strain curves of the materials tested, as well as the anisotropic parameters in terms of the R-values. These parameters are to be used in the finite element model in order to simulate the material behaviour.

Additionally, as presented in Section 1.1, since many sheet forming processes involve loading, unloading, and reverse loading during the forming process, a test that captures the material behaviour in unloading and reverse loading is required. Therefore, uniaxial tension-compression tests were conducted. These tests are to be used to compare the experimental stress-strain curves to those obtained from the tension-compression finite element models and to validate the numerical results.

Moreover, in order to study the effect of material anisotropy on springback, without including other forming parameters, such as blank holding force, simple bending experiments are performed. Also, because the sheets experience bending and unbending during forming, the simple bending tests were performed in a manner so that a multiple bending process takes place, in which, the simple bending specimens were bent in the reverse direction. The process was repeated so that it covers four stages of bending and reverse bending, namely B, BR, BRB, and BRBR. These tests are to be used in comparing the experimental results to those obtained from the finite element simulations of the simple multiple bending tests and are used in validating the model.

Furthermore, in order to include the forming parameters, such as the blank holding force, and their effects, combined with the effect of material anisotropy, on the final springback angle, 2D draw-bending experiments were performed. These draw-bending experiments are to be used for comparing the springback angles, with respect to blank holding force as well as the material anisotropy, and the thickness of the formed specimens with those calculated by the 2D draw-bending simulations. The experiments are used as a tool to assess the dependency of the springback angles, and thickness, on the forming parameters and material anisotropy, as well as to validate the finite element model.

Finally, as a general summary, Tables (3.2) and (3.3) list all the experiments performed, and discussed, in this chapter along with the number of repeats each experiment was conducted. The discussions of the test results are presented in Chapter 4; moreover, the variations between the experimental results are presented in Appendix (B).

Table (3.2) List of uniaxial tension and tension-compression experiments performed

Experiment type	Material	Orientation	Number of test repeats
Uniaxial tension	SS410 (Thick)	0°	7
		45°	7
		90°	7
	SS410 (Thin)	0°	4
		45°	4
		90°	4
	DP600/300 (Thick)	90°	3
	DP600/300 (Thin)	90°	3
	DP600/400	90°	3
	IN718	0°	4
		45°	4
		90°	4
Uniaxial tension-compression	SS410 (Thick)	0°	3
		45°	3
		90°	3
	SS410 (Thin)	0°	4
		45°	4
		90°	4
	DP600/300 (Thick)	90°	3
	DP600/300 (Thin)	90°	3
	DP600/400	90°	3
	IN718	0°	4
		45°	4
		90°	4

Table (3.3) List of bending experiments performed

Experiment type	Material	BHF (kN)	Orientation	Number of test repeats
Simple-multiple-bending	SS410 (Thin)		0°	4
			45°	4
			90°	4
	DP600/300 (Thin)		90°	3
	IN718		0°	4
			45°	4
			90°	4
2D draw-bending	SS410 (Thick)	0	0°	3
			45°	3
			90°	3
		11	0°	3
			45°	3
			90°	3
		22	0°	3
			45°	3
			90°	3
	SS410 (Thin)	0	0°	3
			45°	3
			90°	3
		11	0°	3
			45°	3
			90°	3
	DP600/300 (Thick)	0	90°	3
		11		3
		22		3
	DP600/300 (Thin)	0	90°	3
		11		3
		22		3
	DP600/400	0	90°	3
		11		3
		22		3
	IN718	0	0°	3
			45°	3
			90°	3
		11	0°	3
			45°	3
			90°	3
		22	0°	3
			45°	3
			90°	3

CHAPTER 4

Experimental Results

4.1. Simple Tension Tests

During the tension test, the tensile force is recorded as a function of the displacement of the machine head. The deformation could be in the gage section or in one or both of the gripping areas. Therefore, force versus tensile displacement would be of a little value to accurately describe the material behaviour. As a result, a normalization with respect to specimen dimensions would lead to more accurate representation of the material response. Such that

$$\sigma_{eng} = \frac{F_i}{A_o} \tag{4.1}$$

where σ_{eng} is the engineering stress, F_i is the instantaneous tensile load measured by the load cell during testing, and A_o is the gage initial cross-sectional area.

The instantaneous engineering strain, ε_{eng}, can be obtained from the change in the gage – section length such that

$$\varepsilon_{eng} = \frac{L_i - L_o}{L_o} \tag{4.2}$$

where L_o and L_i are the initial and instantaneous gage length, respectively. The engineering strain is measured directly during the test by attaching an extensometer to the gage section. Accordingly, a record of the instantaneous force and strain is easily obtained while loading.

The engineering stress, Eq. (4.1), is calculated as a function of the initial area. However, the area of the gage section is changing while loading. Therefore, it is desirable to have the material behaviour in terms of true stress and true strain, so that

$$\sigma = \frac{F_i}{A_i} \tag{4.3}$$

where A_i is the instantaneous gage cross-sectional area when the force F_i is applied.

Since the elastic strains are very small compared to the plastic strains, then the change in volume caused by elastic deformation can be neglected (Khan and Huang, 1995). Moreover, since the plastic deformation is volume preserving, then the assumption of constancy of volume is held, so that $A_oL_o = A_iL_i$. This constancy of volume assumption is based on the experimental observations of Bridgman (Khan and Hunag, 1995). Therefore, using this constancy of volume assumption, the true stress and strain can be written as

$$\begin{aligned} \sigma &= \sigma_{eng}\left(1+\varepsilon_{eng}\right) \\ \varepsilon &= \ln\left(\frac{L_i}{L_o}\right) = \ln\left(1+\varepsilon_{eng}\right) \end{aligned} \tag{4.4}$$

In the current study, a 25.40 mm (1.00 in.) – gage extensometer was attached to the test specimens to measure the engineering length strain as the tensile load is applied. The engineering stress was calculated according to Eq. (4.1) and hence the true stress and strain were calculated according to Eqs. (4.4), respectively.

4.1.1. Effect of Specimen Orientation

For the SS410 thick specimens ($t \approx 1.575$ mm), it was observed that the stress-strain curves obtained from the different specimens' orientation are almost identical. Specimens showed consistency in their response with respect to the orientation to the rolling direction. It was observed that the 45° specimens experience larger stresses than the 0° and the 90° test specimens. Moreover, there was no significant difference between the behaviours of the later two directions. The tests were repeated for different sheets and the same observations were obtained. Figure (4.1) shows the true stress-strain curves for specimens tested from these sheets.

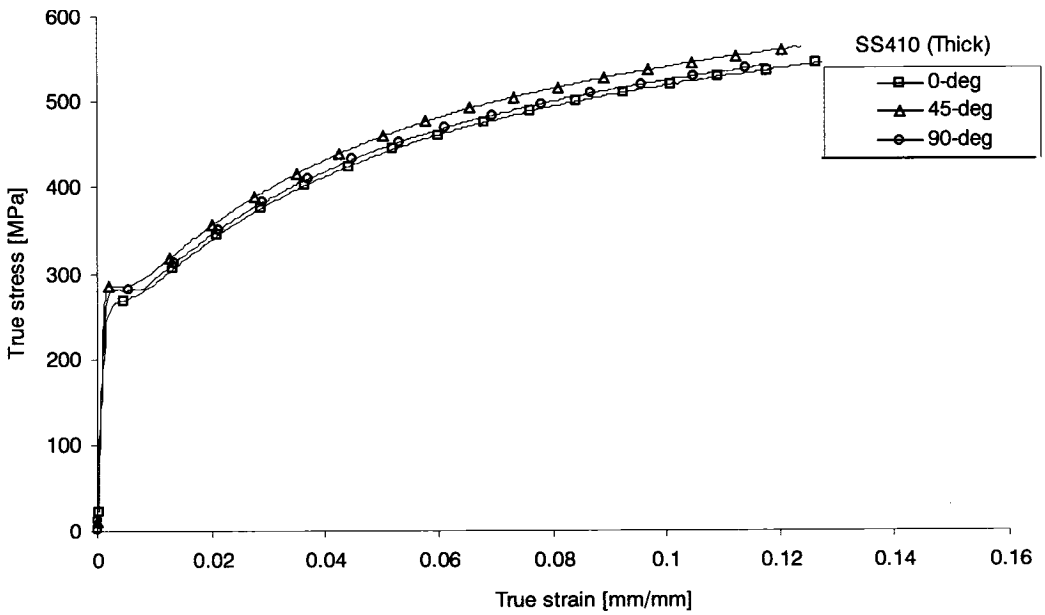

Fig. (4.1) Stress-strain curves for SS410 (thick) with different specimen orientations

The SS410 thin specimens (t ≈ 0.686 ~ 0.787 mm) exhibited behaviour, with respect to specimen orientation, almost the same as the other tested SS410 thick sheets. Again, it was observed that the 45° specimens experience larger stresses than the 90° and the 0° specimens for all the sheets tested. Figure (4.2) shows the stress-strain curves for specimens tested from these sheets; the experimental variations for the uniaxial tests are listed in Appendix (B1). It was also observed that these specimens did not have noticeable lower and upper yield points as in the thicker sheets from the same material.

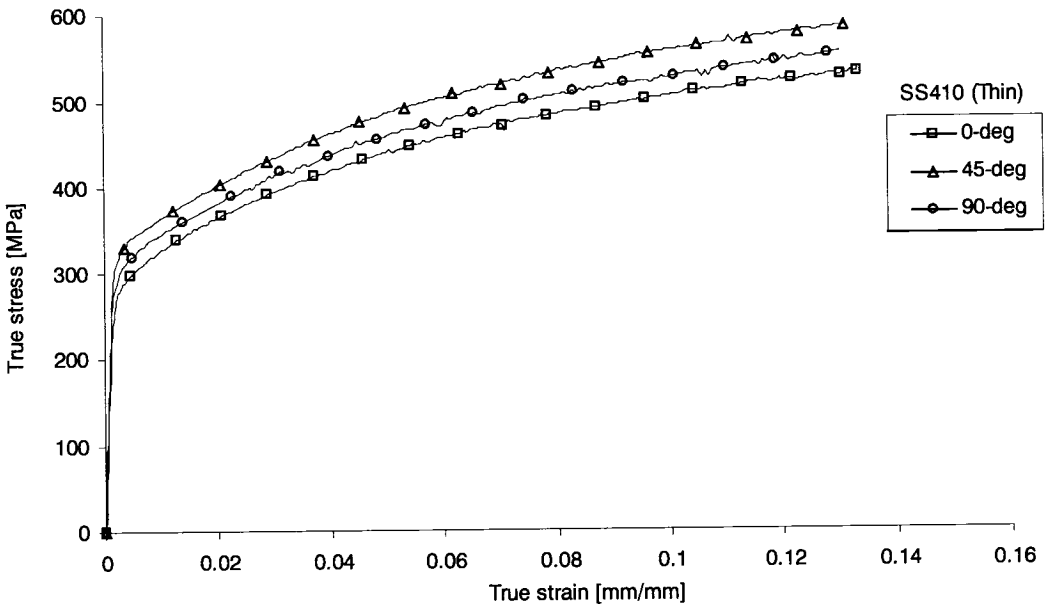

Fig. (4.2) Stress-strain curves for SS410 (thin) with different specimen orientations

As reported in several studies about DP steels 600/300 and DP 600/400 (Ray, 1986, Schedin and Melander, 1987, Sakaki *et al.*, 1990, Nakamachi *et al.*, 2001, and Xie and Nakamachi, 2002), the orientation to the rolling direction does not have a significant effect on the material behaviour, i.e. almost perfectly isotropic material. Therefore, the DP sheets tested (t ≈ 1.045 ~ 1.741 mm) in this study were assumed to be isotropic and hence the effect of orientation was neglected and, therefore, not presented in this section. The stress – strain curves for the tested sheets will be shown later in Section 4.1.3.

As for the IN718 specimens (t ≈ 0.633 ~ 0.653 mm), it was observed that the 45° specimens experience lower stresses than stresses calculated for the other two directions. On the other hand, the 0° and the 90° specimens showed almost identical behaviour. This was also observed in the test repeats for other sheets of this material. Figure (4.3) shows the stress-strain curves for the IN718 tested specimens.

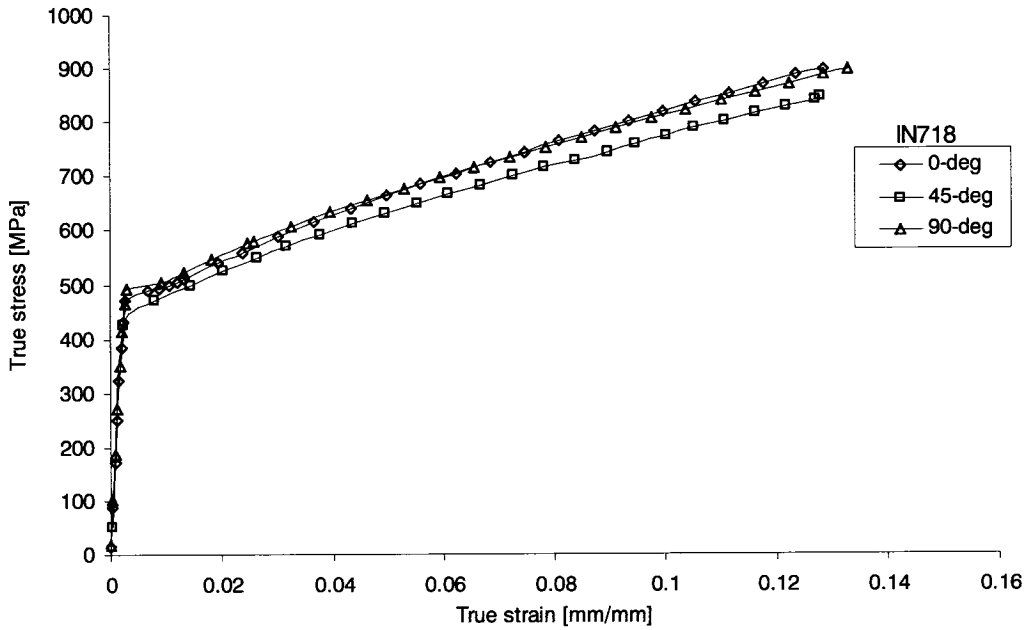

Fig. (4.3) Stress-strain curves for inconel 718

Different specimens at the same direction to rolling were prepared and tested from the sheets and the effect of specimen orientation on the yield stress was studied. The yield stress of the specimen was obtained from the stress – strain curve at a strain offset of approximately 0.002 and was determined as the average of the yield stresses obtained at the same direction from the repeated tests. Table (4.1) along with Fig. (4.4) show the variation of the yield stresses of SS410 and IN718, with respect to the specimen orientation.

From Figs. (4.1) to (4.4), it is shown that the difference in mechanical properties in terms of stress–strain with respect to the specimen orientation is relatively small. Also, as

shown in Table (4.1), the difference in yield stresses with respect to the orientation varies from approximately 6.00% to 9.00% for the different materials. As mentioned in Section 2.5, it was reported that it is common to have a 10% variation in the yield stress for sheets tested from the same batch (Lindkvist and Lindbäck, 2004). Therefore, average values can be considered for the sheets, as will be discussed in Section 4.1.3. The experimental variations for the performed uniaxial tests are presented in Appendix (B1).

Table (4.1) Tensile yield stresses

Material	Thickness (mm)	Orientation	Tensile yield stress (MPa)	Difference % $\frac{\sigma_Y\|_{max} - \sigma_Y\|_{min}}{\sigma_Y\|_{max}} \times 100$
SS410 (Thick)	1.575	0°	265	7.02
		45°	285	
		90°	280	
SS410 (Thin)	0.686 ~ 0.787	0°	295	9.23
		45°	325	
		90°	315	
IN718	0.635 ~ 0.661	0°	480	6.00
		45°	470	
		90°	500	

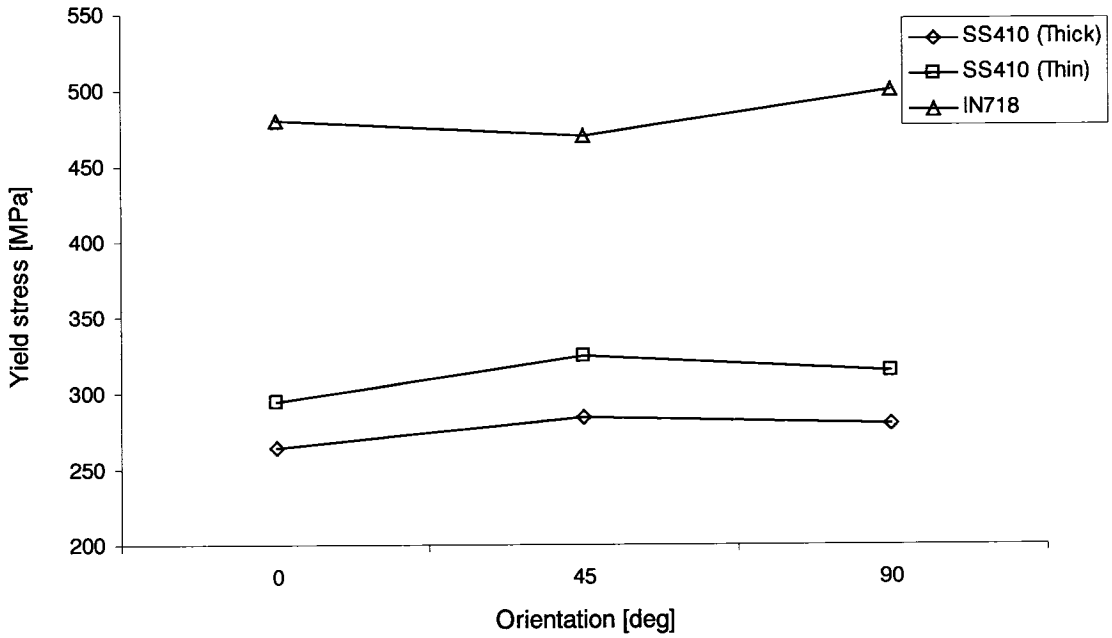

Fig. (4.4) Effect of specimen orientation on the yield stress for SS410 and IN718 sheets

4.1.2. Sheet Anisotropy

Directional properties of sheet metals produced by rolling arise from the orientation of grains. Therefore, the plastic properties of rolled sheets differ from the through-thickness direction and vary with orientation in the plane of the sheet (Lee and To, 1995).

As mentioned in Section 2.2, at a given angle (φ) to the rolling direction, the anisotropy of the sheet is characterized by the plastic strain ratio, R-value, R_φ. Recalling Eq. (2.11) and substituting $\varepsilon_l = \ln\left(\frac{L}{L_o}\right)$ and $\varepsilon_w = \ln\left(\frac{W}{W_o}\right)$, R_φ can be obtained from

$$R_{\varphi} = \frac{-\ln\left(\frac{W}{W_o}\right)}{\ln\left(\frac{L}{L_o}\right)+\ln\left(\frac{W}{W_o}\right)} \tag{4.5}$$

In this study, L_o and L are the initial and final gage length, respectively, which are measured using a digital caliper with an accuracy of approximately 0.025 mm. W_o and W are the initial and final width, respectively, which are measured using a digital micrometer with an accuracy of approximately 0.005 mm. Hence, the normal anisotropy parameter, $\overline{R}$, and the planar anisotropy parameter, ΔR, can be calculated from Eqs. (2.12) and (2.13), respectively.

Mellor (1982) reported that experimental results for a Ti-115 specimen, loaded uniaxially along the rolling direction, showed that the R-value, R_{φ}, is constant in the elastic region, rapidly changes at yielding, and becomes constant again after a certain strain.

Moreover, Schedin and Melander (1987) reported that the plastic anisotropy parameters, $\overline{R}$ and ΔR, were determined at a true strain of approximately 0.15. Furthermore, Gilmour *et al.* (2004) also reported that the R-values determined near a uniform strain limit between 0.02 and 0.13, consistently produce the most accurate model results irrespective of the calibration method.

In this research, the R-values for the tested sheets were calculated at the end of the extensometer range, i.e. engineering strain of approximately 0.14. Table (4.2) lists the R-values for each sheet, the normal anisotropy parameter, $\overline{R}$, and the planar anisotropy parameter, ΔR. It was observed that, for the SS410 specimens, there is a considerable variation in the anisotropy parameters between thick and thin sheets, which might have an effect during the forming process. For the DP Steels, as mentioned in Section 4.1.1, the anisotropic behaviour was neglected since the average R-value was reported close to 1.00 (Ray, 1986, Schedin and Melander, 1987, Sakaki *et al.*, 1990, Nakamachi *et al.*, 2001, and Xie and Nakamachi, 2002). On the other hand, for the IN718, there is a

considerable variation in the directional properties of the sheets. Moreover, the value of the average R-value, $\overline{R} = 1.55$, cannot be neglected. This means that the strain ratios are not the same when the specimens are deformed, which also indicates the relatively high anisotropic behaviour of that material, when compared to the other materials in this study, as well as other materials such as high strength steel ($\overline{R} = 0.94$), deep drawing quality steel ($\overline{R} = 1.14$), and aluminum ($\overline{R} = 0.8$).

A graphical representation of the values listed in Table (4.2) is shown in Fig. (4.5). It is shown that the anisotropy parameter for the SS410 sheets varies around the value of 1.0 for the three orientations. However, for the IN718, it is shown that the value of directional anisotropy decreases with the increase in the angle of orientation to the rolling direction. Also, the SS410 thin sheets experience the highest planar anisotropy, ΔR, while the rest of the materials slightly deviate around the 0.5 value. Moreover, for the normal anisotropy parameter, $\overline{R}$, it is shown that SS410 thin sheets and IN718 experience the highest anisotropic behaviour among the other sheets.

Table (4.2) *R*-values for the tested sheets

Material	Thickness (mm)	Directional anisotropy parameters	Average anisotropy parameters
SS410 (Thick)	1.575	R_0 = 0.9193 R_{45} = 0.7975 R_{90} = 1.4533	$\overline{R}$ = 0.9919 ΔR = 0.3888
SS410 (Thin)	0.686 ~ 0.787	R_0 = 1.2938 R_{45} = 0.7555 R_{90} = 2.0172	$\overline{R}$ = 1.2055 ΔR = 0.9000
DP 600/300 (Thick) DP 600/300 (Thin) DP 600/400	1.741 1.045 1.700	N/A	$\overline{R}$ = 0.92 ~ 1.04 ΔR = 0.42 ~ 0.60
IN718	0.635 ~ 0.661	R_0 = 2.5182 R_{45} = 1.3051 R_{90} = 1.0632	$\overline{R}$ = 1.5479 ΔR = 0.4857

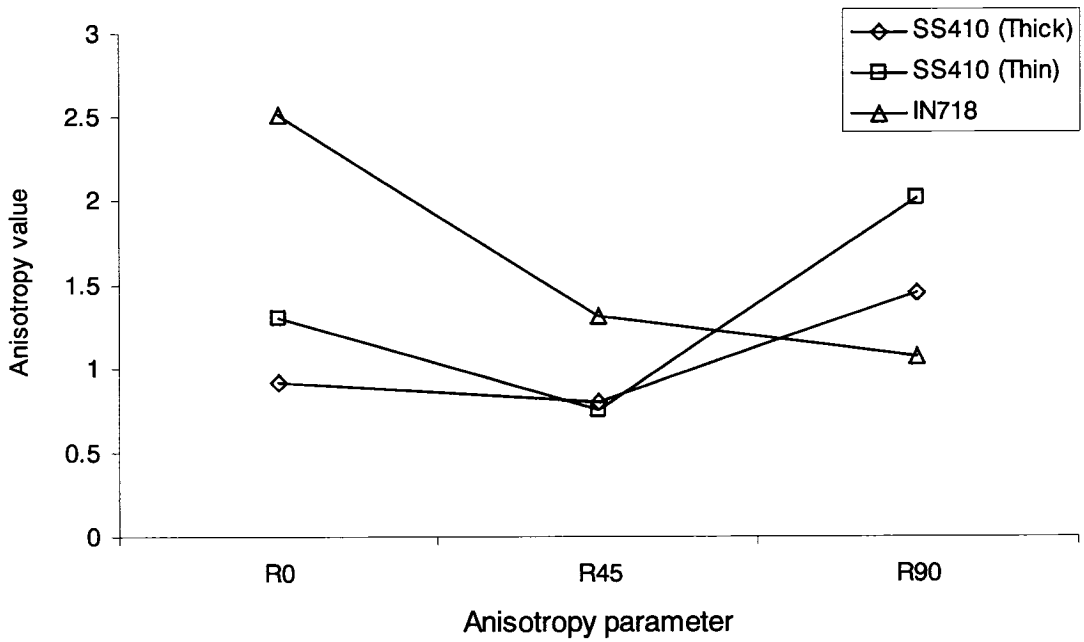

Fig. (4.5) Directional anisotropy parameters for SS410 and IN718 sheets

4.1.3. Constitutive Relations

Stress-strain curves for many metals can be approximated mathematically by power-law hardening (Han, 1992),

$$\sigma = K\varepsilon^n \tag{4.6}$$

where n is the strain-hardening exponent and K is the strength coefficient. K and n are material properties and, accordingly, can be used to compare the mechanical behaviour of the sheets. To determine K and n for each sheet, a best fit curve was constructed using EXCEL®. The best fit curves were constructed using the average stress-strain curves of the three directions (0°, 45°, and 90°) for the tested specimens. The average values were calculated as

$$\text{Average stress} = \frac{\sigma|_0 + \sigma|_{45} + \sigma|_{90}}{3}$$
$$\text{Average strain} = \frac{\varepsilon|_0 + \varepsilon|_{45} + \varepsilon|_{90}}{3} \tag{4.7}$$

where $\sigma|_\varphi$ and $\varepsilon|_\varphi$ represent the true stress and true strain with respect to the angle φ to the rolling direction, respectively. These average curves are used subsequently in the numerical implementation, along with the hardening parameters K and n.

Figures (4.6) and (4.7) show the average stress-strain curves for the SS410 and IN718 tested sheets, respectively. Figure (4.8) shows a comparison between the tensile stress-strain curves for the DP steels tested sheets. Values of K and n were obtained from the curve fit of the sheets and are listed in Table (4.3).

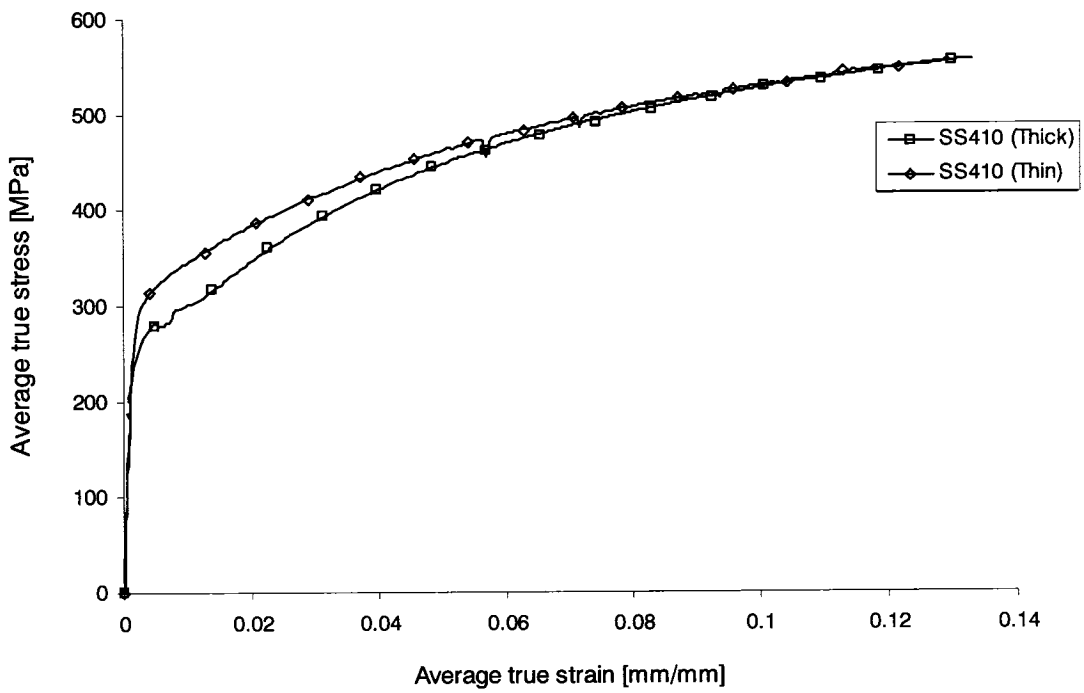

Fig. (4.6) Average stress-strain curves for SS410 tested sheets

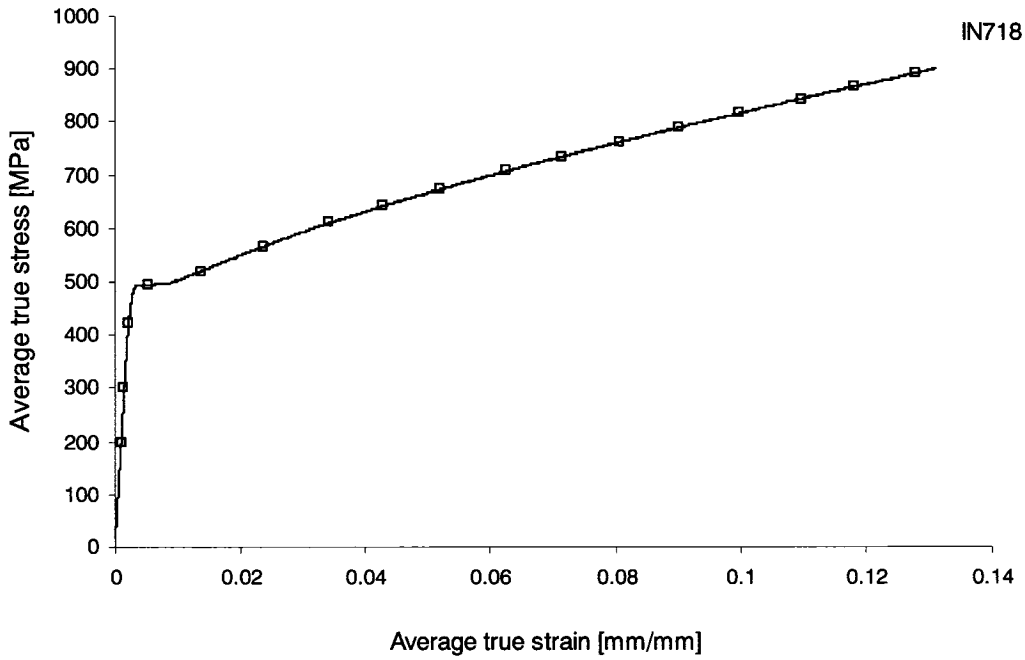

Fig. (4.7) Average stress-strain curve for IN718

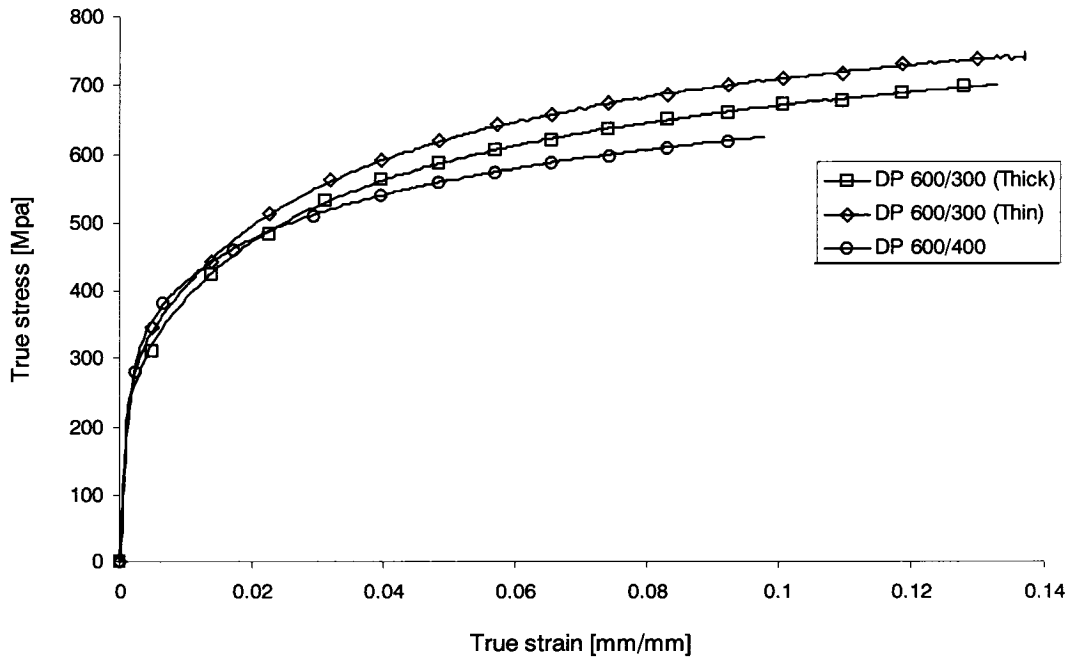

Fig. (4.8) Stress-strain curves for the three DP sheets tested

Table (4.3) List of material properties

Material	Thickness (mm)	K (MPa)	n
SS410 (Thick)	1.575	933	0.248
SS410 (Thin)	0.686 ~ 0.787	841	0.200
DP 600/300 (Thick)	1.741	1164	0.236
DP 600/300 (Thin)	1.045	1214	0.231
DP 600/400	1.700	987	0.190
IN718	0.635 ~ 0.661	1568	0.276

For the SS410 sheets, it was found that the n value for the SS410 thick sheets is higher than that of the thin sheets, which indicates lower hardening of the later sheet, as observed from the experiments.

In the case of DP steels, the difference between the K values for the thick and thin DP 600/300 sheets is not significantly large, which also indicates that these sheets have similar tensile properties. In the case of DP 600/400 sheets, the K and n values are significantly smaller than those for the DP 600/300.

As mentioned in Section 4.1.1, the effect of orientation on the yield stress is relatively small and, therefore, an average value of the yield stress from the three orientations can be used to characterize the material. Table (4.4) lists the average values of the tensile yield stresses of the materials tested in this study. From this point onward, these values will be referred to as the yield stress of the materials included herein.

Table (4.4) Yield stresses of the tested materials

Material	Thickness (mm)	Average tensile yield stress (MPa)
SS410 (Thick)	1.575	275
SS410 (Thin)	0.686 ~ 0.787	310
DP 600/300 (Thick)	1.741	295
DP 600/300 (Thin)	1.045	320
DP 600/400	1.700	335
IN718	0.635 ~ 0.661	480

4.2. Uniaxial Tension-Compression Tests

The 25.40 mm (1.00 in.) – gage extensometer was attached to the test specimens, as described in Section 3.2, to measure the instantaneous engineering length strain as the load is applied. Equation (4.1) is used to calculate the engineering stress, σ_{eng}, and Equations (4.4) are used to calculate the true stress and true strain, σ and ε, respectively. In these tests, the specimens were strained up to approximately 2.5% true strain in tension and the anti-buckling device, explained in Section 3.3, was used when applying the compressive loads. For SS410 and IN718 specimens, tension-compression tests were carried out for the different directions to the rolling, namely 0°, 45°, and 90°. In the case of the DP steels, specimens only in the transverse direction, 90°, were tested. Figures (4.9) to (4.12) show the stress-strain curves for the tested sheets.

As shown in Fig. (4.9), the SS410 thick sheets exhibit almost the same behaviour for the three directions. The slight concave shape in the curves can be attributed to the fact that the material has upper and lower yield points and that is the region that follows the material yielding before the uniform increase in the true stress. On the other hand, as mentioned in Section 4.1.1, SS410 thin sheets do not have upper and lower yields; therefore, as in Fig. (4.10), the region after yielding appears to be uniform. It is worth

mentioning that this behaviour does not appear in the compression stage and the materials exhibit rapid work hardening after yielding in compression.

For the DP steels, Fig. (4.11), it is shown that all the sheets tested experience uniform (smooth) loading and unloading behaviour. The yield in compression is relatively low and rapid work hardening takes place. In general, the three sheets exhibit a similar behaviour in tension and in compression.

Finally, for the IN718, Fig. (4.12), it is shown that the specimens tested in the three directions have almost the same behaviour and the effect of orientation does not have a serious effect. Again, a slight concave shape in the curve appears in the small region after yielding, which can be attributed to the same reason as in the SS410 thick sheets.

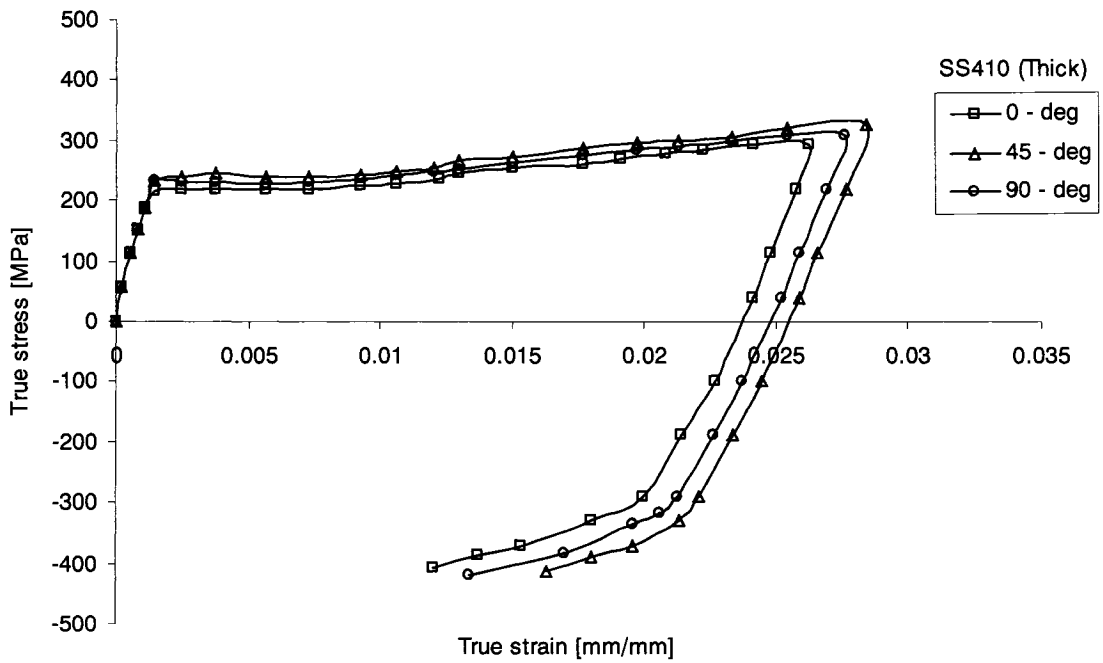

Fig. (4.9) Stress-strain curves for tension-compression tests of SS410 (thick) sheets

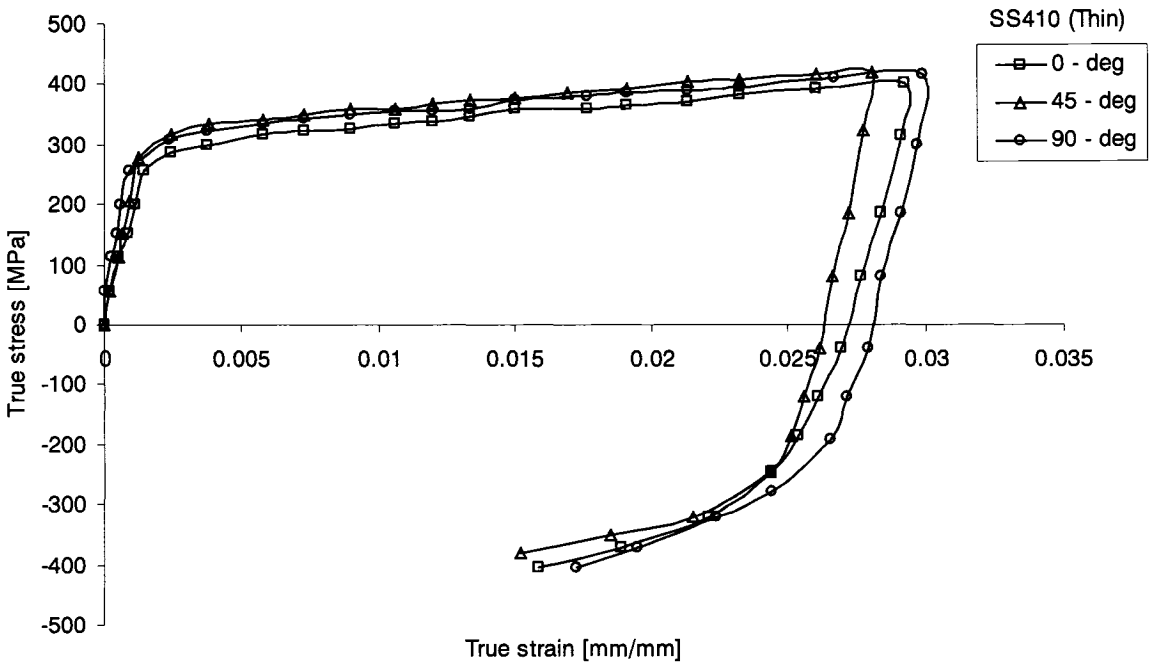

Fig. (4.10) Stress-strain curves for tension-compression tests of SS410 (thin) sheets

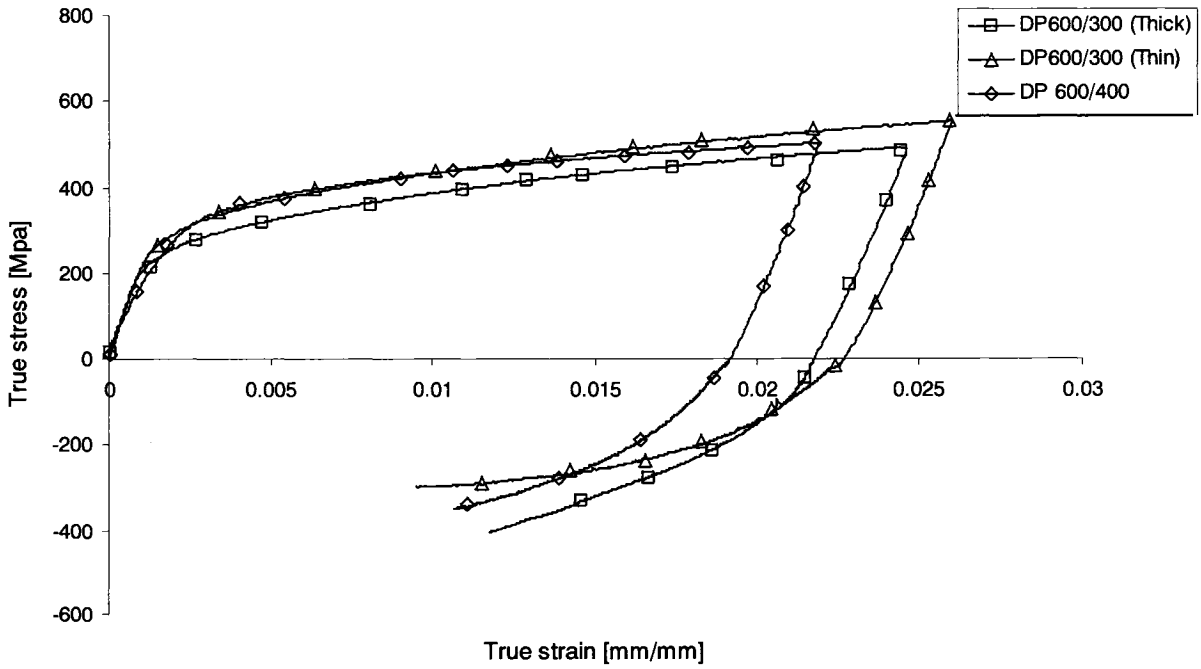

Fig. (4.11) Stress-strain curves for tension-compression tests of DP sheets

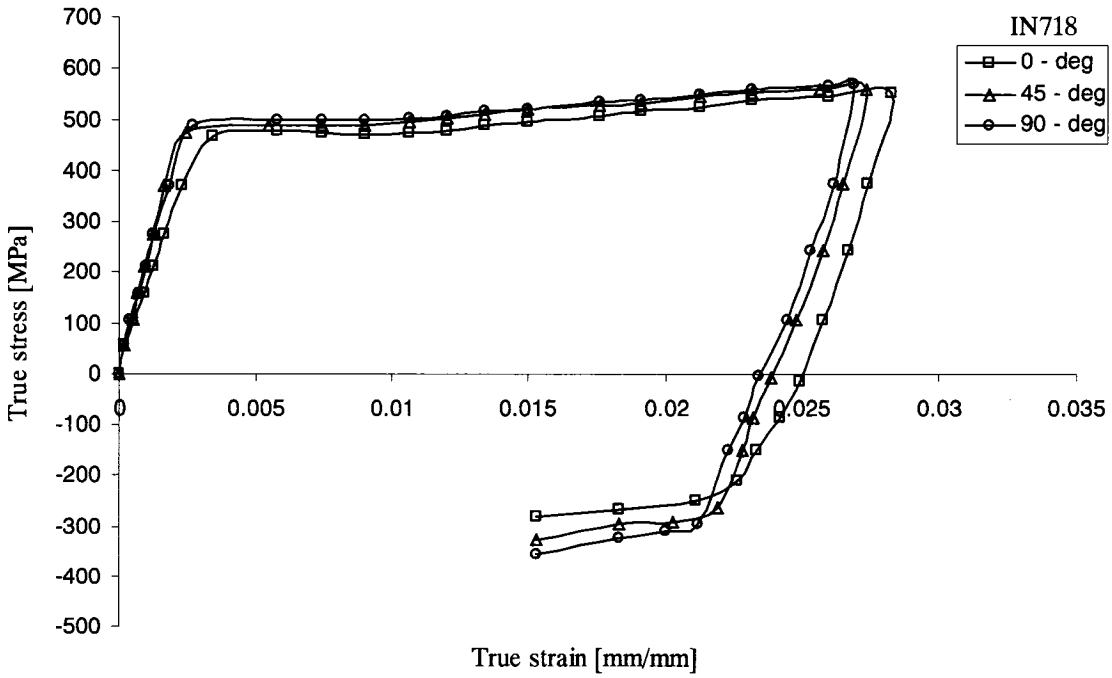

Fig. (4.12) Stress-strain curves for tension-compression tests of IN718 sheets

In a similar manner to the tensile tests, an average curve is constructed for each of the SS410 sheets and the IN718 sheets. The average stress-strain curves for the three orientations were obtained for both materials and shown in Figs. (4.13) and (4.14). As mentioned in Section 4.2, the average values are used later in Chapter 5 to compare the material behaviour obtained from the simulations to those obtained experimentally.

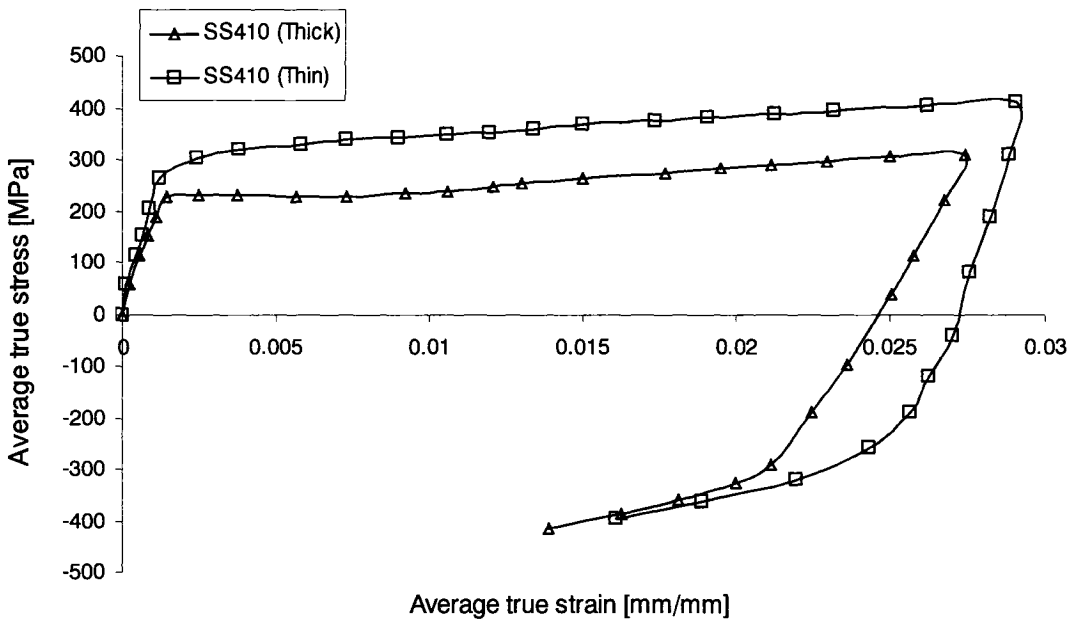

Fig. (4.13) Average stress-strain curves for tension-compression tests of SS410 sheets

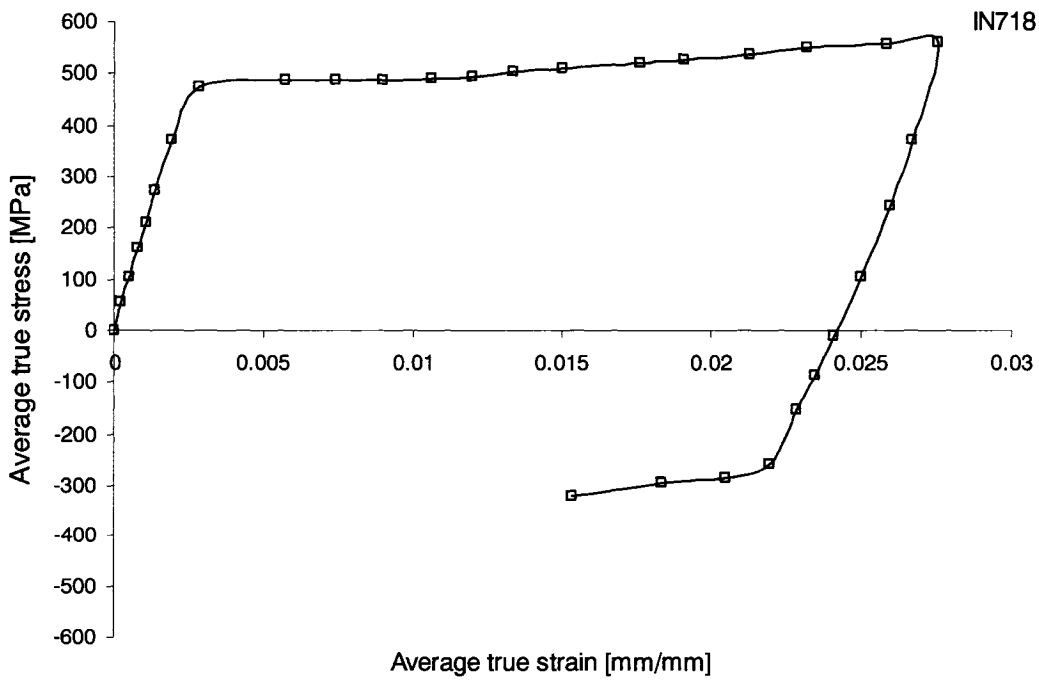

Fig. (4.14) Average stress-strain curves for tension-compression tests of IN718 sheets

4.3. Simple Bending Results

Because the springback is more pronounced in thin sheets, simple bending experiments were conducted only on thin sheets. As discussed in Section 3.4.2, each specimen was deformed in a series of multiple bend procedures, B, BR, BRB, and BRBR. The effect of orientation was also studied for all the specimens. Each set of experiments was repeated at least three times to examine the accuracy and repeatability of the test data. The value of the final springback angle after bending was obtained according to Eq. (3.1). All values of the springback angles for the different test sets are listed in Appendix (B2). Table (4.5) lists the average values of the springback angles obtained from all sets. Herein, these values will be referred at as the springback angles in simple bending.

Table (4.5) Springback angles for simple bending with respect to specimen orientation

Material	Orientation	Springback angle (deg)			
		B	BR	BRB	BRBR
SS410 (Thin)	0°	12.23	12.83	13.00	13.27
	45°	12.06	12.84	12.56	12.86
	90°	12.67	13.01	13.01	13.65
	Average	12.32	12.89	12.86	13.26
IN718	0°	21.99	23.03	23.53	24.24
	45°	22.22	23.55	23.93	24.64
	90°	22.22	23.32	24.18	24.57
	Average	22.14	23.30	23.88	24.48

In all cases, it was found that the deviation between the measured springback angles for each specimen's orientation (0°, 45°, 90°) is almost the same as the deviation between the angles measured of the same orientation for the different sets, as shown in Fig. (4.15). This finding draws the primary conclusion that the effect of sheet anisotropy on the springback angle is not very significant for the tested steel sheets. Moreover, the change of angle with respect to the bending process changes only slightly, which also draws the

conclusion that the Bauschinger effect, regardless of its presence, does not have a significant effect on the springback angles.

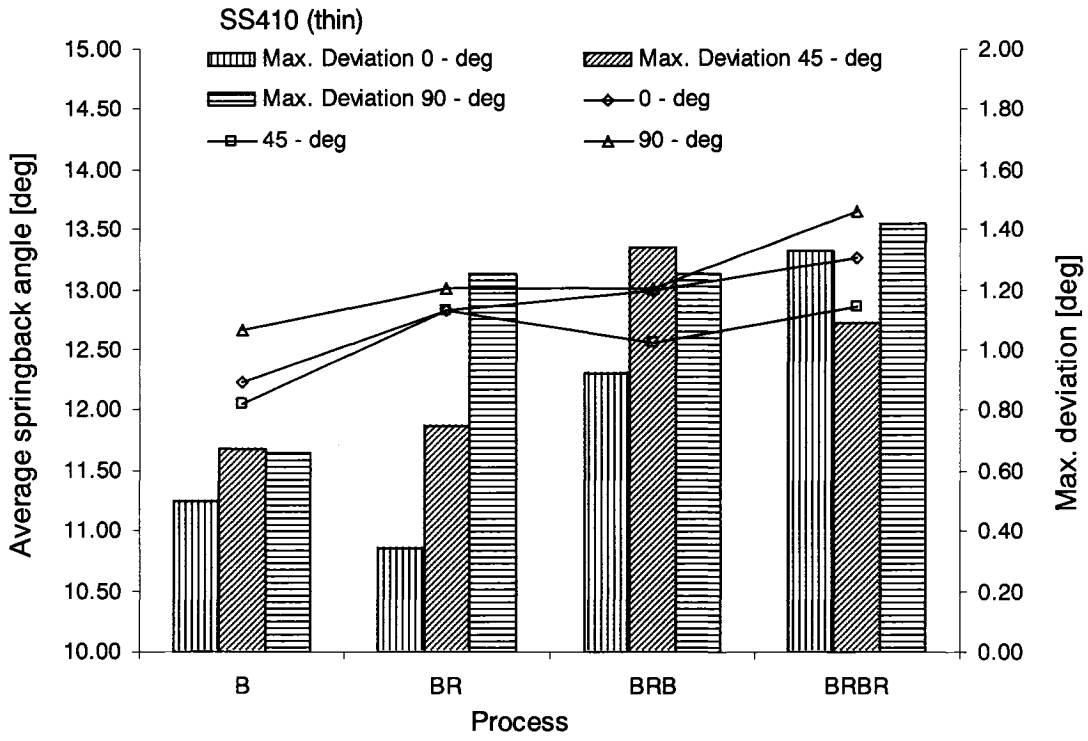

Fig. (4.15) Average springback angles with the maximum deviation between the measurements for simple bending processes of SS410 thin specimens

For the IN718 specimens it was observed that the change in specimen orientation did not highly affect the change in the springback angle, Fig. (4.16). However, it was observed that the springback angle slightly increases with the increase of deformation stage, the multiple bend. The angle is neither as constant as the SS410 thin specimens, nor decreasing as in some aluminum alloys as reported by Gau and Kinzel (2001). This finding, for the IN718, draws the attention of the importance of the accurate characterization for this material, especially when reversing the load direction.

Additionally, it is worth mentioning that it was noticed that the maximum deviation in the 45° specimens in the BRB process is high; this can be attributed to the variability in different portions of the sheet itself that took place where the specimen was cut. Experimental variations for the simple bending experiments are calculated and listed in Appendix (B2).

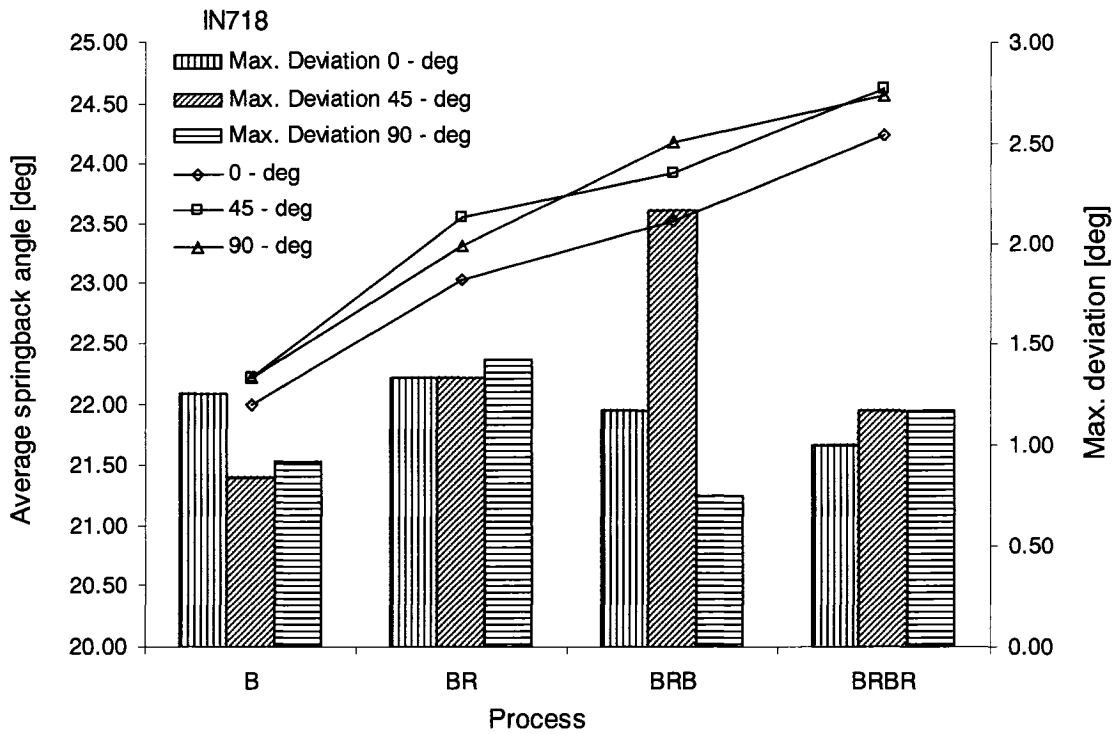

Fig. (4.16) Average springback angles with the maximum deviation between the measurements for simple bending processes of IN718 specimens

Finally, the average of the springback angles for each process for the three materials are plotted and shown in Fig. (4.17). It is shown that the stainless steel and the DP steel specimens experienced relatively close and steady springback angles, between 12.00° and 14.00°, with a difference of about 1.00°. However, in the case of IN718, the springback angles are large, in the range of 22.00° to 25.00°, and increasing with the deformation

process with a difference of about 2.50°. This again draws the attention of better characterization in order to accurately predict the springback angles for this material.

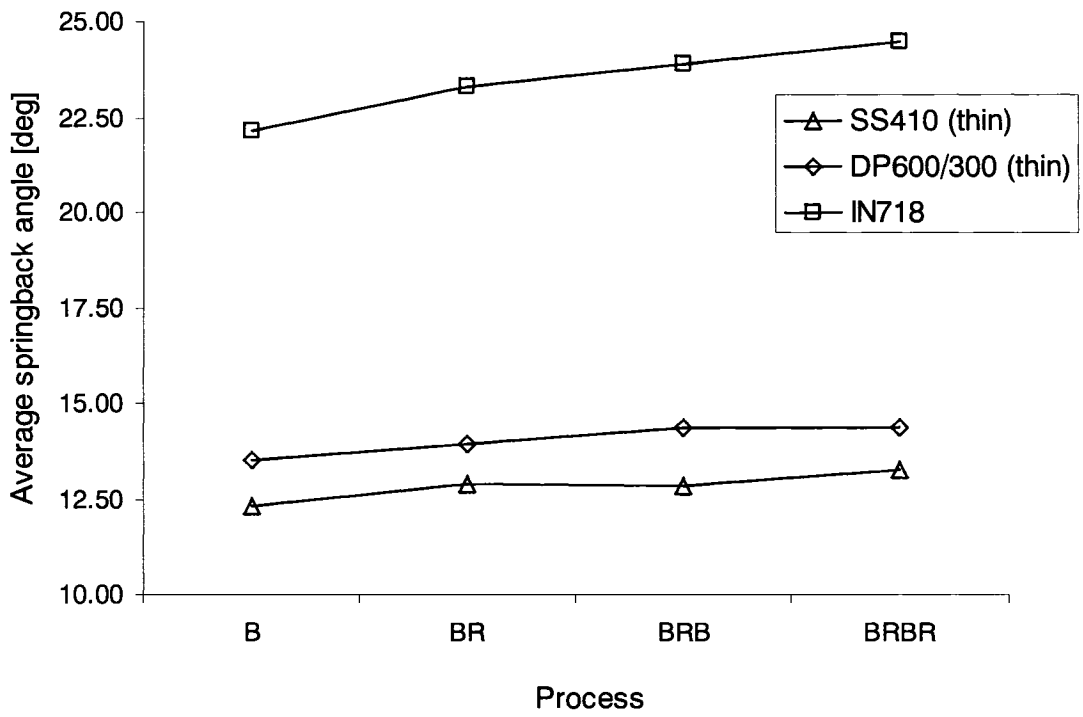

Fig. (4.17) Average springback angles for the multiple bending processes for the three tested materials

4.4. Draw Bending Results

In the draw bending experiments, two main issues were studied; the effect of specimen orientation to the rolling direction and the effect of blank holding force. The effect of both parameters on the required forming load, springback angles, and specimen thickness change was examined and explained in the following sections.

4.4.1. Effect of Orientation and BHF on Forming Loads

To examine the effect of specimen orientation on the required forming load, 25.40 by 228.60 mm (1.00 by 9.00 in.) strips at different orientations (0°, 45°, and 90°) with respect to the rolling direction were cut from the sheets. Specimens were tested at minimum and maximum blank holding forces.

4.4.1.1. SS410 Sheets

Figure (4.18) shows the load versus displacement curves for the thick SS410 specimens; it is clear that for the 0 kN BHF, only bending, there is almost no difference in the required force with respect to the specimen orientation. The only observation is that, for the specimens tested under 22 kN, the 45° specimens required slightly less force to be deformed.

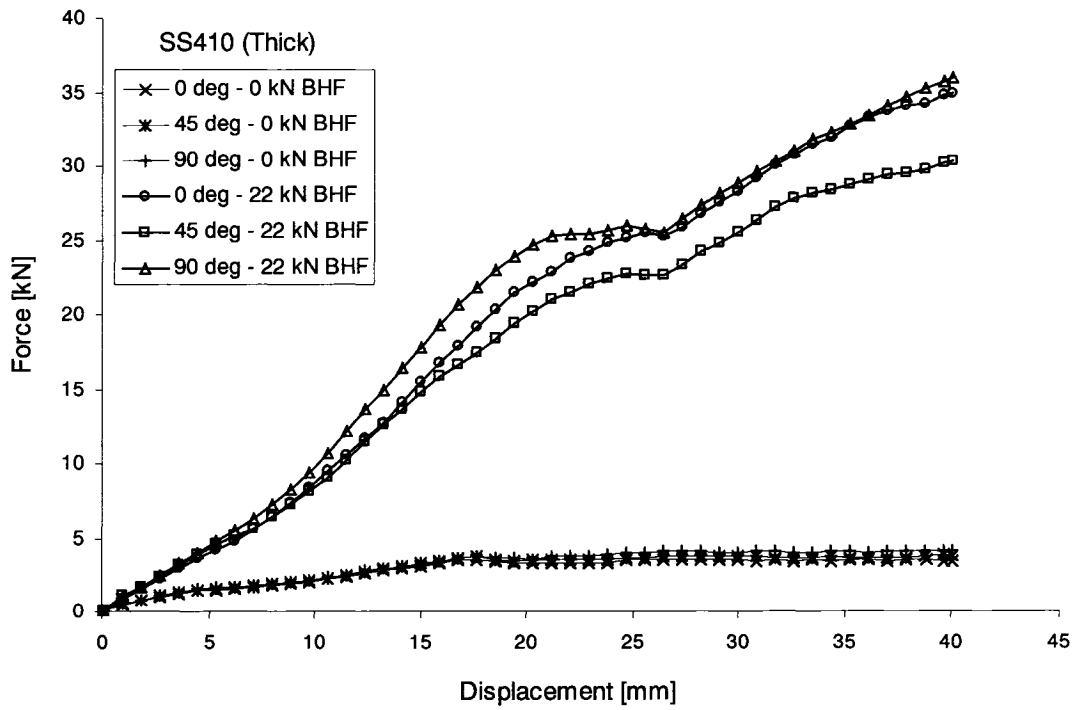

Fig. (4.18) Effect of orientation on forming load for minimum and maximum BHFs for thick SS410 specimens

When the SS410 thin specimens were tested under the maximum BHF, 22 kN, all specimens experienced failure in very early stages of the draw-bending operation. Also, all specimens failed under a BHF of 16.5 kN, as shown in Figs (4.19) and (4.20); therefore, the maximum BHF applied to the SS410 thin specimens was 11 kN.

Figure (4.21) shows the force versus displacement curves for the minimum and maximum BHF (0 and 11 kN) for the thin SS410 specimens. No significant difference between the curves for different orientations can be noticed. From these results and previous findings, it can be concluded that specimen orientation has a minimal effect on the material behaviour for the SS410 specimens, both thick and thin ones, and hence ignoring it in the numerical simulations will not have a significant effect on the results.

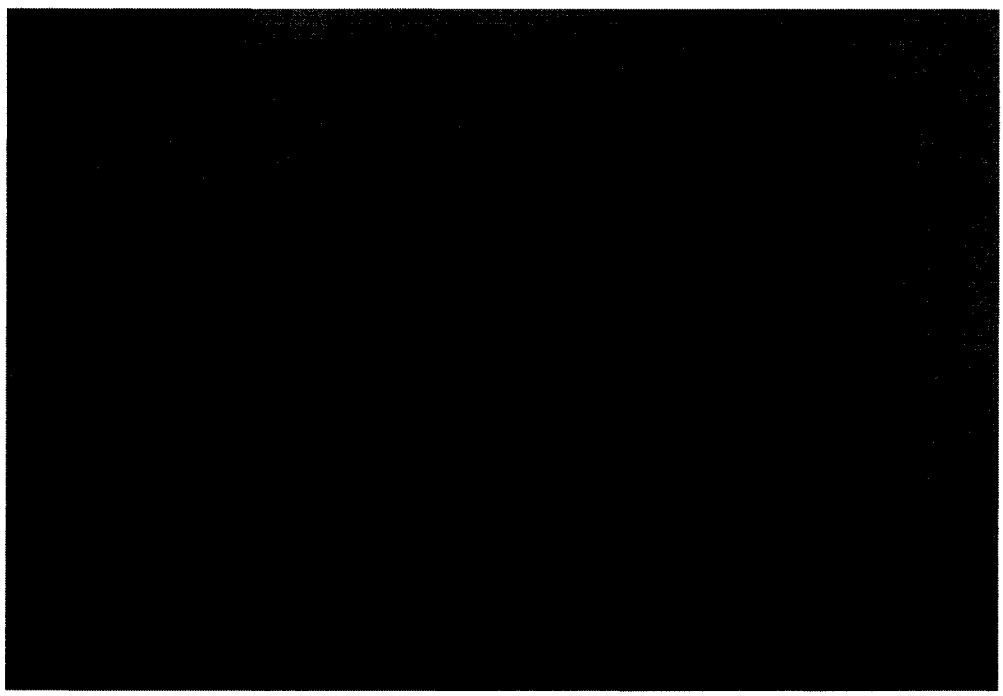

Fig. (4.19) Failure in the thin SS410 specimen under 16.5 kN

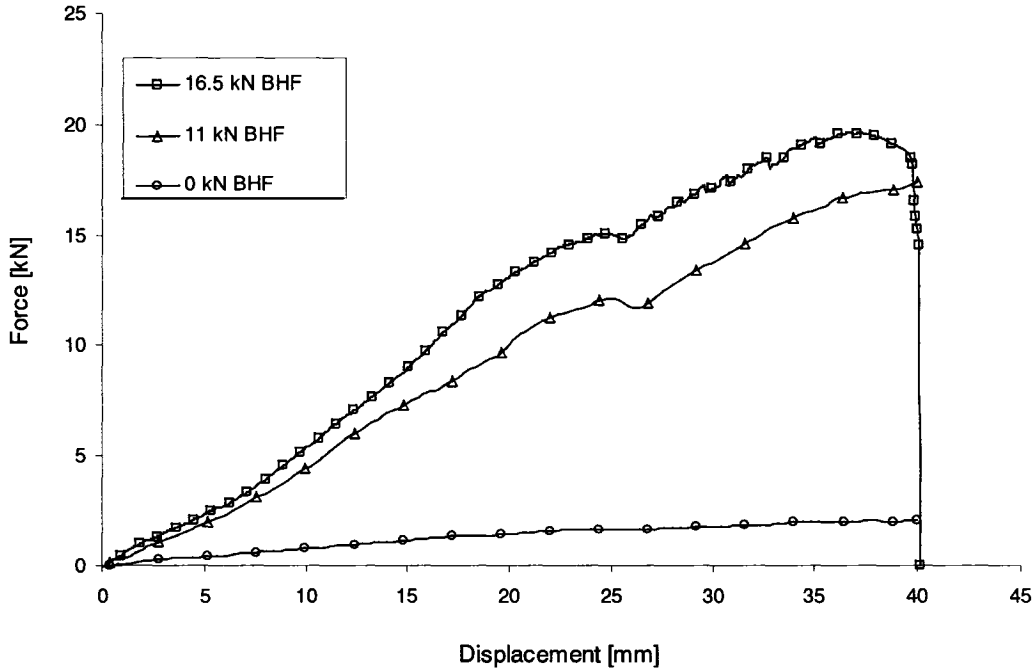

Fig. (4.20) Load-displacement diagram for the SS410 thin sheets under various BHFs

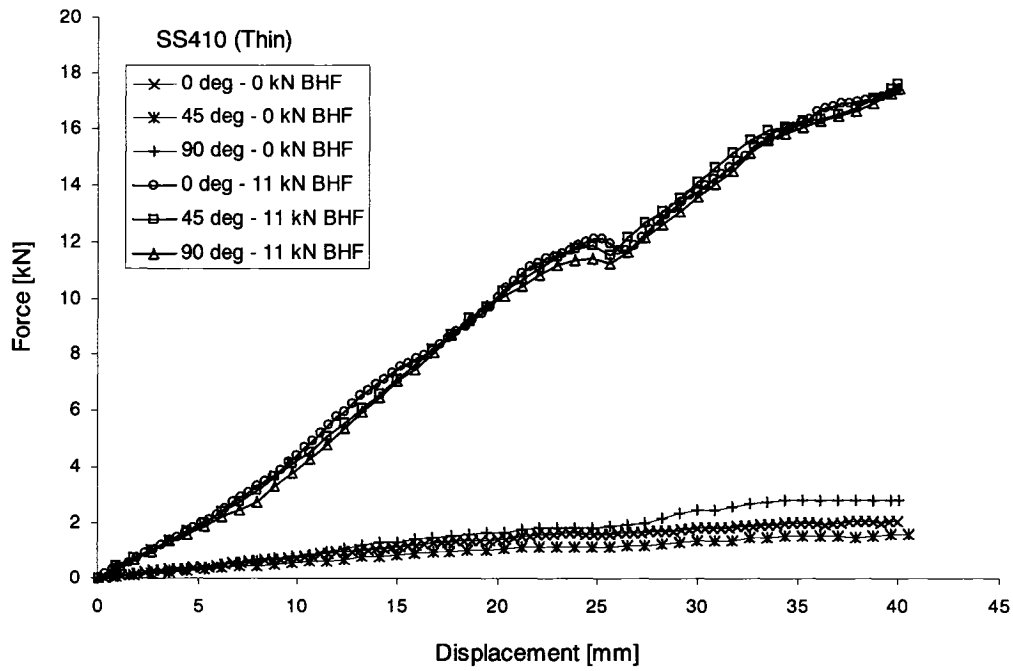

Fig. (4.21) Effect of orientation on forming load for minimum and maximum BHFs for thin SS410 specimens

4.4.1.2. DP 600/300 and 600/400 Sheets

For the DP steels, as mentioned in Sections 4.1.1 and 4.1.2, the effect of orientation was neglected and accordingly specimens with different orientation were not tested for the draw-bending experiments. Therefore, specimens cut at 90° to the rolling direction were tested for the effect of BHF on springback, as will be discussed later in Section 4.4.3. Figures (4.22) to (4.24) show the effect of increasing the blank holding force on the load required to deform the specimens. As expected, increasing the BHF will result in an increase in the required forming force. As can be noticed in Fig. (4.23), for thin DP 600/300 deformed under 11 and 22 kN, there is a slight drop in the force then the loading continues to increase. This observation can be attributed to the fact that the whole cross section of the material might have experienced yield when the load reached approximately 8.50 kN. Finally, a comparison between the forming loads, under the maximum BHF of 22 kN, for the three DP sheets tested is shown in Fig. (4.25). As expected, the required load increases with the increase in the thickness of the sheets of the same material.

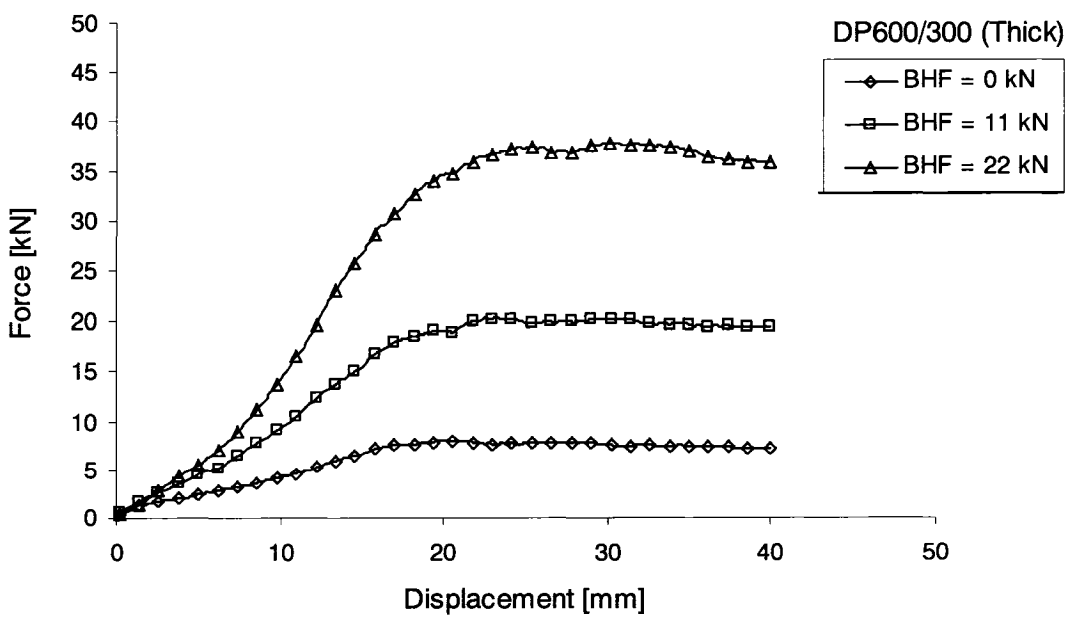

Fig. (4.22) Effect of BHF on forming load for minimum, intermediate, and maximum BHFs for thick DP600/300

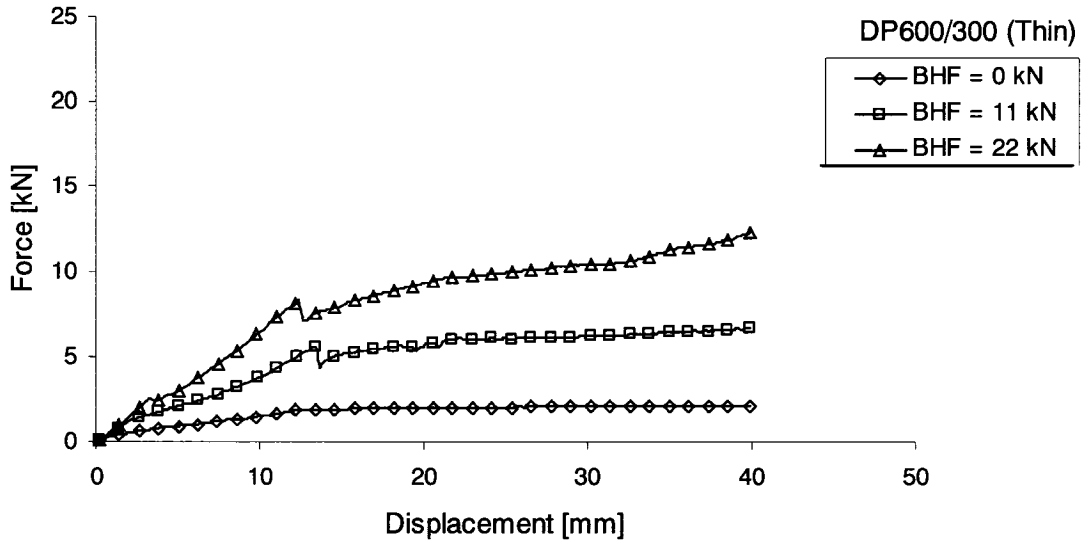

Fig. (4.23) Effect of BHF on forming load for minimum, intermediate, and maximum BHFs for thin DP600/300

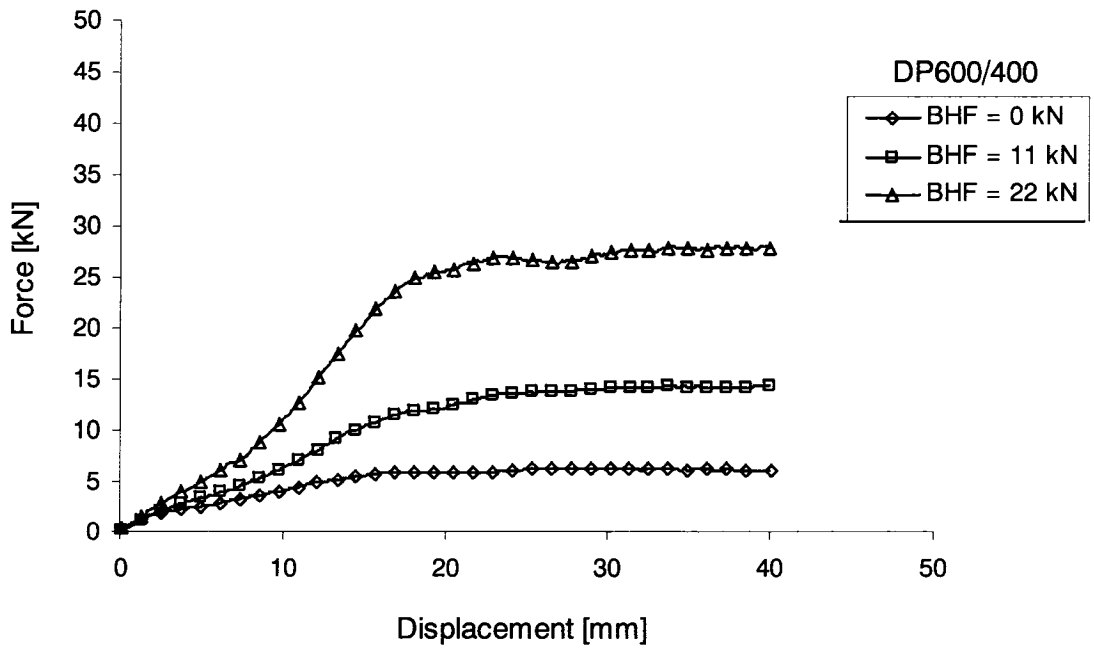

Fig. (4.24) Effect of BHF on forming load for minimum, intermediate, and maximum BHFs for DP600/400

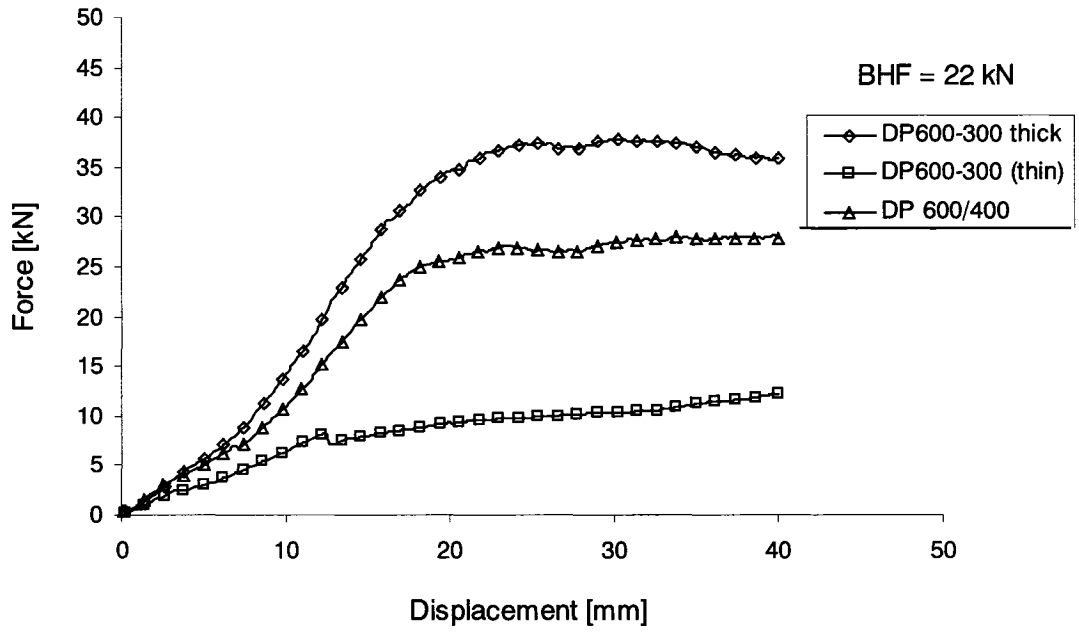

Fig. (4.25) Comparison between the required forming force at the maximum BHF for the three DP sheets

4.4.1.3. IN718 Sheets

Applying minimum and maximum BHF (0 and 22 kN) when testing the IN718, specimens were deformed to the required depth (40.00 mm) without failure. Figure (4.26) shows the force vs. displacement for the three specimen orientations. It can be seen that for a BHF of 0 kN there is a negligible difference in the required load for the three orientations. However, for the BHF of 22 kN, one can see that the difference increases with increasing displacement. Up to about 20.00 mm of drawing depth, the difference in the forming load is not very significant; however, it is recognizable that beyond that value the difference increases. The 45° specimen shows the least required force and the 90° specimen shows the largest forming load.

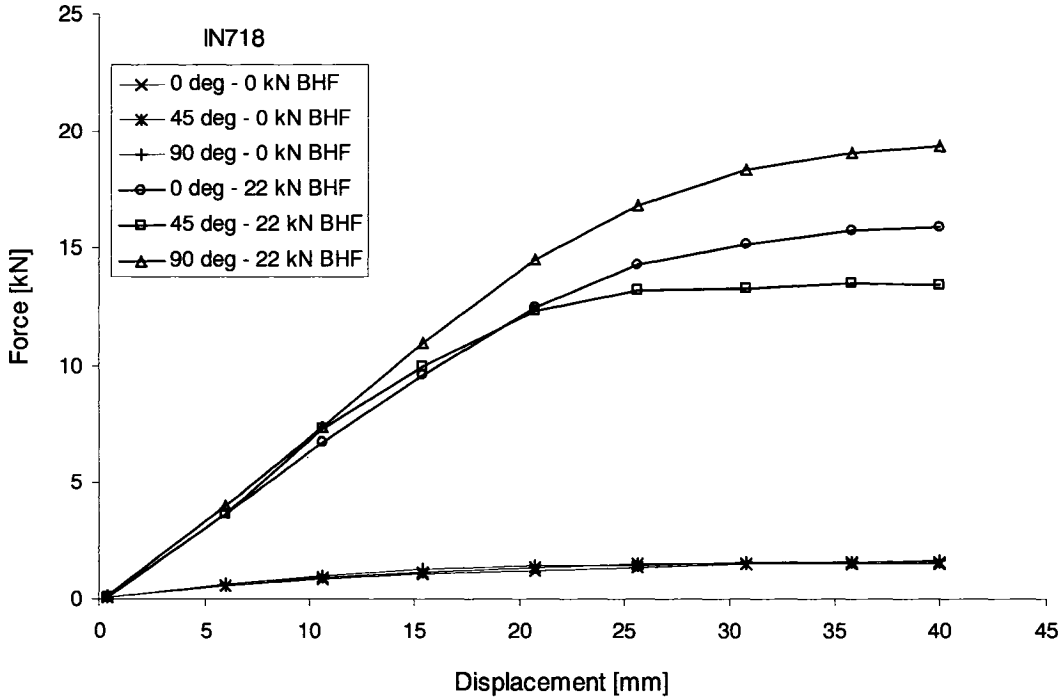

Fig. (4.26) Effect of orientation on forming load for minimum and maximum BHFs for IN718 specimens

4.4.2. Effect of Orientation on Springback Angles

The effect of orientation on springback angle was studied for the SS410 and IN718 sheets. Figures (4.27) show the springback angles under BHF of 0 kN. It is shown that, when the process is pure bending, there is no significant change in the angles with respect to specimen orientation. The variations of springback angles are listed in Appendix (B3). It can also be deduced that the thinner the sheet the greater the springback angle, as shown for the SS410 thick and thin specimens.

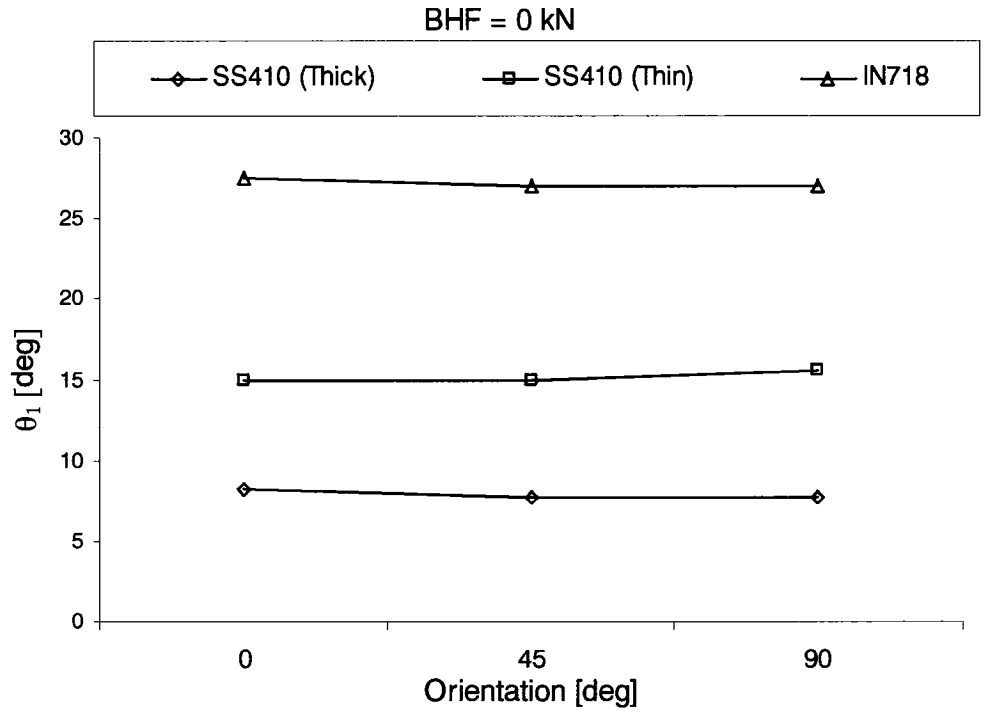

(a)

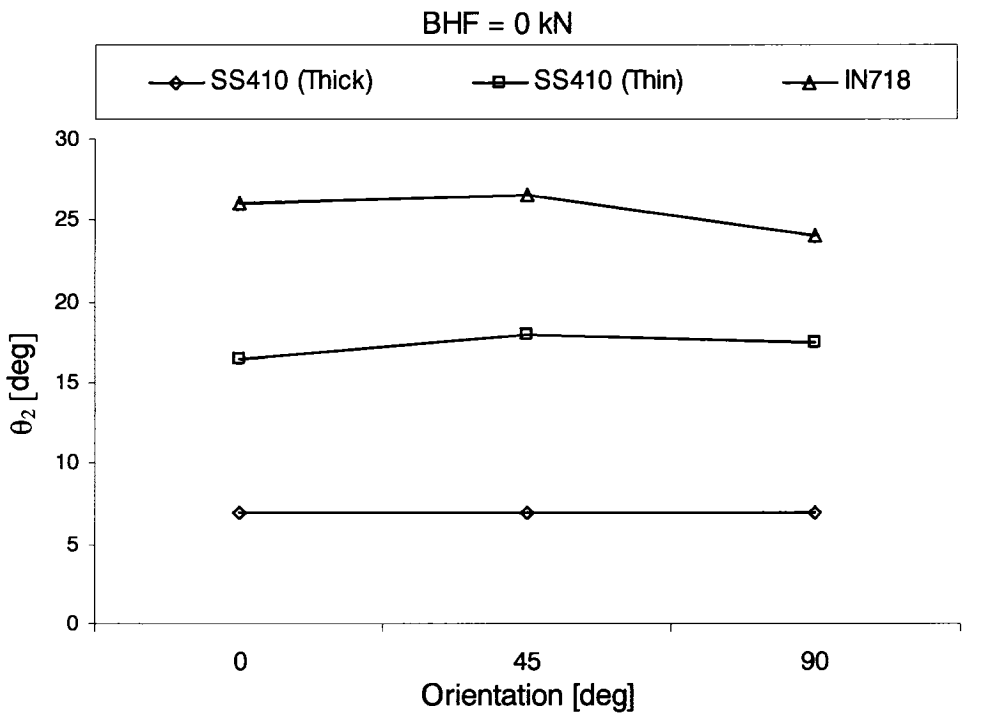

(b)

Fig. (4.27) Effect of orientation on springback angles for 0 kN BHF, (a) θ_1 and (b) θ_2

With the application of a higher blank holding force of 11 kN, as shown in Fig. (4.28), it was observed that, for the SS410 specimens, the change in orientation does not significantly affect the springback angle. The same observation cannot be said for the IN718 specimens; it is shown that the angles change with respect to the orientation to the rolling direction, with a maximum difference of about 5.50° observed with the change in the specimen's orientation, especially with the 45° specimens. Increasing the BHF to 22 kN, in the case of the thick SS410 and IN718, one can observe that, Fig. (4.29), the springback angles for the SS410 were not significantly affected by the change of the specimen's orientation. However, for the IN718 specimens, the difference is more pronounced in the 90° specimens. It is worth mentioning here that, as will be discussed in Chapter 6, that this difference in the springback angles for the IN718 with respect to the specimen orientation is not captured by the finite element model, discussed in Chapter 5, due to the fact that only normal anisotropy is considered. However, the general behaviour of the material is captured in an average sense.

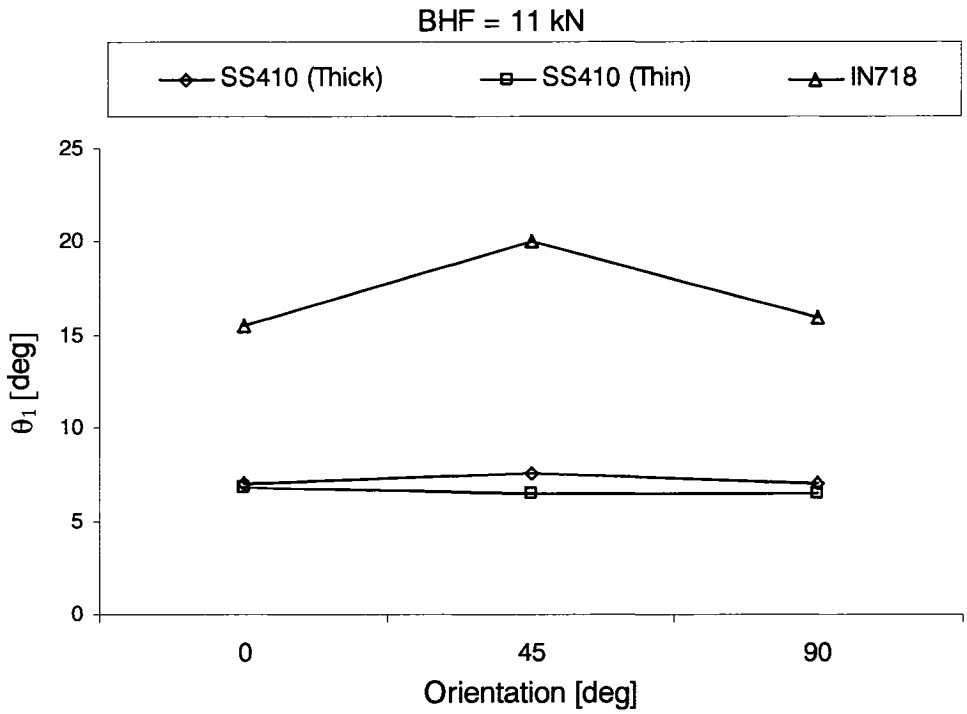

(a)

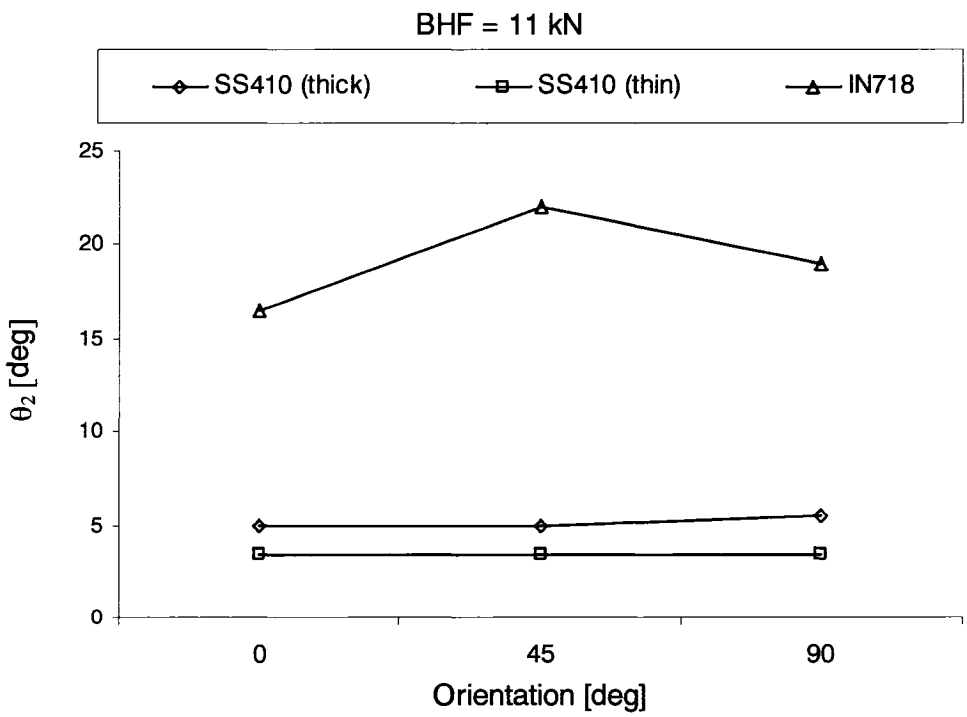

(b)

Fig. (4.28) Effect of orientation on springback angles for 11 kN BHF, (a) θ_1 and (b) θ_2

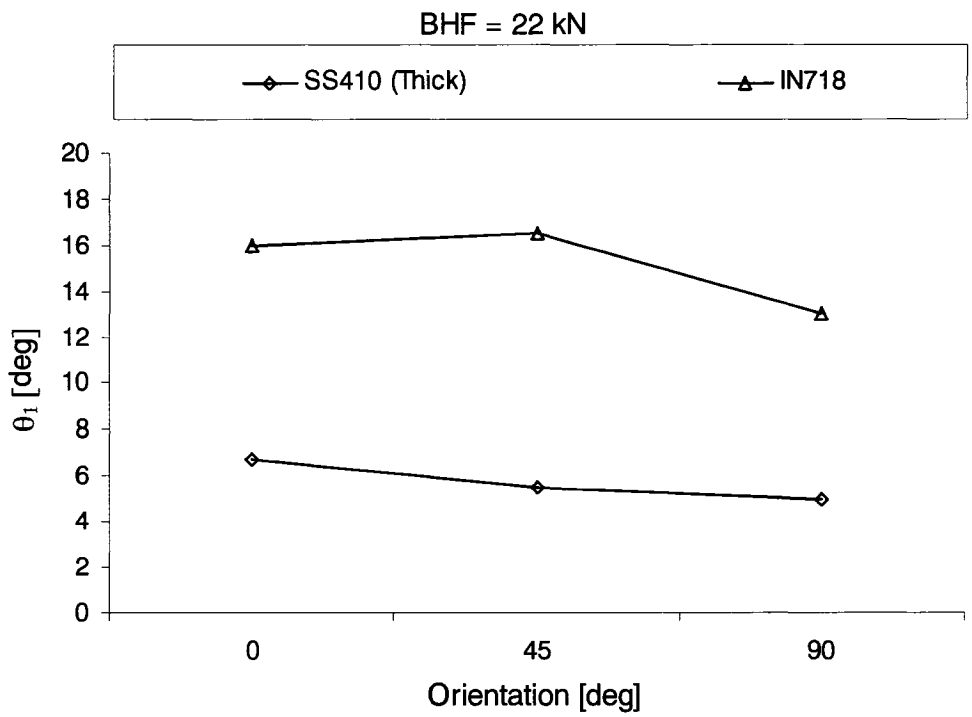

(a)

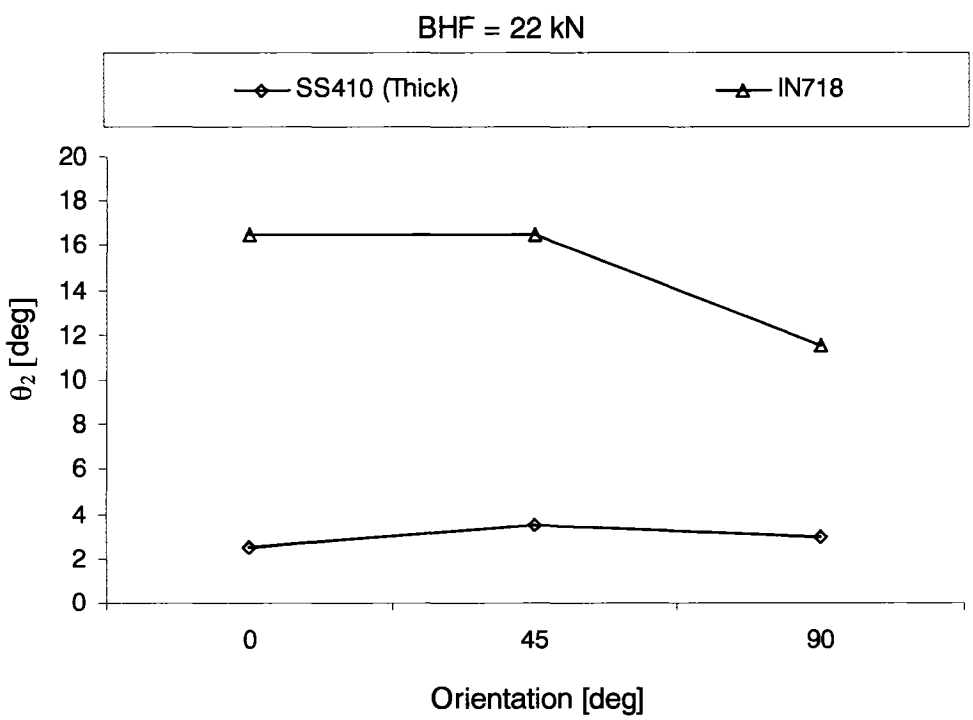

(b)

Fig. (4.29) Effect of orientation on springback angles for 22 kN BHF, (a) θ_1 and (b) θ_2

4.4.3. Effect of BHF on Springback Angles

Since the effect of BHF is more pronounced in the thin specimens, sheets tested were classified as *thick* for sheets of thickness of 1.50 mm or more and *thin* for sheets of thickness of about 1.00 mm or less. In the later category, the DP600/300 (thin), with t = 1.045 mm is included.

Figure (4.30) shows the effect of BHF on the springback angles for the thick specimens. It is shown that increasing the BHF will result in a reduction in the springback angles. However, the amount of reduction of the angles is not very significant; it was observed that the maximum angle reduction with the increase in the BHF was 2.75° for θ_1 and 4.00° for θ_2, which was observed for the SS410 (thick) specimens. For the DP steel specimens, both 600/300 (thick) and 600/400, the reduction in angles was not more than 2.50° with the increase in the BHF from 0 to 22 kN. Specimens that were formed under the maximum BHF did not experience sufficient strain distribution through thickness that would result in a dramatic change in the springback angles. The main reason for such a small change in springback angles is the relatively large thickness of the specimens.

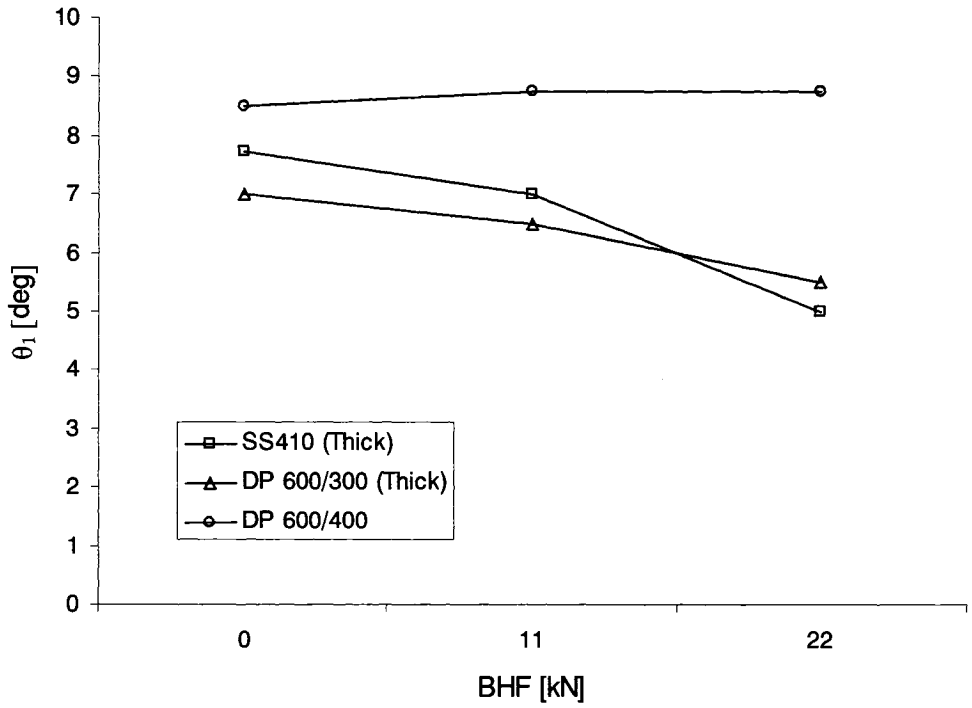

(a)

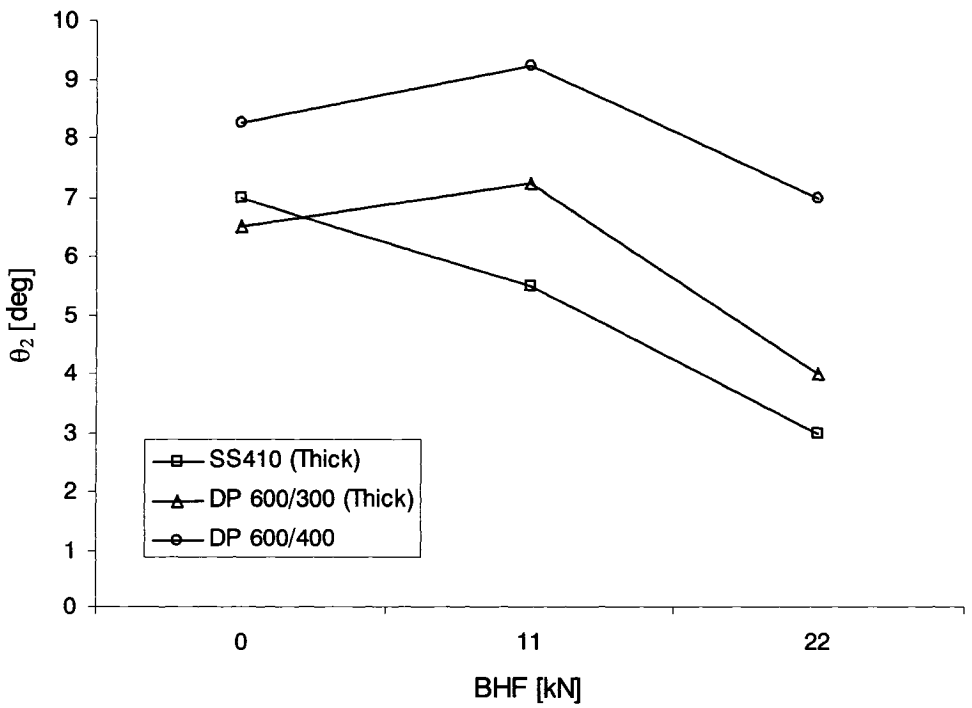

(b)

Fig. (4.30) Effect of BHF on springback angles for thick specimens, (a) θ_1 and (b) θ_2

On the other hand, for the thin specimens group, which includes: SS410 (thin), DP 600/300 (thin) and IN718, it can be seen that the change in BHF dramatically reduces the springback angles. Figure (4.31) shows such a reduction. The IN718 specimens experienced the highest reduction in springback angles for about 14.00^{o} and 11.50^{o} for θ_1 and θ_2, respectively. Second in the amount of reduction is the SS410 (thin) specimens; a large reduction in springback angles was also observed, with the increase of the BHF from 0 to 11 kN. The amount of reduction in θ_1 and θ_2 was 9.00^{o} and 14.00^{o}, respectively. Finally, for the DP 600/300 (thin), the amount of springback angles reduction was observed to be almost the same as in the thick specimens. The reduction in θ_1 was 6.50^{o} and θ_2 was 4.75^{o}. This can be attributed to the relatively higher thickness than the other thin specimens.

Figure (4.32) shows a comparison between the springback angles for specimens made of the same materials but different thicknesses. It can be seen clearly that: (1) thin materials experience higher springback angles after forming, (2) the amount of stretch caused by the increase in the BHF directly affect the reduction in springback angles for thin materials and does not have the same influence on the thick specimens, mainly because of their relatively higher thickness. Figure (4.33) shows the effect of increasing the BHF on the amount of stretch the specimen experiences. As can be seen, for a BHF of 0 kN the bending process dominates and the stretch over the punch radius does not take place. Increasing the BHF to 11 kN and 22 kN, the specimens are formed around the punch and die radii and accordingly experience more stretch; which is translated into more plastic deformation and therefore lower springback angles.

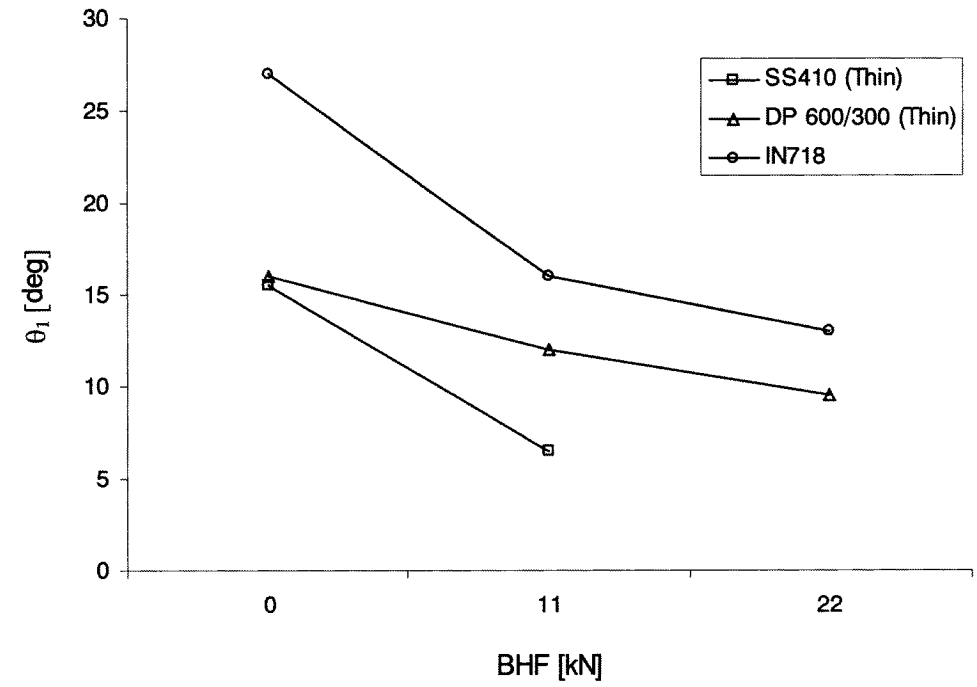

(a)

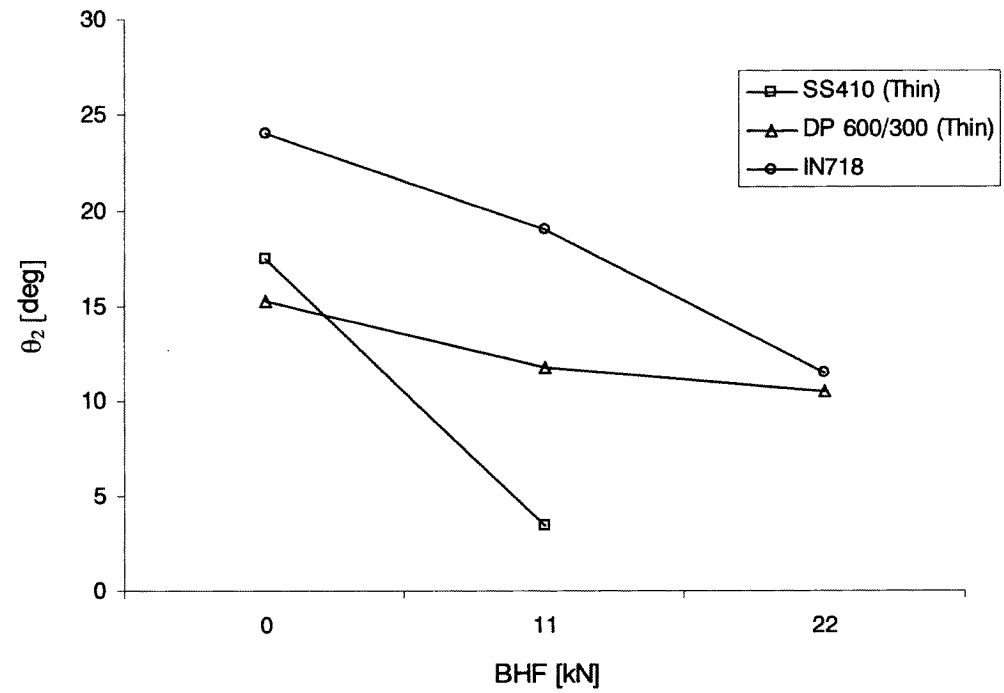

(b)

Fig. (4.31) Effect of BHF on springback angles for thin specimens, (a) θ_1 and (b) θ_2

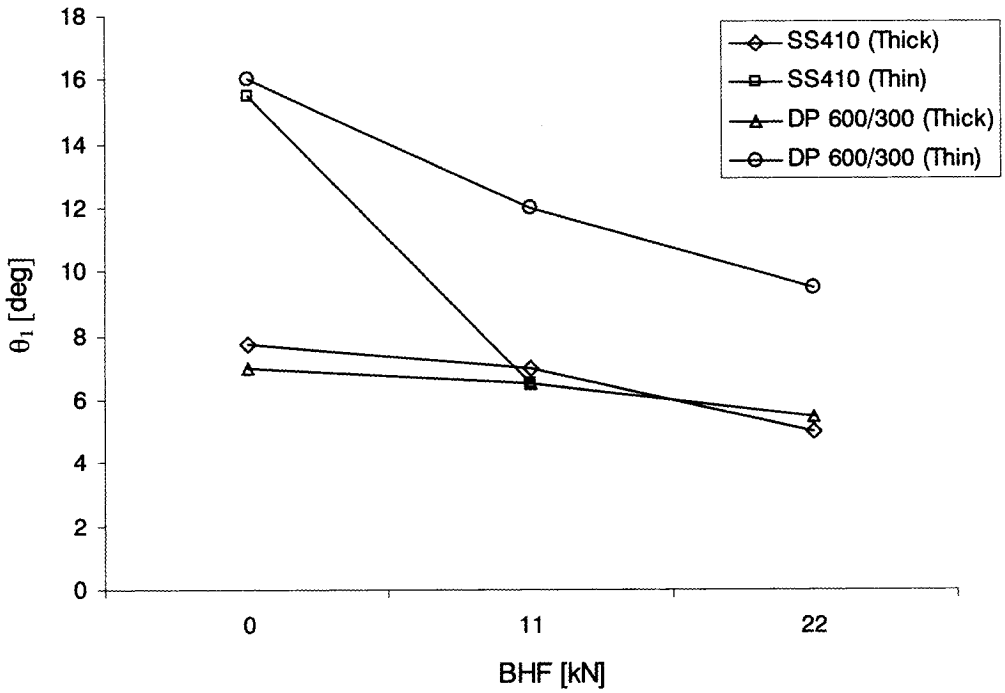

(a)

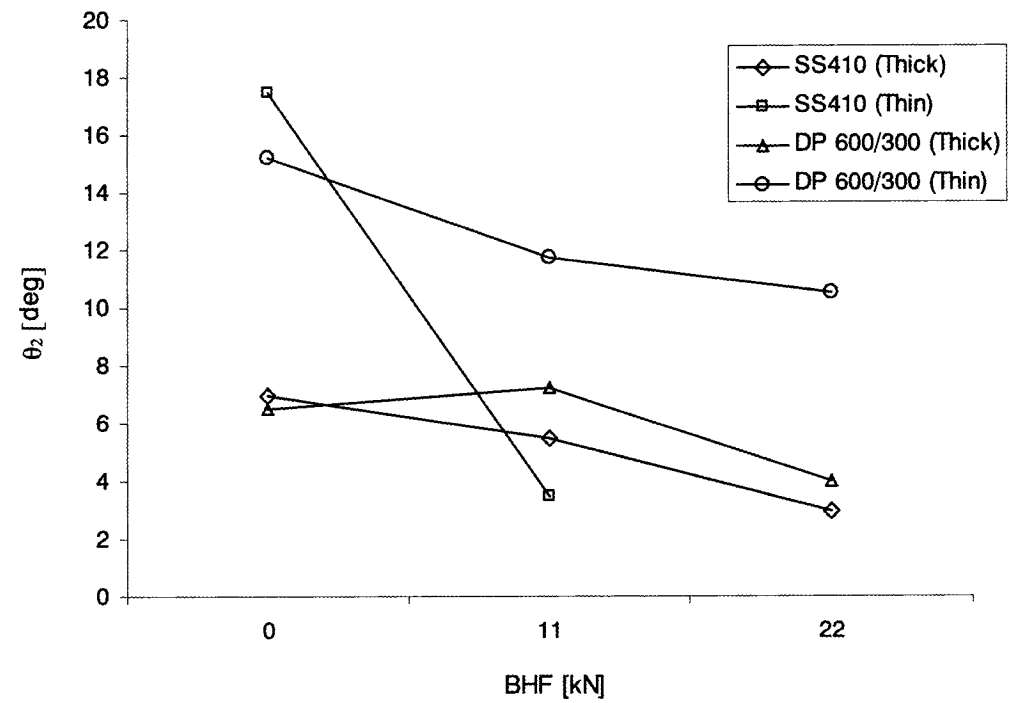

(b)

Fig. (4.32) Effect of BHF on springback angles for thick and thin steel specimens, (a) θ_1 and (b) θ_2

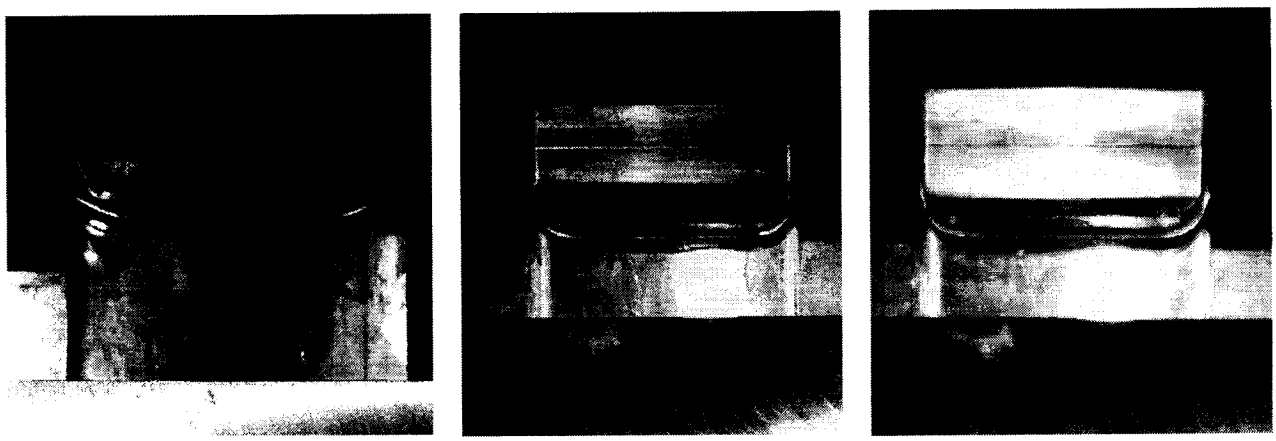

BHF = 0 kN BHF = 11 kN BHF = 22 kN

Fig. (4.33) Effect of increasing the BHF on the amount of specimen's stretch for thick SS410

4.4.4. Effect of Orientation and BHF on Final Thickness

The effect of specimen orientation and BHF on the final thickness of the specimens, thinning, was also studied. It is expected that there should be a reduction in thickness with the increase in the BHF, due to the stretch in the specimen and the assumption of constancy of volume of the material.

To measure the reduction in thickness, specimens with different orientations ($\varphi = 0^{o}$, 45^{o}, and 90^{o}) were formed under different BHF (0, 11, and 22 kN). The thickness was measured at the middle of both left and right side walls of the specimens and the average thickness through the side walls is calculated and plotted against the specimen orientation to the rolling direction, as shown in Figs. (4.34) to (4.36). It is shown that for a BHF of 0 kN, there is no effect of orientation on the final thickness. This is an obvious observation since the part did not experience any stretch and the process is only bending. Increasing the BHF, one will start to realize that there is a slight change in the final thickness of the part, especially for specimens deformed under the maximum BHF of 22 kN. The change is still not dramatic; however, it represents the change in strains along the specimen's thickness due to the presence of sheet anisotropy.

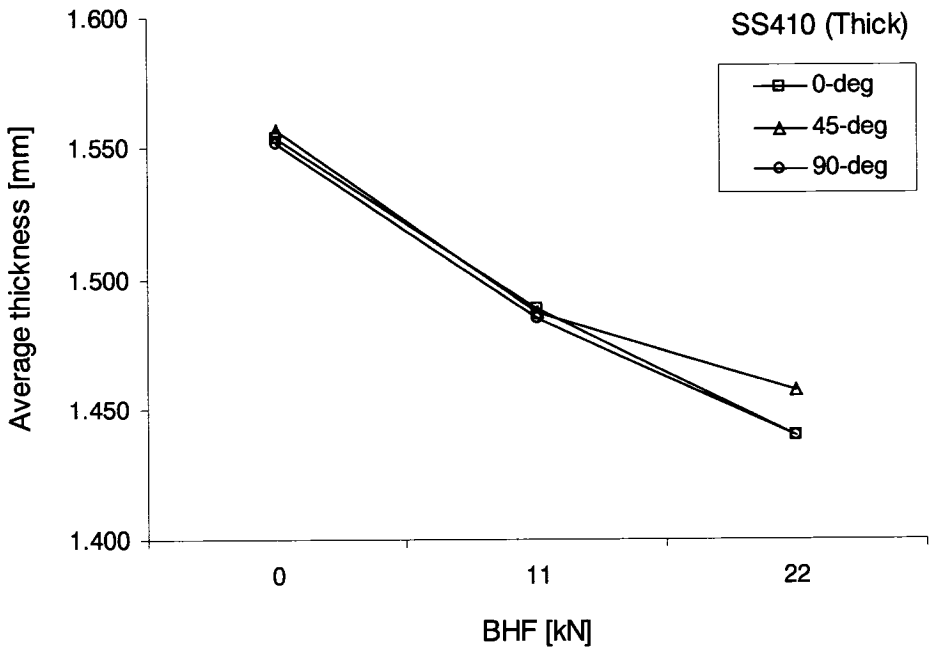

Fig. (4.34) Effect of orientation and BHF on the final thickness for SS410 thick specimens

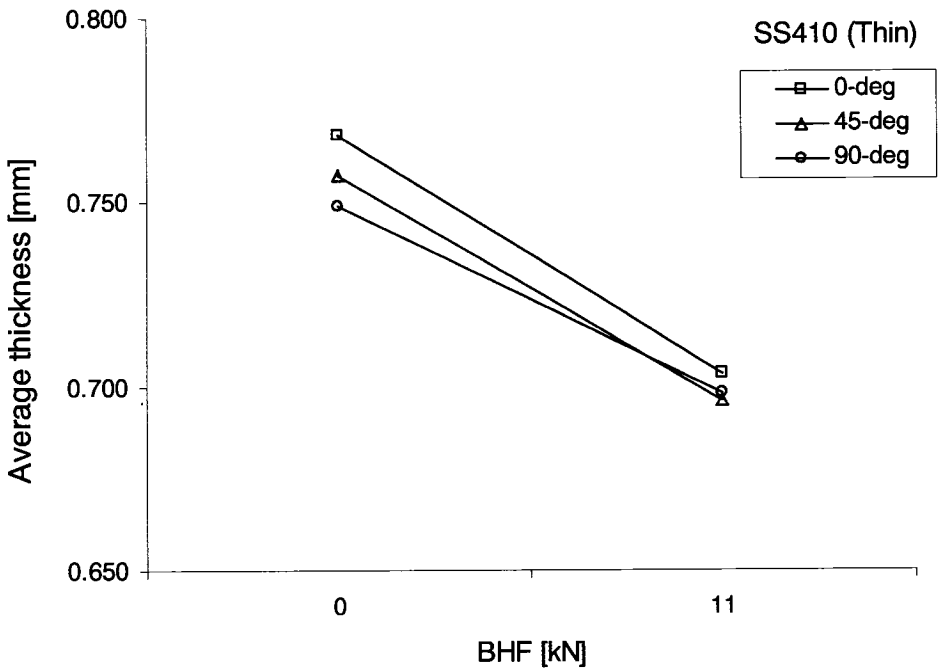

Fig. (4.35) Effect of orientation and BHF on the final thickness for SS410 thin specimens

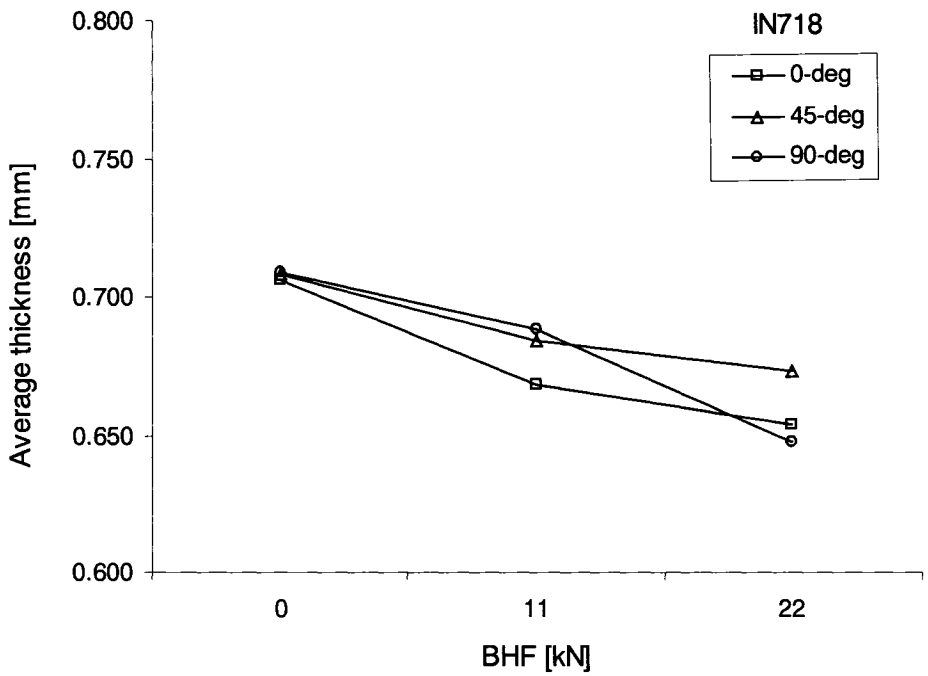

Fig. (4.36) Effect of orientation and BHF on the final thickness for IN718 specimens

The overall effect of BHF on final thickness for all the sheets tested is shown in Fig. (4.37). It is worth mentioning that for the SS410 and IN718 sheets the thickness shown is the average of the thicknesses of the three orientations. The average was calculated and plotted against the BHF for the different materials in the study. Again, as expected, the increase in the BHF will result in a decrease in the final thickness of the deformed part. It is worth mentioning here that sometimes increasing the BHF is favorable because of the reduction in the springback; however, thinning might occur and accordingly fracture. This is why choosing an optimum BHF for forming operations is vital (Siebel, 1954, Chait, 1973, and Gotoh *et al.*,1997).

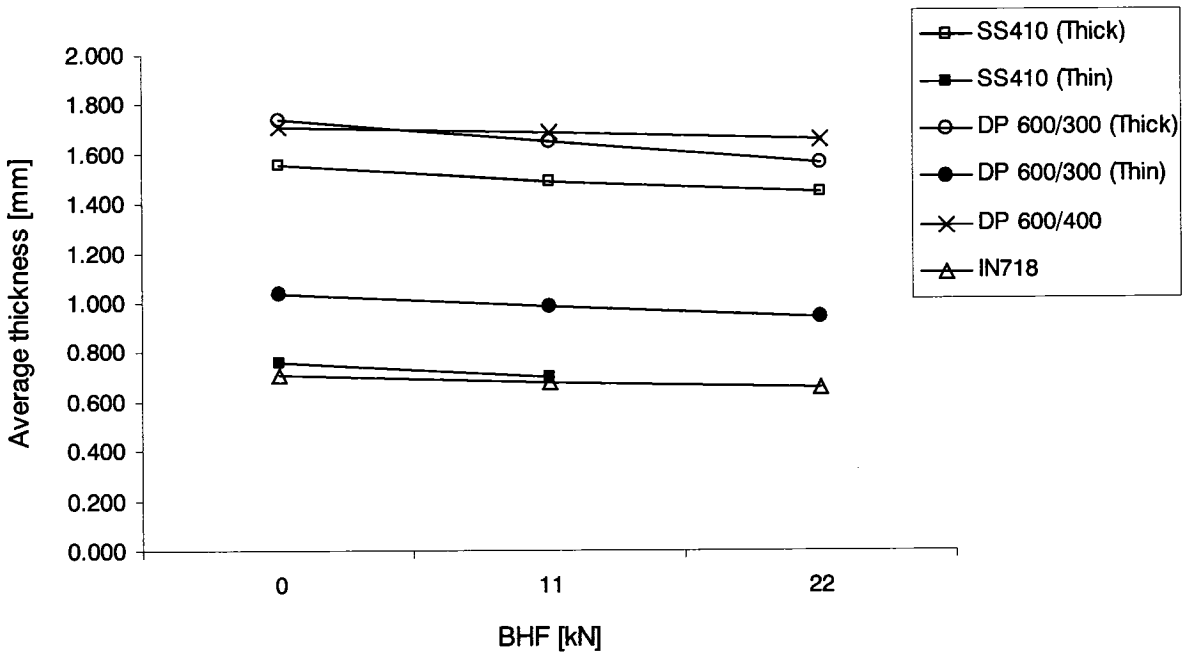

Fig. (4.37) Effect of BHF on the final thickness for all the materials studied

CHAPTER 5

Material Modeling and Numerical Implementation

5.1. Introduction

To properly model the material behaviour, elastic and plastic relations must be considered. For the plastic part of the deformation history, the three basic relations in the theory of plasticity have to be implemented. These relations, as discussed before, are the yield criterion, the flow rule, and the hardening model. In this chapter, each of these topics is discussed in detail in order to be implemented into the finite element code. For the yield criterion, it was reported by other researchers that, in contrast to many other criteria, the full behaviour of orthotropic materials can be described by Hill's 1948 yield formulation (Barlat and Lian, 1989). Also, the formulation has been widely used and validated by numerous experiments and reported to be suitable for specific metals and

textures, especially steels. The criterion was also reported to be easy to implement in analytical or numerical sheet metal forming processes (Barlat and Lian, 1989, Cazacu and Barlat, 2003 and Bron and Besson, 2004). Therefore, in this study, the Hill's 1948 anisotropic yield criterion is adopted for sheet metals with initial normal anisotropy parameter $\bar{R}$.

Furthermore, as for the flow rule, the associated flow rule is implemented. Finally, for the hardening model, as shown in Section 2.4, models using a single yield surface were first developed to describe monotonic loading; however, they do not provide realistic results when cyclic loading is involved. To extend the applicability to cyclic loading, multiple yield surfaces were accommodated in the theory of plasticity. It was also shown that the use of either isotropic or kinematic hardening alone does not predict accurate results for springback simulations. Therefore, a combined hardening model that uses both effects, isotropic and kinematic, and also uses multiple yield surfaces is proposed in this work. It is noteworthy that the literature on simulating complex loading conditions using multiple yield surface models is relatively sparse. This can be mainly attributed to the inherent complexity of these models, which also requires a substantial amount of computation. Therefore, the aim of this work is to present a relatively simple multiple yield surface model to demonstrate this approach.

5.2. Material Constitutive Model

5.2.1. Model Assumptions

The deformation history of the material can be any combination of elastic loading, plastic loading, elastic unloading, elastic reverse loading, and finally, plastic reverse loading. It can be divided into two steps, elastic deformation and plastic deformation, so that

$$d\varepsilon_{ij}^{total} = d\varepsilon_{ij}^{el} + d\varepsilon_{ij}^{pl} \tag{5.1}$$

where $d\varepsilon_{ij}^{total}$ is the total strain increment, $d\varepsilon_{ij}^{el}$ is the elastic strain increment, and $d\varepsilon_{ij}^{pl}$ is the plastic strain increment. The formulation of each of the deformation steps is presented in the following sections.

The material behaviour in the elastic region is governed by Hooke's law. In addition, to properly reflect the real material behaviour in the plastic region, a model that incorporates the Bauschinger effect in its description must be taken into consideration. As discussed previously, the isotropic hardening rule does not account for the Bauschinger effect. Moreover, the kinematic hardening rule does not account for the change of the size of the yield surface. Therefore, a more generalized hardening assumption that accounts for both the change in size and the translation of the yield surface is needed for a better material description.

In this work, a combined hardening model is presented. The hardening assumption follows the classical isotropic hardening formulation in addition to the implementation of the multiple yield surface formulations presented by Mróz (1967) and Gau and Kinzel (2001). To implement both effects, isotropic and kinematic hardening assumptions, the plastic strain increment, $d\varepsilon_{ij}^{pl}$, in Eq. (5.1), is divided into two parts. One part is the contribution of the plastic strain increment due to the isotropic hardening and the other is the contribution of the plastic strain increment due to the kinematic hardening. The full description of the model is discussed in the Combined Hardening section.

To proceed, the following assumptions were suggested by Gau and Kinzel (2001). For the sheet shown in Fig. (5.1) they studied the influence of the Bauschinger effect on the deformation history, internal stress distribution, and the final shape after springback. The following assumptions were considered in their work and are adopted in this study:

(i) Plane stress in 3-direction, $(\sigma_{13} = \sigma_{31} = \sigma_{23} = \sigma_{32} = \sigma_{33} = 0)$,

(ii) Only normal anisotropy, $\bar{R}$, is considered,

(iii) Bauschinger effect is considered,

(iv) Planes normal to the sheet reference remain plane during deformation,

(v) Mid-plane is considered to be bending–strain free,

(vi) Total tangential strain in 1-direction is the summation of bending and membrane strains, and

(vii) Volume conservation is assumed, $\Delta V = 0$.

Furthermore, the assumption of plane-strain in the 2-direction, $d\varepsilon_{22} = 0$, was implemented in their study. However, for generalization of the model, this assumption was omitted from this work.

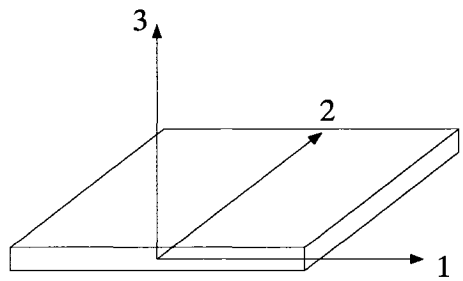

Fig. (5.1) Sheet before deformation with principal directions

5.2.1. Elastic Behaviour

5.2.1.1. Elastic Loading

During elastic deformation, strains can be calculated using Hooke's law. The general form of Hooke's law for plane stress, $(\sigma_{13} = \sigma_{23} = \sigma_{33} = 0)$, can be written as

$$\begin{aligned}
\varepsilon_{11}^{el} &= \frac{1}{E}\left(\sigma_{11} - \nu\sigma_{22}\right) \\
\varepsilon_{22}^{el} &= \frac{1}{E}\left(\sigma_{22} - \nu\sigma_{11}\right) \\
\varepsilon_{33}^{el} &= \frac{-\nu}{E}\left(\sigma_{11} + \sigma_{22}\right) \\
\varepsilon_{12}^{el} &= \frac{1+\nu}{E}\sigma_{12}
\end{aligned} \tag{5.2}$$

and, therefore, the elastic strain increments can be expressed in the form

$$\begin{aligned}
d\varepsilon_{11}^{el} &= \frac{1}{E}\left(d\sigma_{11} - \nu d\sigma_{22}\right) \\
d\varepsilon_{22}^{el} &= \frac{1}{E}\left(d\sigma_{22} - \nu d\sigma_{11}\right) \\
d\varepsilon_{33}^{el} &= \frac{-\nu}{E}\left(d\sigma_{11} + d\sigma_{22}\right) \\
d\varepsilon_{12}^{el} &= \frac{1+\nu}{E}d\sigma_{12}
\end{aligned} \tag{5.3}$$

5.2.1.2. Elastic Unloading and Elastic Reverse Loading

At the end of the loading process, immediately before the unloading takes place, the stress in an element, σ_{ij}^{end}, is determined from the state of stress that exists just prior to $F\left(\sigma_{ij}\right) < 0$. This σ_{ij}^{end} is considered as the highest previously reached value of σ_{ij} immediately before the beginning of the unloading. The state of unloading and reverse elastic loading is reached when the yield function is evaluated and the stress state satisfies the condition

$$F\left(\sigma_{ij}\right) < 0 \tag{5.4}$$

Furthermore, the state of stress at the end of the unloading and elastic reverse loading process, $\sigma_{ij}^{reverse}$, is considered as the lowest previously reached value of σ_{ij} immediately

before the beginning of the plastic reverse loading and when the yield function is evaluated so that

$$F\left(\sigma_{ij}\right)=0 \tag{5.5}$$

Since the process is elastic, then Hooke's law can be applied to determine the strains in the element, in a similar manner to the elastic loading process. The state of unloading and elastic reverse loading is shown schematically in Fig. (5.2).

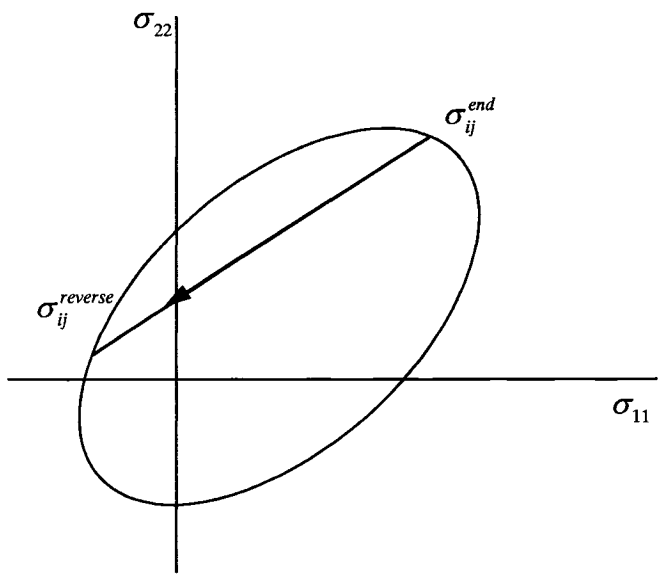

Fig. (5.2) Stresses at end of loading and unloading processes for multiaxial case

5.2.2. Yield Function

As discussed in Section 2.3, conventional structural metals initially deform elastically; however, as the stress levels attain the flow stress value the material starts to deform

plastically with a much lower effective modulus. The yield function or the flow stress function defines the bounds of the plastic domain.

The shape of the yield function, defined for each material, describes the stress space or the flow stress surface for that particular material. A number of mathematical approaches were described in Section 2.3. The von Mises criterion is most commonly used in design calculations involving metals.

In sheet metal forming simulations, especially when springback is considered, it is common to assume that only normal anisotropy exists. For example, Wang *et al.* (1993) reported that springback increases with the increase in the normal anisotropy. Pourboghrat and Chu (1995a and b) and Pourboghrat *et al.* (2000) used Hill's 1948 yield criterion with normal anisotropy in their springback simulations. Leu (1997) concluded that springback is almost proportional to the normal anisotropic value $\overline{R}$.

On the other hand, research conducted to investigate the effect of planar anisotropy, or the effect of ΔR, was mainly conducted to investigate its effect on the earing problem in deep drawing. Kumar (2002) reported that the earing tendency during drawing is highly affected by planar anisotropy. Geng and Wagoner (2002) reported that planar anisotropy plays an important role in problems where anticlastic curvature is observed. Also, Li *et al.* (2003) reported that planar anisotropy has a direct effect on the earing behaviour.

Based on the above reported results and since the main goal is to investigate the springback in sheet metal forming, a yield criterion that includes the material normal anisotropy can be utilized in the analysis. In this study, Hill's 1948 theory for planar isotropic material (i.e. including only the normal anisotropy) is implemented. The general form of the yield function that includes both the change of size and the translation of the yield surface has the form

$$F\left(\sigma_{ij},\alpha_{ij},\bar{\varepsilon}^{p}\right)=s_{11}^{2}+s_{22}^{2}-\frac{2\bar{R}}{\left(\bar{R}+1\right)}s_{11}s_{22}+\frac{2\left(2\bar{R}+1\right)}{\left(\bar{R}+1\right)}s_{12}^{2}$$
$$+\frac{2}{\left(\bar{R}+1\right)}\left(s_{33}^{2}-s_{11}s_{33}-s_{22}s_{33}\right)-\bar{\sigma}^{2}\left(\bar{\varepsilon}^{p}\right)=0 \tag{5.6}$$

where $\bar{R}$ is the normal anisotropy parameter, $s_{ij}=\left(\sigma_{ij}-\alpha_{ij}\right)$, α_{ij} are the back stress components, and $\bar{\sigma}$ is the effective stress presented as a function of the effective plastic strain, $\bar{\varepsilon}^{p}$.

The yield function, for isotropic hardening materials, that includes only change in the size of the yield surface, where the components of α_{ij} = 0, reduces to the form

$$F\left(\sigma_{ij},\bar{\varepsilon}^{p}\right)=\sigma_{11}^{2}+\sigma_{22}^{2}-\frac{2\bar{R}}{\bar{R}+1}\sigma_{11}\sigma_{22}+\frac{2\left(2\bar{R}+1\right)}{\bar{R}+1}\sigma_{12}^{2}$$
$$+\frac{2}{\bar{R}+1}\left(\sigma_{33}^{2}-\sigma_{11}\sigma_{33}-\sigma_{22}\sigma_{33}\right)-\bar{\sigma}^{2}\left(\bar{\varepsilon}^{p}\right)=0 \tag{5.7}$$

The von Mises yield criterion, when plotted, takes the shape of a cylinder in the stress space and an ellipse in the 2-D stress plots. The effect of anisotropy, expressed through the $\bar{R}$–value, on the size of the yield surface, for an isotropic hardening assumption, is shown in Fig. (5.3). It is shown that the change in the $\bar{R}$– value results in a change of the size of the yield surface.

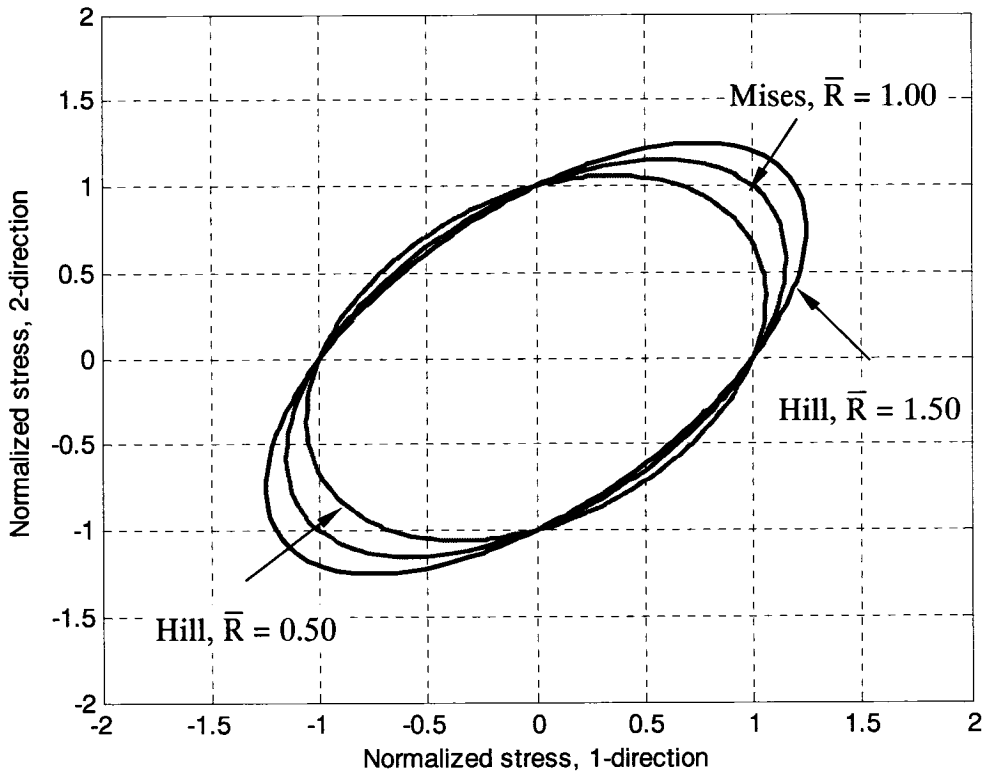

Fig. (5.3) Effect of normal anisotropy, $\bar{R}$–value, on the yield surface size for isotropic-hardening materials

When considering pure kinematic hardening, there is no change in the size of the yield surface, that is $\bar{\sigma}^2\left(\bar{\varepsilon}^p\right)$ = constant. In that case, the yield function, Eq. (5.6), reduces to the form

$$F\left(\sigma_{ij},\alpha_{ij}\right)=s_{11}^2+s_{22}^2-\frac{2\bar{R}}{\left(\bar{R}+1\right)}s_{11}s_{22}+\frac{2\left(2\bar{R}+1\right)}{\left(\bar{R}+1\right)}s_{12}^2 +\frac{2}{\left(\bar{R}+1\right)}\left(s_{33}^2-s_{11}s_{33}-s_{22}s_{33}\right)-k_o^2=0 \tag{5.8}$$

where $s_{ij} = \left(\sigma_{ij} - \alpha_{ij}\right)$ and k_o is a constant that describes the size of the yield surface. The effect of the change in the back stress values, α_{ij}, in Eq. (5.8) can be seen in Fig. (5.4). It is shown, as an example that for an isotropic material, $\bar{R}$ = 1, that the yield surface's size remains unchanged while translating in the stress space.

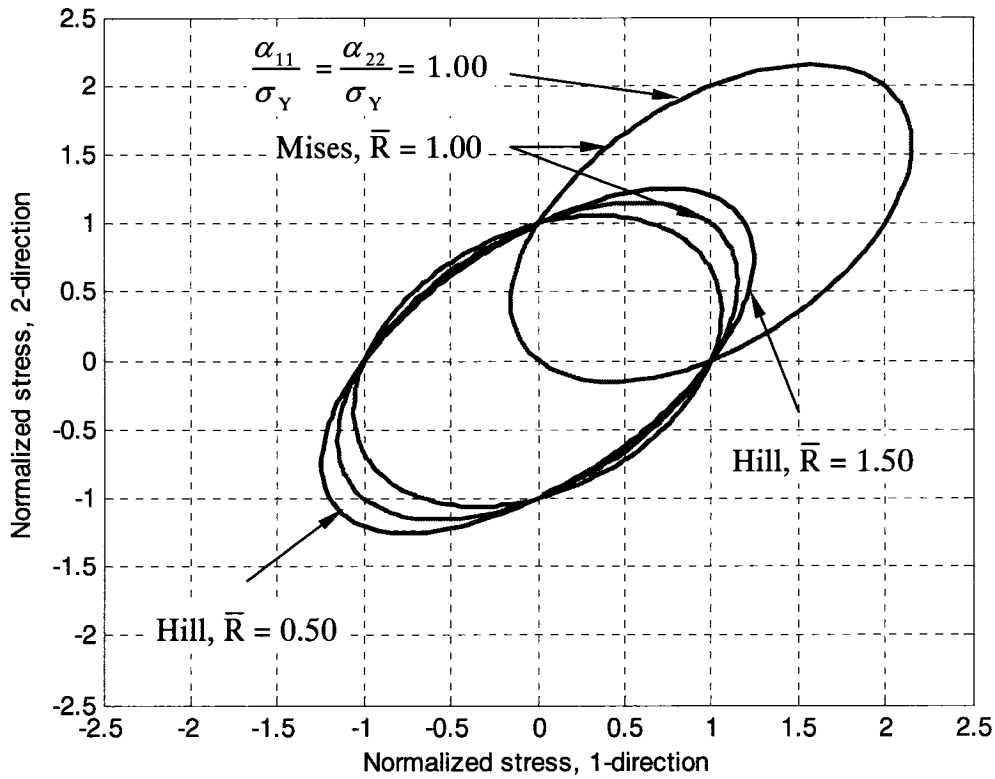

Fig. (5.4) Effect of back stress components, α_{ij}, on the yield surface position for an anisotropic material with kinematic-hardening

5.2.3. Plastic Flow Potential

In elasticity theory, it is known that the strain is related to the stress through an elastic potential function, the complementary strain energy, U_c, such that

$$\varepsilon_{ij}^{el} = \frac{\partial U_c}{\partial \sigma_{ij}} \tag{5.9}$$

Von Mises proposed a generalization to that principal and applied it to plasticity theory so that there exits a plastic potential function $g(\sigma_{ij})$, such that the plastic strain increment can be written as (Hill, 1950 and Khan and Huang, 1995)

$$d\varepsilon_{ij}^{pl} = d\lambda \frac{\partial g(\sigma_{ij})}{\partial \sigma_{ij}} \tag{5.10}$$

where $d\lambda$ is a proportional positive scalar factor. A common approach in plasticity theory is to let $g(\sigma_{ij})$ be identical to the yield function, $F(\sigma_{ij})$ so that

$$d\varepsilon_{ij}^{pl} = d\lambda \frac{\partial F(\sigma_{ij})}{\partial \sigma_{ij}} \tag{5.11}$$

In this case, such a representation is called the associated flow rule. It was shown experimentally that the plastic behaviour of metals can be well described by the associated flow rule. On the other hand, when the potential function $g(\sigma_{ij})$ is not the same as the yield function, the flow rule in this case is called nonassociated; which better represents the plastic behaviour of porous materials, rocks, concrete, and soils (Khan and Huang, 1995).

Since $F(\sigma_{ij})$ is equal to a constant on the yield surface then $\frac{\partial F(\sigma_{ij})}{\partial \sigma_{ij}}$ must be perpendicular to the surface. Thus, the plastic strain vector represented in 2D stress space must be normal to the yield surface, as shown in Fig. (5.5).

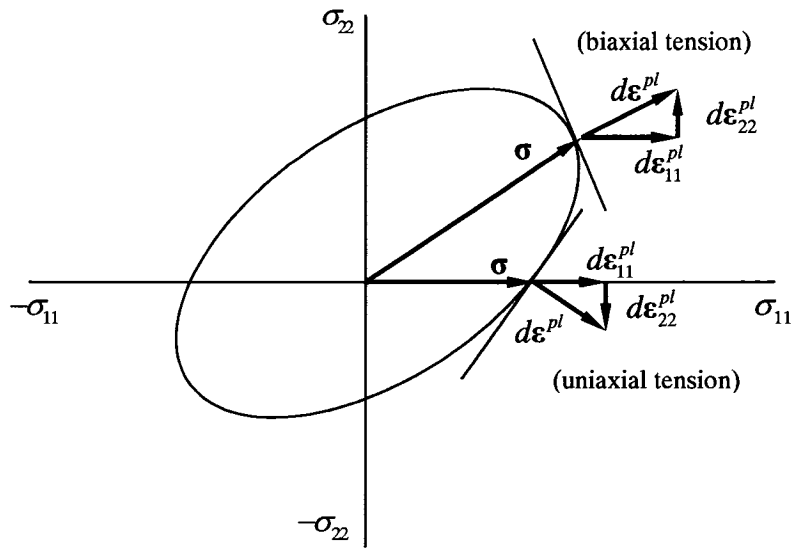

Fig. (5.5) Normality of the plastic strain increment

For nonlinear kinematic hardening behaviour, which is the case in this study, the associated flow rule is considered and the plastic strain increment takes the form

$$d\varepsilon_{ij}^{pl} = \frac{1}{K^p}\left(n_{ij} d\sigma_{kl}\right) n_{kl} \tag{5.12}$$

where K^p is the workhardening modulus, a generalization of the notion of tangent plastic modulus in the uniaxial stress state (Mróz, 1967), and n_{ij} is the outward unit normal to the yield surface; which is given by (Khan and Huang, 1995)

$$n_{ij} = \frac{\dfrac{\partial F}{\partial \sigma_{ij}}}{\left[\dfrac{\partial F}{\partial \sigma_{kl}} \dfrac{\partial F}{\partial \sigma_{kl}}\right]^{\frac{1}{2}}} \tag{5.13}$$

From Eq. (5.12), it is implied that the plastic flow is caused by the normal component of $d\sigma_{kl}$ and takes a normal direction to the load or yield surface, which is denoted by the unit normal vector at the loading point.

In multiple– and two–surface plasticity theory; for example, Mróz model, which is considered in this study, the yield surfaces must have the same normal at the contact point; which avoids the surfaces intercepting each other. To insure this condition, the translation of the yield surface follows that

$$d\alpha_{ij} = d\mu\left(\sigma_{ij} - \alpha_{ij}\right) \tag{5.14}$$

The parameter dμ is greater than zero and is obtained from the condition that the stress point remains on the yield surface (Mróz, 1967), thus

$$\left(d\alpha_{ij} - d\sigma_{ij}\right)\frac{\partial F}{\partial \sigma_{ij}} = 0 \tag{5.15}$$

5.2.4. Hardening Rule

The hardening assumption is needed to calculate the stress increments in the plastic deformation. For the purpose of including combined hardening, different hardening assumptions, isotropic and kinematic, are discussed below.

5.2.4.1. Isotropic Hardening

With isotropic hardening, the Bauschinger effect cannot be described. As a result, the internal stresses are always overestimated when a metal element undergoes cyclic loading.

5.2.4.1.1. Plastic Loading

As discussed in Section 5.2.2, isotropic hardening, Eq. (5.7), can be expressed as

$$F\left(\sigma_{ij},\bar{\varepsilon}^{p}\right)=f\left(\sigma_{ij}\right)-\bar{\sigma}^{2}\left(\bar{\varepsilon}^{p}\right)=0 \tag{5.16}$$

where $\bar{\sigma}$ and $\bar{\varepsilon}^{p}$ are the effective stress and the effective plastic strain, respectively. The plastic strain increment, due to isotropic hardening, $d\varepsilon_{ij}^{pl,iso}$, in terms of $\bar{\sigma}$ and $\bar{\varepsilon}^{p}$, can be calculated as

$$d\varepsilon_{ij}^{pl,iso}=\frac{\partial\bar{\sigma}}{\partial\sigma_{ij}}d\bar{\varepsilon}^{p} \tag{5.17}$$

Consequently, from Eqs. (5.7) and (5.17), the plastic strain increments, after the differentiation of Eq. (5.7) and setting $\sigma_{33} = 0$, can be calculated as

$$\begin{aligned}
d\varepsilon_{11}^{pl,iso}&=\frac{\partial\bar{\sigma}}{\partial\sigma_{11}}d\bar{\varepsilon}^{p}=\frac{\sigma_{11}-\dfrac{\bar{R}}{\bar{R}+1}\sigma_{22}}{\bar{\sigma}}d\bar{\varepsilon}^{p}\\
d\varepsilon_{22}^{pl,iso}&=\frac{\partial\bar{\sigma}}{\partial\sigma_{22}}d\bar{\varepsilon}^{p}=\frac{\sigma_{22}-\dfrac{\bar{R}}{\bar{R}+1}\sigma_{11}}{\bar{\sigma}}d\bar{\varepsilon}^{p}\\
d\varepsilon_{12}^{pl,iso}&=\frac{\partial\bar{\sigma}}{\partial\sigma_{12}}d\bar{\varepsilon}^{p}=\frac{\dfrac{\left(2\bar{R}+1\right)}{\bar{R}+1}\sigma_{12}}{\bar{\sigma}}d\bar{\varepsilon}^{p}
\end{aligned} \tag{5.18}$$

and the plastic strain increment in the thickness direction will take the form

$$d\varepsilon_{33}^{pl,iso} = \frac{\partial \bar{\sigma}}{\partial \sigma_{33}} d\bar{\varepsilon}^{p} = \frac{\dfrac{-(\sigma_{11}+\sigma_{22})}{\bar{R}+1}}{\bar{\sigma}} d\bar{\varepsilon}^{p} \tag{5.19}$$

Finally, the effective plastic strain increment can be determined by

$$d\bar{\varepsilon}^{p} = \left[\left(d\varepsilon_{11}^{pl,iso}\right)^2 + \left(d\varepsilon_{22}^{pl,iso}\right)^2 + \frac{2\bar{R}}{1+\bar{R}} \left(d\varepsilon_{11}^{pl,iso}\right)\left(d\varepsilon_{22}^{pl,iso}\right) + \frac{2\bar{R}+1}{1+\bar{R}} \left(d\varepsilon_{12}^{pl,iso}\right)^2 \right]^{\frac{1}{2}} \tag{5.20}$$

where $d\varepsilon_{11}^{pl,iso}$, $d\varepsilon_{22}^{pl,iso}$, and $d\varepsilon_{12}^{pl,iso}$ were previously defined.

Furthermore, the total strain increments, due to purely isotropic hardening, are the summation of the elastic part and the plastic part of the deformation history, they can take the form

$$d\varepsilon_{ij}^{total,iso} = d\varepsilon_{ij}^{el} + d\varepsilon_{ij}^{pl,iso} \tag{5.21}$$

Accordingly, from Eqs. (5.3), (5.18) and (5.19), $d\varepsilon_{ij}^{total,iso}$ can be defined as

$$\begin{aligned}
d\varepsilon_{11}^{total,iso} &= d\varepsilon_{11}^{el} + d\varepsilon_{11}^{pl,iso} = \frac{1}{E}\left(d\sigma_{11} - \nu d\sigma_{22}\right) + \frac{\sigma_{11} - \dfrac{\bar{R}}{\bar{R}+1}\sigma_{22}}{\bar{\sigma}} d\bar{\varepsilon}^{p} \\
d\varepsilon_{22}^{total,iso} &= d\varepsilon_{22}^{el} + d\varepsilon_{22}^{pl,iso} = \frac{1}{E}\left(d\sigma_{22} - \nu d\sigma_{11}\right) + \frac{\sigma_{22} - \dfrac{\bar{R}}{\bar{R}+1}\sigma_{11}}{\bar{\sigma}} d\bar{\varepsilon}^{p} \\
d\varepsilon_{12}^{total,iso} &= d\varepsilon_{12}^{el} + d\varepsilon_{12}^{pl,iso} = \frac{1+\nu}{E} d\sigma_{12} + \frac{\dfrac{\left(2\bar{R}+1\right)}{\bar{R}+1}\sigma_{12}}{\bar{\sigma}} d\bar{\varepsilon}^{p}
\end{aligned} \tag{5.22}$$

and the total strain increment in the thickness direction would take the form

$$d\varepsilon_{33}^{total,iso} = d\varepsilon_{33}^{el} + d\varepsilon_{33}^{pl,iso} = \frac{-\nu}{E}\left(d\sigma_{11} + d\sigma_{22}\right) + \frac{\dfrac{-\left(\sigma_{11}+\sigma_{22}\right)}{\bar{R}+1}}{\bar{\sigma}} d\bar{\varepsilon}^{p} \tag{5.23}$$

After setting the equations for the total strain increments, the next step is to derive formulas for the stress increments. Hence, from Eq. (5.16)

$$dF = \frac{\partial F}{\partial \sigma_{ij}} d\sigma_{ij} + \frac{\partial F}{\partial \bar{\varepsilon}^{p}} d\bar{\varepsilon}^{p} = 0 \tag{5.24}$$

and by using the chain rule, $\dfrac{\partial F}{\partial \bar{\varepsilon}^{p}}$ is calculated as

$$\frac{\partial F}{\partial \bar{\varepsilon}^{p}} = \frac{\partial F}{\partial \bar{\sigma}} \frac{d\bar{\sigma}}{d\bar{\varepsilon}^{p}} = 2\bar{\sigma} \frac{d\bar{\sigma}}{d\bar{\varepsilon}^{p}} \tag{5.25}$$

Therefore,

$$dF = \frac{\partial F}{\partial \sigma_{11}} d\sigma_{11} + \frac{\partial F}{\partial \sigma_{22}} d\sigma_{22} + \frac{\partial F}{\partial \sigma_{33}} d\sigma_{33} + \frac{\partial F}{\partial \sigma_{12}} d\sigma_{12} - 2\bar{\sigma} \frac{d\bar{\sigma}}{d\bar{\varepsilon}^{p}} d\bar{\varepsilon}^{p} = 0 \tag{5.26}$$

The term $\dfrac{d\bar{\sigma}}{d\bar{\varepsilon}^{p}}$, in the previous equations, can be defined as the plastic modulus, such that

$$\frac{d\bar{\sigma}}{d\bar{\varepsilon}^{p}} = \bar{K} \tag{5.27}$$

$\bar{K}$ is greater than zero for work-hardening materials and also a variable that depends on the material properties.

Furthermore, using Hill's criterion, Eq. (5.7), one obtains the following set of derivatives

$$\begin{aligned}
\frac{\partial F}{\partial \sigma_{11}} &= \frac{2\left[\left(\bar{R}+1\right)\sigma_{11}-\bar{R}\sigma_{22}\right]}{\left(\bar{R}+1\right)} \\
\frac{\partial F}{\partial \sigma_{22}} &= \frac{2\left[\left(\bar{R}+1\right)\sigma_{22}-\bar{R}\sigma_{11}\right]}{\left(\bar{R}+1\right)} \\
\frac{\partial F}{\partial \sigma_{12}} &= \frac{4\left(2\bar{R}+1\right)}{\left(\bar{R}+1\right)}\sigma_{12} \\
\frac{\partial F}{\partial \sigma_{33}} &= \frac{-2\left[\sigma_{11}+\sigma_{22}\right]}{\left(\bar{R}+1\right)}
\end{aligned} \tag{5.28}$$

Accordingly, by using Eqs. (5.26), (5.27), and (5.28), the yield criterion can take the form

$$\left(\sigma_{11}-\frac{\bar{R}}{\left(\bar{R}+1\right)}\sigma_{22}\right)d\sigma_{11}+\left(\sigma_{22}-\frac{\bar{R}}{\left(\bar{R}+1\right)}\sigma_{11}\right)d\sigma_{22}+\left(\frac{2\left(2\bar{R}+1\right)}{\left(\bar{R}+1\right)}\sigma_{12}\right)d\sigma_{12}-\bar{\sigma}\bar{K}d\bar{\varepsilon}^{p}=0 \tag{5.29}$$

A MAPLE® script was used to implement the equations for the total strain increments Eqs. (5.22) to solve for expressions of $d\sigma_{11}, d\sigma_{22}$, and $d\sigma_{12}$; the script for obtaining such expressions is shown in Appendix (C).

The value of $\bar{K}$ in the previous equations can be determined from the tensile tests. If the effective stress – strain relation follows the Holloman power law

$$\bar{\sigma}=K\left(\varepsilon^{total,iso}\right)^{n} \tag{5.30}$$

where ε^{total} is the total strain, K is the stress coefficient and n is the strain exponent, then

$$\bar{\sigma} = K\left(\varepsilon^{el} + \bar{\varepsilon}^{p}\right)^{n} \tag{5.31}$$

Differentiating the above equation, Eq. (5.31), an expression of $\frac{d\bar{\sigma}}{d\bar{\varepsilon}^{p}}$ can be obtained as

$$\frac{d\bar{\sigma}}{d\bar{\varepsilon}^{p}} = \bar{K} = \frac{nE}{E\left(\frac{\bar{\sigma}}{K}\right)^{\frac{1-n}{n}} - n} \tag{5.32}$$

The detailed derivation of Eq. (5.32) is presented in Appendix (D).

5.2.4.2. Kinematic Hardening

As discussed previously, the kinematic hardening model takes into accounts the change in the yield stress in the reverse loading direction; which is known as the Bauschinger effect. Accordingly, the formulation discussed in this section deals with the translation of the yield surface and the description of the back stress components. Since Mróz multiple – surface criterion is applied in this work, the formulation shown below is carried out for one yield surface and similarly repeated for each consequent yield surface.

5.2.4.2.1. Plastic Loading

As discussed in Section 5.2.2, the yield criterion, Eq. (5.6), when considering kinematic hardening, reduces to the form in Eq. (5.8), where k_o is a constant which corresponds to the size of the yield surface, usually taken as the yield stress, σ_Y, in the uniaxial tension in the planar direction.

Expanding Eq. (5.8), by letting $s_{ij} = \left(\sigma_{ij} - \alpha_{ij}\right)$, where α_{ij} are the back stress components, it can be written in component–form, based on Hill's criterion, as (Gau and Kinzel, 2001)

$$F=(\sigma_{11}-\alpha_{11})^2+(\sigma_{22}-\alpha_{22})^2-\frac{2\bar{R}}{\bar{R}+1}(\sigma_{11}-\alpha_{11})(\sigma_{22}-\alpha_{22})+\frac{2(2\bar{R}+1)}{\bar{R}+1}(\sigma_{12}-\alpha_{12})^2$$
$$+\frac{2}{\bar{R}+1}\left[(\sigma_{33}-\alpha_{33})^2-(\sigma_{11}-\alpha_{11})(\sigma_{33}-\alpha_{33})-(\sigma_{22}-\alpha_{22})(\sigma_{33}-\alpha_{33})\right]-k_o^2=0 \tag{5.33}$$

The plastic strain increment can be determined by (Khan and Huang, 1995)

$$d\varepsilon_{ij}^{pl,kin}=\frac{1}{K^p}\frac{\dfrac{\partial F}{\partial\sigma_{ij}}\dfrac{\partial F}{\partial\sigma_{kl}}d\sigma_{kl}}{\dfrac{\partial F}{\partial\sigma_{mn}}\dfrac{\partial F}{\partial\sigma_{mn}}} \tag{5.34}$$

where K^p is a proportionality factor and is called the plastic modulus. From Eq. (5.34) and applying plane stress conditions $(\sigma_{13}=\sigma_{31}=\sigma_{23}=\sigma_{32}=\sigma_{33}=0)$, the plastic strain increment can be computed from

$$d\varepsilon_{ij}^{pl,kin}=\frac{1}{K^p}\frac{\dfrac{\partial F}{\partial\sigma_{ij}}\left[\dfrac{\partial F}{\partial\sigma_{11}}d\sigma_{11}+2\dfrac{\partial F}{\partial\sigma_{12}}d\sigma_{12}+\dfrac{\partial F}{\partial\sigma_{22}}d\sigma_{22}\right]}{\left(\dfrac{\partial F}{\partial\sigma_{11}}\right)^2+2\left(\dfrac{\partial F}{\partial\sigma_{12}}\right)^2+\left(\dfrac{\partial F}{\partial\sigma_{22}}\right)^2+\left(\dfrac{\partial F}{\partial\sigma_{33}}\right)^2} \tag{5.35}$$

Carrying out the differentiation of the yield function, Eq. (5.33), with respect to the stress components, in a similar manner as in Eq. (5.28), one will obtain

$$\frac{\partial F}{\partial \sigma_{11}} = \frac{2\left[\left(\bar{R}+1\right)\left(\sigma_{11}-\alpha_{11}\right)-\bar{R}\left(\sigma_{22}-\alpha_{22}\right)\right]}{\left(\bar{R}+1\right)}$$
$$\frac{\partial F}{\partial \sigma_{22}} = \frac{2\left[\left(\bar{R}+1\right)\left(\sigma_{22}-\alpha_{22}\right)-\bar{R}\left(\sigma_{11}-\alpha_{11}\right)\right]}{\left(\bar{R}+1\right)}$$
$$\frac{\partial F}{\partial \sigma_{12}} = \frac{4\left(2\bar{R}+1\right)}{\left(\bar{R}+1\right)}\left(\sigma_{12}-\alpha_{12}\right) \tag{5.36}$$
$$\frac{\partial F}{\partial \sigma_{33}} = \frac{-2\left[\left(\sigma_{11}-\alpha_{11}\right)+\left(\sigma_{22}-\alpha_{22}\right)\right]}{\left(\bar{R}+1\right)}$$

Accordingly, by the use of Eqs. (5.35) and (5.36), the plastic strain increments can be defined as

$$d\varepsilon_{11}^{pl,kin} = \frac{\mathbb{C}_1}{K^p}\frac{2\left[\left(\bar{R}+1\right)\left(\sigma_{11}-\alpha_{11}\right)-\bar{R}\left(\sigma_{22}-\alpha_{22}\right)\right]}{\left(\bar{R}+1\right)}$$
$$d\varepsilon_{22}^{pl,kin} = \frac{\mathbb{C}_1}{K^p}\frac{2\left[\left(\bar{R}+1\right)\left(\sigma_{22}-\alpha_{22}\right)-\bar{R}\left(\sigma_{11}-\alpha_{11}\right)\right]}{\left(\bar{R}+1\right)}$$
$$d\varepsilon_{12}^{pl,kin} = \frac{\mathbb{C}_1}{K^p}\frac{4\left(2\bar{R}+1\right)\left(\sigma_{12}-\alpha_{12}\right)}{\left(\bar{R}+1\right)} \tag{5.37}$$
$$d\varepsilon_{33}^{pl,kin} = \frac{\mathbb{C}_1}{K^p}\frac{-2\left[\left(\sigma_{11}-\alpha_{11}\right)+\left(\sigma_{22}-\alpha_{22}\right)\right]}{\left(\bar{R}+1\right)}$$

where $\mathbb{C}_1$ is defined as a function of the stress increments, $d\sigma_{11}, d\sigma_{22}$, and $d\sigma_{12}$, and is written as

$$\mathbb{C}_1 = \frac{\left[\frac{\partial F}{\partial \sigma_{11}}d\sigma_{11}+2\frac{\partial F}{\partial \sigma_{12}}d\sigma_{12}+\frac{\partial F}{\partial \sigma_{22}}d\sigma_{22}\right]}{\left(\frac{\partial F}{\partial \sigma_{11}}\right)^2+2\left(\frac{\partial F}{\partial \sigma_{12}}\right)^2+\left(\frac{\partial F}{\partial \sigma_{22}}\right)^2+\left(\frac{\partial F}{\partial \sigma_{33}}\right)^2} \tag{5.38}$$

Furthermore, to obtain the total strain increments, for a purely kinematic hardening model, components of the plastic strain increments should be added to those of the elastic strains, so that

$$d\varepsilon_{ij}^{total,kin} = d\varepsilon_{ij}^{el} + d\varepsilon_{ij}^{pl,kin} \tag{5.39}$$

which, from Eq. (5.2) and in terms of the plastic strain components in Eq. (5.37) and Eq. (5.38) gives

$$\begin{aligned} d\varepsilon_{11}^{total,kin} &= \frac{1}{E}\left(d\sigma_{11} - \nu d\sigma_{22}\right) + d\varepsilon_{11}^{pl,kin} \\ d\varepsilon_{22}^{total,kin} &= \frac{1}{E}\left(d\sigma_{22} - \nu d\sigma_{11}\right) + d\varepsilon_{22}^{pl,kin} \\ d\varepsilon_{12}^{total,kin} &= \frac{1+\nu}{E} d\sigma_{12} + d\varepsilon_{12}^{pl,kin} \end{aligned} \tag{5.40}$$

and the total strain increment in the thickness direction would take the form

$$d\varepsilon_{33}^{total,kin} = \frac{-\nu}{E}\left(d\sigma_{11} + d\sigma_{22}\right) + d\varepsilon_{33}^{pl,kin} \tag{5.41}$$

Substituting Eqs. (5.37) and Eq. (5.38) into Eqs. (5.40) and solving simultaneously, using a MAPLE® script, expressions for stress increments $d\sigma_{11}$, $d\sigma_{22}$, and $d\sigma_{12}$ can be obtained. The MAPLE® script for obtaining such expressions is shown in Appendix (E).

To completely define the stress increment, K^p must be defined. In uniaxial tension, if the test is performed in the rolling direction, then σ_{11} has a non-zero value and $\sigma_{22} = \sigma_{33} = \sigma_{12} = 0$; therefore, from Eq. (5.35)

$$d\varepsilon_{11}^{pl,kin} = \frac{1}{K^p} \frac{\left(1+\bar{R}\right)^2}{2\left(\bar{R}^2 + \bar{R} + 1\right)} d\sigma_{11} \tag{5.42}$$

and hence,

$$K^p = \frac{d\sigma_{11}}{d\varepsilon_{11}^{pl,kin}} \frac{\left(1+\bar{R}\right)^2}{2\left(\bar{R}^2+\bar{R}+1\right)} \tag{5.43}$$

However, as a generalization of the uniaxial notation, the parameter K^p is defined as (Mróz, 1967), which is evaluated at each increment.

$$K^p = \frac{d\boldsymbol{\sigma} \cdot d\boldsymbol{\varepsilon}^{pl,kin}}{\left(d\boldsymbol{\varepsilon}^{pl,kin}\right)^2} = \frac{d\sigma_{ij} d\varepsilon_{ij}^{pl,kin}}{d\varepsilon_{ij}^{pl,kin} d\varepsilon_{ij}^{pl,kin}} \tag{5.44}$$

In order to completely define the plastic strain increment and, accordingly, the stress increment, the back stress, α_{ij}, must be calculated. Based on Ziegler's kinematic hardening rule, the back stress increment, $d\alpha_{ij}$, increment is obtained from (Ziegler, 1959)

$$d\alpha_{ij} = \left(\sigma_{ij} - \alpha_{ij}\right) d\mu \tag{5.45}$$

where dμ is a positive scalar quantity that is determined by the condition that a point on the yield surface remains on the yield surface in plastic flow (Ziegler, 1959). This condition for dμ is given by

$$\left(d\sigma_{ij} - d\alpha_{ij}\right) \frac{\partial F}{\partial \sigma_{ij}} = 0 \tag{5.46}$$

and from Eq. (5.45) follows at once

$$d\mu = \frac{\left(\frac{\partial F}{\partial \sigma_{ij}}\right) d\sigma_{ij}}{(\sigma_{kl} - \alpha_{kl}) \frac{\partial F}{\partial \sigma_{kl}}} \tag{5.47}$$

which leads to

$$d\mu = \frac{\left\{ \begin{array}{l} \left[(\sigma_{11} - \alpha_{11}) - \frac{\bar{R}}{1+\bar{R}} (\sigma_{22} - \alpha_{22}) \right] d\sigma_{11} + \left[\frac{2(2\bar{R}+1)}{(\bar{R}+1)} (\sigma_{12} - \alpha_{12}) \right] d\sigma_{12} \\ + \left[(\sigma_{22} - \alpha_{22}) - \frac{\bar{R}}{1+\bar{R}} (\sigma_{11} - \alpha_{11}) \right] d\sigma_{22} \end{array} \right\}}{\mathbb{C}_2} \tag{5.48}$$

where

$$\begin{aligned} \mathbb{C}_2 = {} & (\sigma_{11} - \alpha_{11}) \left[(\sigma_{11} - \alpha_{11}) - \frac{\bar{R}}{1+\bar{R}} (\sigma_{22} - \alpha_{22}) \right] + (\sigma_{12} - \alpha_{12}) \left[\frac{2(2\bar{R}+1)}{(\bar{R}+1)} (\sigma_{12} - \alpha_{12}) \right] \\ & + (\sigma_{22} - \alpha_{22}) \left[(\sigma_{22} - \alpha_{22}) - \frac{\bar{R}}{1+\bar{R}} (\sigma_{11} - \alpha_{11}) \right] \end{aligned} \tag{5.49}$$

5.2.4.2.2. Unloading Process and Reverse Loading

For the elastic unloading, the same principle discussed in Section 5.2.1.2 can be applied. Also, the same formulation for plastic loading, discussed in Section 5.2.4.2.1, can be used for the reverse loading process. The reverse loading is determined when the yield function is evaluated and

$$F(\sigma_{ij}) = 0 \tag{5.50}$$

Accordingly, in a similar manner, Eqs. (5.37) to (5.40) are used to calculate the stress increments in the unloading – reverse loading part. Furthermore, Eqs. (5.45) to (5.49) are

used to determine the back stress increment during unloading and the reverse loading processes.

5.2.4.3. Combined Isotropic-Kinematic Hardening

As mentioned in Section 5.2.1, the combined hardening model, utilized in this work, consists of both isotropic and kinematic hardening components with multiple – yield surface formulation. Accordingly, each yield surface, when activated or becomes current, is allowed to expand and to translate during the plastic deformation stage.

Once a yield surface is activated, it experiences uniform expansion and rigid body translation until it touches a subsequent surface. At that point, the subsequent surface is activated. All other surfaces within the activated surface only experience translation when the activated surface translates in the stress space.

Therefore, the total strain increment in each step, $d\varepsilon_{ij}^{total,combined}$, consists of two parts, an isotropic portion, $d\varepsilon_{ij}^{total,iso}$, that accounts for the uniform change in size and a kinematic portion, $d\varepsilon_{ij}^{total,kin}$, that accounts for the translation of the yield surface in the stress space, so that

$$d\varepsilon_{ij}^{total,combined} = Xd\varepsilon_{ij}^{total,iso} + (1-X)d\varepsilon_{ij}^{total,kin} \tag{5.51}$$

where X is a weighting factor between 0 and 1, and $d\varepsilon_{ij}^{total,iso}$ and $d\varepsilon_{ij}^{total,kin}$ are the total strains due to isotropic and kinematic hardening, respectively. When X = 0, the model reduces to pure kinematic hardening and when X = 1 the model reduces to a pure isotropic hardening. In this study, it is assumed that each component of the strain increments, isotropic and kinematic, has the same contribution to the final total strain increment; therefore, the value of X was set to 0.5.

To account for the isotropic hardening portion; the stress and strain increments due to the expansion of the yield surface are obtained from the isotropic hardening formulation presented in Section 5.2.4.1. Thus, the strain increments are computed using Eq. (5.22) and accordingly the corresponding stress increments. The value of the parameter $\bar{K}$ in Eq. (5.27) is obtained at each increment for the activated yield surface.

Since yield surfaces cannot penetrate each other, the maximum size of the activated yield surface $f^{(l)}$ was set to be ninety per cent, 90%, of the size of the subsequent yield surface $f^{(l+1)}$ based on the experimental setup that in reverse loading the stress-strain curves terminate after a plastic strain of less than five per cent, 5%, and the steady portion of the curve can be either a continuation or parallel to the initial stress-strain curve (Ragai and Nemes, 2005, Gau and Kinzel, 2001, and Tan *et al.*, 1994).

To account for the kinematic hardening portion, the concept of multiple yield surfaces is utilized in this work, based on Mróz (1967) and Gau and Kinzel (2001) models. In Mróz model, it is assumed that beginning from zero stress until the initiation of yielding, all yield surfaces remain fixed and are centered at the origin of the stress space, Fig. (5.6a). Upon further loading, the initial yield surface $f^{(1)}$, corresponds to σ_Y of the material in the planar direction, begins to move until it touches the second surface $f^{(2)}$, corresponds to $\sigma_o^{(2)}$, which is the size of the second yield surface, and so on. To describe mathematically the motion of the surfaces, in case, for example, two surfaces $f^{(l)}$ and $f^{(l+1)}$, the first surface is defined by the equation

$$F\left(\sigma_{ij}-\alpha_{ij}^{f^{(l)}}\right)-\left(\sigma_o^{f^{(l)}}\right)^2=0 \tag{5.52}$$

and the subsequent surface is defined by

$$F\left(\sigma_{ij}-\alpha_{ij}^{f^{(l+1)}}\right)-\left(\sigma_o^{f^{(l+1)}}\right)^2=0 \tag{5.53}$$

where $\sigma_o^{f^{(l)}}$ and $\sigma_o^{f^{(l+1)}}$ denote the size of surfaces $f^{(l)}$ and $f^{(l+1)}$, respectively, which are identified from the uniaxial loading.

If a stress point, $\sigma_{ij}^{f^{(l)}}$, lies on the surface $f^{(l)}$, then the instantaneous translation of $f^{(l)}$ will occur along the same direction of the outward normal to that surface until it reaches a stress point, $\sigma_{ij}^{f^{(l+1)}}$, that lies on the surface $f^{(l+1)}$. Therefore,

$$\sigma_{ij}^{f^{(l+1)}} - \alpha_{ij}^{f^{(l+1)}} = \frac{\sigma_o^{f^{(l+1)}}}{\sigma_o^{f^{(l)}}}\left(\sigma_{ij}^{f^{(l)}} - \alpha_{ij}^{f^{(l)}}\right) \tag{5.54}$$

and the translation of the first surface $f^{(l)}$ can be described mathematically as

$$d\alpha_{ij}^{f^{(l)}} = \frac{d\mu}{\sigma_o^{f^{(l)}}}\left[\left(\sigma_o^{f^{(l+1)}} - \sigma_o^{f^{(l)}}\right)\sigma_{ij}^{f^{(l)}} - \left(\alpha_{ij}^{f^{(l)}}\sigma_o^{f^{(l+1)}} - \alpha_{ij}^{f^{(l+1)}}\sigma_o^{f^{(l)}}\right)\right] \tag{5.55}$$

During such process, all other surfaces except the initial one remain stationary. If the material is further loaded, the two surfaces $f^{(l)}$ and $f^{(l+1)}$ translate together, while other surfaces remain fixed in position, until they touch the third surface $f^{(l+2)}$. If the load continues, this process is repeated for the consecutive yield surfaces, as shown in Fig. (5.6b).

The parameter dμ in Eq. (5.47) is determined based on the condition that the stress point remains on the yield surface, so that

$$\left(d\alpha_{ij}^{f^{(l)}} - d\sigma_{ij}\right)\frac{\partial F}{\partial \sigma_{ij}} = 0 \tag{5.56}$$

and; therefore,

$$\frac{\partial F^{f^{(l)}}}{\partial \sigma_{ij}} d\sigma_{ij} + \frac{\partial F^{f^{(l)}}}{\partial \alpha_{ij}} d\alpha_{ij} = \frac{\partial F^{f^{(l)}}}{\partial \sigma_{ij}} d\sigma_{ij} - \frac{\partial F^{f^{(l)}}}{\partial \sigma_{ij}} d\alpha_{ij}$$
$$= \frac{\partial F^{f^{(l)}}}{\partial \sigma_{ij}} d\sigma_{ij} - \frac{\partial F}{\partial \sigma_{ij}} \left(\sigma_{ij}^{f^{(l+1)}} - \sigma_{ij} \right) d\mu^{f^{(l)}} = 0 \tag{5.57}$$

Hence, Eq. (5.47), for the parameter dμ becomes

$$d\mu = \frac{\left(\frac{\partial F}{\partial \sigma_{ij}} \right) d\sigma_{ij}}{\left(\sigma_{kl}^{f^{(l+1)}} - \sigma_{kl}^{f^{(l)}} \right) \frac{\partial F}{\partial \sigma_{kl}}} \tag{5.58}$$

If unloading and reverse loading is initiated, all yield surfaces remain still during elastic unloading until yielding occurs in the reverse direction and reverse loading begins. In that stage, the first surface $f^{(l)}$ will translate alone until it touches the second surface $f^{(l+1)}$, Fig. (5.6c), and upon further loading the two surfaces translate together until they touch the third one, $f^{(l+2)}$, Fig. (5.6d), and so on. If the reverse loading increases, the surfaces translate together by a similar manner.

The sizes of the yield surfaces, $\sigma_o^{f^{(l)}}$, $\sigma_o^{f^{(l+1)}}$, ... are defined from the uniaxial tension tests, as will be shown later in Section 5.3.2 for the materials included in this research. Figure (5.7) shows the intervals where the size of each surface is determined with respect to position of the stress – strain curve.

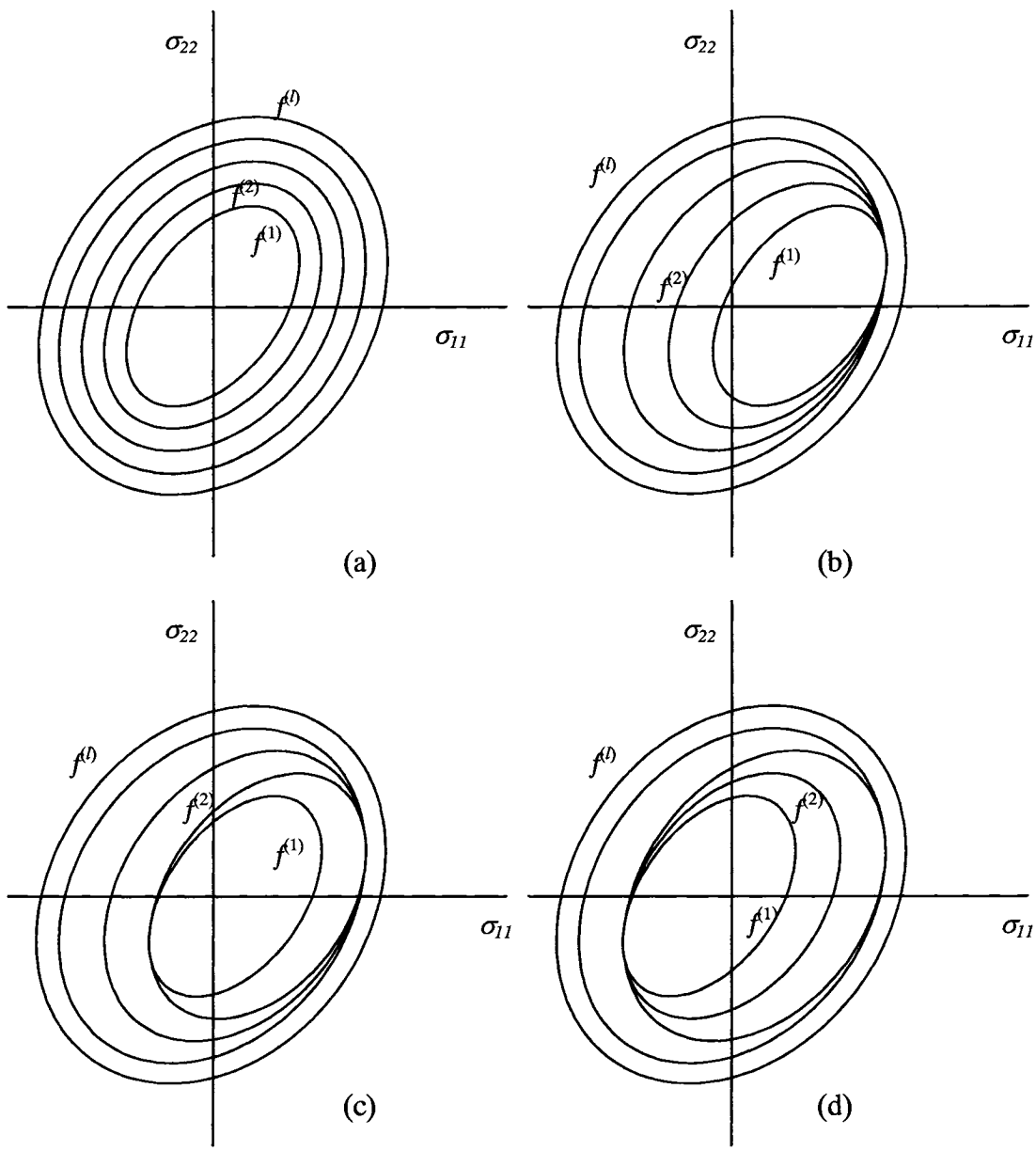

Fig. (5.6) Representation of the stress space for Mróz yield surfaces (a) before plastic deformation, (b) after further plastic deformation takes place, (c) reverse loading, and (d) after further reverse loading

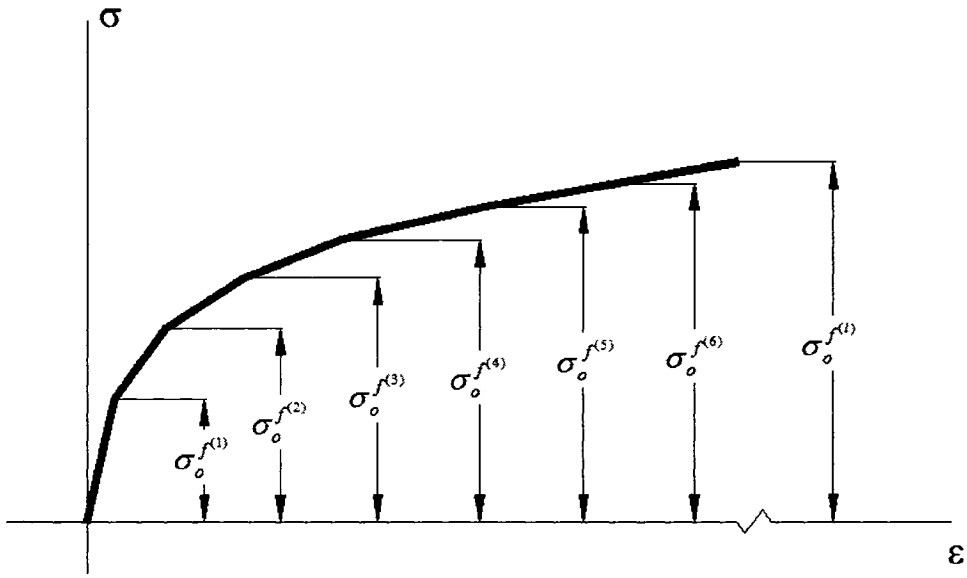

Fig. (5.7) Determination of the initial sizes of the yield surfaces

One of the advantages of using the Mróz model is that it captures the nonlinear hardening behaviour and smooth transition from the elastic to plastic regime realistically well (Chun *et al.*, 2002a). Also, the Mróz model has the advantage of describing the Bauschinger effect as well as the cyclic hardening or softening of the material (Chaboche, 1986). However, since only the bounding surface is allowed to expand, it puts a limitation on the model. This weakness in the Mróz model was dealt with in this current study, as explained before, by allowing the activated yield surface to expand and translate at the same time while all the surfaces within that surface only experience translation. This adds more difficulty in formulating the model; however, it provides a more accurate reflection of the material behaviour.

The current study utilizes Hill's 1948 yield criterion, and Ziegler's kinematic hardening model is implemented for the translation of the yield surface. Accordingly, for the kinematic hardening portion, the plastic strain increments are obtained using Eq. (5.35) where the plastic modulus K^p is determined for each yield surface from Eq. (5.44). Furthermore, the back stress increment for each surface is calculated using the Mróz model from Eqs. (5.45) and (5.47). After two surfaces are in contact, i.e. $f^{(l)}$ and $f^{(l+1)}$, the plastic modulus K^p for the surface $f^{(l+1)}$ is used in the calculations of the stress and

back stress increments as long as this surface is activated, until $f^{(l+2)}$ is in contact with $f^{(l)}$ and $f^{(l+1)}$. Then, the plastic modulus K^p for the surface $f^{(l+2)}$ is used, and so on. It is worth mentioning that if the stress state is between two yield surfaces $f^{(l)}$ and $f^{(l+1)}$, the plastic modulus K^p for yield surface $f^{(l)}$ is used in the calculations. Furthermore, when the loading process ends, the current state of the yield surfaces is considered to be the initial state for the unloading and reverse loading process.

The mathematical expressions discussed above, for the combined hardening model, were implemented into the finite element code ABAQUS through a user subroutine. A detailed discussion of the finite element model is to be discussed in the next section.

5.3. Numerical Implementation

5.3.1. Material Model

The general purpose finite element package ABAQUS is used in this study to perform the required modeling tasks. One of the powerful features of that package is its ability to implement various constitutive models and material behaviour through user-defined subroutines, which adds flexibility in defining the behaviour of numerous materials that simple elastic-plastic assumptions fail to predict.

In the literature review, it was shown that for better prediction of the material behaviour, the Bauschinger effect must be considered for metals that undergo cyclic loading. The general purpose code, ABAQUS, includes two kinematic hardening models, which can describe the Bauschinger effect, namely linear kinematic and nonlinear isotropic/kinematic models. However, these existing models can only be used within limitations. The linear kinematic hardening model is attained by assuming a linearized plastic range with a constant work-hardening; which affects the ability of the model to provide accurate results. The second model, with isotropic/kinematic hardening

assumption, provides better approximation of the material behaviour; however, it can only be used with the von Mises yield criterion, assuming a perfectly isotropic material (ABAQUS, 2003).

In summary, the yield criteria implemented within the general purpose code, ABAQUS, are von Mises for isotropic materials and Hill's for both normal and planar anisotropic materials. As for the hardening models, it includes isotropic hardening, Prager and Ziegler linear kinematic hardening, and Chaboche and Lemaitre nonlinear isotropic/kinematic hardening for isotropic materials. The combination of material anisotropy with nonlinear combined hardening model is not available in the general purpose package (ABAQUS, 2003). Therefore, for accurate description of the material anisotropic behaviour, taking into account the cyclic loading conditions, a more precise model for springback prediction needs to be implemented into the finite element package; which will be a user-defined subroutine.

Material behaviour obtained from the tensile testing experiments, material constitutive model, and the hardening rule presented previously are implemented into finite element simulations to study the effect of material anisotropy on springback in the sheet metal after forming. The parameters being passed into the model are the stress-strain curve, the hardening parameters, K and n, as well as the normal anisotropy parameter, $\bar{R}$, for each material.

The material user-defined subroutine consists of a constitutive model that can be used for a more accurate description of the real material behaviour. The subroutine is called at every integration point and the data passed through it, from the last converged increment, are stress, strain, internal variables, and the total strain increment while the output of the code is the updated stress and the internal variables, plus the material stiffness matrix, $\frac{d\boldsymbol{\sigma}}{d\boldsymbol{\varepsilon}}$, when the implicit time integration is adopted.

One of the drawbacks of using the Mróz multiple yield surface concept is the need for additional memory to store the position of all the yield surfaces. As mentioned in Section 2.4.3, describing the actual material behaviour using the Mróz model requires a large number of yield surfaces, each surface requires the storage of a tensor variable and a scalar quantity. This in return affects the time needed for calculation. Therefore, to simplify the modeling problem, only ten (10) yield surfaces were created. The first yield surface is the initial one without the back stress component and the last one is the one that corresponds to a true strain of twenty five per cent, extrapolated from the experimental data. This adds more surfaces within a limited region to better capture the material behaviour, as shown in Fig. (5.8).

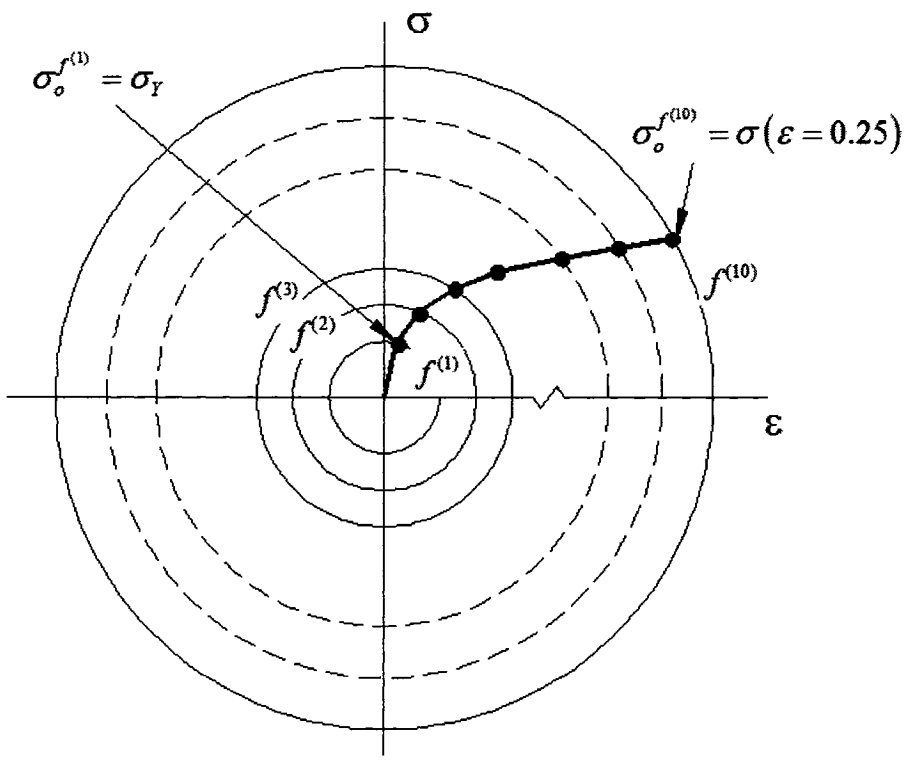

Fig. (5.8) Uniaxial stress – strain curve in multi-yield surface model

It is worth mentioning that the same concept of creating yield surfaces was used by Gau and Kinzel (2001) by creating twenty (20) yield surfaces. The first one represents the initial yield and the bounding one corresponds to a true strain of fifty per cent. However,

their model was not implemented into a finite element code. In this study, yield surfaces are generated from the material behaviour obtained from experiments, as discussed in Section 4.1, with the corresponding $\bar{R}$-value for each material. In summary, the material data defined in the model included the elastic behaviour in terms of the elastic modulus, E and Poisson's ratio, ν. The plastic behaviour was defined from the discretized stress–strain curve starting at zero plastic strain. The hardening parameters K and n obtained from the approximated power law were defined. Finally, the normal anisotropy parameter $\bar{R}$ was also implemented in the model.

The yield surfaces generated for the SS410 sheets are shown in Fig. (5.9); however, only the initial and the bounding surface, not the nested surfaces, for the other materials included in this study, are shown for visualization purposes in Figs. (5.10) and (5.11). Other aspects of the finite element model, such as geometry or element type are discussed in the next sections.

After the yield surfaces are generated and stored, upon loading, the corresponding yield surface is activated and its corresponding parameters are calculated. The value of $\bar{K}$ is obtained at each increment (m), as shown in Fig. (5.12), and is used to determine the stress and the strain values at the succeeding increment (m+1), so that

$$\bar{K}(m) = \frac{d\bar{\sigma}(m)}{d\bar{\varepsilon}^{p}(m)} \tag{5.59}$$

and accordingly, the total stresses and equivalent strains for the proceeding increment (m+1) are computed as

$$\begin{aligned} \sigma_{11}(m+1) &= \sigma_{11}(m) + d\sigma_{11} \\ \sigma_{22}(m+1) &= \sigma_{22}(m) + d\sigma_{22} \\ \sigma_{12}(m+1) &= \sigma_{12}(m) + d\sigma_{12} \\ \bar{\varepsilon}^{p}(m+1) &= \bar{\varepsilon}^{p}(m) + d\bar{\varepsilon}^{p} \end{aligned} \tag{5.60}$$

Furthermore, after determining the parameter dμ, using Eq. (5.47), and similar to Eq. (5.45), the new center of the yield surface is calculated by

$$\alpha_{ij}(m+1) = \alpha_{ij}(m) + d\alpha_{ij} \tag{5.61}$$

where $(m+1)$ is the current increment and (m) is the previous one.

The flow chart shown in Fig. (5.13) shows where the user-defined code fits into the finite element analysis step. At the first iteration of an increment, the user-defined code is called twice. During the first call, the initial stiffness matrix is formed using the current configuration of the model at the start of the increment. During the second call, a new stiffness matrix is created based on the updated configuration of the model. In the subsequent iterations, the user-defined code is called only once to calculate the updated stiffness. In these iterations, the corrections to the model's configurations are calculated using the stiffness previously calculated at the end of a previous iteration. The detailed function of the user-defined code developed in this study is presented in the flow chart shown in Fig. (5.14).

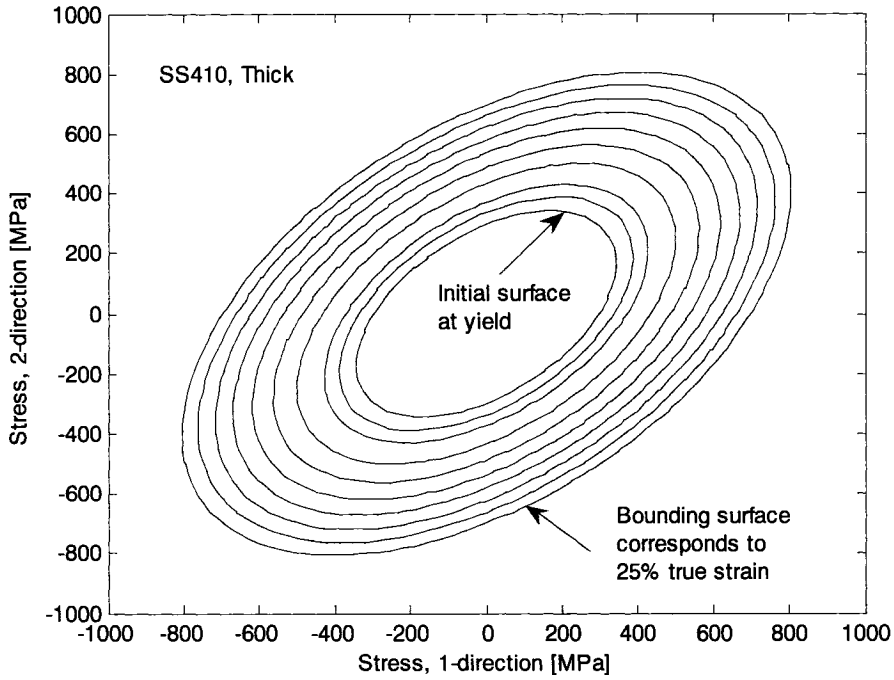

(a)

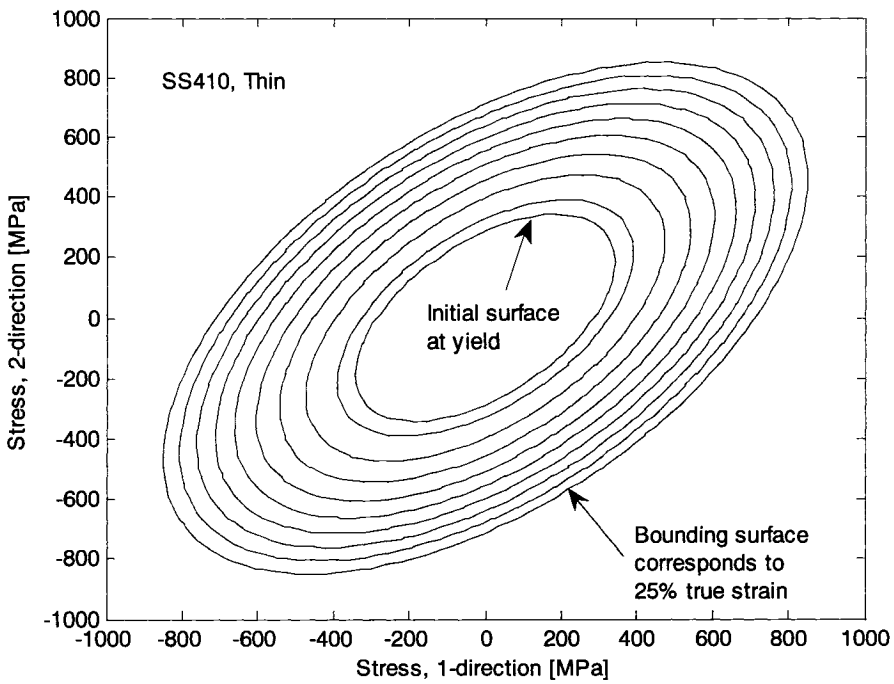

(b)

Fig. (5.9) Generated yield surfaces for (a) thick SS410, and (b) thin SS410

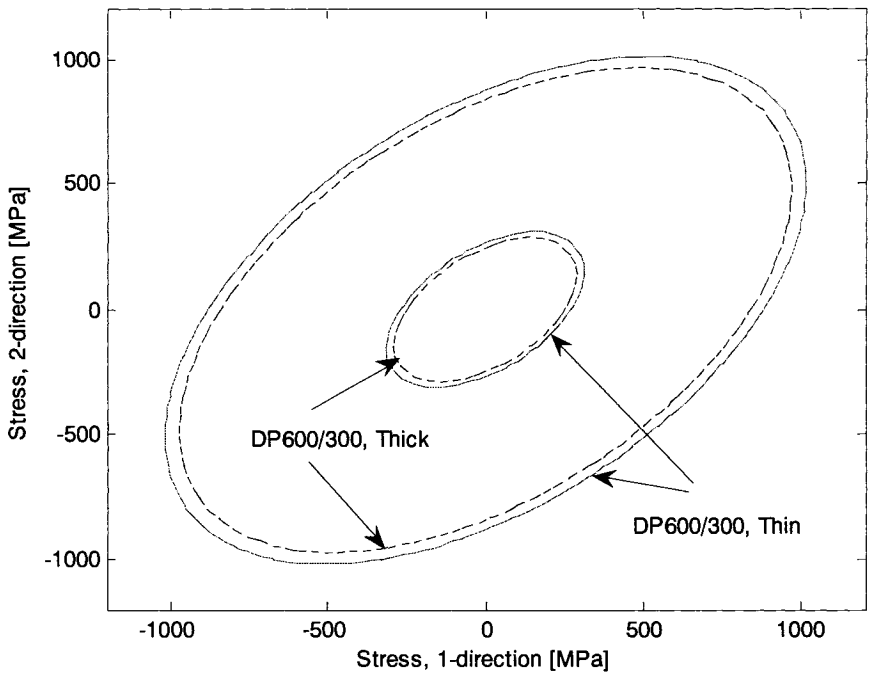

(a)

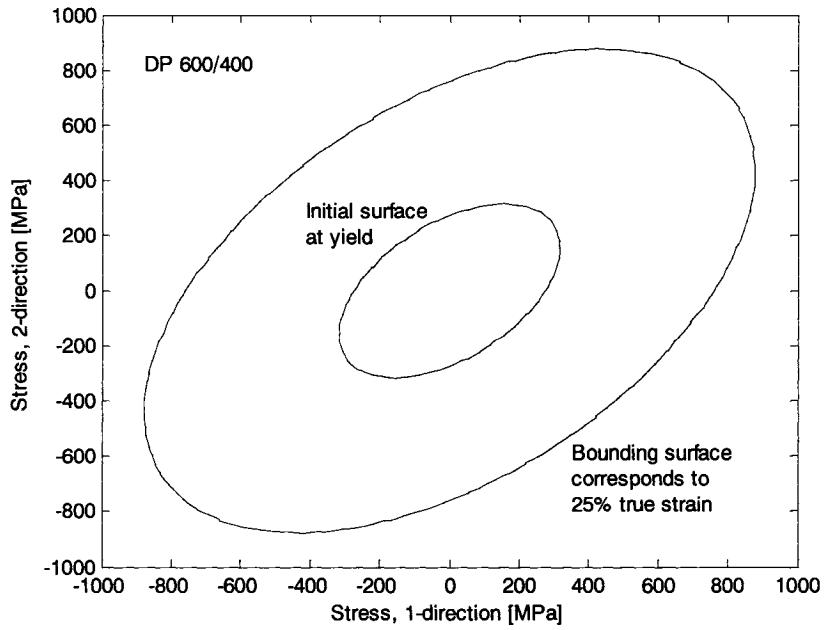

(b)

Fig. (5.10) Initial and bounding yield surfaces for (a) thick and thin DP600/300, and (b) DP600/400

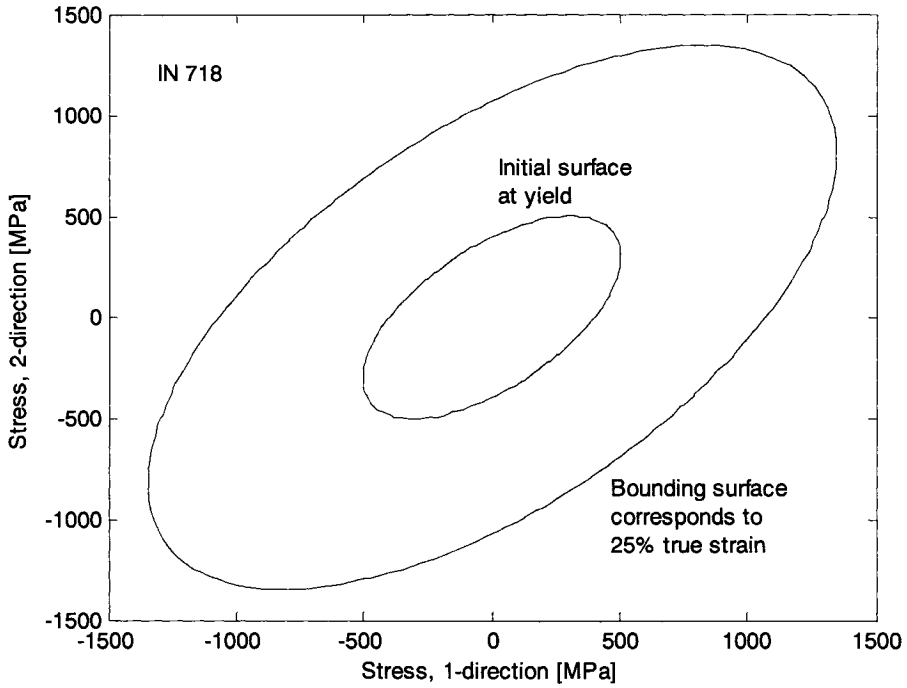

Fig. (5.11) Initial and bounding yield surfaces for IN18

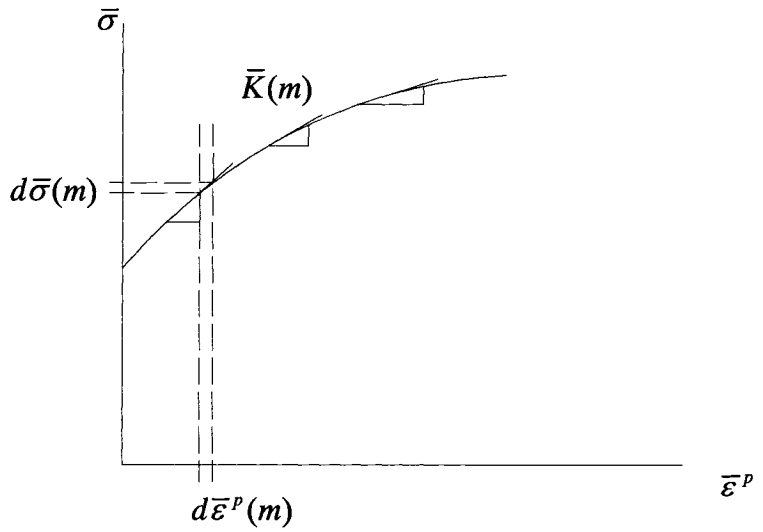

Fig. (5.12) Defining $\bar{K}$ for each increment

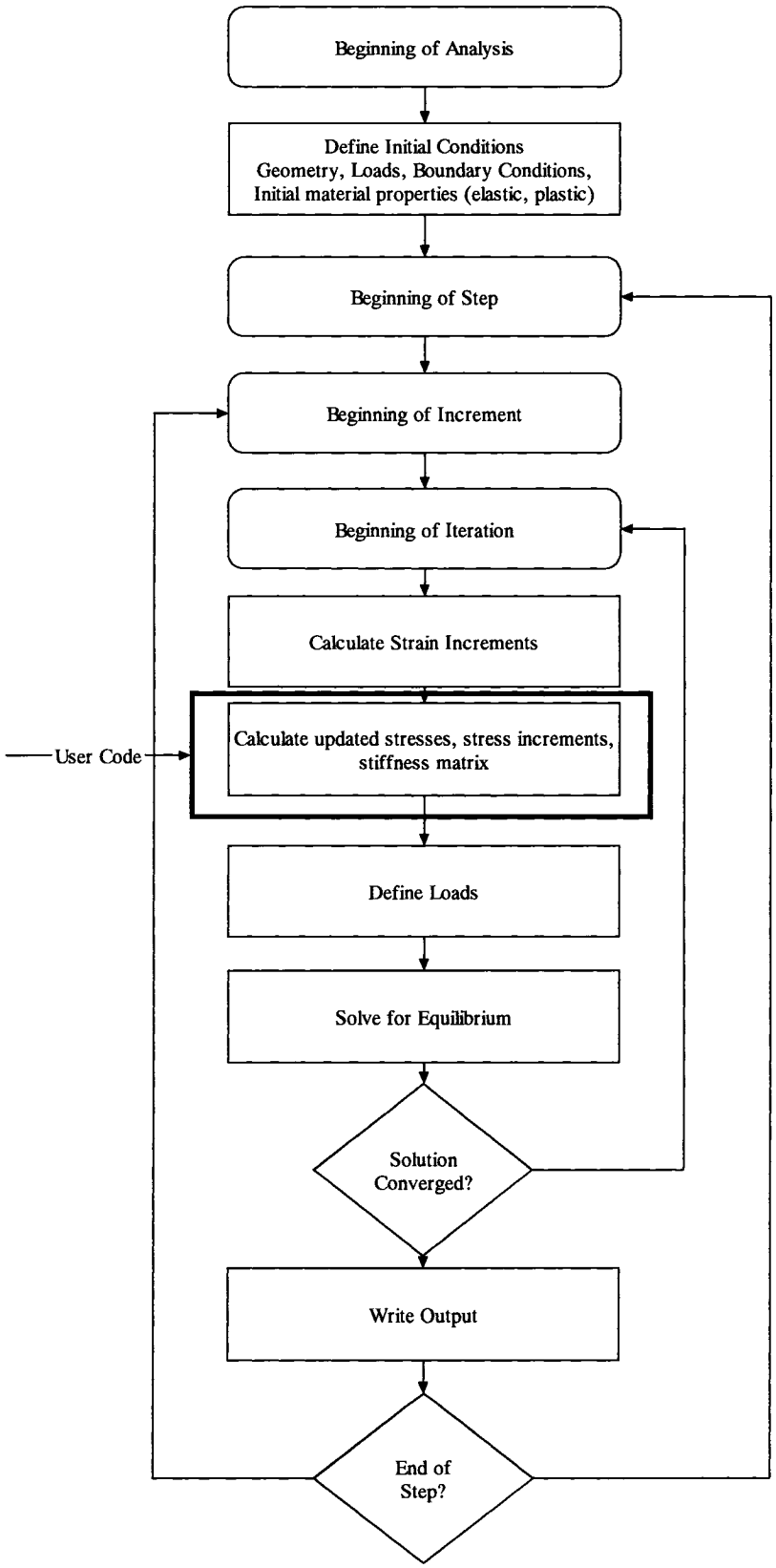

Fig. (5.13) Global flow chart for a finite element step

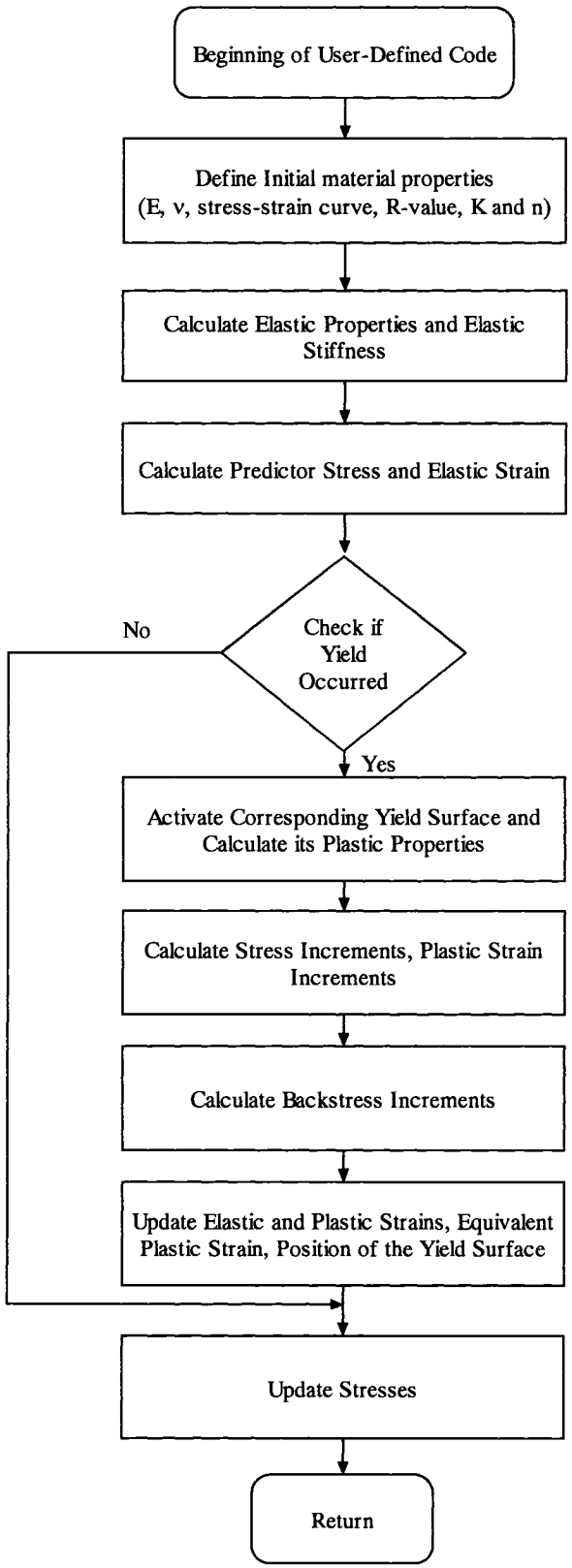

Fig. (5.14) Flow chart for the user-defined code

5.3.2. Flow Stress Evolution

During deformation, the material is deformed at a constant strain rate during the specified time step at increment (m). At the end of that increment, a trial predictor stress for the next increment (m+1) is calculated and the yield stress function can be written as

$$F(m+1) = F\left[\sigma_{ij}(m+1), \bar{\varepsilon}^{p}(m+1)\right] = 0 \tag{5.62}$$

where F(m+1) is a trial state of yielding. This trial state is computed assuming that the entire strain within the increment is elastic, so that

$$F(m+1) = F\left[\sigma_{ij}(m+1), \bar{\varepsilon}^{p}(m)\right] = 0 \tag{5.63}$$

In order to reach the stage of the flow stress evolution when the material deforms plastically the trial yield stress function must be greater than zero, so that

$$F(\sigma_{ij})(m+1) > 0 \tag{5.64}$$

Therefore, the stress is scaled back to the yield surface. After scaling back the stress to the yield surface, the equivalent plastic strain increment $d\bar{\varepsilon}^{p}$ is then calculated.

If the trial predictor stress is outside the yield surface, the material is plastically deformed until the stress value is returned to the actuated yield surface along the direction defined by the vector from the center of the yield surface to the elastic trial stress (ABAQUS, 2003).

During each iteration, the plastic strain increment is adjusted until the equivalent plastic strain is computed and updated. The remaining elastic strain increments are then used to calculate a new value for the trial stress for the subsequent increment.

5.3.3. Shell Elements

Using shell elements in sheet metal forming simulations is a common procedure that has been utilized recently. They are considered as a compromise between continuum and membrane elements. The reason is that shell elements require less computational time than continuum elements while the effect of bending is taken into account. Many researchers have used shell elements in their work; for example, Tang *et al.* (2001) modeled the S-rail forming and the subsequent springback using triangular shell elements, Ragai and Younan (2001 and 2003) used ABAQUS axisymmetric shell elements in modeling superplastic forming (SPF) operations; and Fereshteh-Saniee and Montazeran (2003) used ANSYS shell-51 element type in their deep drawing simulations;

Specifically, ABAQUS element type S4R, a four-node-reduced-integration general purpose shell element, has been used extensively in sheet metal forming simulations. Huang *et al.* (2001) used ABAQUS in modeling the bending-unbending springback process using two types of elements, S4R and eight-node-biquadratic plane strain elements (CPE8). They reported that, in general, the strain histories predicted by both element types are similar. However, the difference between shell and plane strain elements in predicting stress distribution increases with the increase of curvature. Higher accuracy in predicting stresses and strains was obtained using the models with the S4R shell elements.

Moreover, Wang and Cao (2000) used S4R elements in modeling and predicting side-wall wrinkling in sheet metal forming; Song et el. (2001) modeled the springback in flanging using the same type of element; Chun *et al.* (2002a) also used it in modeling draw-bead tests; Geng *et al.* (2002) used this type of element in modeling the reverse bend tests; and Li *et al.* (2002a) used it in modeling the springback of the draw-bending tests.

In addition, Rasmussen *et al.* (2003) used the same type of elements to model the compression of stainless steel plates. Wang *et al.* (2004b) used S4R elements in modeling creep and springback of aluminum sheets. Also this type of element was used by Wang *et al.* (2005) in modeling the anticlastic curvature and springback in the draw-bending process. Furthermore, the unconstrained bending and the subsequent springback was modeled by Lee *et al.* (2005a) using the S4R elements with one integration point through the blank thickness.

To calculate the cross-sectional behaviour of the shell elements used for the current study, S4R, Simpson's rule is used by ABAQUS as the default integration method with five integration points through the thickness of the shell. It was reported that, for complex nonlinear cases, normally no more than nine integration points are required if Simpson's rule is implemented. It was also reported that Simpson's rule should be used if the stress and strain components are required at the surface of the shell (ABAQUS, 2003); which is the case in this study. The other through thickness integration method provided by the program is the Gauss quadrature method. The disadvantage of using this method is that the results are not provided on the shell surface.

For the elastic region, the change in thickness of the shell element is calculated as a function of the in-plane deformation and plane stress condition, $\sigma_{33} = 0$, so that,

$$d\varepsilon_{33} = -\frac{\nu}{1-\nu}\left(d\varepsilon_{11} + d\varepsilon_{22}\right) \tag{5.65}$$

As for the plastically deformed region of the material, the subsequent change of thickness is calculated based on the incompressibility condition on the reference surface of the shell elements, so that

$$d\varepsilon_{33} = -d\varepsilon_{11} - d\varepsilon_{22} \tag{5.66}$$

Incrementally, the through thickness strain estimates are determined and the stress increments are adjusted using the updated thickness strain increment and the iterations continue until a certain convergence criterion is met, as shown in Fig. (5.15).

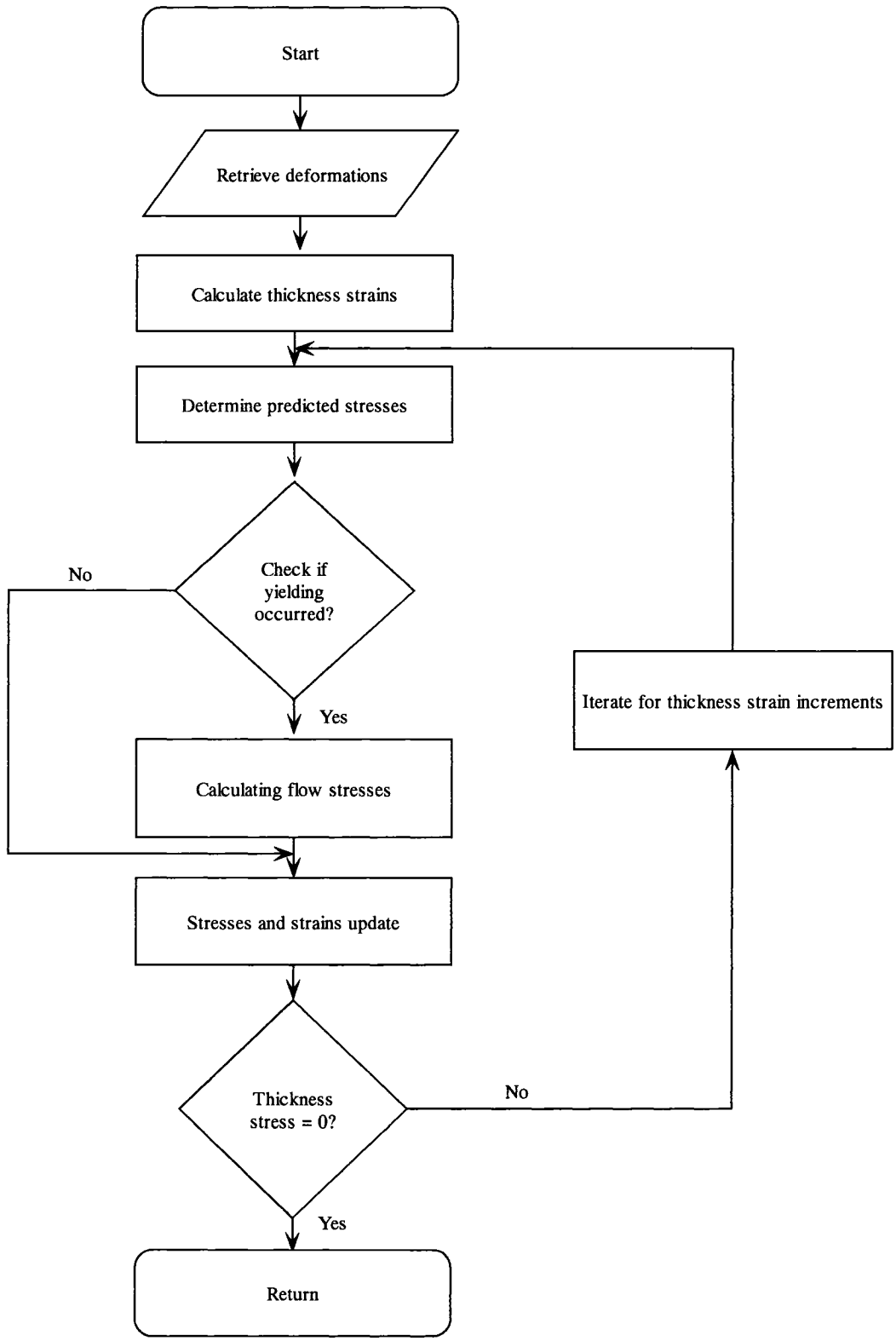

Fig. (5.15) Material response for shell elements

5.4. Model Testing and Validation

The existing hardening assumptions in ABAQUS, namely isotropic and kinematic, both linear and nonlinear, hardening models, do not describe actual material behaviour when undergoing reverse loading, in terms of stress-strain behaviour.

To test the proposed model, a series of simulations were conducted using one element that experiences cyclic loading and the output, in terms of stress and strain, was compared to the tension – compression experiments.

Testing a simple model helps in eliminating other modeling problems that could be associated with, for example, contact or any other geometrical issues. The geometry of the model was chosen to be 25.4 mm by 6.35 mm, to represent one quarter of the gage length of a tensile specimen, as shown in Fig. (5.16). The element was tested by specifying a displacement and using symmetry boundary conditions. The top edge of the element was stretched to represent a maximum of 3% strain corresponding to the experimental procedure explained in Section 4.2.

The results of the simple tension-compression simulations, in terms of stress – strain curves, were compared to those obtained experimentally. It is shown that using the linear kinematic and isotropic hardening assumptions does not capture the real behaviour of the material, especially when the direction of the loading is reversed. However, using the developed material model described in this chapter, the behaviour of the material during reverse loading is captured more precisely. Figures (5.17) to (5.22) show a comparison between the isotropic and the kinematic hardening assumptions and both the experimental and material model results. It is clear that the proposed model predicts more accurate material behaviour.

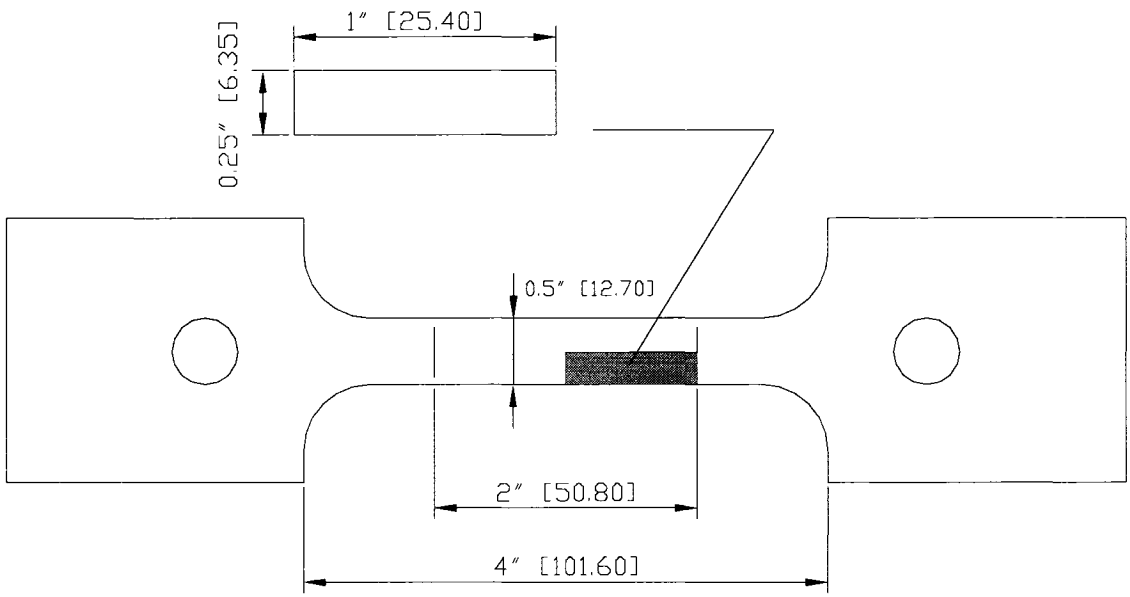

Fig. (5.16) Dimensions of test element

In all cases, the isotropic hardening model is capable of fitting the monotonic tensile curves almost perfectly, as shown in the figures. The reason is attributed to the fact that the isotropic hardening model is governed by the same rule during the monotonic loading through a curve fit to the tensile data passed into the program. However, during reverse loading, there is an offset in the stress – strain curve because the softening of the material and the Bauschinger effect are ignored in that model.

Furthermore, the kinematic hardening model is based on linearizing the stress – strain relationship. That is the reason behind the poor fitting between the monotonic tension data obtained from both the experiments and the model. Also, when the direction of the load is reversed, the unloading and reverse loading behaviour is not well – captured by the model, since the size of the yield surface remains unchanged. Obviously, the model accounts for the Bauschinger effect; however, it does not properly account for the strain hardening in the reverse loading.

Finally, the proposed model, which accounts for both effects, i.e., isotropic and kinematic hardening, shows acceptable agreement with the experimental data. Therefore, this model is used, as will be discussed in the next chapter, for simulating metal forming processes and in prediction of the springback angle after forming.

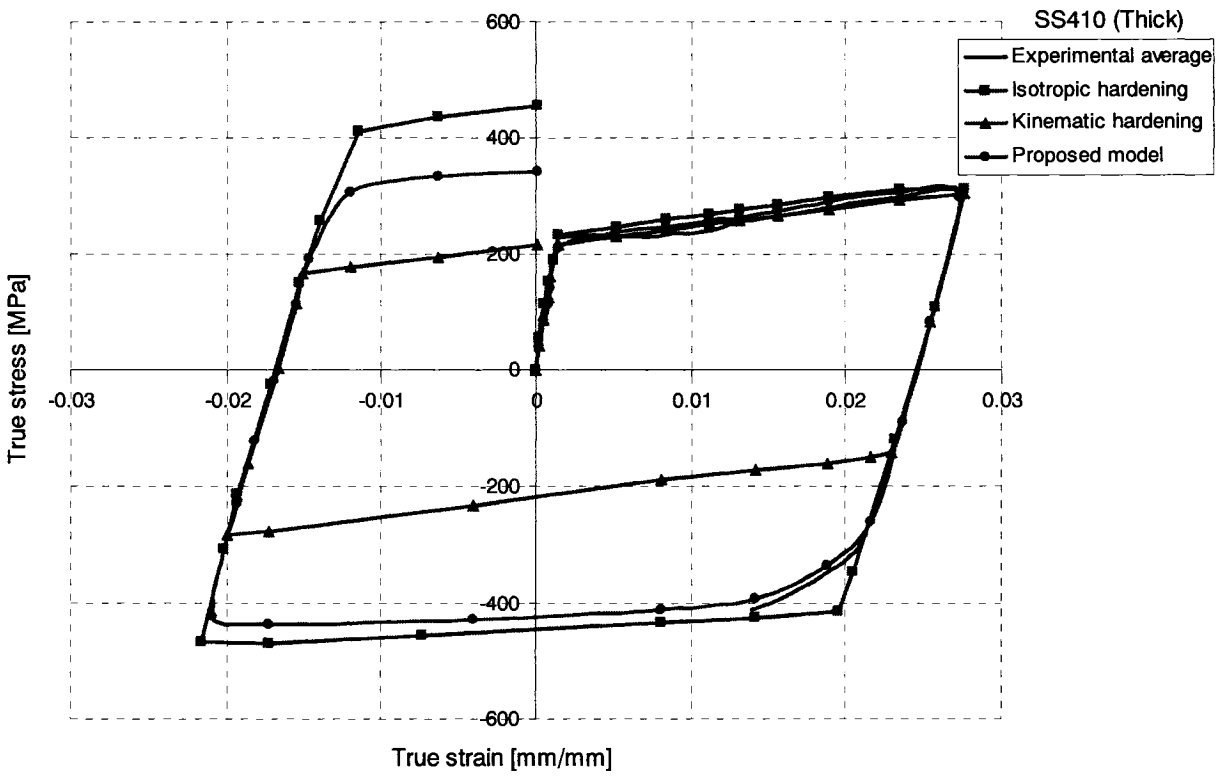

Fig. (5.17) Stress – strain curves for simulations and experiments for the thick SS410

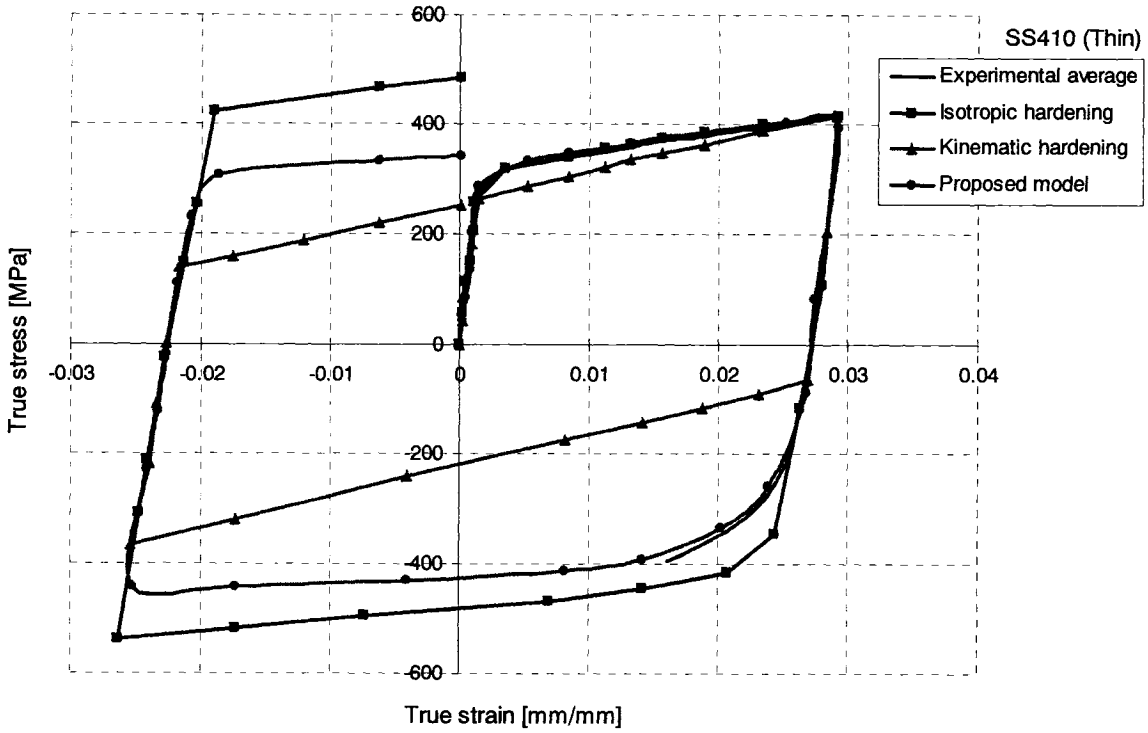

Fig. (5.18) Stress – strain curves for simulations and experiments for thin SS410

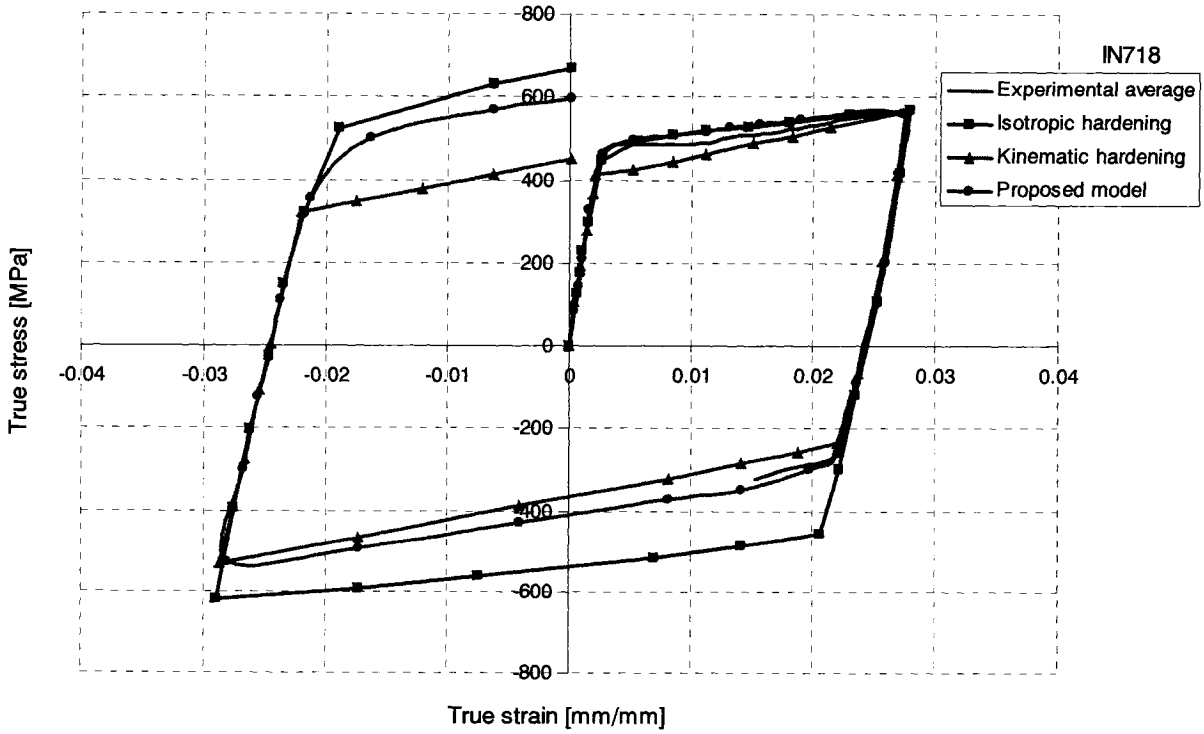

Fig. (5.19) Stress – strain curves for simulations and experiments for IN718

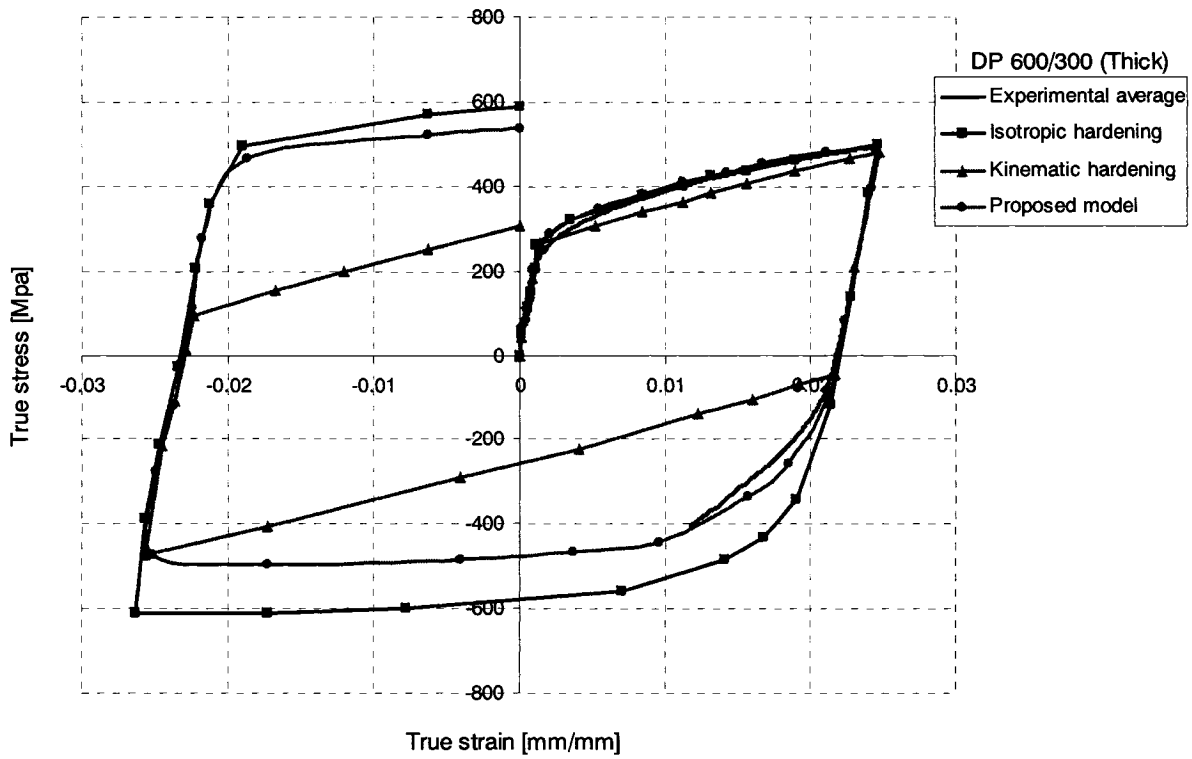

Fig. (5.20) Stress – strain curves for simulations and experiments for thick DP 600/300

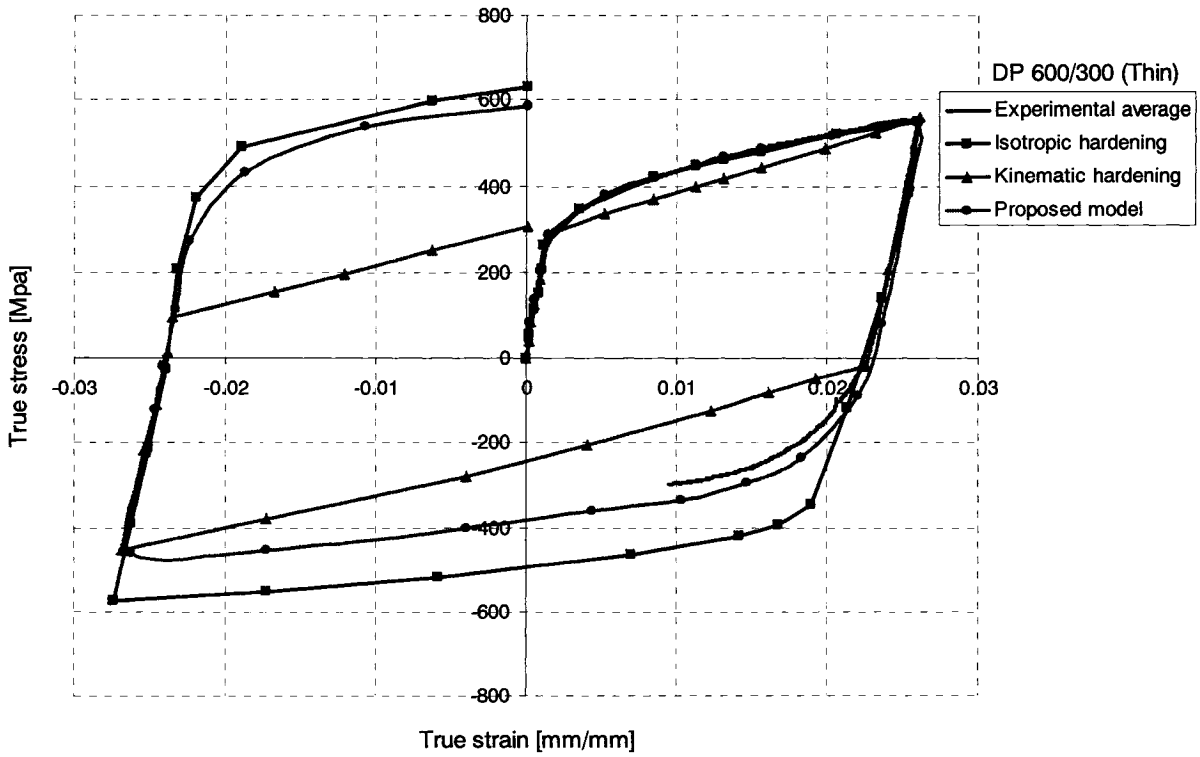

Fig. (5.21) Stress – strain curves for simulations and experiments for thin DP 600/300

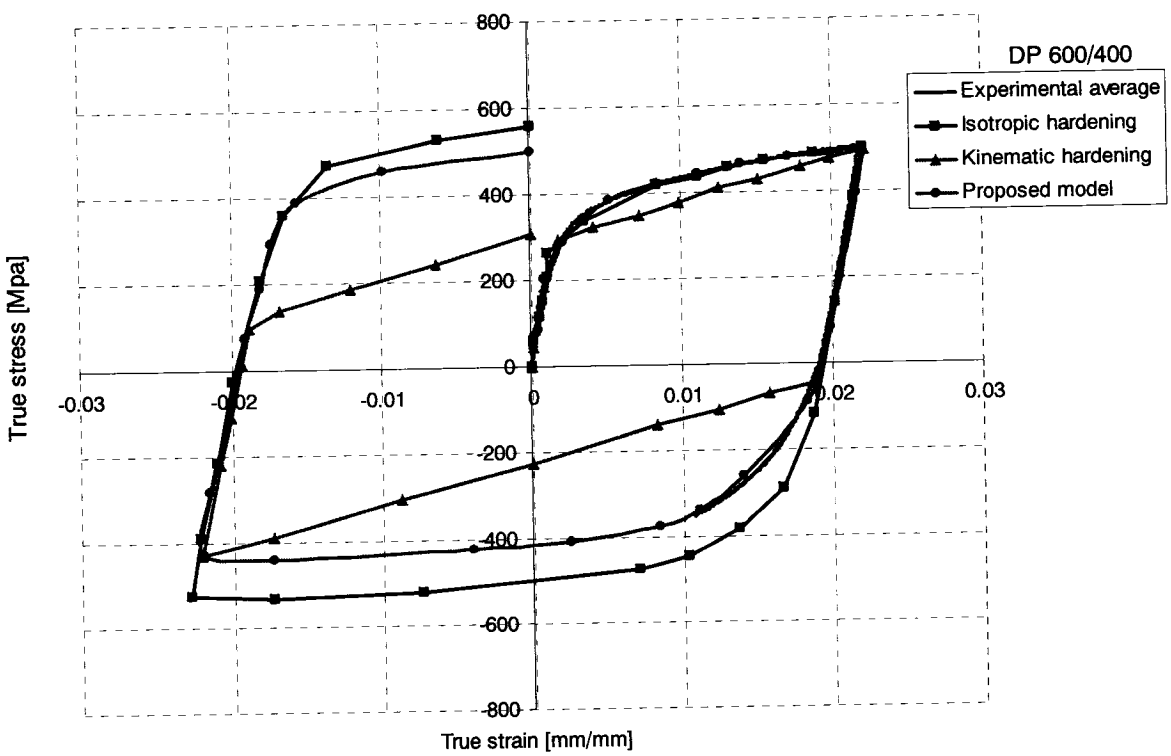

Fig. (5.22) Stress – strain curves for simulations and experiments for DP 600/400

CHAPTER 6

Finite Element Simulations and Results

6.1. Simulations

6.1.1. Simple Bending Simulations

The geometry of the tooling in the simple bending simulations is shown in Fig. (6.1). In these simulations, the tools, die and punch, were modeled as rigid bodies and the sheet was modeled using shell elements. In the experiments, the sample is removed from the fixture, flipped, and placed back in the die for the reverse bending processes. This procedure creates some difficulties when modeled. To avoid such a complicated procedure, a modified arrangement in tooling was implemented in the model. The

modeled tooling arrangement consists of a double- die sandwiching the sheet and a double-tip punch to perform the process in two directions, as discussed below.

To simulate the effect of the die radius on the springback angle in the reverse bending process, a second die should be present at the top of the sheet instead of the regular sheet holder. Therefore, another die with the exact configuration as the base die was implemented in the model for that purpose. The two dies are fixed in the original position and treated as non-deformable rigid bodies.

To perform the reverse bending process, the modified model contains a double-tip punch that can perform the bending action in both directions. After the first bending process (B) is performed, the punch remains in its lower position. When reversing the punch stroke direction, going upward, the reverse bending process takes place, as shown in Fig. (6.2). This process was modeled in four loading steps. The first step is for the bending process (B), the second for (BR), the third for (BRB), and finally the fourth is for the (BRBR). In each of the processes, the punch moves a sufficient displacement so that it has no contact with the sheet. This allows the sheet to experience springback after forming each bending stage. The punch strokes and the springback stages for each bending process are shown in Fig. (6.3).

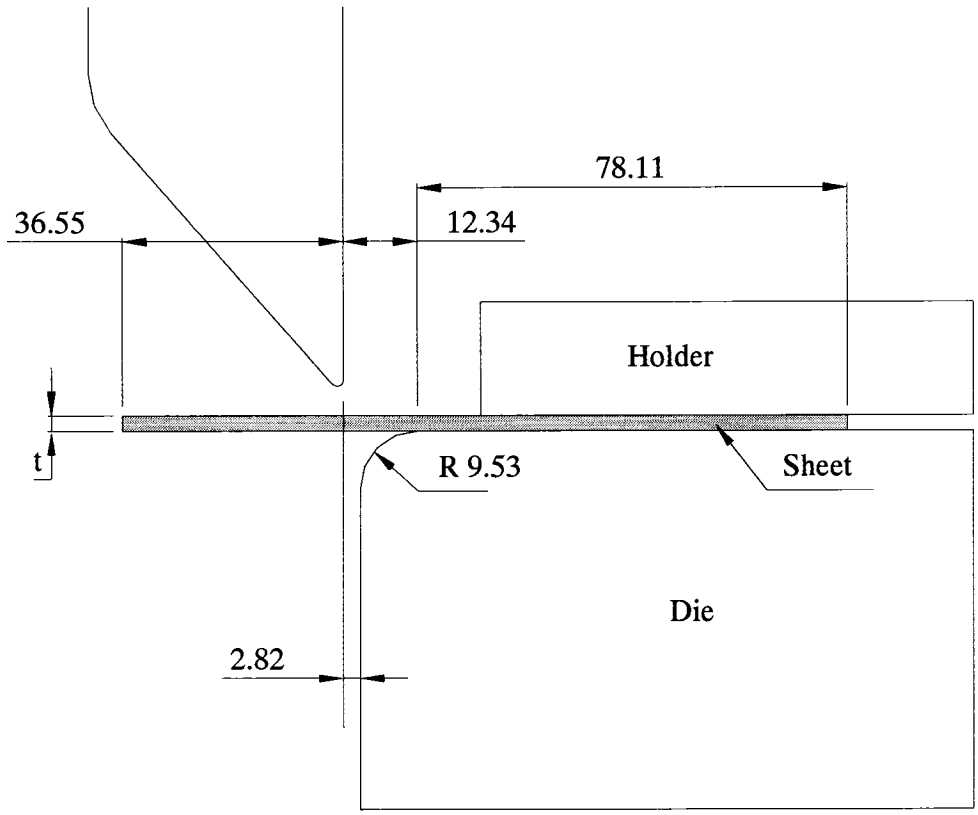

Fig. (6.1) Geometry implemented in the simple bending simulations (dimensions in mm.)

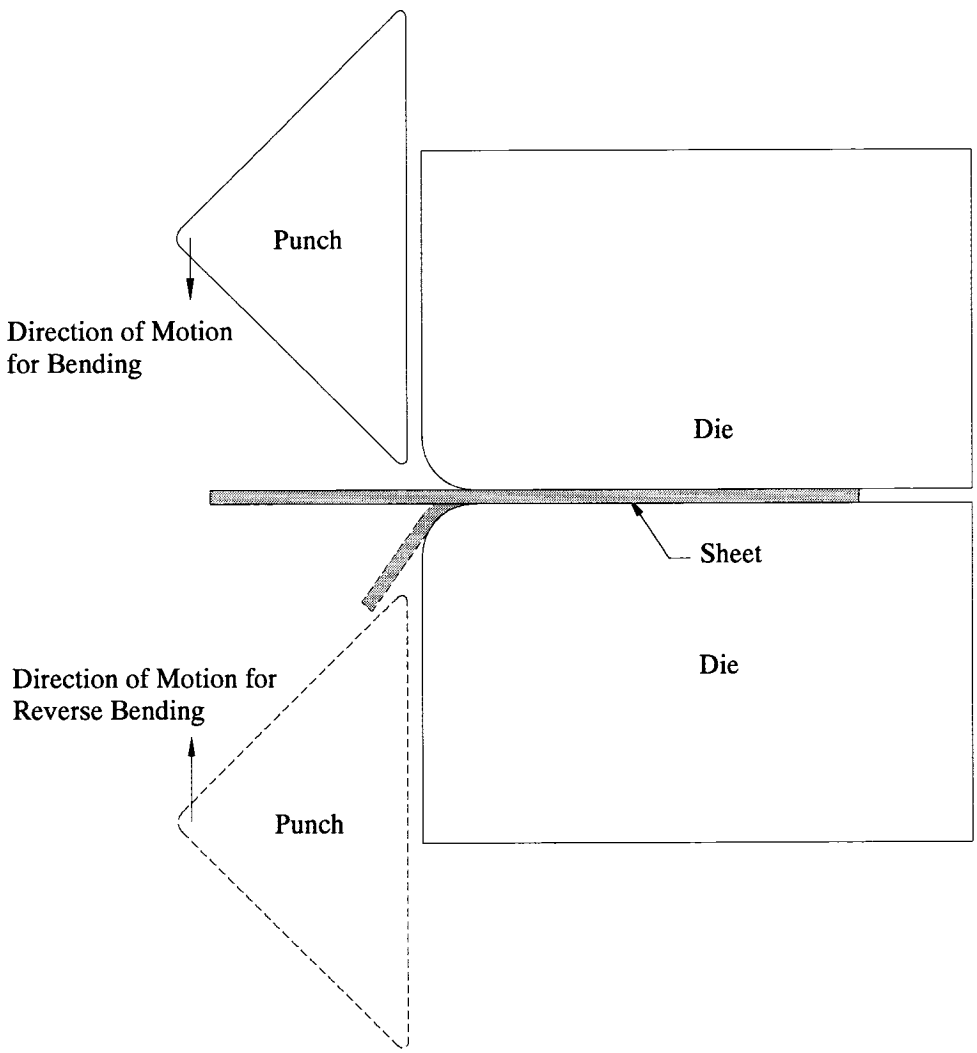

Fig. (6.2) Tooling configuration for simple bending simulations

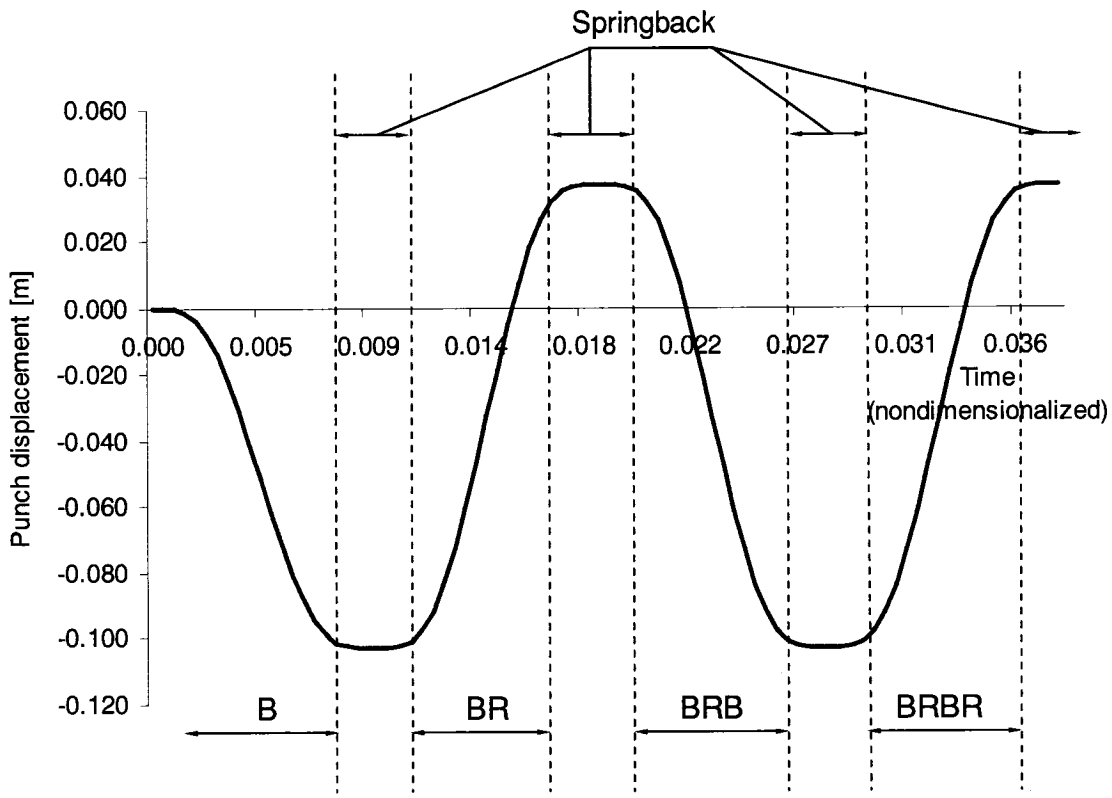

Fig. (6.3) Punch displacement for the multiple bending processes with the corresponding springback after each process

6.1.2. 2D Draw Bending Simulations

The previous model was also extended to simulate the draw-bending experiments. The tooling in the simulations consists of a die, a punch, and a blank holder. Since the specimen is placed in the die symmetrically, the model was reduced to simulate only one half of the experiment geometry, as shown in Fig. (6.4), taking into account all the symmetry conditions, i.e. boundary conditions. The geometry used in the simulation is shown in Fig. (6.5).

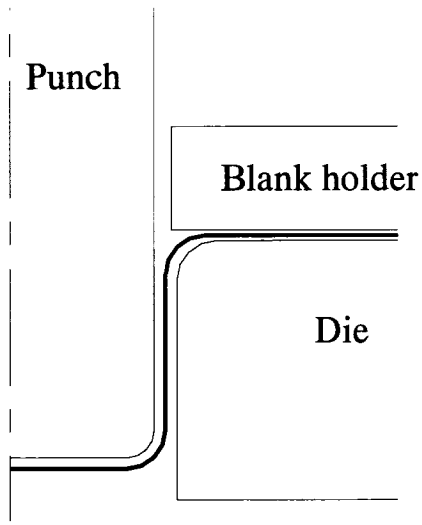

Fig. (6.4) Half model of draw bending used for simulation

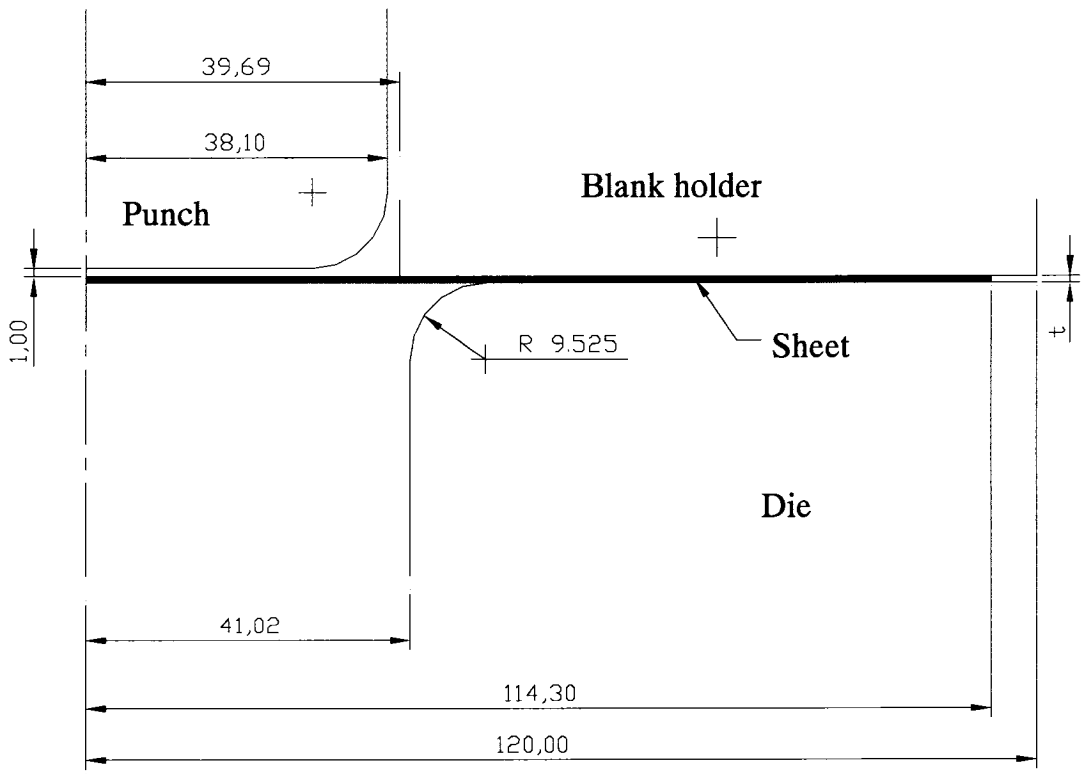

Fig. (6.5) Model dimensions for draw bending simulations (dimensions in mm.)

The die, punch, and blank holder, were modeled as non deformable rigid bodies. The sheet was modeled using shell elements. Modeling parameters such as friction coefficient between the tools and the sheet and number of elements used in modeling the blank are discussed in Sections 6.2.1 and 6.2.2, respectively.

The draw bending simulations were performed in four steps. The first step is to move the blank holder with a prescribed displacement to accommodate for the sheet thickness, so that the lower surface of the blank holder touches the upper surface of the sheet.

In the second step, the blank holding force (BHF) is applied. In this step, the BHF is scaled, to represent the real BHF applied in the experiments. using the formula

$$BHF_{simulation} = \frac{BHF_{experiment}}{2} \frac{\text{element width}}{\text{specimen width}} \tag{6.1}$$

where the factor 2 in the denominator is for the symmetry condition and the ratio between the element width in simulation to the specimen width in experiments is to scale the amount of BHF required to be applied in the simulation that represents the actual BHF in the experiments.

After applying the BHF, the punch starts to move down, in the third step, with a prescribed velocity profile until the end of the punch stroke. A sensitivity analysis for the punch velocity, to choose an optimum value in the simulations, was performed and discussed latter in Section 6.2.3.

In the fourth step, all the contact pairs defined between the blank and the tools are removed, which allows the blank to move freely after removing all the loads. The displacement obtained at the end of the step represents the springback.

It is noteworthy that the simulations conducted, using the existing isotropic hardening model, were performed using the ABAQUS/Explicit code. However, modeling anisotropic materials using the existing kinematic hardening model cannot be implemented in ABAQUS/Explicit. Therefore, the simulations using the existing kinematic model and the material model developed in this study were conducted using the ABAQUS/Standard code.

6.2. Sensitivity Analysis for Draw Bending Simulations

6.2.1. Coefficient of Friction

The influence of friction between the blank and the tools significantly affects the drawability of the sheet. i.e. increasing the friction between the blank and the tools will increase the punch load and accordingly the shear stress. Hu *et al.* (1998) reported that in case of a low coefficient of friction, reported at 0.15, more friction will result in an increase in the punch load promoting sheet thinning near the punch radius and sheet thickening near the outer edge of the blank.

One of the unknowns in the experiments is the magnitude and the effect of the friction which hinders the sheet from slipping on the tool surface perpendicular to the punch motion. The coefficient of friction is an experimental factor that is one over which there is relatively less control and difficulty to measure accurately (Gomes *et al.*, 2001). Therefore, in sheet metal forming simulations, authors often use a coefficient of friction value that best simulates the blank-tool interaction behaviour.

The default model that describes the tool-blank interaction in the finite element package ABAQUS is the Coulomb friction concept. This model assumes that relative motion between the sheet and the tools does not occur when the equivalent frictional or shear stress, τ_{eq}, is less than a critical value, τ_{crit}, at which sliding of the surfaces starts. This

critical value is determined as a function of the contact pressure between the mating surfaces. The frictional stress and the critical value are obtained from

$$\tau_{eq} = \left[\tau_1^2 + \tau_2^2\right]^{\frac{1}{2}}$$
$$\tau_{crit} = \mu p \tag{6.2}$$

where p is the contact pressure between the surfaces, μ is the coefficient of friction and τ_1 and τ_2 are two orthogonal components of shear stress, along the interface between the two bodies. These components act in the slip directions of the contact surfaces (ABAQUS, 2003).

Pourboghrat and Chu (1995a) modeled the 2D draw bending and the subsequent springback of Al2008-T alloy and mild steel. In their simulations, 8-noded plane strain elements along with an isotropic hardening model were used in ABAQUS. The coefficient of friction used in all models was 0.12 to best simulate the sheet-tooling contact interface.

Moreover, Samuel (2000) studied the process variables in 2D draw bending of aluminum, mild steel and stainless steel. The Coulomb friction model was adopted and the simulations were carried out using the MARC finite element package. The coefficients of friction used, for each material, were 0.162, 0.143, and 0.128, respectively. It was reported that the effect of the coefficient of friction on springback highly depends on the blank holding force; however, as a general trend, the increase in the friction coefficient decreases the springback and sidewall curls.

Furthermore, Papeleux and Ponthot (2002) also studied the effect of process parameters on springback in 2D draw-bending. It was reported that the friction coefficient is one of the difficult parameters to determine experimentally because of its variability on the curved and flat parts of both the die and the punch. In their simulations, using METAFORM, constant friction coefficients were assumed along the analysis. Three

materials were modeled, namely mild steel, HSS, and aluminum, with friction coefficients 0.144, 0.129, and 0.162, respectively.

Throughout the literature, many authors have modeled sheet forming processes. Surprisingly, the variation in the values of the coefficients of friction reported confirms that it cannot to be ignored. Kridli and El-Gizawy (1998) and Ragai and Younan (2001 and 2003) modeled the superplastic forming of aluminum alloys and used a high coefficient of friction of 0.3 between the sheet and the die. Asnafi (2001) used a coefficient of friction of 0.10 in his study of springback of double-curved autobody panel made of steel and aluminum sheets. Also, it was assumed that the coefficient remains constant during the forming process. Nakamachi *et al.* (2001) modeled the drawability of some sheet metals using elastic/crystalline viscoplastic finite element analyses. The values used for the coefficients of friction were 0.15, 0.10, and 0.12 for mild steel, DP steel and HSS, respectively. Chun *et al.* (2002b) assumed constant uniform friction coefficients for all contacting surfaces in their cup drawing analyses. The coefficients of friction used were 0.168 for Al6016-T4, 0.17 for HSS, and 0.15 for Al6022-T4 alloys. Geng and Wagoner (2002) used a coefficient of friction of 0.15 in their draw-bending simulation of Al6022-T4. Kuwabara *et al.* (2004) modeled the stretch bending experiments using a coefficient of friction of 0.10 between the specimen and the die and the specimen and the blank holder. The coefficient of friction between the specimen and the punch was 0.03. Takamura *et al.* (2004) used a coefficient of 0.15 between all mating surfaces. Ahmetoglu *et al.* (2004) modeled the hydroforming process for IN718 and set the coefficient of friction between the sheet and the die to be 0.06 and between the sheet and punch to be 0.12. Finally, Gilmour *et al.* (2004) modeled the stretch forming of Al2024-T3 alloy using an arbitrarily set value of the coefficient of friction of 0.40 between the sheet and the die.

Since there is no accurate measure for the coefficient of friction in the experiments carried out in this study, choosing an optimum value in the simulation depended on trial and error. Choosing a low coefficient of friction would assist the blank to slide between the die and the blank holder and accordingly increasing the elastic region during bending,

which accordingly contributes to an increase in the springback. On the other hand, increasing the coefficient of friction will result in a decrease in the springback angle. Figure (6.6) shows the effect of changing the coefficient of friction for some trials in simulating the SS410 thick sheets. Accordingly, in this study, to find the coefficient of friction that best correlates to the experiments, several values were tested.

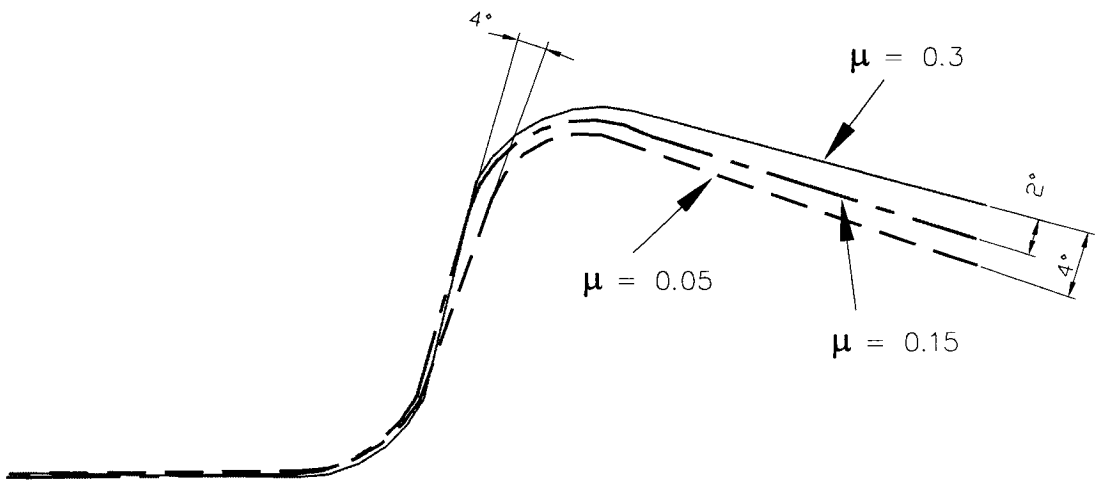

Fig. (6.6) Effect of the coefficient of friction on the final springback angle for thick SS410

Using a constant blank holding force of 11.0 kN for all materials and varying the coefficients of friction throughout the simulations, several values for the coefficient of friction were tried and the values that gave the best geometry compared to the experiments are listed in Table (6.1) for the three materials under investigation. The values listed in Table (6.1) are used throughout the analysis for the various models.

Table (6.1) Coefficients of friction used in the simulations for different materials

Material	SS410	DP steel	IN718
Coefficient of friction (μ)	0.144	0.160	0.100

6.2.2. Number of Elements

Clausen *et al.* (2001) modeled the stretch bending of aluminum extrusions using shell elements with five integration points through the thickness. It was reported in their work that increasing the number of integration points did not have a significant influence on the model parameters.

Li *et al.* (2002a) conducted a mesh sensitivity analysis in their simulation of the draw-bend test. The total numbers of elements in their models were 150, 300, 600, 900, 1200, and 2400. It was reported that using a non uniform mesh with 600 elements along the length of the specimen gave reliable results.

Park and Oh (2004) modeled the 2D draw-bending process and its subsequent springback with different mesh sizes. The main aim of their work was to develop a shell element with enhanced bending performance; however, a sensitivity analysis of the required number of elements using the conventional shell element (S4R) was also conducted. The specimen was modeled using 10 elements along the width and the number of elements along the length was varied from 30 to 300 elements. It was found that with the increase of the number of elements the simulation results converge to a certain shape. It was reported that the minimum number of elements required for convergence is 150 elements along the length of the specimen, as shown in Fig. (6.7). It is, however, worth mentioning that the minimum number of elements needed in the simulation, using their developed element formulation, is 70 elements along the length of the specimen.

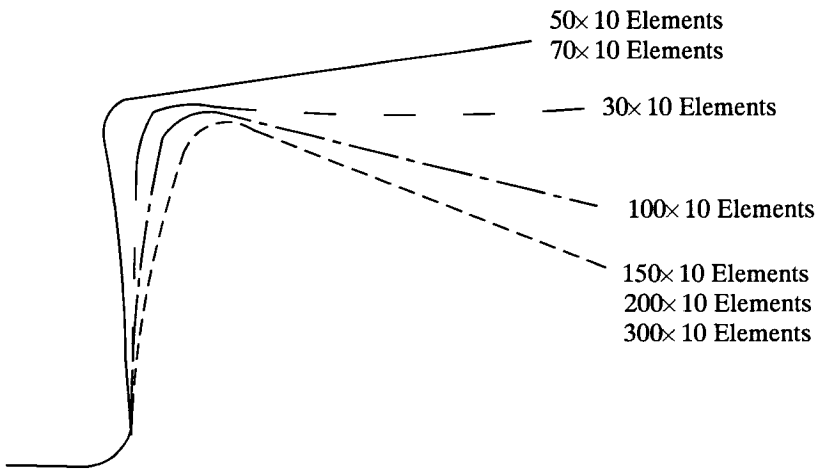

Fig. (6.7) Sensitivity analysis for springback prediction using S4R elements (adapted from Park and Oh, 2004)

In the present work, simulations with different mesh sizes took place. Models with 175, 250, 400, and 6700 elements were tested. In this section, only the two models using 6700 and 175 elements are discussed. For these two considered models, the shell elements (S4R) were used in the analysis. In the first model, 100 elements were used along the length of the specimen and 67 elements were used along the width; a total of 6700 elements that models the full specimen's geometry. The second model consists of 175 elements along the length of the specimen and a one element of 5.00 mm width along the width of the specimen, as shown in Fig. (6.8).

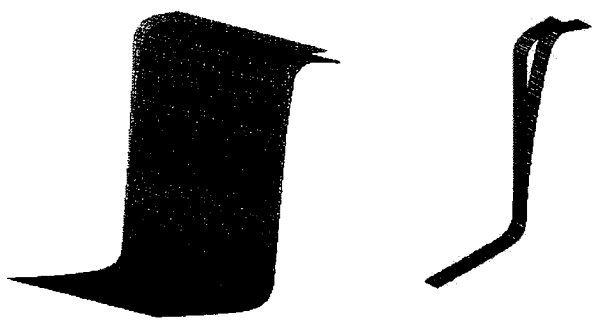

(a) (b)

Fig. (6.8) (a) Full-width model (b) one-segment model

The 6700-element models take more than seventeen hours CPU time on a 733 MHz machine. Therefore, by appropriate scaling of the one-segment model to the corresponding blank holding force, one can obtain reasonably accurate results for the full specimen width using a lower number of elements. The scaling of the BHF applied on the specimen follows the relationship presented in Eq. (6.1).

The comparison between the two models is shown in Fig. (6.9). It can be seen that the two models converge to a similar final shape. Taking into account the large CPU time required to run the 6700-element models, the 175-element models, that takes approximately eight hours to run the analysis, are preferred. Therefore, in all of the simulations, the 175-element model is used.

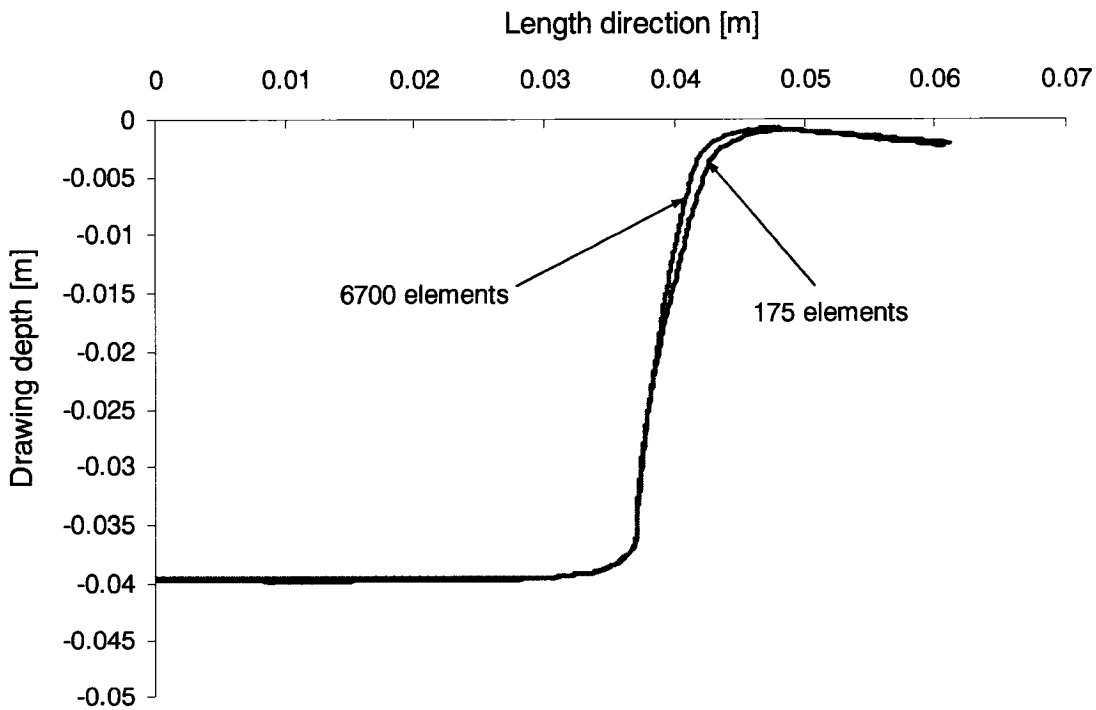

Fig. (6.9) Effect of number of elements on the final shape

6.2.3. Punch Speed

Applying the principles of virtual work, the equation of motion in the current configuration of the finite element analysis takes the form

$$M\ddot{u} + P = F \tag{6.3}$$

where M is the mass matrix, u is the generalized nodal displacement vector, P is the internal force vector, and F is the external force vector. When using explicit integration methods to simulate quasi-static events, it is highly desirable to use relatively low punch speeds so that the inertia term in Eq. (6.3) can be neglected avoiding undesirable oscillations and simplifying the solution procedure (Tang, 1994). This will result in a simplification of the equation of motion, Eq. (6.3), to the equation of equilibrium, so that

$$P = F \tag{6.4}$$

which is a set of highly nonlinear equations solved incrementally.

On the other hand, without sacrificing the accuracy of the results, it is common to run forming simulations at higher speeds than those used in the experiments. Therefore, speeds used in the simulation still need to be low enough not to introduce inertia effects on the obtained results (Lee *et al.*, 2005a).

Nakamachi *et al.* (2001) used a maximum punch speed of 20 m/s with a 10.00 mm stroke in their deep drawing simulations. The punch accelerated linearly until the maximum speed was reached and then the velocity kept constant for the remainder of the simulation. It was reported that using this speed would result in elimination of the dynamic effects on deformation, stress, and strain.

In their simulations of can drawing, Gotoh *et al.* (2003) used a punch speed of 10 m/s to eliminate the dynamic effects on the simulated results. Also, Lee *et al.* (2005a), in their 2D draw-bending simulations, used the same punch velocity to eliminate the inertial effect.

Analysis using the isotropic hardening model was conducted in two stages. The first stage, which includes application of the BHF and the 2D-draw bending, was performed using ABAQUS/Explicit. The second stage, removing the contact surfaces and obtaining the springback, was performed using ABAQUS/Standard. It is worth mentioning that all the analyses performed using the kinematic hardening and the developed material model were performed using entirely ABAQUS/Standard.

When using ABAQUS/Explicit the dynamic response is one of the important factors that should be taken into consideration because of the inertia effect that might influence the results of the simulation (ABAQUS, 2003). Accordingly, a proper velocity value for the punch had to be chosen such that its effect on the results is minimal. Several values for punch velocity were considered using the model. The velocity was varied from 60 m/s to 2 m/s. It was found that with high velocities of 60, 30, and 15 m/s an inertia effect was observed. The comparison of the results was based on force-displacement curves obtained from both experiments and simulations for 0 kN BHF. Going from 8 m/s to 2 m/s, the inertia effect was minimized, as shown Fig. (6.10). Therefore, a relatively low speed of 4 m/s was chosen for the analysis. This punch speed is used in all the simulation results presented in the following sections.

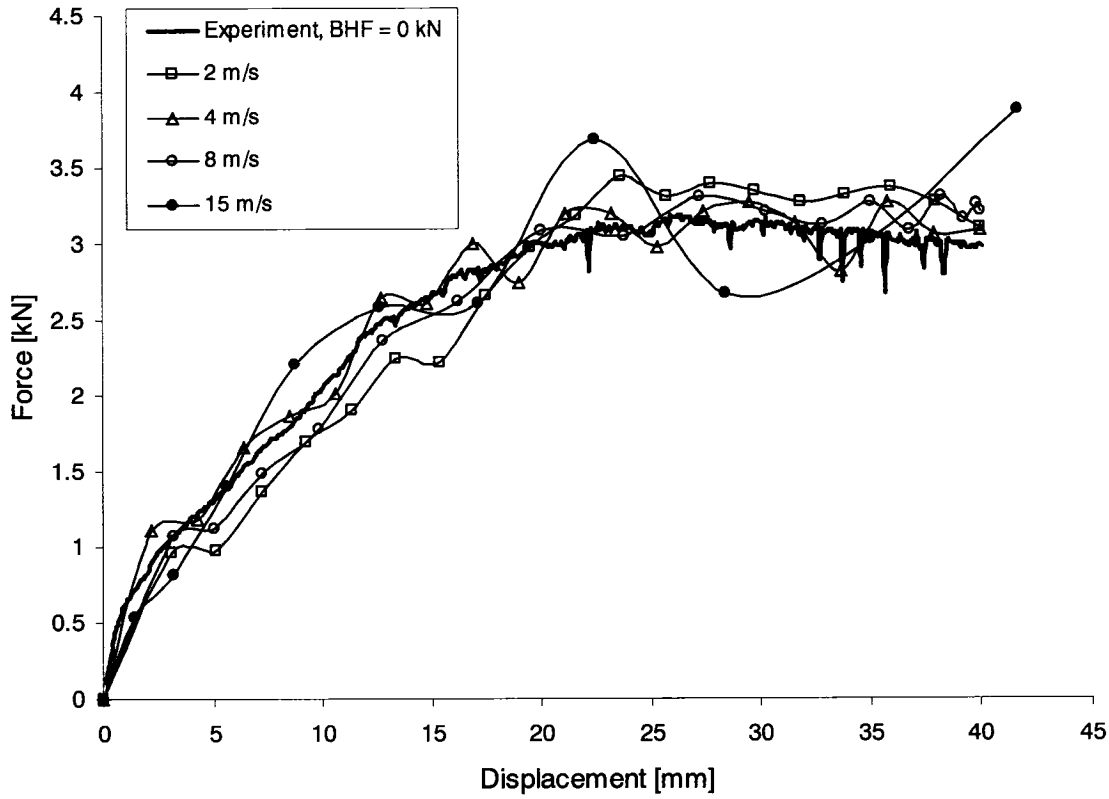

Fig. (6.10) Force-displacement for various punch speeds

6.3. Simulations Results

6.3.1. Simple Bending

As discussed in Section 4.3, springback is more pronounced in thin sheets; therefore, simple bending experiments were conducted only for thin SS410, thin DP 600/300, and IN718 sheets. Accordingly, the simulations for simple bending were carried out only to represent these tests.

In order to compare the output of the simulations to the experimental results, the average springback angle from the experiment sets was calculated, as discussed in the previous chapter. Simulations using ABAQUS isotropic and kinematic hardening models were

conducted and their results were also compared to the results obtained from the proposed combined hardening model.

Figures (6.11) to (6.13) show the comparison between the experiments and the simulations. In all cases, it is shown that the springback angle obtained using the ABAQUS isotropic hardening model is overestimated. On the other hand, the ABAQUS kinematic hardening model underestimates the springback angle. These findings were addressed in this work, which indicates the need for a combined hardening model that accurately predicts the springback angle.

As shown in the figures, the model proposed in this work predicts the springback angle fairly well in simple bending for all the materials tested. The value of the springback angle obtained from the simulations, using the proposed model, lies within the measurement differences discussed in Chapter 4, which indicates that the model is in fair agreement with the experiments and can be expanded to cover a more complicated forming operation.

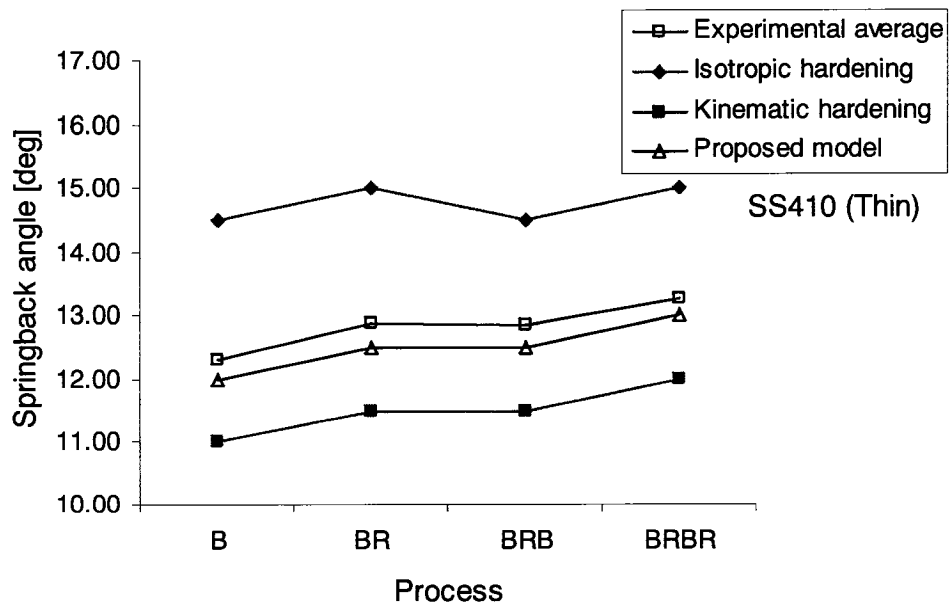

Fig. (6.11) Comparison between springback angles obtained from simple bending experiments and different simulation models for thin SS410

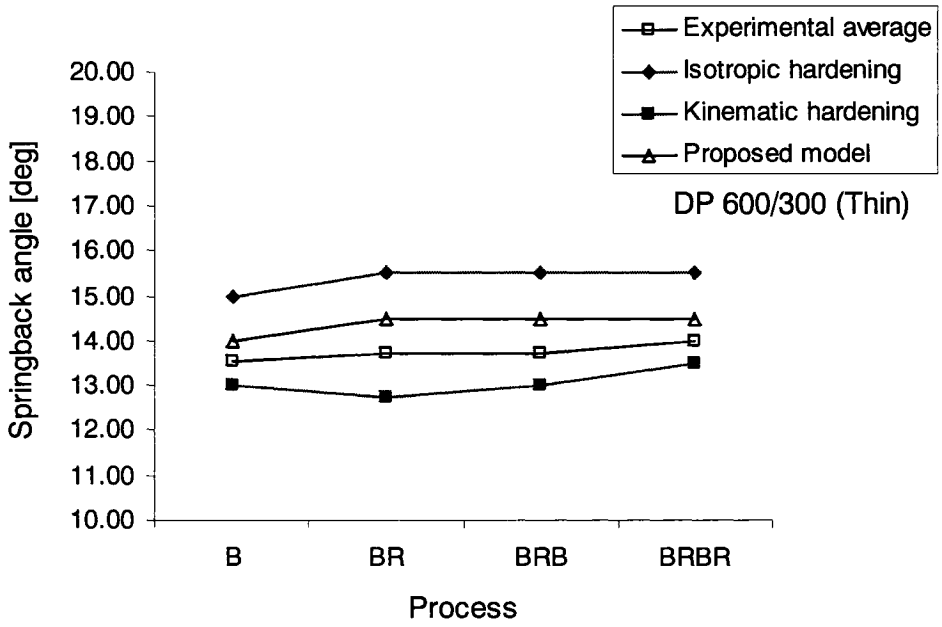

Fig. (6.12) Comparison between springback angles obtained from simple bending experiments and different simulation models for thin DP 600/300

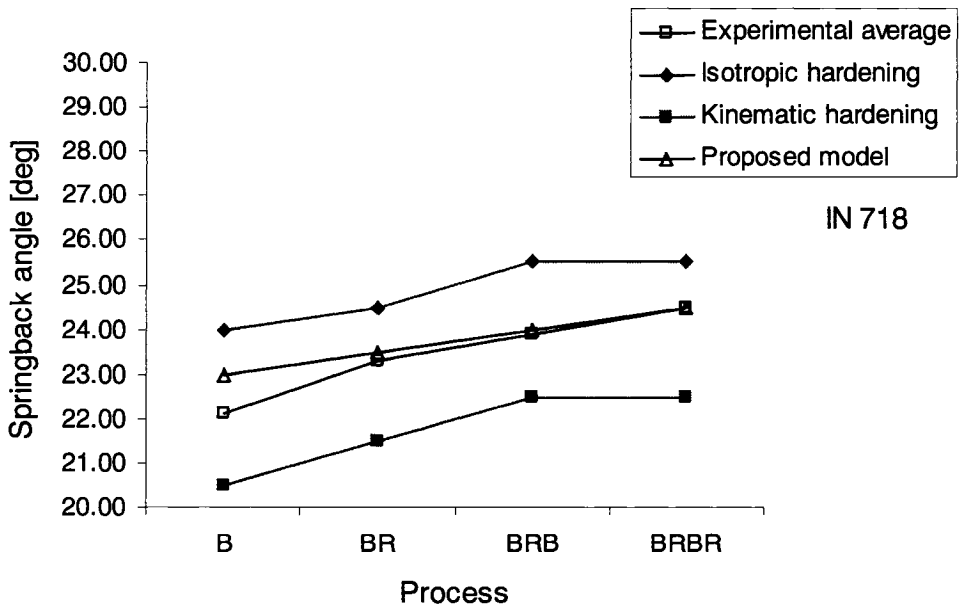

Fig. (6.13) Comparison between springback angles obtained from simple bending experiments and different simulation models for IN718

6.3.2. 2D Draw Bending

6.3.2.1. Effect of BHF on Springback Angles

The proposed model has been used to simulate the material behaviour in the 2D draw bending experiments. The effect of the BHF was investigated through a series of simulations using isotropic and kinematic hardening models and the model developed in this work. The results from the simulations in terms of springback angles were obtained and compared to the experimental results obtained and discussed in Section 4.4. Figures (6.14) to (6.19) show the comparison between the experimental results and the results obtained from the finite element simulations. As a general statement, it can be seen that both pure isotropic and pure kinematic models do not accurately predict the springback angles after bending. The isotropic hardening models over-predict the angles and the kinematic hardening models underestimate them. On the other hand, the developed model shows fairly good agreement with the experimental results.

In some cases, researchers reported that in modeling some of the materials a certain hardening model, pure isotropic or pure kinematic, is dominant. This statement cannot be said as a general conclusion for the materials tested in this study. For the SS410 simulations, Figs. (6.14) and (6.15), it can be seen that the isotropic hardening and the kinematic hardening models bound the experimental values, especially for the springback angle θ_1.

For the thick and thin DP 600/300, the same observation can be said for θ_1. However, for θ_2 and a BHF of 22 kN, it can be seen in Fig, (6.16) that both the springback angle obtained from the experiments and the combined hardening model lies outside that boundary. It still shows that the increase of the BHF results in a decrease of the springback angle, but it also shows that the isotropic and the kinematic hardening models failed to predict a more accurate value of the angle. For the thin DP 600/300, Fig. (6.17), the measured angle θ_2 for the 11 kN BHF is closer to the value predicted by the isotropic hardening simulation. As for the DP 600/400 simulations, Fig. (6.18), the springback

angles θ_1 and θ_2 predicted by the three models agree fairly well with the experimental results. However, only at a BHF of 22 kN the predicted angles lie below those measured from the experiments.

The results obtained from the simulations of the IN718, Fig. (6.19), agree with the previous observation of the bounding limits of the springback angles. Generally, the combined model is in good agreement with the experimental results. It is worth mentioning that the change in the springback angle with respect to orientation combined with BHF, for this material, is not captured by the model, simply because of the fact that planar anisotropy or directional properties are not considered within the developed model. However, the general behaviour of the material with respect to the BHF is well captured by the model in an average sense. Including directional properties can be implemented in a future research work as an extension to the proposed model developed in this work.

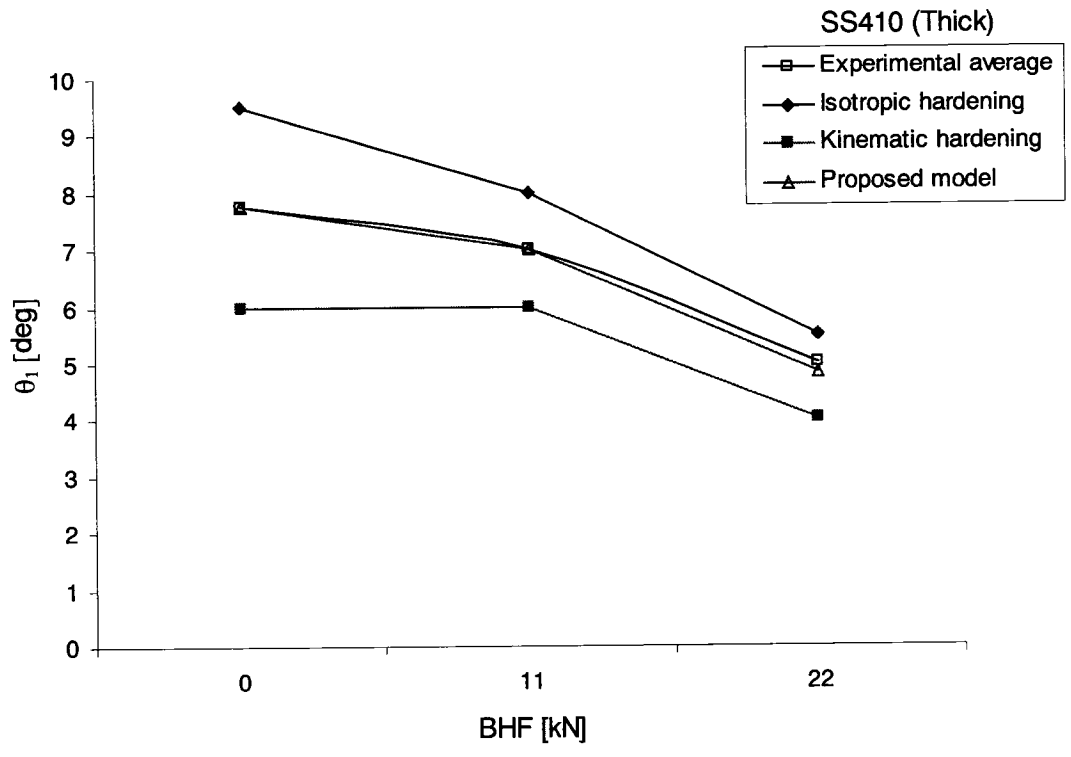

(a)

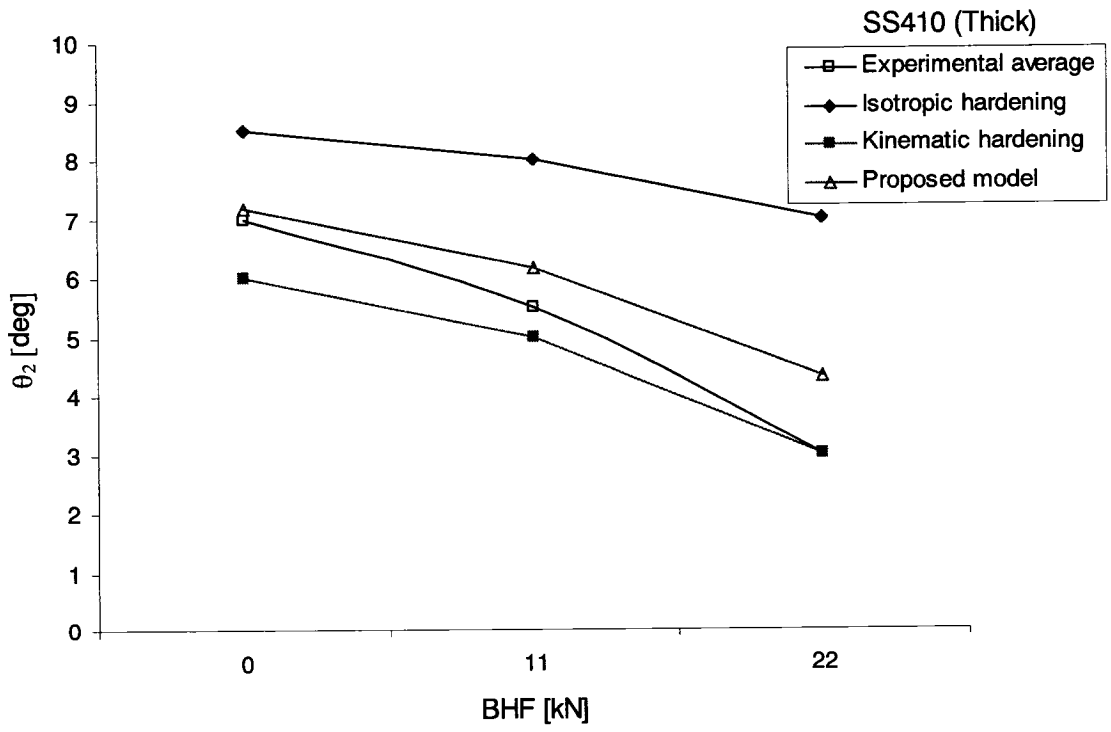

(b)

Fig. (6.14) Effect of BHF on springback angles obtained from simulations for thick SS410 specimens, (a) θ_1 and (b) θ_2

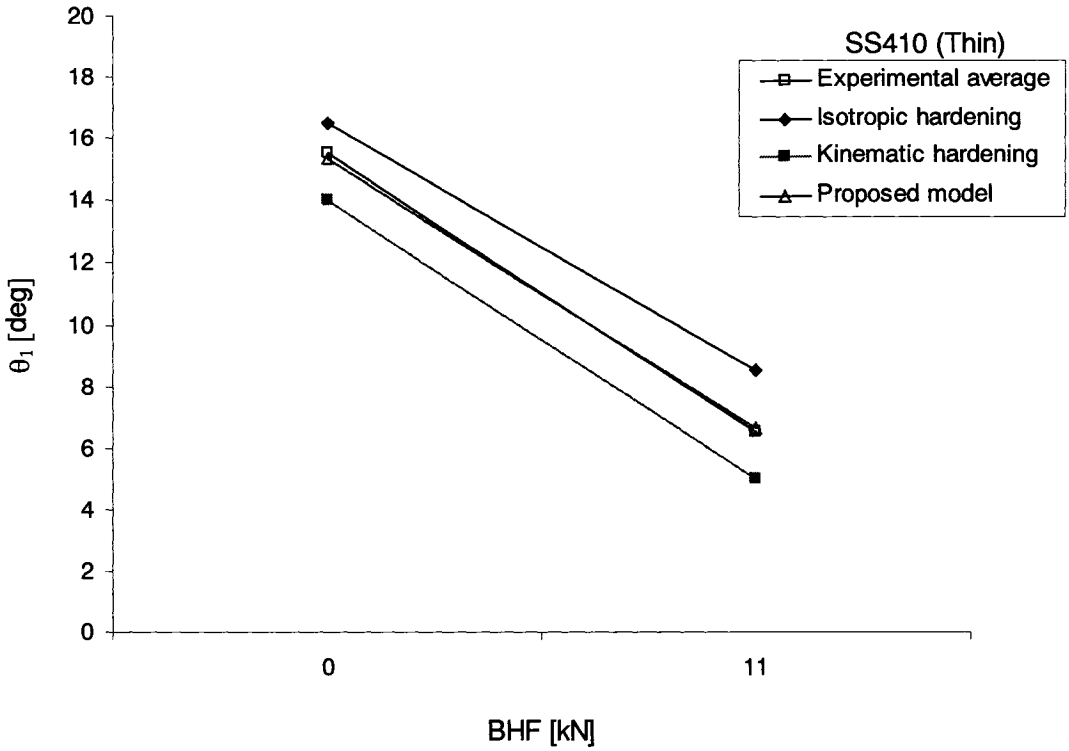

(a)

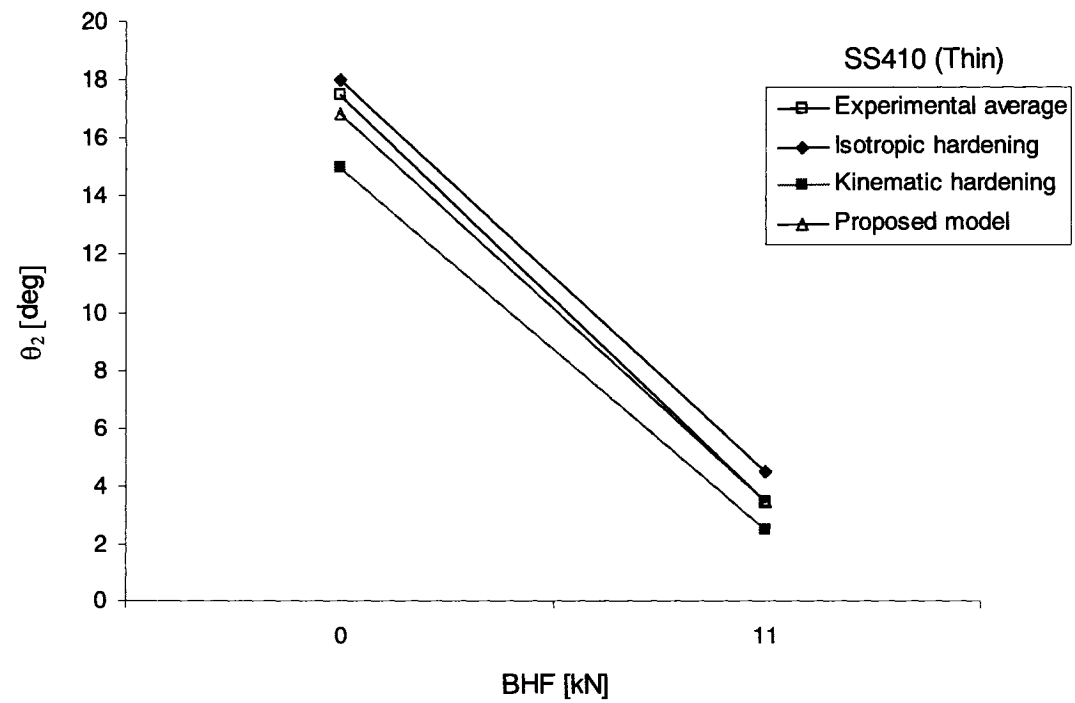

(b)

Fig. (6.15) Effect of BHF on springback angles obtained from simulations for thin SS410 specimens, (a) θ_1 and (b) θ_2

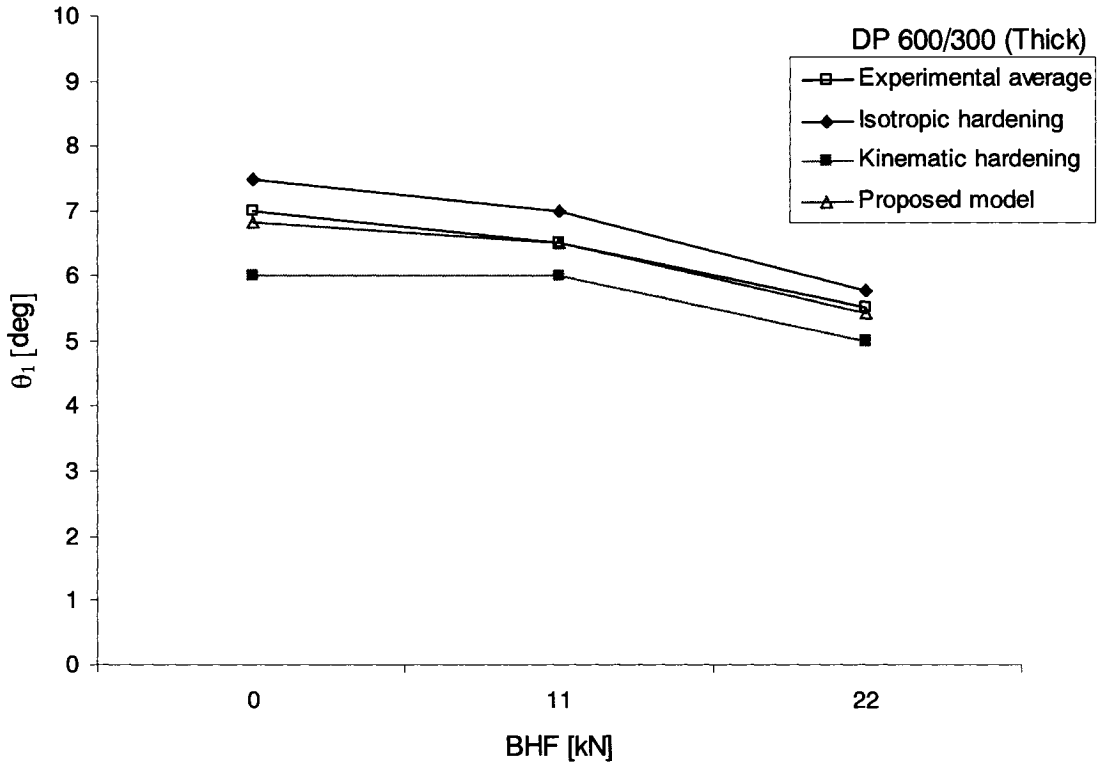

(a)

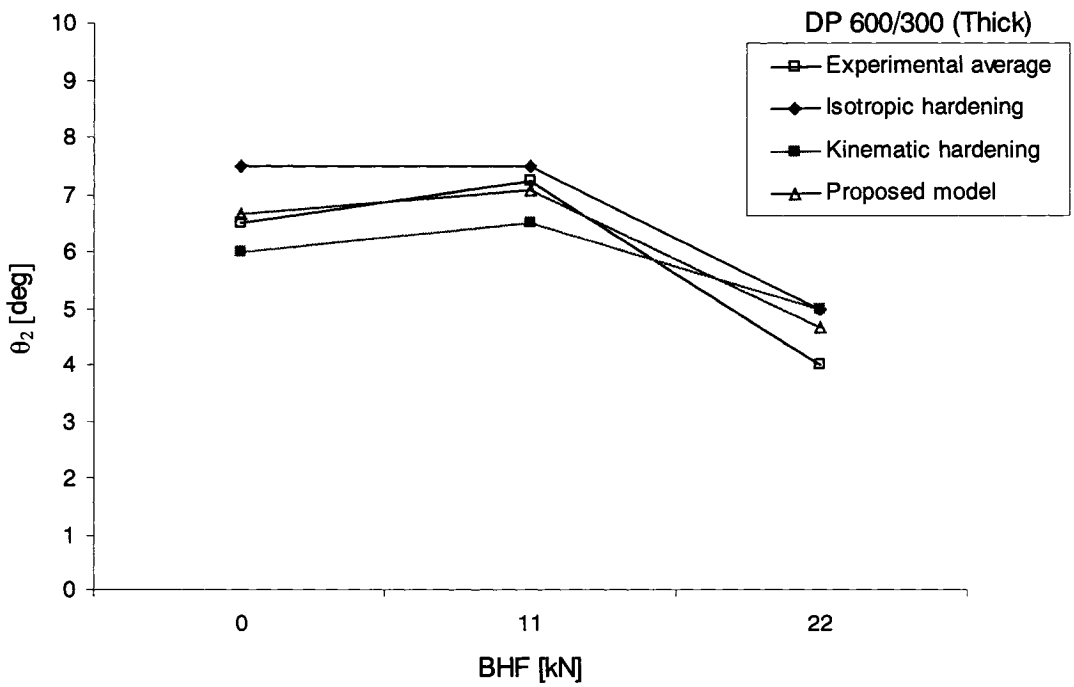

(b)

Fig. (6.16) Effect of BHF on springback angles obtained from simulations for thick DP 600/300 specimens, (a) θ_1 and (b) θ_2

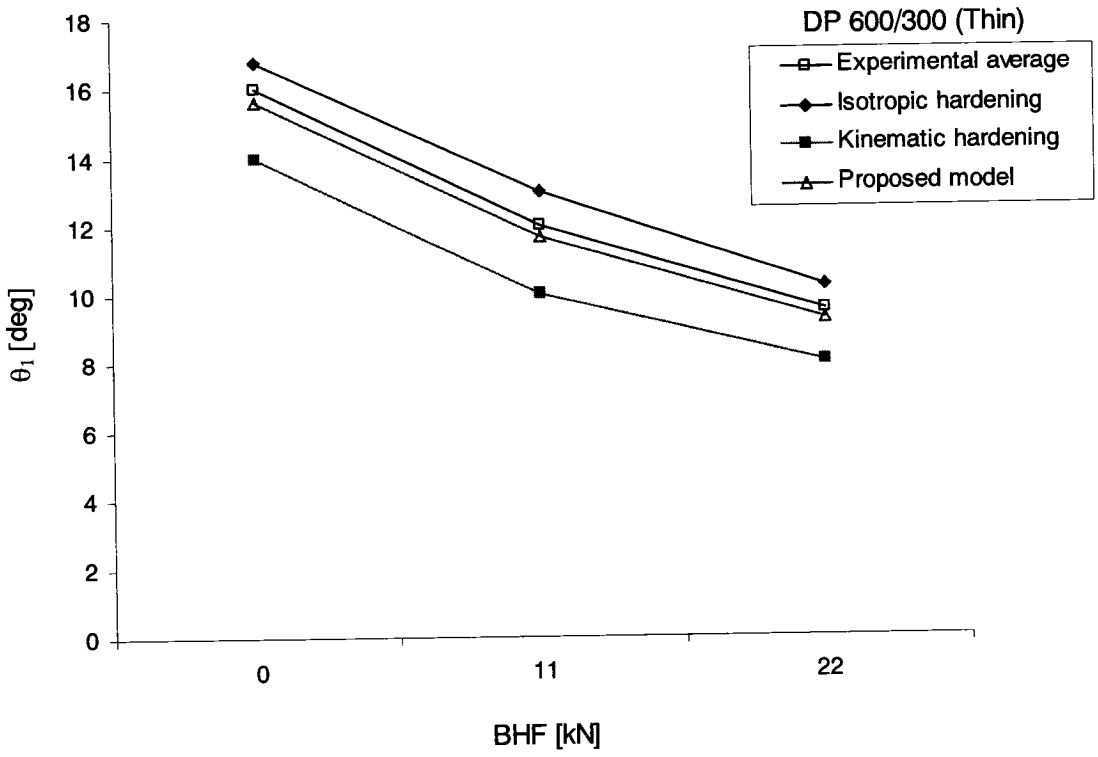

(a)

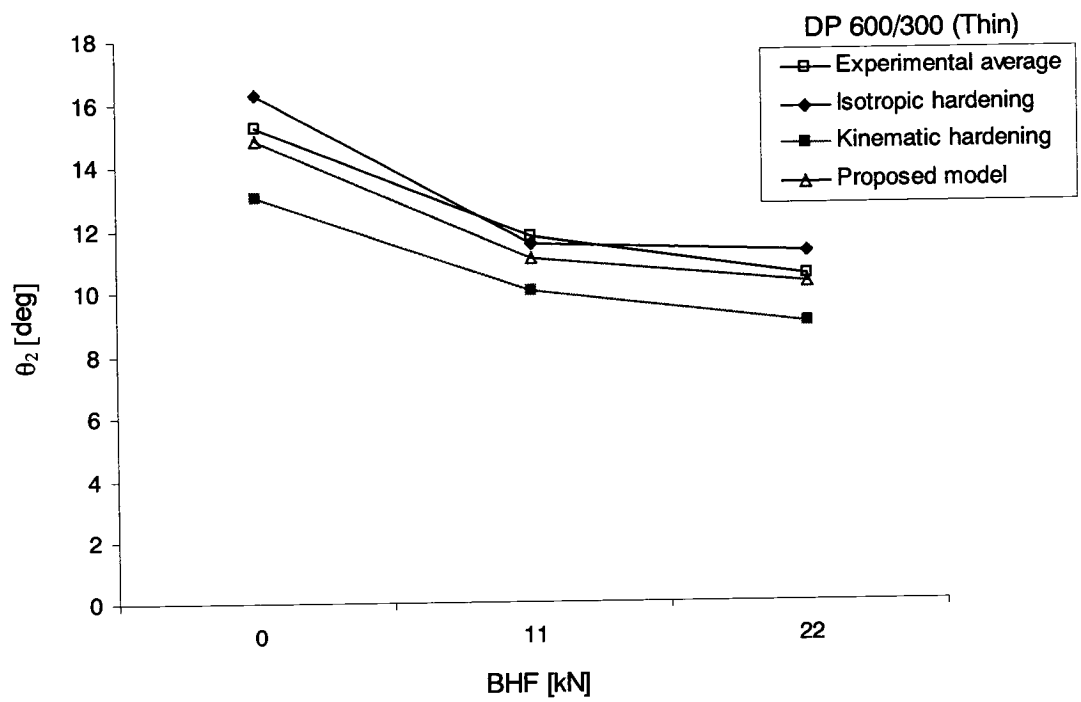

(b)

Fig. (6.17) Effect of BHF on springback angles obtained from simulations for thin DP 600/300 specimens, (a) θ_1 and (b) θ_2

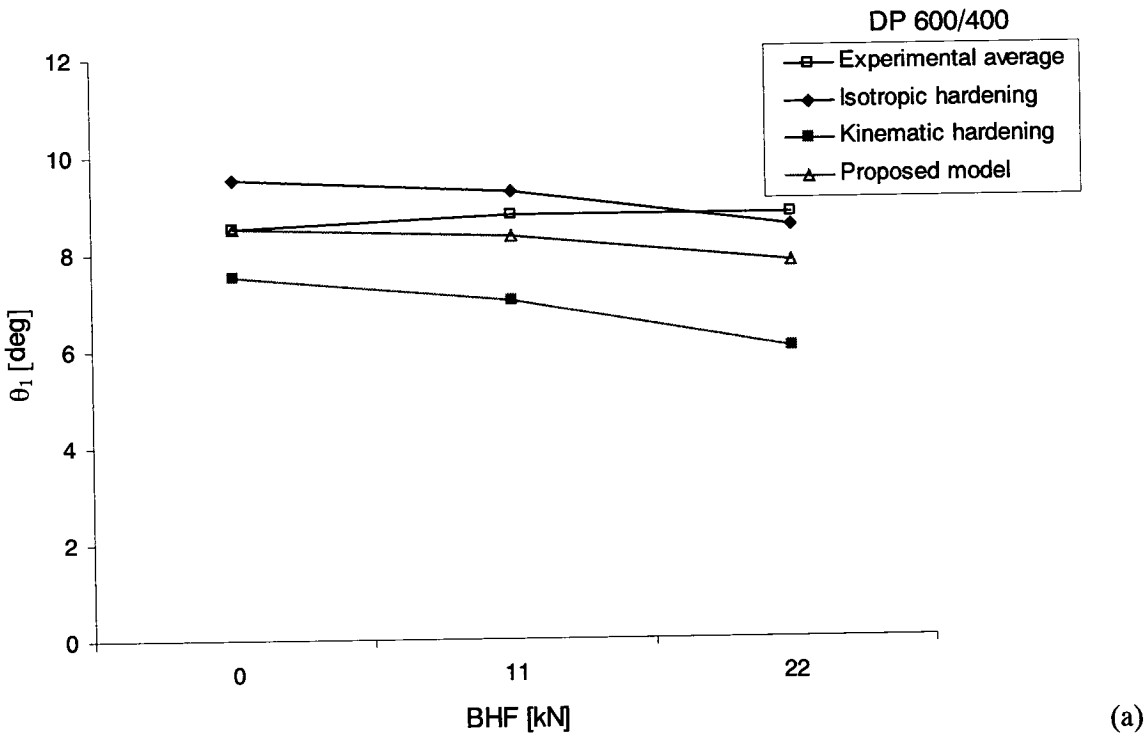

(a)

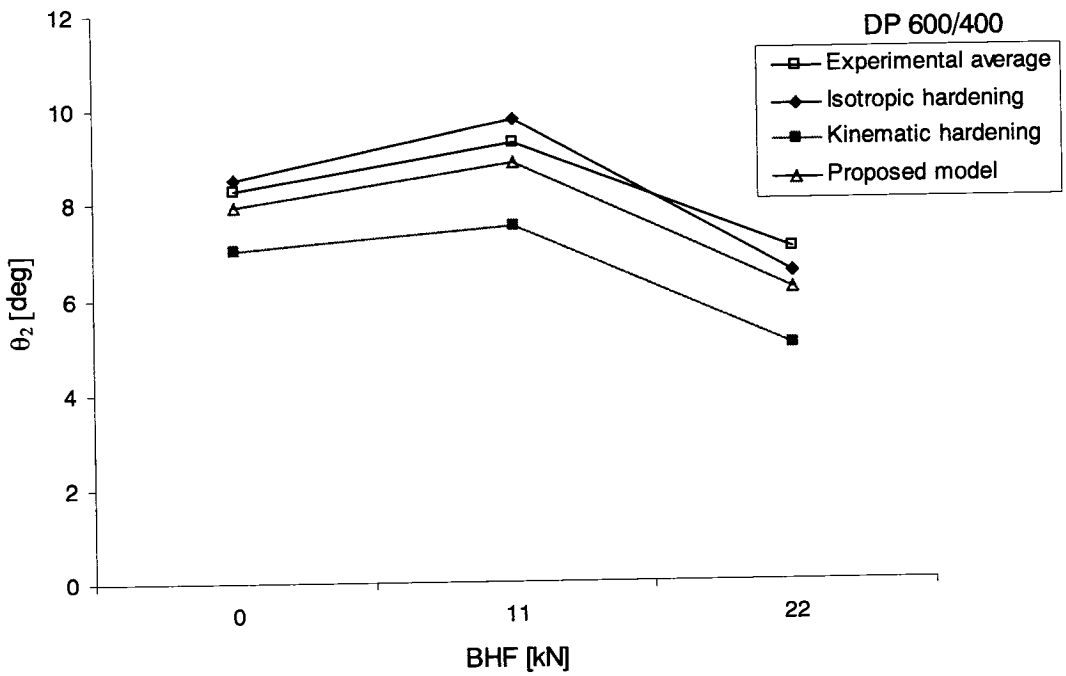

(b)

Fig. (6.18) Effect of BHF on springback angles obtained from simulations for DP 600/400 specimens, (a) θ_1 and (b) θ_2

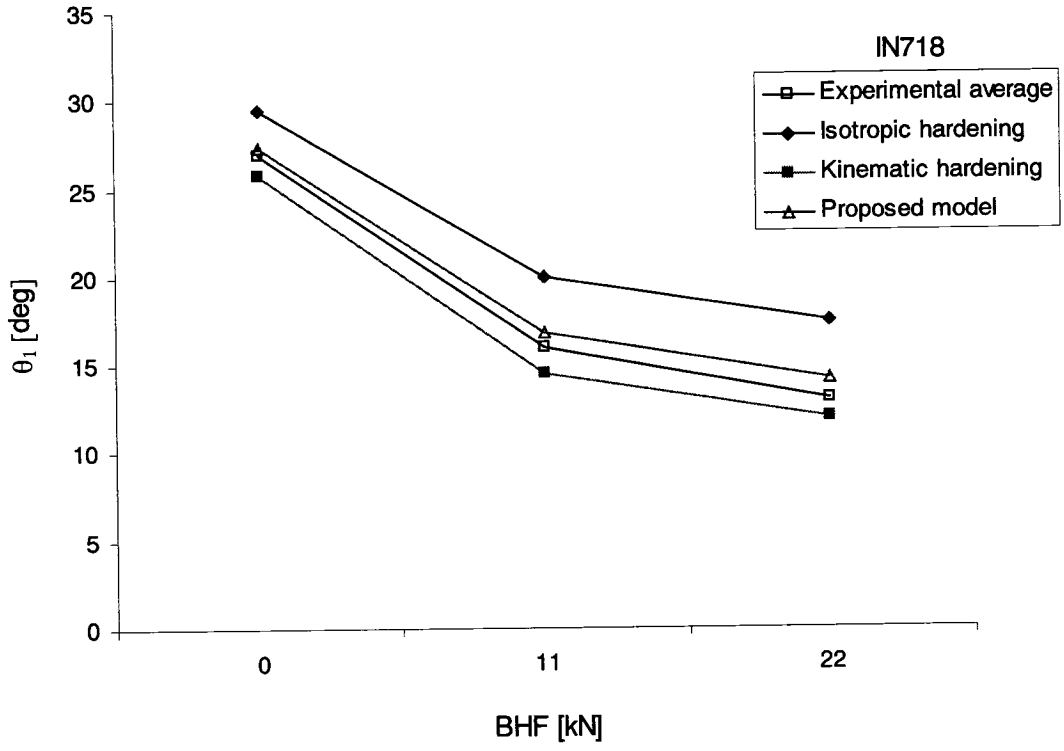

(a)

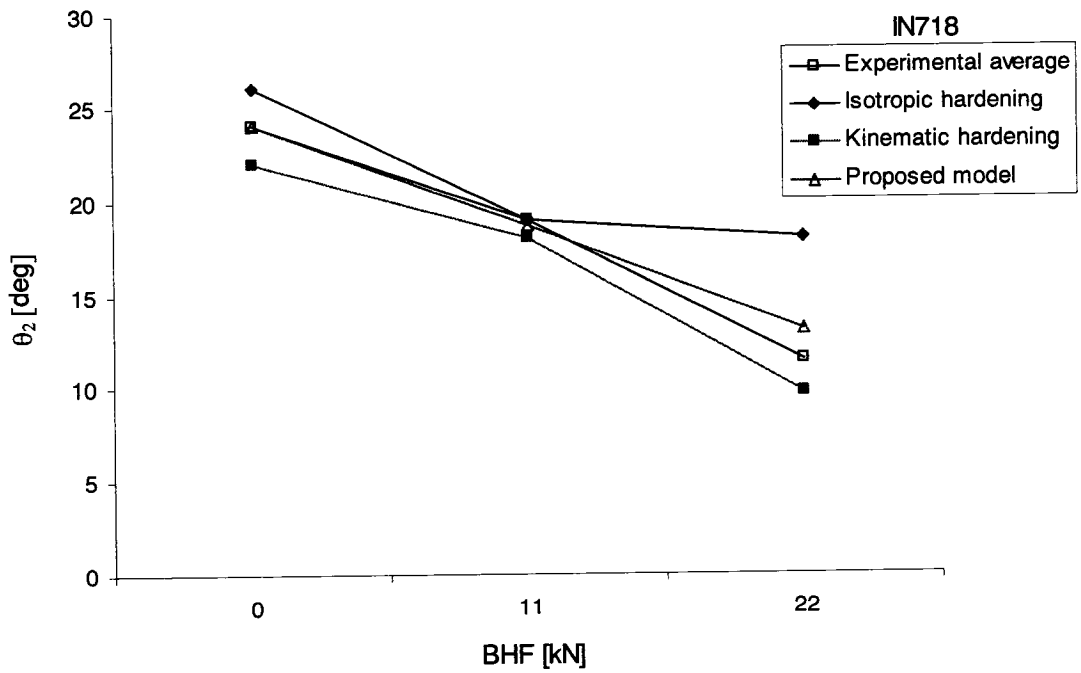

(b)

Fig. (6.19) Effect of BHF on springback angles obtained from simulations for IN718 specimens, (a) θ_1 and (b) θ_2

6.3.2.2. Effect of BHF on Thickness

Since thinning is one of the problems associated with sheet metal forming, it is important that the simulation predicts the thickness of the part after forming. This will assist in knowing the critical areas where rupture or product defects might take place. Therefore, the final thickness obtained from the experiments was compared to those calculated by the code using the proposed material model. It is worth mentioning that due to the small difference in the thickness calculated by the three models (isotropic, kinematic and the proposed model), only the results obtained from the proposed model are presented in this section. Figures (6.20) to (6.25) show the final thickness calculated by the finite element simulations compared to those measured experimentally. It is shown that the model captures the thinning that occurs in the specimens due to the increase of the BHF fairly well and thus can be used in evaluating the thickness of a real part. Figure (6.26) shows the absolute per cent error in thickness between the measured values and the values obtained from the simulations. The absolute per cent error is computed as

$$\text{Error } \% = \left| \frac{t|_{\text{experiment}} - t|_{\text{simulation}}}{t|_{\text{experiment}}} \right| \times 100 \qquad (6.5)$$

As can be seen in Fig. (6.26), the maximum error obtained between the experimental measurements and the simulations is about 5%. This finding, along with the computed springback angles, concludes that the model is capable of capturing the material behaviour during forming and can be used in simulating real parts.

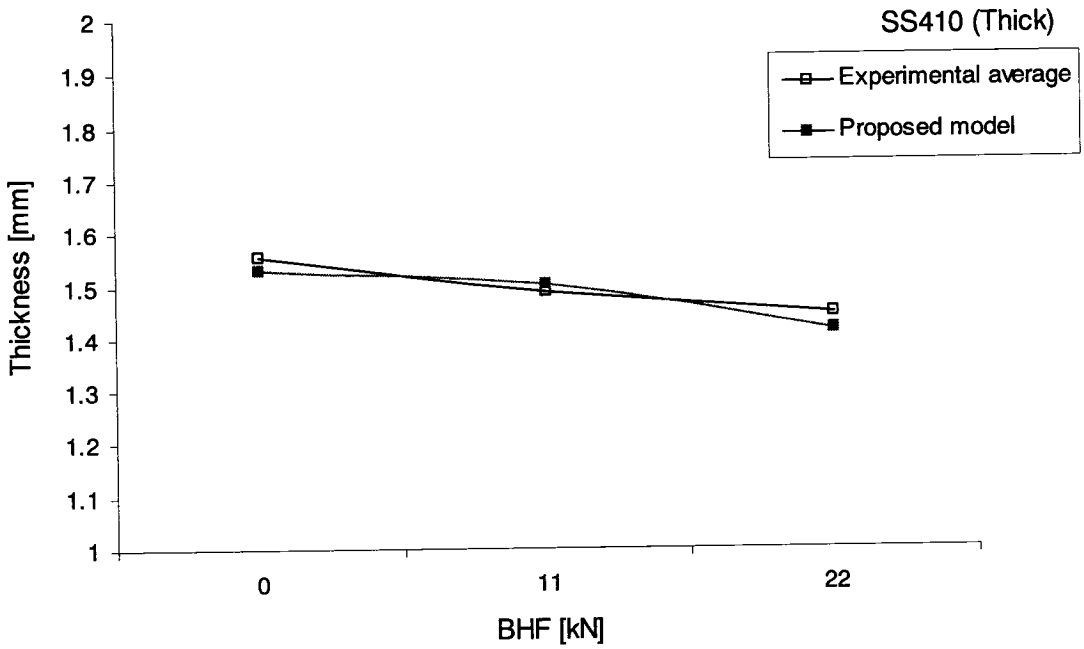

Fig. (6.20) Effect of BHF on the final thickness for SS410 thick specimens

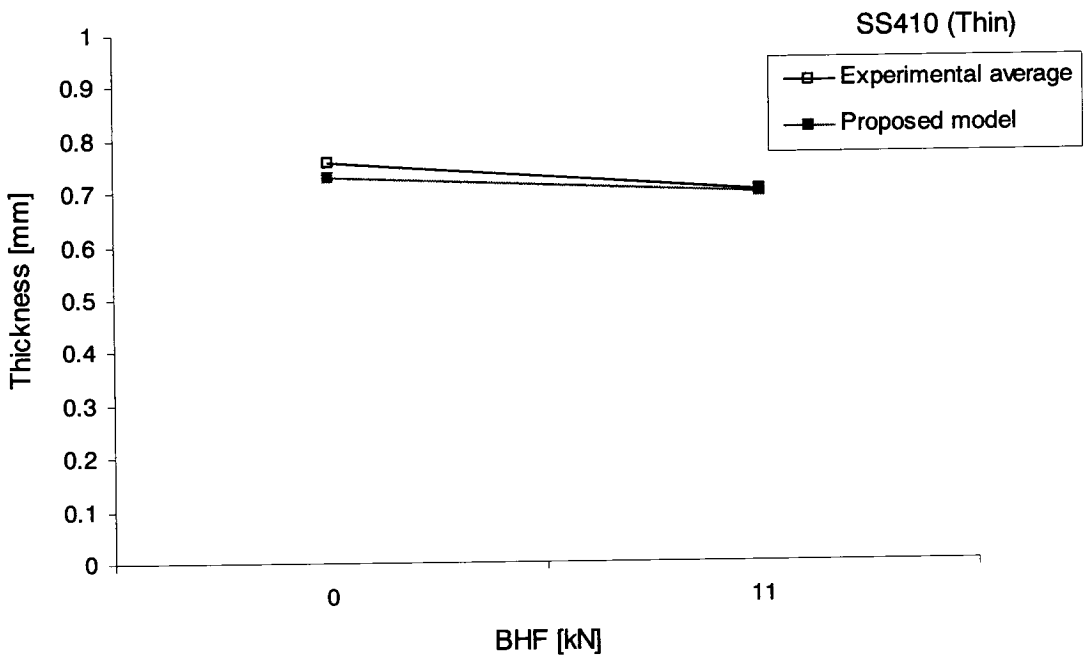

Fig. (6.21) Effect of BHF on the final thickness for SS410 thin specimens

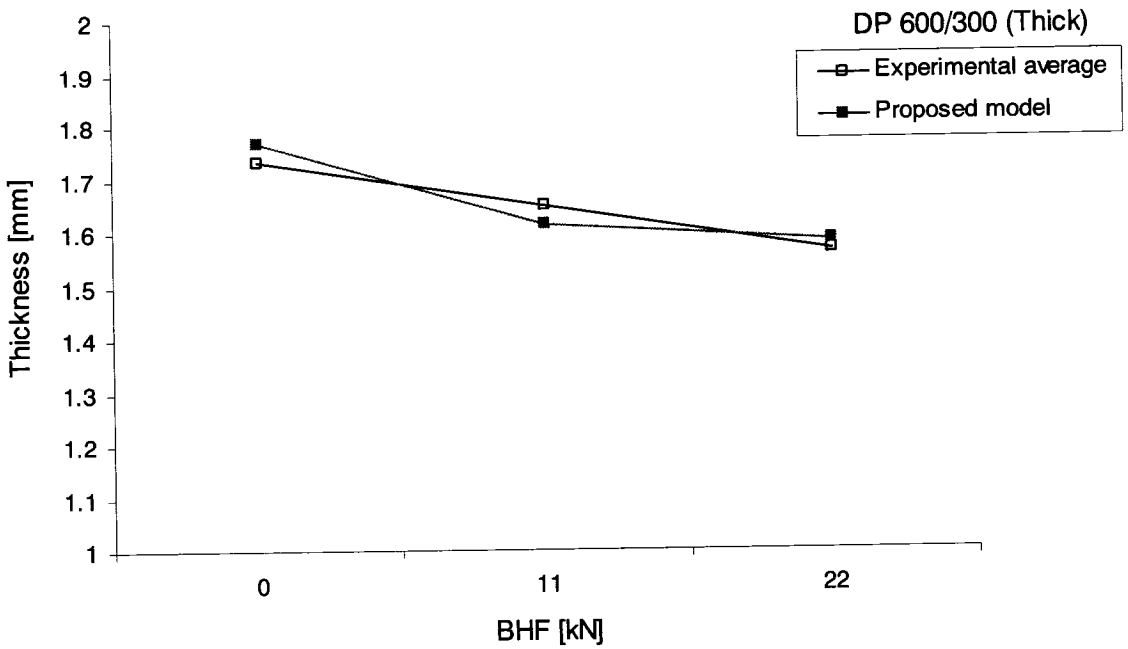

Fig. (6.22) Effect of BHF on the final thickness for DP 600/300 thick specimens

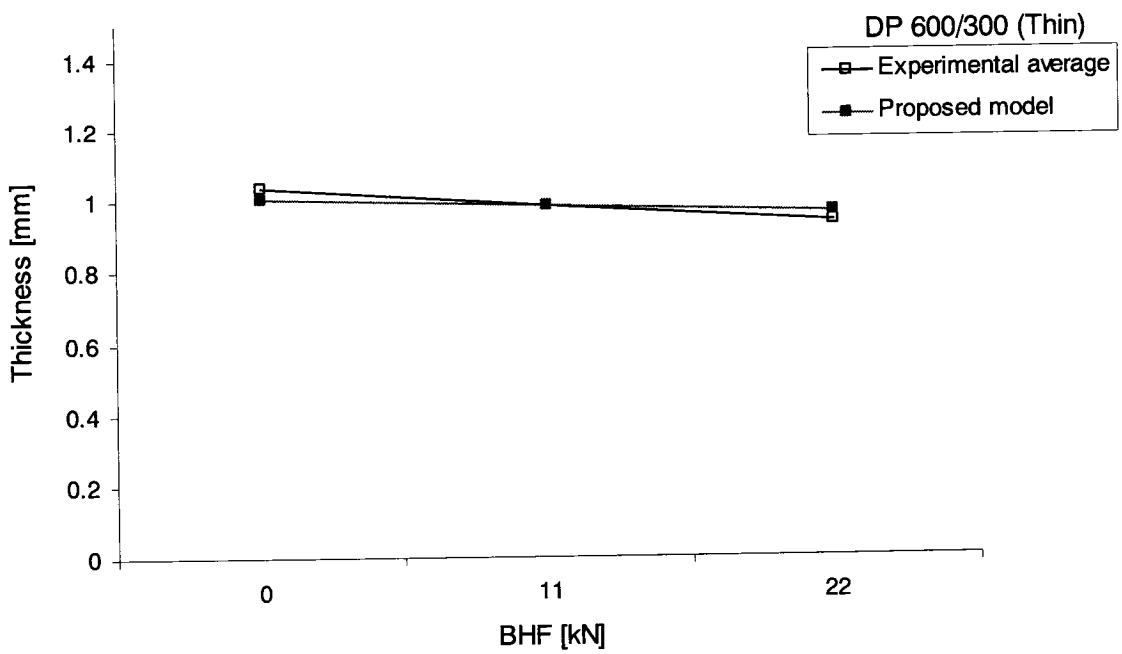

Fig. (6.23) Effect of BHF on the final thickness for DP 600/300 thin specimens

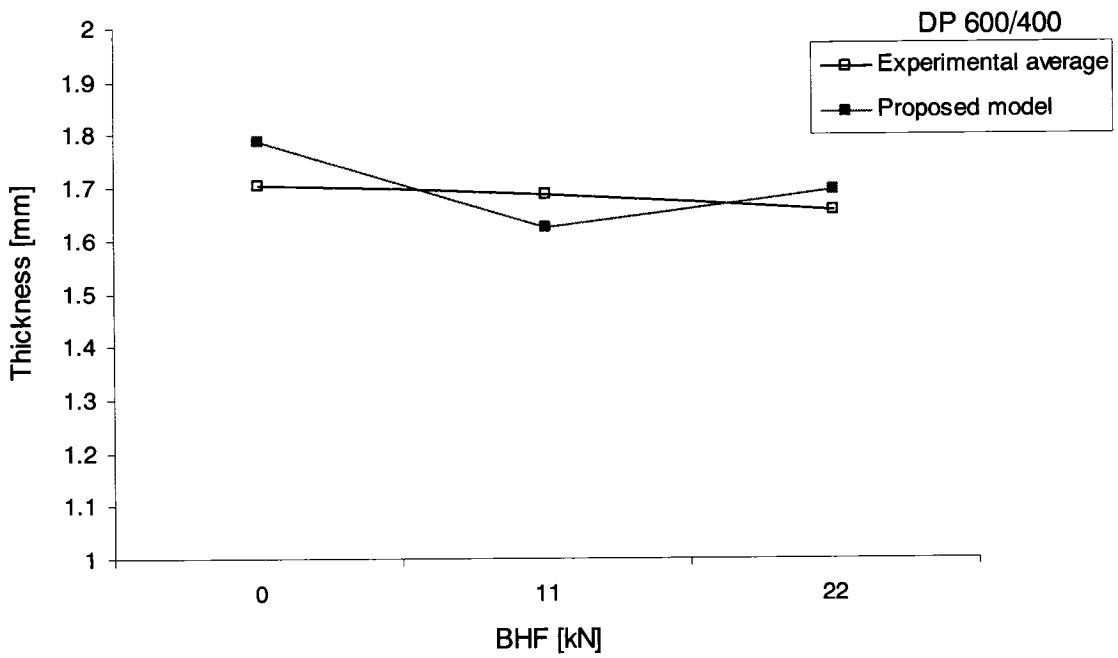

Fig. (6.24) Effect of BHF on the final thickness for DP 600/400 specimens

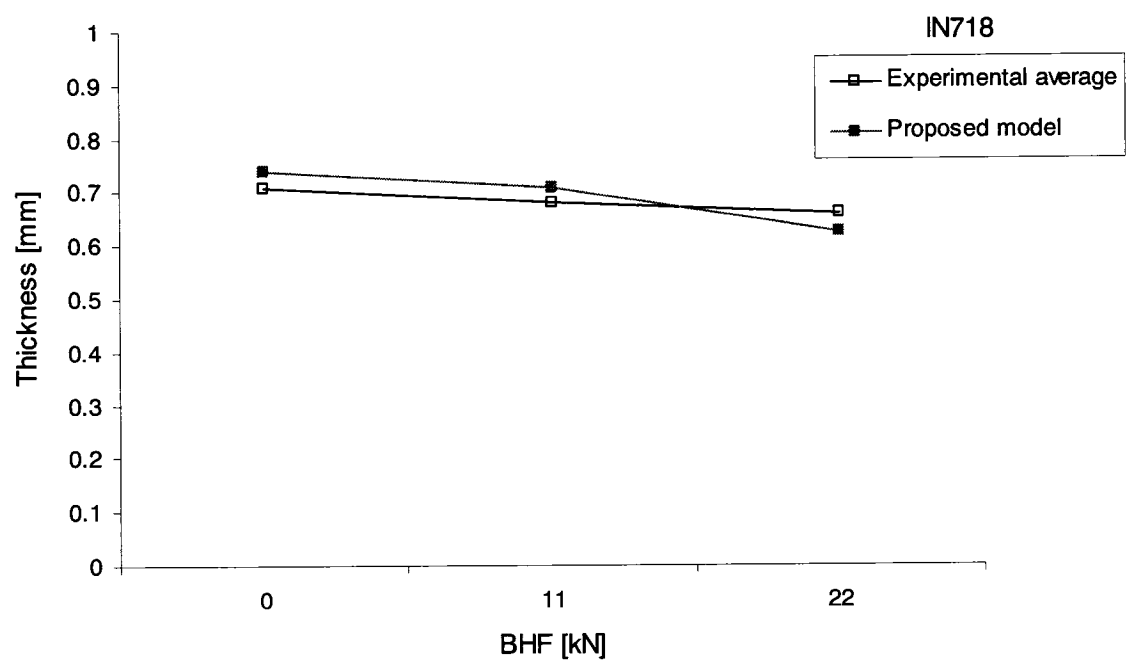

Fig. (6.25) Effect of BHF on the final thickness for IN718 specimens

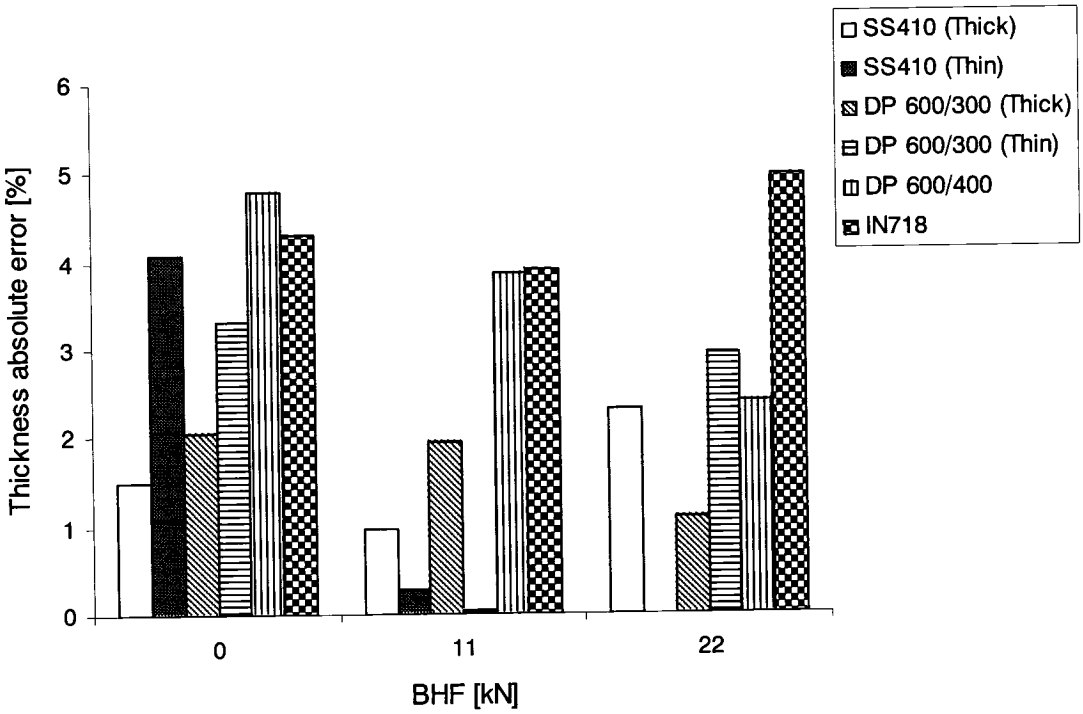

Fig. (6.26) The absolute error for thickness calculations between experiments and simulations

CHAPTER 7

Conclusions and Recommendations

7.1. Conclusions

This section contains a summary of the major findings drawn from this research work. The organization of this section is divided into two parts. The first part discusses the experimental work and the second part discusses the simulations and their correlation with the experiments.

7.1.1. Experimental Findings

In this work, four types of experiments were performed, namely standard uniaxial tension, uniaxial tension-compression, simple multiple bending, and 2D draw bending experiments. The tests were conducted on three types of materials, namely stainless steel 410, dual-phase steels 600/300 and 600/400, and inconel 718 alloy. The following are the major findings of the experimental work:

Stainless steel and inconel 718 specimens cut from the tested sheets at 0°, 45°, and 90° to the rolling direction and tensile and tensile/compressive loads were applied to determine the material behaviour as well as to determine the anisotropy parameters. The normal anisotropy parameter, $\bar{R}$, and the planar anisotropy parameter, ΔR, were determined for both materials. The dual-phase steels tested were considered as perfectly isotropic materials.

The difference in the $\bar{R}$ calculated for the thick and thin stainless steel 410 sheets is considerable. The thin sheets showed higher $\bar{R}$, which is in agreement with other researchers. For the thick sheets, $\bar{R} \approx 1.0$, and for the thin sheets, $\bar{R} \approx 1.21$. Moreover, the planar anisotropy parameter, ΔR, for the stainless steel sheets varied between ≈ 0.40 and 0.90, which is an indication to the existence of planar anisotropy of the sheets. However, as shown in the forming experiments, planar anisotropy, regardless of its existence, did not have a considerable effect on the springback angles for these sheets.

For the inconel 718, the normal anisotropy parameter, $\bar{R} \approx 1.55$, is an indication that normal anisotropy plays an important role and cannot be neglected for this material. On the other hand, the planar anisotropy parameter, $\Delta R \approx 0.50$, did not have a significant role on springback neither in simple bending nor in draw bending under 0 kN BHF. However, its role on springback angle is more pronounced when forming takes place under high BHF.

From the standard tension tests, power law hardening parameters K and n were determined for all the materials tested. The difference in the hardening parameter K for the stainless steel 410 was found to be relatively small; however, the thin sheets were found to have lower hardening due to a lower n value. This finding is in agreement with other researchers since the anisotropy of these thin sheets was found to be higher than the anisotropy of the thick ones.

The dual-phase steel 600/300 thick and thin sheets showed almost similar mechanical behaviour with almost no difference in the K and n values. On the other hand, the dual-phase steel 600/400 showed the lowest strength coefficient, K, and strain hardening exponent, n, among all the dual-phase steels tested. This finding is expected and is attributed to the process followed in manufacturing the DP 600/400 sheets.

Generally, the inconel 718 showed the highest K and n among all the materials tested in this study, which draws the attention to its superior material behaviour and hence the wide variety of applications that it can be used for.

The effect of specimen orientation on springback angles was examined in simple bending experiments. It was found that orientation does not have a significant effect on springback for all the materials tested.

After multiple simple bending operations, a strange behaviour was observed in the inconel 718 specimens. It was found that the specimens experienced an increase in the springback angle rather than a decrease due to the multiple forming. The material hardened under cyclic loading rather than softened and therefore the angle increased after forming. This interesting finding drew the attention to the need for proper modeling of the hardening behaviour for this material.

In draw bending experiments of stainless steel 410 the effect of orientation was found to be minimal on springback angles. However, it is significant in the case of inconel 718 sheets, especially when combined with higher blank holding forces.

The effect of orientation on the required forming loads was also not significant for the stainless steel 410 sheets. However, a difference can be seen in the inconel 718, specimens especially when reaching higher forming loads.

For all the thick sheets tested from stainless steel 410 and dual-phase steels 600/300 and 600/400, it is found that the blank holding force does not have a significant effect on the springback angles. However, it is more substantial in the forming of thin sheets. This finding is in agreement with other researchers that thin sheets experience more springback. As a general conclusion, the increase in the blank holding force would result in a decrease in the springback angles due to the increase of the plastic strain experienced by the specimen.

Finally, as a result of increasing the blank holding force, as expected, the thickness of the specimen decreases. This finding is in physical agreement with the concept of the constancy of volume of the materials.

7.1.2. Simulation Findings

A model that includes both the isotropic hardening effect and the Mróz kinematic hardening formulation has been developed in this work and compared to both the existing isotropic and linear kinematic hardening models in ABAQUS.

Since the effect of planar anisotropy was not significant in terms of stress – strain curves and springback angles in simple bending, the developed model takes into account only the normal anisotropy of the materials.

The existing isotropic and linear kinematic hardening models in ABAQUS did not accurately predict the material behaviour in the tension compression tests. However, the developed model showed good agreement with the experimental results in terms of stress – strain curves.

For the multiple simple bending simulations, the existing models clearly showed a range of results between the isotropic and the kinematic hardening models where the experimental results for the springback angles lied within that range. The developed model showed very good agreement with the experimental findings and also showed that it can capture the material behaviour in multiple forming stages.

In the draw bending simulations, the developed model showed better agreement with the experiments than the existing models in terms of the springback angles. Also the model captured well the effect of increasing the blank holding force on the springback angles. It is worth mentioning that since the model utilizes only the normal anisotropy, it does not capture the difference in the springback angles for the inconel 718 with respect to the specimen orientation combined with the increase in the BHF.

The developed model captured well the thinning of the specimens due to the increase in the BHF within an accuracy of 5%. Accordingly, the model can be used in predicting the critical zones in forming operations. As a result, it can be used as a tool to predict some of the optimum forming conditions.

7.2. Statement of Originality

In this work the following can be considered as a contribution to the literature:

1- A modified model that uses normal anisotropy, isotropic hardening formulation and Mróz multiple–surface kinematic hardening formulation was developed and implemented in the finite element simulations is presented in this work.
2- The developed material model is considered as a generic model that is ready to be used in real forming operations of sheet metal products, with minimal experimental testing required to determine the material properties and model parameters.
3- To the best of the author's knowledge, at the time of this publication, springback of stainless steel 410 and inconel 718 sheets is studied for the first time in this work.

4- Also, to the best of the author's knowledge, anisotropy of inconel 718 was never discussed elsewhere in the literature.

5- With the increase in the use of stainless steel 410 and inconel 718 in the aerospace industry, the developed model can add an extra tool to verify forming conditions, predict springback angles, and check for critical zones in a product before proceeding with the real forming processes.

6- The following publications resulted from the current work:

   a- Ragai, I., and Nemes, J.A., *Springback in Aerospace Sheet Metal Materials*, accepted in the 3rd International Symposium on Aerospace Materials and Manufacturing Processes: Emerging Materials, Manufacturing, and Repair Techniques, COM 2006, 45th Conference of Metallurgists, Montreal, Canada, October 1 – 4, 2006.

   b- Ragai, I., Lazim, D. and Nemes, J.A., *Anisotropy and Springback in Draw-Bending of Stainless Steel 410: Experimental and Numerical Study*, Journal of Manufacturing Processing Technology, Vol. 166, pp. 116-127, 2005.

   c- Ragai, I., and Nemes, J.A., *Experimental Investigation of Springback of Dual-Phase Steels*, SAE 2005 Conf. & Exhibit, Detroit, Michigan, U.S.A., April 11-14, 2005.

   d- Ragai, I., Lazim, D. and Nemes, J.A., Springback in Draw-Bending of Inconel 718 and Modeling of Stainless Steel Cone Support Part, 2003 (Technical Report).

   e- Ragai, I., Lazim, D. and Nemes, J.A., Springback in Draw-Bending of Stainless Steel, Type 410, 2002 (Technical Report).

7.3. Future Work and Recommendations

The following can be considered as potential future tasks that can be done to enhance the model capability:

1- A fully anisotropic yield function that includes both normal and planar anisotropy of the material can be implemented within the current model. Such yield function can take any of the anisotropic yield function forms discussed in Section 2.3. However, the appropriate parameters must be determined to be implemented within the simulations.

2- The influence of strain rate properties can be considered in a future work since many forming operations are conducted at high speeds. That consideration could help for more accurate springback prediction. In this case, a strain rate parameter can be introduced to the yield function and the formulation of the model can then be carried out to determine the strain and stress increments.

3- The influence of tool stiffness (die, punch, and blank holder) can be considered in further modeling, in conjunction with the developed material model, to examine its effect on the springback angles. When modeling the tools, instead of assuming they are rigid parts, a specific stiffness can be added to the model and the influence of that stiffness on springback can be examined.

4- As noted previously the use of a Coulomb friction coefficient needed to be adjusted to reflect the accurate friction between the tools and the sheets. It was reported by some authors (Gilmour *et al.*, 2004) that the accuracy of the predicted strains can be improved by using a load-dependent friction coefficient. This methodology in combination with the developed model can be used to enhance the accuracy of predicting the springback in complex geometries.

APPENDIX A

Bending Angle Calculation for Simple Bending Experiments

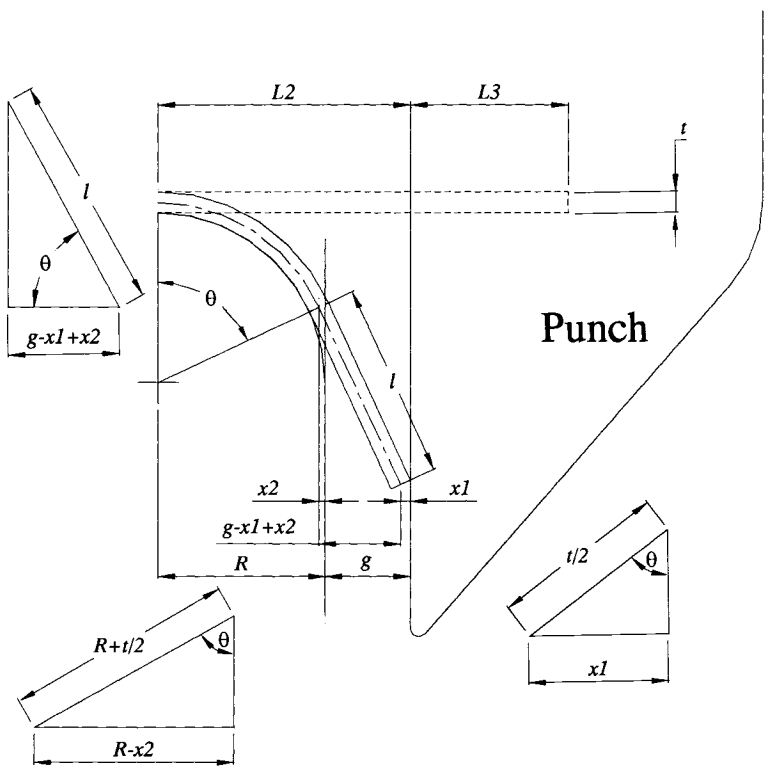

Before bending

$Length = L_2 + L_3$

After bending

$$Length = L_2 + L_3 = \left(R + \frac{t}{2}\right)\theta + l \tag{A.1}$$

$$\cos\theta = \frac{g - x_1 + x_2}{l}$$

$$l = \frac{1}{\cos\theta}\left[g - x_1 + x_2\right]$$

$$l = \frac{1}{\cos\theta}\left[L_2 - R - x_1 + x_2\right] \tag{A.2}$$

$$\sin\theta = \frac{x_1}{\left(t/2\right)}$$

$$x_1 = \frac{t}{2}\sin\theta \tag{A.3}$$

Also,

$$\sin\theta = \frac{R - x_2}{\left(R + t/2\right)}$$

$$\left(R + t/2\right)\sin\theta = R - x_2$$

$$x_2 = R\sin\theta + \frac{t}{2}\sin\theta - R \tag{A.4}$$

Substituting Eqs. (A.3) and (A.4) into Eq. (A.2)

$$l = \frac{1}{\cos\theta}\left[L_2 - R - \frac{t}{2}\sin\theta - R\sin\theta - \frac{t}{2}\sin\theta + R\right]$$

$$l = \frac{1}{\cos\theta}\left[L_2 - R\sin\theta - t\sin\theta\right] \tag{A.5}$$

Substituting Eqs. (A.5) into Eq. (A.1)

$$L_2 + L_3 = \left(R + \frac{t}{2}\right)\theta + \frac{1}{\cos\theta}\left[L_2 - R\sin\theta - t\sin\theta\right]$$

$$L_2\cos\theta + L_3\cos\theta = \left(R + \frac{t}{2}\right)\theta\cos\theta + L_2 - R\sin\theta - t\sin\theta$$

$$L_2\left(1 - \cos\theta\right) - L_3\cos\theta + \left(R + \frac{t}{2}\right)\theta\cos\theta - R\sin\theta - t\sin\theta = 0 \tag{A.6}$$

Equation (A.6) can then be used to calculate the bending angle before springback.

APPENDIX B

Experimental Variations

B1. Experimental Variations for Uniaxial Tension Tests

Material	Number of sheets tested	Orientation	Number of specimens	True strain	Average value of true stress (MPa)	Maximum measured value (MPa)	Minimum measured value (MPa)	Deviation (+) (%)	Deviation (-) (%)
SS410 (Thick)	5	0	7	0.03	380	393	371	3.53	2.21
				0.06	460	471	449	2.40	2.34
				0.09	507	529	500	4.39	1.24
				0.12	540	570	526	5.60	2.41
		45	7	0.03	400	423	381	5.83	4.50
				0.06	480	490	468	2.06	2.46
				0.09	530	549	524	3.63	1.00
				0.12	560	591	554	5.45	1.02
		90	7	0.03	385	396	367	2.98	4.58
				0.06	465	475	452	2.18	2.68
				0.09	512	523	490	2.13	4.24
				0.12	550	565	525	2.66	4.35
SS410 (Thin)	2	0	4	0.03	395	403	384	2.07	2.71
				0.06	450	464	433	3.14	3.66
				0.09	495	512	483	3.37	2.43
				0.12	525	547	507	4.21	3.33
		45	4	0.03	435	450	424	3.49	2.41
				0.06	505	522	484	3.42	3.99
				0.09	545	576	535	5.64	1.69
				0.12	575	597	564	3.86	1.91
		90	4	0.03	415	428	406	3.22	1.99
				0.06	475	503	459	5.90	3.23
				0.09	520	547	503	5.23	3.08
				0.12	545	578	534	5.96	1.91
DP600/300 (Thick)	2	90	3	0.03	525	555	513	5.81	2.07
				0.06	610	624	593	2.21	2.71
				0.09	660	692	640	4.82	2.89
				0.12	690	726	665	5.27	3.44

Material	Number of sheets tested	Orientation	Number of specimens	True strain	Average value of true stress (MPa)	Maximum measured value (MPa)	Minimum measured value (MPa)	Deviation (+) (%)	Deviation (-) (%)
DP600/300 (Thin)	2	90	3	0.03	555	576	546	3.87	1.61
				0.06	645	666	623	3.20	3.25
				0.09	695	730	675	5.00	2.72
				0.12	730	755	720	3.41	1.35
DP600/400	2	90	3	0.03	515	527	501	2.30	2.75
				0.06	580	596	567	2.79	2.18
				0.09	615	629	594	2.26	3.32
				0.12	625	646	612	3.43	2.00
IN718	3	0	4	0.03	590	614	570	4.04	3.24
				0.06	700	724	682	3.49	2.48
				0.09	790	837	754	5.94	4.26
				0.12	875	894	861	2.16	1.61
		45	4	0.03	565	576	547	2.02	3.13
				0.06	665	703	642	5.70	3.26
				0.09	750	768	739	2.40	1.47
				0.12	825	850	791	3.03	3.99
		90	4	0.03	600	628	581	4.72	2.99
				0.06	700	737	689	5.24	1.47
				0.09	785	823	751	4.90	4.16
				0.12	865	885	855	2.34	1.16

B2. Variations in Springback angles for Multiple-Simple Bending Experiments

Material	Orientation	Set #	t (mm)	Springback angle (deg)			
				Process			
				B	BR	BRB	BRBR
SS410 (Thin)	0°	1	0.723	12.43	12.68	13.35	13.93
		2	0.723	12.35	12.93	12.43	12.93
		3	0.723	11.93	12.68	13.10	12.60
		4	0.72	12.19	13.02	13.11	13.61
		Max. deviation		0.50	0.34	0.92	1.33
		Average		12.23	12.83	13.00	13.27
	45°	1	0.728	12.36	13.36	12.02	13.52
		2	0.726	12.01	12.68	12.26	12.43
		3	0.728	11.69	12.61	13.36	12.61
		4	0.727	12.16	12.69	12.61	12.86
		Max. deviation		0.67	0.75	1.34	1.09
		Average		12.06	12.84	12.56	12.86
	90°	1	0.728	12.44	13.61	13.28	14.44
		2	0.728	12.36	12.86	12.11	13.02
		3	0.729	12.86	12.36	13.27	13.44
		4	0.727	13.02	13.19	13.36	13.69
		Max. deviation		0.66	1.25	1.25	1.42
		Average		12.67	13.01	13.01	13.65

Material	Orientation	Set #	t (mm)	Springback angle (deg)			
				Process			
				B	BR	BRB	BRBR
DP600/300	0°	1	1.052	13.46	n/a	n/a	n/a
		2	1.047	13.95	13.62	14.70	13.62
		3	1.048	13.88	13.96	14.88	14.13
		4	1.039	13.77	14.86	14.27	15.19
		Max. deviation		0.49	1.24	0.61	1.57
		Average		13.77	14.15	14.62	14.31
	45°	1	1.045	13.45	13.37	13.95	13.95
		2	1.045	13.70	13.28	14.70	13.45
		3	1.046	13.87	13.95	14.70	14.20
		4	1.038	13.77	14.11	14.44	14.94
		Max. deviation		0.42	0.83	0.75	1.49
		Average		13.70	13.68	14.45	14.14
	90°	1	1.038	13.02	13.86	14.19	14.69
		2	1.039	13.44	13.52	13.94	14.19
		3	1.045	12.95	14.20	14.37	14.53
		4	1.04	13.19	14.36	13.69	14.94
		Max. deviation		0.49	0.84	0.68	0.75
		Average		13.15	13.99	14.05	14.59

Material	Orientation	Set #	t (mm)	Springback angle (deg)			
				Process			
				B	BR	BRB	BRBR
IN718	0°	1	0.644	22.30	23.80	23.13	24.97
		2	0.644	21.80	23.05	23.38	23.97
		3	0.644	21.30	22.47	23.30	23.97
		4	0.645	22.55	22.80	24.30	24.05
		Max. deviation		1.25	1.33	1.17	1.00
		Average		21.99	23.03	23.53	24.24
	45°	1	0.642	22.30	24.38	22.55	25.30
		2	0.647	21.98	23.56	24.39	24.23
		3	0.643	21.88	23.22	24.05	24.13
		4	0.642	22.72	23.05	24.72	24.88
		Max. deviation		0.84	1.33	2.17	1.17
		Average		22.22	23.55	23.93	24.64
	90°	1	0.642	22.72	24.30	23.80	25.30
		2	0.64	21.80	23.22	24.22	24.13
		3	0.643	21.80	22.88	24.13	24.13
		4	0.639	22.55	22.88	24.55	24.72
		Max. deviation		0.92	1.42	0.75	1.17
		Average		22.22	23.32	24.18	24.57

B3. Variations in Springback angles for 2D Draw-Bending Experiments

Material	Number of sheets tested	BHF (kN)	Orientation	Number of specimens	Average springback angle, θ_1 (deg)	Maximum measured value (deg)	Minimum measured value (deg)	Deviation (+) (%)	Deviation (-) (%)
SS410 (Thick)	5	0	0°	3	8.25	8.75	8.00	6.06	2.89
			45°	3	7.75	8.25	7.50	6.45	3.07
			90°	3	7.75	8.00	7.50	3.23	3.12
		11	0°	3	7.00	7.25	6.75	3.57	3.48
			45°	3	7.50	7.75	7.50	3.33	0.00
			90°	3	7.00	7.25	6.75	3.57	3.46
		22	0°	3	6.75	7.00	6.50	3.70	3.55
			45°	3	5.50	5.75	5.25	4.55	4.40
			90°	3	5.00	5.25	5.00	5.00	0.00
SS410 (Thin)	2	0	0°	3	15.00	15.75	14.50	5.00	3.20
			45°	3	15.00	15.50	14.75	3.33	1.62
			90°	3	15.50	16.00	15.00	3.23	3.11
	2	11	0°	3	6.75	7.00	6.50	3.70	3.61
			45°	3	6.50	6.75	6.25	3.85	3.72
			90°	3	6.50	7.00	6.25	7.69	3.64
DP600/300 (Thick)	2	0	90°	3	7.00	7.50	6.75	7.14	3.40
		11		3	6.50	6.75	6.25	3.85	3.72
		22		3	5.50	5.75	5.50	4.55	0.00
DP600/300 (Thin)	2	0	90°	3	16.00	17.00	15.25	6.25	4.45
		11		3	12.00	12.50	11.50	4.17	4.01
		22		3	9.50	9.75	9.25	2.63	2.57
DP600/400	2	0	90°	3	8.50	8.75	8.25	2.94	2.86
		11		3	8.75	9.25	8.50	5.71	2.72
		22		3	8.75	9.00	8.50	2.86	2.77
IN718	3	0	0°	3	27.50	28.75	26.50	4.55	3.49
			45°	3	27.00	28.25	26.50	4.63	1.77
			90°	3	27.00	28.00	26.50	3.70	1.79
		11	0°	3	15.50	16.00	14.75	3.23	4.66
			45°	3	20.00	20.50	19.75	2.50	1.22
			90°	3	16.00	16.50	15.75	3.13	1.51
	3	22	0°	3	16.00	16.50	15.75	3.13	1.52
			45°	3	16.50	17.50	15.75	6.06	4.30
			90°	3	13.00	13.75	12.75	5.77	1.82

Material	Number of sheets tested	BHF (kN)	Orientation	Number of specimens	Average springback angle, θ_2 (deg)	Maximum measured value (deg)	Minimum measured value (deg)	Deviation (+) (%)	Deviation (-) (%)
SS410 (Thick)	5	0	0°	3	7.00	7.25	7.00	3.57	0.00
			45°	3	7.00	7.25	6.75	3.57	3.45
			90°	3	7.00	7.25	6.75	3.57	3.50
		11	0°	3	5.00	5.25	4.75	5.00	4.79
			45°	3	5.00	5.25	5.00	5.00	0.00
			90°	3	5.50	5.75	5.25	4.55	4.42
		22	0°	3	2.50	2.50	2.25	0.00	9.57
			45°	3	3.50	3.50	3.25	0.00	6.99
			90°	3	3.00	3.00	2.75	0.00	8.16
SS410 (Thin)	2	0	0°	3	16.50	16.75	15.75	1.52	4.45
			45°	3	18.00	18.75	17.25	4.17	4.00
			90°	3	17.50	18.25	17.25	4.29	1.37
	2	11	0°	3	3.50	3.50	3.50	0.00	0.00
			45°	3	3.50	3.50	3.25	0.00	6.96
			90°	3	3.50	3.75	3.50	7.14	0.00
DP600/300 (Thick)	2	0	90°	3	6.50	6.75	6.25	3.85	3.77
		11		3	7.25	7.50	7.00	3.45	3.33
		22		3	4.00	4.25	4.00	6.25	0.00
DP600/300 (Thin)	2	0	90°	3	15.25	15.75	14.50	3.28	4.74
		11		3	11.75	12.50	11.50	6.38	2.02
		22		3	10.50	11.25	10.25	7.14	2.25
DP600/400	2	0	90°	3	8.25	8.75	8.00	6.06	2.86
		11		3	9.25	9.50	9.00	2.70	2.60
		22		3	7.00	7.25	6.75	3.57	3.40
IN718	3	0	0°	3	26.00	27.25	25.25	4.81	2.74
			45°	3	26.50	27.75	25.75	4.72	2.69
			90°	3	24.00	24.75	23.50	3.13	2.03
		11	0°	3	16.50	17.25	16.00	4.55	2.89
			45°	3	22.00	23.25	21.75	5.68	1.08
			90°	3	19.00	19.75	18.25	3.95	3.79
	3	22	0°	3	16.50	17.25	16.00	4.55	2.90
			45°	3	16.50	17.00	16.25	3.03	1.48
			90°	3	11.50	12.00	11.25	4.35	2.10

APPENDIX C

MAPLE® Script for the Stress Components in Isotropic Hardening Model

```
> restart;
> a:=(s11-(R/(1+R)*s22))/sigma;
```

$$a := \frac{s11 - \frac{Rs22}{1+R}}{\sigma}$$

```
> b:=(s22-(R/(1+R)*s11))/sigma;
```

$$b := \frac{s22 - \frac{Rs11}{1+R}}{\sigma}$$

```
> c:=(2*R+1)/(R+1)*s12/sigma;
```

$$c := \frac{(2R+1)s12}{(1+R)\sigma}$$

```
>
dep=sqrt(de11^2+de22^2+de11*de22*(2*R)/(1+R)+de12^2*((2*R+1
)/(1+R)));
```

$$dep = \sqrt{de11^2 + de22^2 + \frac{2de11de22R}{1+R} + \frac{de12^2(2R+1)}{1+R}}$$

```
> Eq1:=de11[iso-total]=1/E*(ds11-nu*ds22)+a*dep;
```

$$Eq1 := de11_{iso-total} = \frac{ds11 - \nu ds22}{E} + \frac{\left(s11 - \frac{Rs22}{1+R}\right)dep}{\sigma}$$

```
> Eq2:=de22[iso-total]=1/E*(ds22-nu*ds11)+b*dep;
```

$$Eq2 := de22_{iso-total} = \frac{ds22 - \nu ds11}{E} + \frac{\left(s22 - \frac{Rs11}{1+R}\right)dep}{\sigma}$$

```
> Eq3:=de12[iso-total]=(1+nu)/E*ds12+c*dep;
```

$$Eq3 := de12_{iso-total} = \frac{(1+\nu)ds12}{E} + \frac{(2R+1)s12dep}{(1+R)\sigma}$$

```
> eqns := { Eq1,Eq2,Eq3 }:
> solve( eqns,{ds11, ds22, ds12});
```

$d\sigma_{11}$ is calculated as:

$$ds11=-(\nu\, de22_{iso-total}\sigma R+deps22R+\nu\, depRs11-depRs11+de11_{iso-total}\sigma R-\nu\, deps22R+\nu\, de22_{iso-total}\sigma-deps11+de11_{iso-total}\sigma-\nu\, deps22)E/(\sigma(-1-R+\nu^2+\nu^2R))$$

$d\sigma_{22}$ is calculated as:

$$ds22=-E(de22_{iso-total}\sigma+de22_{iso-total}\sigma R+depRs11+\nu\, de11_{iso-total}\sigma-deps22-deps22R-\nu\, depRs11+\nu\, de11_{iso-total}\sigma R-\nu\, deps11+\nu\, deps22R)/(\sigma(-1-R+\nu^2+\nu^2R))$$

and $d\sigma_{12}$ is calculated as:

$$ds12=\frac{E(de12_{iso-total}\sigma+de12_{iso-total}\sigma R-2s12depR-s12dep)}{\sigma(1+R+\nu+\nu R)}$$

APPENDIX D

Determination of the Hardening Parameter $\bar{K}$

From Holloman power law

$$\begin{aligned}\bar{\sigma} &= K\left(\varepsilon^{el} + \bar{\varepsilon}^{p}\right)^{n} \\ &= K\left(\frac{\bar{\sigma}}{E} + \bar{\varepsilon}^{p}\right)^{n}\end{aligned} \tag{D.1}$$

one can get, after rearranging the variables in the equation

$$\bar{\varepsilon}^{p} = \left(\frac{\bar{\sigma}}{K}\right)^{\frac{1}{n}} - \frac{\bar{\sigma}}{E} \tag{D.2}$$

therefore,

$$\frac{d}{d\bar{\varepsilon}^{p}}\left[\left(\frac{\bar{\sigma}}{K}\right)^{\frac{1}{n}} - \frac{\bar{\sigma}}{E}\right] = 1 \tag{D.3}$$

Accordingly,

$$\left[\frac{1}{n}\left(\frac{\bar{\sigma}}{K}\right)^{\frac{1-n}{n}} - \frac{1}{E}\right]\frac{d\bar{\sigma}}{d\bar{\varepsilon}^{p}} = 1 \tag{D.4}$$

and hence,

$$\frac{d\bar{\sigma}}{d\bar{\varepsilon}^p} = \frac{1}{\frac{1}{n}\left(\frac{\bar{\sigma}}{K}\right)^{\frac{1-n}{n}} - \frac{1}{E}} = \frac{nE}{E\left(\frac{\bar{\sigma}}{K}\right)^{\frac{1-n}{n}} - n} = \bar{K} \tag{D.5}$$

APPENDIX E

MAPLE® Script for the Stress Components in Kinematic Hardening Model

```
> restart;
> del1[el]:=1/E*(ds11-nu*ds22):
> de22[el]:=1/E*(ds22-nu*ds11):
> de12[el]:=(1+nu)/E*ds12:
-----------------------------------------------------------
> df11:=2/(R+1)*((R+1)*s11-R*s22):
> df22:=2/(R+1)*((R+1)*s22-R*s11):
> df33:=-2/(R+1)*(s11+s22):
> df12:=4/(R+1)*(2*R+1)*s12:
-----------------------------------------------------------
>
C1=(df11*ds11+2*df12+ds12+df22*ds22)/(df11^2+2*df12^2+df22^
2+df33^2):
> Eq1:=del1[kin-total]=del1[el]+2*C1/(Kp*(R+1))*((R+1)*s11-
R*s22);
```

$$Eq1 := de11_{kin-total} = \frac{ds11 - \nu\, ds22}{E} + \frac{2\,C1\,((R+1)\,s11 - R\,s22)}{Kp\,(R+1)}$$

```
> Eq2:=de22[kin-total]=de22[el]+2*C1/(Kp*(R+1))*((R+1)*s22-
R*s22);
```

$$Eq2 := de22_{kin-total} = \frac{ds22 - \nu\, ds11}{E} + \frac{2\,C1\,((R+1)\,s22 - R\,s22)}{Kp\,(R+1)}$$

```
> Eq3:=de12[kin-
total]=de12[el]+4*C1/(Kp*(R+1))*((2*R+1)*s12);
```

$$Eq3 := de12_{kin-total} = \frac{(1+\nu)\,ds12}{E} + \frac{4\,C1\,(2R+1)\,s12}{Kp\,(R+1)}$$

```
> eqns := { Eq1,Eq2,Eq3 }:
> solve( eqns,{ds11, ds22, ds12});
```

$d\sigma_{11}$ is calculated as:

$$ds11 = E\,(-de11_{kin-total}\,Kp\,R - de11_{kin-total}\,Kp - 2\,C1\,R\,s22 - \nu\,de22_{kin-total}\,Kp\,R + 2\,C1\,R\,s11 + 2\,C1\,s11 - \nu\,de22_{kin-total}\,Kp + 2\,\nu\,C1\,s22) \,/\, (Kp\,(-R - 1 + \nu^2 R + \nu^2))$$

$d\sigma_{22}$ is calculated as:

$$ds22 = (-de22_{kin-total}\, Kp\, R - \nu\, de11_{kin-total}\, Kp\, R - 2\, R\, \nu\, C1\, s22 + 2\, \nu\, C1\, R\, s11 + 2\, C1\, s22 - de22_{kin-total}\, Kp - \nu\, de11_{kin-total}\, Kp + 2\, \nu\, C1\, s11)\, E \,/\, (Kp\, (-R - 1 + \nu^2\, R + \nu^2))$$

and $d\sigma_{12}$ is calculated as:

$$ds12 = -\frac{E\,(-de12_{kin-total}\, Kp\, R - de12_{kin-total}\, Kp + 8\, C1\, s12\, R + 4\, C1\, s12)}{Kp\,(R + 1 + \nu\, R + \nu)}$$

REFERENCES

ABAQUS (2003) Theory, User's, and Example Problems Manuals, Hibbit, Karlson & Sorensen, Inc.

Aerens, R. (1997) Characterization of Material by Bending, *Proceedings of the 5th International Conference on Sheet Metal: SHEMET'97*, Singh, U.P. Shirvani, B., Geiger, M. and Kals, H.J.J. (eds), Belfast, UK, April 8 – 10, pp 251– 262.

Ahmetoglu, M., Hua, J., Kulukuru, S. and Altan, T (2004) Hydroforming of Sheet Metal Using A Viscous Pressure Medium, *Journal of Materials Processing Technology*, Vol. 146, pp. 97–107.

American Iron and Steel Institute (2003) Characterization of Formability of New Generation High Strength Steels for Automotive Applications, Final Report, AISI, Southfield, Michigan.

Appiah, E. and Jain, M. (2004) A new constitutive model for prediction of springback in sheet metal forming, *Proceedings of the 8th International Conference on Numerical Methods in Industrial Forming Processes*, Ghosh, S., Castro, J.C. and Lee, J.K. (eds.), Columbus, Ohio, June 13 – 17, pp 1651 – 1657.

Asnafi, N. (2001) On Springback of Double-Curved Autobody Panels, *International Journal of Mechanical Sciences*, Vol. 43, pp. 5-37.

ASTM Standard E 517-98 (1998) Standard Test Method for Plastic Strain Ratio *r* for Sheet Metal, Annual Book of ASTM Standards, ASTM, 501-508.

ASTM Standard E8M (1999) Standard Test Methods for Tension Testing of Metallic Materials, Annual Book of ASTM Standards. ASTM, 78-98.

Banabic, D., Kuwabara, T., Balan, T., and Comsa, D.S. (2004) An Anisotropic Yield Criterion for Sheet Metals, *Journal of Materials Processing Technology*, Vols. 157-158, pp. 462-465.

Banabic, D., Kuwabara, T., Balan, T., Comsa, D.S. and Julean, D. (2003) Non-Quadratic Yield Criterion for Orthotropic Sheet Metals under Plane-Stress Conditions, *International Journal of Mechanical Sciences*, Vol. 45, pp. 797-811.

Barlat, F. and Lian, J. (1989) Plastic Behavior and Stretchability of Sheet Metals. Part I: A Yield Function for Orthotropic Sheets Under Plane Stress Conditions, *International Journal of Plasticity,* Vol. 5, pp. 51-66.

Bate, P.S. and Wilson, D.V. (1986) Analysis of the Bauschinger Effect, *Acta Metallurgica*, Vol 34, No. 6, pp. 1097-1105.

Bayraktar, E. and Altintas, S. (1996) Square Cup Deep Drawing and 2-D Draw-Bending Analysis of Hadfield Steel, *Journal of Materials Processing Technology*, Vol. 60, 183-190.

Bjørkhaug, L. and Welo, T. (2004) Local Calibration of Aluminium Profiles in Rotary Stretch Bending – Anisotropy Effects, *Proceedings of the 8th International Conference on Numerical Methods in Industrial Forming Processes*, Ghosh, S., Castro, J.C. and Lee, J.K. (eds.), Columbus, Ohio, June 13 – 17, pp 749 – 754.

Boger, R.K., Wagoner, R.H., Barlat, F., Lee M.G., and Chung K. (2005) Continuous, Large Strain, Tension/Compression Testing of Sheet Material, *International Journal of Plasticity,* Vol. 21, pp. 2319-2343.

Boresi, A.P., Schmidt, R.J. and Sidebottom, O. M. (1993) Advanced Mechanics of Materials, John Wiley & Sons Inc., New York.

Bron, F. and Besson, J. (2004) A Yield Function for Anisotropic Materials: Application to Aluminum Alloys, *International Journal of Plasticity*, Vol. 20, pp. 937–963.

Bruhns, O.T., Gupta, N.K., Meyers, A.T.M. and Xiao, H. (2003) Bending of an Elastoplastic Strip with Isotropic and Kinematic Hardening, *Archive of Applied Mechanics*, Vol. 72, pp. 759-778.

Brunet, M., Morestin, F. and Godereaux, S. (2001) Nonlinear Kinematic Hardening Identification for Anisotropic Sheet Metals With Bending-Unbending Tests, *Journal of Engineering Materials and Technology*, Vol. 123, pp. 378-383.

Buranathiti, T., and Cao, J. (2004) An Effective Analytical Model for Springback Prediction in Straight Flanging Processes, *International Journal of Materials and Product Technology*. Vol. 21, No. 1-3, pp. 137-153.

Cao, J., Kinsey, B. and Solla, S.A. (2000a) Consistent and Minimal Springback Using a Stepped Binder Force Trajectory and Neural Network Control, *Journal of Engineering Materials and Technology*, Vol. 122, pp. 113-118.

Carden, W.D., Geng, L.M., Matlock, D.K. and Wagoner, R.H. (2002) Measurement of Springback, *International Journal of Mechanical Sciences*, Vol. 44, pp. 79-101.

Carleer B.D., Streppel, A.H., Koenis, P.T.G. and Huétink, J. (1996) The Analysis of Planar Anisotropic Sheet Metal, Sheet Metal, *Proceedings of the International Conference on Sheetmetal: SHEMET '96*, Kals, H.J.J., Shirvani, B., Singh, U.P. and Geiger, M. (eds.), Enschede, The Netherlands, April 1–3 1996.

Cazacu, O. and Barlat, F. (2003) Application of the Theory of Representation to Describe Yielding of Anisotropic Aluminum Alloys, *International Journal of Engineering Science*, Vol. 41, pp. 1367–1385.

Cazacu, O. and Barlat, F. (2004) A Criterion for Description of Anisotropy and Yield Differential Effects in Pressure-Insensitive Metals, *International Journal of Plasticity*, Vol. 20, pp. 2027–2045.

Cazacu, O., Barlat, F. and Nixon, M.E. (2004) New Anisotropic Constitutive Models for HCP Sheet Forming Simulations, *Proceedings of the 8th International Conference on Numerical Methods in Industrial Forming Processes*, Ghosh, S., Castro, J.C. and Lee, J.K. (eds.), Columbus, Ohio, June 13 – 17, pp 1046 – 1051.

Chaboche, J.L. (1986) Time-Independent Constitutive Theories for Cyclic Plasticity, *International Journal of Plasticity*, Vol. 2, pp. 149-188.

Chait, R. (1973) The Strength Differential of Steel and Ti Alloys as Influenced by Test Temperature and Microstructure, *Scripta Metallurgica*, Vol. 7, No. 4, pp. 351-354.

Chakrabarty, J. (1987) Theory of Plasticity, McGraw-Hill Inc., New York.

Chen, Q., Kawagoishi, N., and Nisitani, H. (2000) Evaluation of Fatigue Crack Growth Rate and Life Prediction of Inconel 718 at Room and Elevated Temperatures, *Materials Science and Engineering A*, Vol. 277, No. 1-2, pp. 250-257.

Chu, C.C. (1984) A Three-Dimensional Model of Anisotropic Hardening in Metals and Its Application to the Analysis of Sheet Metal Formability, *Journal of the Mechanics and Physics of Solids*, Vol. 32, No. 3, pp. 197-212.

Chu, C.C. (1987) The Analysis of Multiaxial Cyclic Problems with an Anisotropic Hardening Model, *International Journal of Solids and Structures*, Vol. 23, No. 5, pp. 569-579.

Chun, B.K., Jinn, J.T. and Lee, J.K. (2002a) Modeling the Bauschinger Effect for Sheet Metals, Part I: Theory, *International Journal of Plasticity*, Vol. 18, pp. 571 .595.

Chun, B.K., Kim, H.Y. and Lee, J.K. (2002b) Modeling the Bauschinger Effect for Sheet Metals, Part II: Applications, *International Journal of Plasticity*, Vol. 18, pp. 597-616.

Clausen, A.H., Hopperstad, O.S. and Langseth, M. (2001) Sensitivity of Model Parameters in Stretch Bending of Aluminium Extrusions, *International Journal of Mechanical Sciences*, Vol. 43, pp. 427-453.

Cleveland, R.M. And Ghosh, A.K. (2002) Inelastic Effects on Springback in Metals, *International Journal of Plasticity*, Vol. 18, pp. 769-785.

Danckert, J. and Nielsen, K.B. (1998) Determination of the Plastic Anisotropy *r* in Sheet Metal Using Automatic Tensile Test Equipment, *Journal of Materials Processing Technology,* Vol. 73, pp. 276 – 280.

DeGarmo, E.P., Black, J.T, and Kohser, R. (1988) Materials and Processes in Manufacturing, Macmillan Publishing Co., New York.

Delannay, L., Logé, R.E., Signorelli, J.W. and Chastel, Y. (2004) Prediction of the planar anisotropy of springback after bending of a textured zinc sheet, *Proceedings of the 8th International Conference on Numerical Methods in Industrial Forming Processes*, Ghosh, S., Castro, J.C. and Lee, J.K. (eds.), Columbus, Ohio, June 13 – 17, pp 1058 – 1063.

Dillamore, I.L., Hazel, R.J., Watson, T.W., and Hadden, P. (1971) An Experimental Study of the Mechanical Anisotropy of Some Common Metals, *International Journal of Mechanical Sciences*, Vol. 13, pp. 1049-1061.

Dingli, J.P., Abdul-Latif, A., and Saanouni, K. (2000) Predictions of the Complex Cyclic Behavior of Polycrystals using a Self-Consistent Modeling, *International Journal of Plasticity*, Vol. 16, pp. 411-437.

Drucker, D.C. (1973) Plasticity Theory, Strength-Differential (SD) Phenomenon, and Volume Expansion in Metals and Plastics, *Metallurgical Transactions*, Vol. 4, pp. 667-673.

Drucker, D.C., and Palgen, L. (1981) On Stress-Strain Relations Suitable for Cyclic and other Loading, *Journal of Applied Mechanics*, Vol. 48, No. 3, pp. 479 – 485.

Du, C., Wu, J., Militisky, M., Principe, J., Garnett, M., and Zhang, L. (2004) Springback Control With Variable Binder Force – Experiments And FEA Simulation, *Proceedings of the 8th International Conference on Numerical Methods in Industrial Forming Processes*, Ghosh, S., Castro, J.C. and Lee, J.K. (eds.), Columbus, Ohio, June 13 – 17, pp 970 – 976.

El-Domiaty, A. A., Shabara, M. A. N. and Al-Ansary, M. D. (1996) Determination of Stretch-Bendability of Sheet-Metals, *International Journal of Machine Tools and Manufacture*, Vol. 36, No. 5, pp. 635-650.

Fereshteh-Saniee, F. and Montazeran, M.H. (2003) A Comparative Estimation of the Forming Load in the Deep Drawing Process, *Journal of Materials Processing Technology*, Vol. 140, pp. 555–561.

Gardiner, F.J. and Philadelphia, PA. (1957) The Springback of Metals, *Transactions of the ASME*, Vol. 79, pp. 1-9.

Gau, J.-T. and Kinzel, G.L. (2001) A New Model for Springback Prediction in which the Bauschinger Effect is Considered, *International Journal of Mechanical Sciences*, Vol. 43, pp. 1813-1832.

Geng, L. and Wagoner, R.H. (2002) Role of Plastic Anisotropy and its Evolution on Springback, *International Journal of Mechanical Sciences*, Vol. 44, 123-148.

Geng, L., Shen, Y. and Wagoner, R.H. (2002) Anisotropic Hardening Equations Derived from Reverse-Bend Testing, *International Journal of Plasticity*, Vol. 18, pp. 743-767.

Gil, C.M., Lissenden, C.J., and Lerch, B.A. (1999a) Unusual Nonlinear Response of Some Metalic Materials, *Mechanics of Materials*, Vol. 31, 565–577.

Gil, C.M., Lissenden, C.J., and Lerch, B.A. (1999b) Determination of Yield of Inconel 718 by Axial-Torsional Loading at Temperatures up to 649°C, *Journal of Testing and Evaluation*, Vol. 27, No. 5, pp. 327-336.

Gilmour, K.R., Leacock, A.G. and Ashbridge, M.T.J. (2004) The Influence of Plastic Strain Ratios on the Numerical Modelling of Stretch Forming, *Journal of Materials Processing Technology*, Vol. 152, pp. 116-125.

Gomes, C.J., Onipede, O., Lovell, M., Norman, B. and Rajgopal, J. (2001) Analysis of Springback Using Simulation and Experimental Design, MF01-248, SME.

Gotoh, H., Katoh, M. and Yamashita, M. (1997) Studies of Stretch-Drawing Process of Sheet Metals, *Journal of Materials Processing Technology*, Vol. 63, pp. 123-128.

Gotoh, M., Kim, Y.-S. and Yamashita, M. (2003) A Fundamental Study of Can Forming by the Stretch-Drawing Process, *Journal of Materials Processing Technology*, Vol. 138, pp. 545–550.

Han, P. (ed.) (1992) Tensile Testing, ASM.

Harth, T., Schwan, S., Lehn, J., and Kollmann, F. G. (2004) Identification of Material Parameters for Inelastic Constitutive Models: Statistical Analysis and Design of Experiments, *International Journal of Plasticity*, Vol. 20, No. 8-9, pp. 1403-1440.

Hertzberg, R.W. (1995) Deformation and fracture Mechanics of Engineering Materials, John Wiley & Sons Inc., New York.

Hill, R. (1948) A Theory of the Yielding and Plastic Flow of Anisotropic Metals, *Proceedings of the Royal Society of London,* Vol. A193, 281–297.

Hill, R. (1950) The Mathematical Theory of Plasticity, Clarendon Press, Oxford.

Hill, R. (1979) Theoretical Plasticity of Textured Aggregates, *Mathematical Proceedings of Cambridge Philosophical Society*, Vol. 85, pp. 179-191.

Hill, R. (1990) Constitutive Modeling of Orthotropic Plasticity in Sheet Metals, , *Journal of the Mechanics and Physics of Solids*, Vol. 38, No. 3, pp. 405-417.

Hodge, P.G. Jr. (1957) General Theory of Piecewise Linear Plasticity Based on Maximum Shear, *Journal of the Mechanics and Physics of Solids*, Vol. 5, pp. 242 – 260.

Hosford, W.F. and Caddell, R.M. (1983) Metal Forming: Mechanics and Metallurgy, Prentice-Hall, Englewood Cliffs, N.J.

Hosford, W.S. (1972) A Generalize Isotropic Yield Criterion, *Journal of Applied Mechanics*, Vol. 39, pp. 607–609.

Hosford, W.S. (1985) Comments On Anisotropic Yield Criteria, *International Journal of Mechanical Sciences*, Vol. 27, No. 7-8, pp. 423-427.

Hosford, W.S. (1996) On the Crystallographic Basis of Yield Criteria, *Textures and Microstructures,* Vols. 26-27, pp. 479-493.

Hu, J., Jonas, J.J. and Ishikawa, T. (1998) FEM Simulation of the Forming of Textured Aluminum Sheets, *Materials Science and Engineering*, Vol. A256, pp. 51-59.

Huang, H.-M., Liu, S.-D. and Jiang, S. (2001) Stress and Strain Histories of Multiple Bending-Unbending Springback Process, *Journal of Engineering Materials and Technology*, Vol. 123, pp. 384-390.

Huétink, J., Streppel, A.H., and Vreede, P.T. (1995) Development of Experimental Verification of Constitutive Elquations for Anisotropic Sheet Metal, *Proceedings of the International Conference on Computational Plasticity: Fundamentals and Applications (COMPLAS)*, Barcelona, Spain, April 3 – 6, pp. 2271–2282.

Huh, H. and Choi, H. (2000) Modified Membrane Finite Element Formulation for Sheet Metal Forming Analysis of Planar Anisotropic Materials, *International Journal of Mechanical Sciences*, Vol. 42, No. 8, pp. 1623-1643.

Inco Alloy International (1985) Inconel Alloy 718, 4th ed.

Iyer, S.K. and Lissenden, C.J. (2000) Inelastic Anisotropy of Inconel 718: Experiments and Mathematical Representation, *Journal of Engineering Materials and Technology*, Vol. 122, 321–326.

Jain, M. (1990) Evolution of Internal Stress Variables During Cyclic Deformation of Copper, *Materials Science and Engineering*, Vol. A128, Pp. 183-193.

Jiang, W. (1994) Study of Two-Surface Plasticity Theory, *Journal of Engineering Mechanics,* Vol. 120, No. 10, 2179-2200.

Jiang, Y. and Kurath, P. (1996) Characteristics of the Armstrong-Frederick type plasticity models, *International Journal of Plasticity*, Vol. 12, No. 3, pp. 387-415.

Karafillis, A.P. and Boyce, M.C. (1992) Tooling Design in Sheet Metal Forming Using Springback Calculations, *International Journal of Mechanical Sciences*, Vol. 34, No. 2, pp. 113-131.

Khan, A.S. and Huang, S. (1995) Continuum Theory of Plasticity, John Wiley & Sons Inc., New York.

Khan, A.S., and Jackson, K.M. (1999) On the Evolution of Isotropic and Kinematic Hardening with Finite Plastic Deformation Part I: Compression/Tension Loading of OFHC Copper Cylinders, *International Journal of Plasticity,* Vol. 15, No. 12, pp. 1265-1275.

Kim, J.-B., Yang. D.-Y, Yoon, J.-W., and Barlat, F. (2000) The Effect of Plastic Anisotropy on Compressive Instability in Sheet Metal Forming, *International Journal of Plasticity*, Vol. 16, pp. 649-676.

Kishi, T. and Tanabe, T. (1973) The Bauschinger Effect and its Role in Mechanical Anisotropy, *Journal of the Mechanics and Physics of Solids*, Vol. 21, No. 5, pp. 303-315.

Kot, R. A. and Morris, J. W. (ed.) (1979) Structure and Properties of Dual-Phase Steels, *Proceedings of a symposium sponsored by the TMS-AIME Heat Treatment Committee at the AIME annual meeting*, New Orleans, L.A., February 19-21.

Kridli, G., and El-Gizawy, A., (1998) Modeling and Evaluation of Superplastic Forming of Weldalite™ 049 Sheet Products., MF98-233, SME.

Krieg, R.D. and Brown, K.H. (1996) Anisotropic Plasticity with Anisotropic Hardening and Rate Dependence, *Journal of Engineering Mechanics*, pp. 317-324.

Kulkarni, P. (2004) Effect of Strain Rates on Springback Predictions in 304-brushed Stainless Steel, *Proceedings of the 8th International Conference on Numerical Methods in Industrial Forming Processes*, Columbus, Ohio, June 13 – 17, pp 790 – 795.

Kulkarni, P. (2004) Effect of Strain Rates on Springback Predictions in 304-brushed Stainless Steel, *Proceedings of the 8th International Conference on Numerical Methods in Industrial Forming Processes*, Ghosh, S., Castro, J.C. and Lee, J.K. (eds.), Columbus, Ohio, June 13 – 17, pp 790 – 795.

Kumar, D.R. (2002) Formability Analysis of Extra-Deep Drawing Steel, *Journal of Materials Processing Technology*, Vol. 130–131, pp. 31–41.

Kuwabara, T., Ikeda, S. and Asano, Y. (2004) Effect of Anisotropic Yield Functions on the Accuracy of Springback Simulation, *Proceedings of the 8th International Conference on Numerical Methods in Industrial Forming Processes*, Ghosh, S., Castro, J.C. and Lee, J.K. (eds.), Columbus, Ohio, June 13 – 17, pp 887 – 892.

Lee, M.-G., Kim D., Kim, C., Wenner, M.L., and Chung, K. (2005a) Spring-Back Evaluation of Automotive Sheets Based on Isotropic-Kinematic Hardening Laws and Non-Quadratic Anisotropic Yield Functions, Part III: Applications, *International Journal of Plasticity*, Vol. 21, pp. 915–953.

Lee, M.-G., Kim D., Kim, C., Wenner, M.L., Wagoner, R.H., and Chung, K. (2005b) Spring-Back Evaluation of Automotive Sheets Based on Isotropic-Kinematic Hardening Laws and Non-Quadratic Anisotropic Yield Functions, Part II: Characterization of Material Properties, *International Journal of Plasticity*, Vol. 21, pp. 883–914.

Lee, S.W. and Yang, D.Y. (1998) An Assessment of Numerical Parameters Influencing Springback in Explicit Finite Element Analysis of Sheet Metal Forming Process, *Journal of Materials Processing Technology*, Vol. 80-81, pp. 60-67.

Lee, W.B. and To, S. (1995) Computer Modeling of the Effect of Rolling Schedule on the Plastic Anisotropy of Cold-Rolled Aluminum Sheets, *Journal of Materials Processing Technology,* Vol. 48, 173–178.

Leu, D.-K. (1997) A Simplified Approach for Evaluating Bendability and Springback in Plastic Bending of Anisotropic Sheet Metals, *Journal of Materials Processing Technology,* Vol. 66, pp. 9-17.

Li, K.P., Carden, W.P. and Wagoner, R.H. (2002a) Simulation of Springback, *International Journal of Mechanical Sciences*, Vol. 44, pp. 103 – 122.

Li, S., Hoferlin, E., Van Bael, A., Van Houtte, P. and Teodosiu, C. (2003) Finite Element Modeling of Plastic Anisotropy Induced by Texture and Strain-Path Change, *International Journal of Plasticity*, Vol. 19, pp. 647-674.

Li, X., Yang, Y., Wang, Y., Bao, J. and Li, S. (2002b) Effect of the Material-Hardening Mode on the Springback Simulation Accuracy of V-Free Bending, *Journal of Materials Processing Technology*, Vol. 123, pp. 209-211.

Lindkvist, G. and Lindbäck, T. (2004) Estimate of Material Parameters using Inverse Modeling and their Application to Sheet Metal Forming Simulations, *Proceedings of the 8th International Conference on Numerical Methods in Industrial Forming Processes*, Ghosh, S., Castro, J.C. and Lee, J.K. (eds.), Columbus, Ohio, June 13 – 17, pp 869 – 874.

Lissenden, C.J., Gil, C.M. and Lerch, B.A. (1999) A Methodology for Determining Rate-Dependent Flow Surfaces for Inconel 718, *Journal of Testing and Evaluatiun*, Vol. 27, No. 6, pp. 402-41.

Liu, G., Lin, Z., and Bao, Y. (2002) Improving Dimensional Accuracy of a U-Shaped Part Through an Orthogonal Design Experiment, *Finite Elements in Analysis and Design*, Vol. 39, No. 2, pp. 107-118.

Logan, R.W. and Hosford, W.F. (1980) Upper-Bound Anisotropic Yield Locus Calculations Assuming <111>-Pencil Glide, *International Journal of Mechanical Sciences*, Vol. 22, No. 7, pp. 419-430.

Lorentzen, T., Daymond, M.R., Clausen, B., and Tome, C.N. (2002) Lattice Strain Evolution during Cyclic Loading of Stainless Steel, *Acta Materialia*, Vol. 50, pp. 1627–1638.

Mattiasson, K. and Sigvant, M. (2004) Material Characterization and Modeling for Industrial Sheet Forming Simulations, *Proceedings of the 8th International Conference on Numerical Methods in Industrial Forming Processes*, Ghosh, S., Castro, J.C. and Lee, J.K. (eds.), Columbus, Ohio, June 13 – 17, pp 875 – 880.

Mellor, P.B. (1982) Experimental Studies of Plastic Anisotropy in Sheet Metal, Mechanics of Solids, Hopkins, H.G. and Sewell, M.J. (eds.), Pergamon Press, Oxford.

Mróz, Z. (1967) On the Description of Anisotropic Workhardening, *Journal of the Mechanics and Physics of Solids*, Vol. 15, pp. 163-175.

Muthler, A., Düster, A., Volk, W., Wagner, M., and Rank, E. (2004) High order finite elements applied to the computation of elastic spring back in sheet metal forming, *Proceedings of the 8th International Conference on Numerical Methods in Industrial Forming Processes*, Ghosh, S., Castro, J.C. and Lee, J.K. (eds.), Columbus, Ohio, June 13 – 17, pp 946 – 951.

Naceur, H., Ben-Elechi, S., Knopf-Lenoir, C., and Batoz, J.L. (2004) Response Surface Methodology for the Design of Sheet Metal Forming Parameters to Control Springback Effects using the Inverse Approach, , *Proceedings of the 8th International Conference on Numerical Methods in Industrial Forming Processes*, Ghosh, S., Castro, J.C. and Lee, J.K. (eds.), Columbus, Ohio, June 13 – 17, pp 1991 – 1996.

Nakamachi, E., Xie, C.L. and Harimoto, M. (2001) Drawability Assessment of BCC Steel Sheet by Using Elastic/Crystalline Viscoplastic Finite Element Analyses, *International Journal of Mechanical Sciences*, Vol. 43, pp. 631-652.

Papeleux, L. and Ponthot, J.-P. (2002) Finite Element Simulation of Springback in Sheet Metal Forming, *Journal of Materials Processing Technology*, Vols. 125–126, pp. 785–791.

Park, D.-W. and Oh, S.-I (2004) A Four-Node Shell Element with Enhanced Bending Performance for Springback Analysis, *Computer Methods in Applied Mechanics and Engineering*, Vol. 193, pp. 2105-2138.

Pearce, R. (1991) Sheet Metal Forming, IOP Publishing Ltd., Bristol.

Pourboghrat, F. and Chu, E. (1995a) Prediction of Spring-back and Side-wall Curl in 2-D Draw Bending, *Journal of Materials Processing Technology*, Vol. 50, pp. 361-374.

Pourboghrat, F. and Chu, E. (1995b) Springback in Plain Strain Stretch/Draw Sheet Forming, *International Journal of Mechanical Sciences*, Vol. 36, No. 3, 327-341.

Pourboghrat, F., Chung, K., and Richmond, O. (1998) A Hybrid Membrane/Shell Method for Rapid Estimation of Springback in Anisotropic Sheet Metals, *Journal of Applied Mechanics*, Vol. 65, 671-684.

Pourboghrat, F., Karabin, M.E., Becker, R.C. and Chung, K. (2000) A Hybrid Membrane/Shell Method for Calculating Springback of Anisotropic Sheet Metals Undergoing Axisymmetric Loading, *International Journal of Plasticity*, Vol. 16, pp. 677-700.

Prager, W. and Providence, R.I. (1956) A New Method of Analyzing Stresses and Strains in Work-Hardening Plastic Solids, *Journal of Applied Mechanics*, Vol. 23, pp. 493–496.

Queener, C.A. and De Angelis, R.J. (1968) Elastic springback and residual Stresses in Sheet Metal Formed by Bending, *ASM Transactions*, Vol. 61, No. 4, pp. 757-768.

Ragai, I. and Younan, M.Y.A. (2001) Finite Element Modeling of Superplastic Forming of Weldalite^{TM} 049 Alloy, 42nd AIAA/ASME/ASCE/AHS/ASC Structural Dynamics, and Materials Conf. & Exhibit, Seattle, Washington, U.S.A., April 16-19.

Ragai, I., and Nemes, J.A. (2005) Experimental Investigation of Springback of Dual-Phase Steels, SAE 2005 Conf. & Exhibit, Detroit, Michigan, U.S.A., April 11-14.

Ragai, I., Younan, M.Y.A. (2003) Numerical Simulation of the Superplastic Forming Process of WeldaliteTM (049) Alloy, SME.

Rasmussen, K.J.R., Burns, T., Bezkorovainy, P. and Bambach, M.R. (2003) Numerical Modelling of Stainless Steel Plates in Compression, *Journal of Constructional Steel Research*, Vol. 59, No. 11, pp. 1345-1362.

Rauch, E.F. (1998) Plastic Anisotropy of Sheet Metals Determined by Simple Shear Tests, *Materials Science and Engineering*, Vol. A241, pp. 179-183.

Ray, R.K. (1986) Orientation Distribution Function Analysis of Texture in a Dual-Phase Steel, *Materials Science and Engineering*, Vol. 77, pp. 169-174.

Sakaki, T., Ohnuma, K., Sugimoto, K. And Ohtakara, Y. (1990) Plastic Anisotropy of Dual-Phase Steels, *International Journal of Plasticity*, Vol.6, pp. 591-613.

Samuel, M. (2000) Experimental and Numerical Prediction of Springback and Side Wall Curl in U-Bendings of Anisotropic Sheet Metals, *Journal of Materials Processing Technology*, Vol. 105, pp. 382-393.

Schedin, E. and Melander, A. (1987) On the Strain Distribution during the Stretch-Forming of Low- and High-Strength Sheet Steels, *Journal of Mechanical Working Technology*, Vol. 15, pp. 181-202.

Sharman, A. Dewes, R.C., and Aspinwall, D.K. (2001) Tool Life when High Speed Ball Nose End Milling Inconel 718™, *Journal of Materials Processing Technology*, Vol. 118, No. 1-3, pp. 29-35.

Siebel, V.-E. (1954) Der Niederhalterdruck beim Tiedziehen, *Stahl und Eisen*, Vol. 74, No. 3, pp. 155-158.

Sinou, J.-J. and Macquaire, B. (2003) Anisotropic Behaviour Law for Sheets Used in Stamping: A Comparative Study of Steel and Aluminium (Loi de Comportement Anisotrope pour Tôles Utilisées en Emboutissage : Étude Comparative de l'Acier et l'Aluminium), *Comptes Rendus Mecanique*, Vol. 331, pp. 33-40.

Skelton, R.P., Maier, H.J., and Christ, H.-J. (1997) The Bauschinger Effect, Masing Model and the Ramberg–Osgood Relation for Cyclic Deformation in Metals, *Materials Science and Engineering*, Vol. A238, pp. 377–390.

Song, N., Qian, D., Cao, J., Liu, W.K., and Li, S. (2001) Effective Models for Prediction of Springback in Flanging, *Journal of Engineering Materials and Technology*, Vol. 123, pp. 456-461.

Sowerby, R., Uko, D.K. And Tomita, Y. (1979) A Review of Certain Aspects of the Bauschinger Effect in Metals, *Materials Science and Engineering*, Vol. 41, pp. 43–58.

Stainless Plate Products (2005) http://www.sppusa.com/

Suh, Y.S., Saunders, F.I., and Wagoner, R.H. (1996) Anisotropic Yield Functions with Plastic-Strain-Induced Anisotropy, *International Journal of Plasticity*, Vol. 12, pp. 417-438.

Swift, H.W. (1948) Plastic Bending Under Tension, *Seventh International Congress for Applied Mechanics*, London, UK, Sept. 5-11.

Takahashi, H., Motohashi, H., and Tsuchida, S. (1996) Development of Plastic Anisotropy in Rolled Aluminum Sheets, *International Journal of Plasticity*, Vol. 12, pp. 935-949.

Takamura, M., Ohura, K., Sunaga, H., Kuwabara, T., Makinouchi, A., and Teodosiu, C. (2004) Sheet Forming Simulation Using a Static FEM Program and Considering the Elastic Deformation of Tools, *Proceedings of the 8th International Conference on Numerical Methods in Industrial Forming Processes*, Ghosh, S., Castro, J.C. and Lee, J.K. (eds.), Columbus, Ohio, June 13 – 17, pp 940 – 945.

Tan, Z., Magnusson, C. and Persson, B. (1994) The Bauschinger Effect in Compression-Tension of Sheet Metals, *Materials Science and Engineering*, Vol. A183, pp. 31-38.

Tan, Z., Persson, B., and Magnusson, C. (1995) Plastic Bending of Anisotropic Sheet Metals, *International Journal of Mechanical Sciences*, Vol. 37, No. 4, 405-421.

Tang, S.C. (1994) Quasi-Static Analysis of Sheet Metal Forming Processes – A Design Evaluation Tool, *Journal of Materials Processing Technology*, Vol. 45, pp. 261-266.

Tang, S.C., Xia, Z.C., and Ren, F. (2001) Application of the Radial Return Method to Compute Stress Increments from Mróz's Hardening Rule, *Journal of Engineering Materials and Technology*, Vol. 123, pp. 398-402.

Uemori, T., Okada, T., and Yoshida, F. (2000) FE Analysis of Springback in Hat-Bending with Consideration of Initial Anisotropy and the Bauschinger Effect, *Key Engineering Materials*, Vols. 177-180, 497-502.

Vij, S. and Date, P.P. (2004) Studies of Variation of Springback with Curved Line of Bend and Variable Balnkholder Force, *Proceedings of the 8th International Conference on Numerical Methods in Industrial Forming Processes*, Ghosh, S., Castro, J.C. and Lee, J.K. (eds.), Columbus, Ohio, June 13 – 17, pp 784 – 789.

Viswanathan, V., Kinsey, B., and Cao, J. (2000) Experimental Implementation of Neural Network Springback Control for Sheet Metal Forming, submitted to *Journal of Engineering Materials and Technology.*

Wang, C., Kinzel, G. and Altan, T. (1993) Mathematical Modeling of Plane-Strain Bending of Sheet and Plate, *Journal of Materials Processing Technology*, Vol. 39, pp. 279-304.

Wang, H. and Barkey, M.E. (1999) A Strain Space Nonlinear Kinematic Hardening/Softening Plasticity Model, *International Journal of Plasticity*, Vol. 15, pp. 755-777.

Wang, J.F., Wagoner, R.H., and Matlock, D.K. (2004a) Effect of Anticlastic Curvature of Aluminum Sheets after the Draw-Bend Test, *Proceedings of the 8th International Conference on Numerical Methods in Industrial Forming Processes*, Ghosh, S., Castro, J.C. and Lee, J.K. (eds.), Columbus, Ohio, June 13 – 17, pp 820 – 825.

Wang, J.F., Wagoner, R.H., Carden, W.D., Matlock, D.K., and Barlat, F. (2004b) Creep and Anelasticity in the Springback of Aluminum, *International Journal of Plasticity*, Vol. 20, No. 12, pp 2209-2232.

Wang, J.F., Wagoner, R.H., Matlock, D.K., and Barlat, F. (2005) Anticlastic Curvature in Draw-Bend Springback, *International Journal of Solids and Structures*, Vol. 42, No. 5-6, pp. 1287-1307.

Wang, X. and Cao, J. (2000) On the Prediction Of Side-Wall Wrinkling in Sheet Metal Forming Processes, *International Journal of Mechanical Sciences*, Vol. 42, pp. 2369-2394.

Weiher, J., Rietman, B., Kose, K., Ohnimus, S., and Petzoldt, M. (2004) Controlling Springback with Compensation Strategies, *Proceedings of the 8th International Conference on Numerical Methods in Industrial Forming Processes*, Ghosh, S., Castro, J.C. and Lee, J.K. (eds.), Columbus, Ohio, June 13 – 17, pp 1011 – 1015.

World Auto Steel (2005) http://www.worldautosteel.org/

Xie, C.L. and Nakamachi, E. (2002) Investigations of the Formability of BCC Steel Sheets by Using Crystalline Plasticity Finite Element Analysis, *Materials and Design*, Vol. 23, pp. 59-68.

Yan,B., Laurin, K., Xu, K., Sadagopan, S., Huang, M., Chintamani, J., and Lalam S. H. (2003) A New Dual Phase Steel for Automotive Body Panels, SAE paper number 2003-01-0518, 2003.

Yoon, J.-W., Pourboghrat, F., Chung, K. and Yang, D.-Y. (2002) Springback Prediction for Sheet Metal Forming Process Using A 3d Hybrid Membrane/Shell Method, *International Journal of Mechanical Sciences*, Vol. 44, pp. 2133–2153.

Yoshida, F. and Uemori, T. (2002) A Model of Large-Strain Cyclic Plasticity Describing the Bauschinger Effect and Workhardening Stagnation, *International Journal of Plasticity*, Vol. 18, pp. 661-686.

Yoshida, F., Uemori, T., and Fujiwara, K. (2002) Elastic–Plastic Behavior of Steel Sheets Under In-Plane Cyclic Tension–Compression at Large Strain, *International Journal of Plasticity*, Vol. 18, pp. 633 – 659.

Yoshida, F., Urabe, M. and Toropov, V.V. (1998) Identification of Material Parameters in Constitutive Model for Sheet Metals from Cyclic Bending Tests, *International Journal of Mechanical Sciences*, Vol. 40, Nos. 2-3, pp. 237-249.

Zaky, A.M., Nassr, A.B. and El-Sebaie, M.G. (1998) Optimum Blank Shape of Cylindrical Cups in Deep Drawing of Anisotropic Sheet Metals, *Journal of Materials Processing Technology*, Vol. 76, pp. 203-211.

Zhao, K.M., and Lee, J.K. (2001a) Material Properties of Aluminum Alloy for Accurate Draw-Bend Simulation, *Journal of Engineering Materials and Technology*, Vol. 123, pp. 287-292.

Zhao, K.M., and Lee, J.K. (2001b) Generation of Cyclic Stress-Strain Curves for Sheet Metals, *Journal of Engineering Materials and Technology*, Vol. 123, pp. 391-397.

Ziegler, H. (1959) A modification of Prager's Hardening Rule, *Quarterly of Applied Mathematics*, pp. 55-65.

Żmudzki, A., Pidvysotskyy, V., Paćko, M. and Kusiak, J. (2004) Minimization of Anisotropic Effect During Thin Cup Free Bulging Process Using the Artificial Neural Networks Optimization Technique, *Proceedings of the 8th International Conference on Numerical Methods in Industrial Forming Processes*, Ghosh, S., Castro, J.C. and Lee, J.K. (eds.), Columbus, Ohio, June 13 – 17, pp 2126 – 2131.